POLITECNICO DI MILANO

School of Industrial and Information Engineering
Department of Chemistry, Materials and Chemical Engineering "Giulio Natta"
Master of Science in
Materials Engineering and Nanotechnology

TiO_2 NANOTUBES FOR THE PHOTOCATALYTIC DEGRADATION OF THREE ORGANIC DYES IN SINGLE, BINARY AND TERNARY MIXTURES

Supervisor:
Prof. Maria Vittoria DIAMANTI

Co – supervisor:
Prof. Maria Pia PEDEFERRI
Ing. Umberto BELLÈ

Filippo Pelizzari 905028

Academic Year 2018 – 2019

Contents

Table of Figures

Table of Tables

Sommario

Lo scopo di questa tesi consiste nel valutare l'applicabilità e l'efficienza dei processi fotocatalitici su campioni di titanio anodizzato per degradare soluzioni contenenti diversi coloranti organici, puntando successivamente all'applicazione di queste tecniche per la purificazione di vere e proprie acque reflue industriali i cui attuali metodi di smaltimento, come adsorbimento e filtrazione, risultano essere estremamente costosi e non troppo efficaci.
"The climate and ecological emergency is right here, right now. But it has only just begun. It will get worse." [1]. Con queste parole Greta Thunberg all'Assemblee Nationale de Paris il 23 luglio 2019 vuole evidenziare come la tematica della crisi ambientale globale sia una delle più grandi sfide che l'umanità deve affrontare al fine di garantire un futuro al pianeta.
Gli agenti chimici inorganici usati nella produzione tessile includono: gli alcali comuni e gli acidi inorganici, silicato di sodio, solfato di sodio e idrosolfato, candeggine, solfato d'ammonio e sodio perborato, cloriti e solfiti.
Viene utilizzato anche un range più vario di materiali organici i quali includono: acidi organici, sapone, amido, oli di oleina, detergenti, ammorbidenti, additivi e agenti coloranti. Questo lavoro si concentra sul degrado dei coloranti organici, in quanto di immediata individuazione e semplice monitoraggio in laboratorio.
Nel capitolo 1 viene presentato lo stato dell'arte partendo dalle proprietà del biossido di titanio e dalla sua produzione con morfologia nanotubolare tramite vari metodi specialmente il metodo dell'anodizzazione che permette di ottenere una struttura specifica con elevata area superficiale. Successivamente verrà spiegato il meccanismo della fotocatalisi specialmente per la fotodegradazione di coloranti organici di cui sono riportate le principali caratteristiche. Alla fine si parlerà di acque reflue provenienti da industrie tessili con un approfondimento sui metodi di smaltimento di quest'ultime e dei complicati metodi di analisi delle soluzioni composte da più coloranti.
Nel secondo capitolo sono presentati tutti i materiali e le macchine utilizzati durante le attività di laboratorio, con una spiegazione dettagliata di tutti i metodi di preparazione e svolgimento adottati per la realizzazione degli esperimenti di fotocatalisi.
Nel terzo capitolo saranno portate le conclusioni ottenute da questi esperimenti per capire quali sono i meccanismi e le cinetiche di reazione e quali sono le loro utili proprietà e quali le limitazioni.

Abstract

The purpose of this thesis is to evaluate the efficiency and the applicability of photocatalytic processes on anodized titanium used to degrade different mixtures made by organic dyes, pointing on the possible application of these techniques for the purification industrial waste waters whose actual disposal methods, like absorbance and filtration, result being extremely expensive and not so efficient.

“The climate and ecological emergency is right here, right now. But it has only just begun. It will get worse.” [1]. With these words Greta Thunberg at the Assemble Nationale de Paris on the 23rd of July 2019 wants to highlight that the thematic of the global environmental crisis is one of the biggest challenges that humanity must deal with to guarantee the future of our planet.

The inorganic chemicals used in textile processing include the common alkalis and inorganic acids, sodium silicate, sodium sulfide and hydrosulfite, bleaches, ammonium sulfate and sodium perborate, chloride and sulfate. An even wider range of organic materials is used which includes organic acids, soap, starch, organic sizes, olein oils, detergents, softeners, dyeing additives and dyes [2]. The experimental work will address the latter pollutants, as they are easy to recognize as well as to study.

In chapter 1 a state of the art is presented about titanium dioxide properties and its production in the form of nanotubes in several ways concentrating on the electrochemical anodization method which provides a specific architecture and a large internal surface area [3].

Subsequently the photocatalysis mechanism is explained mainly for the photodegradation of organic dyes whose principal characteristics are also reported. In the end textile industries wastewaters are presented with a deepening on the problems given by their disposal and the complicated analysis of these solutions made by multiple dyes.

In chapter 2 all the materials and experimental methods utilized during laboratory activities are presented, with also a detailed explanation of all the preparation methods adopted for the realization of photocatalytic experiments.

In chapter 3 the data obtained in the experimental work are reported and discussed to understand which are the kinetics of reactions and what are their useful properties and limitations.

1. Chapter 1 : Introduction and state of art

1.1 Titanium and titanium dioxide

Titanium was once considered a rare metal, but nowadays it is one of the most important and used metals in the industry. The element was first discovered in England by Gregor in 1790, although it did not receive its name until Klaproth named it after the mythological first sons of the earth, the Titans, in 1795. Chemically, titanium is one of the transition elements in group IV and period 4 of Mendeleev's periodic table. It has an atomic number of 22 and an atomic weight of 47.9. Being a transition element, titanium has an incompletely filled d shell in its electronic structure [4].
In Table 1.1 some of titanium most important properties have been reported.

Table 1.1. Summary of physical properties of unalloyed titanium [4]

Property	Value
Atomic number	22
Atomic weight (g/mol)	47.90
Crystal structure	
Alpha, hexagonal, closely packed	
c (Å)	4.6832 ± 0.0004
a (Å)	2.9504 ± 0.0004
Beta, cubic, body centered	
a (Å)	3.28 ± 0.003
Density (g cm^{-3})	4.54
Coefficient of thermal expansion, α, at 20 °C (K^{-1})	8.4×10^{-6}
Thermal conductivity (W/(m K))	19.2
Melting temperature (°C)	1668
Boiling temperature (estimated) (°C)	3260
Transformation temperature (°C)	882.5
Electrical resistivity	
High purity (μΩ cm)	42
Commercial purity (μΩ cm)	55
Modulus of elasticity, α, (GPa)	105
Yield strength, α, (MPa)	692
Ultimate strength, α, (MPa)	785

Titanium has a large variety of applications mostly guided by a synergy of excellent properties. Its high strength combined with a low density, which gives to it the highest

strength-to-weight ratio of all structural metals, has driven the structural applications of this metal in architecture, as well as the aerospace and automotive fields; in addition, the low thermal expansion coefficient and thermal conductivity make it compatible with typical ceramic and construction materials leading to the construction of buildings that are able to provide a significant reduction of the energy needed for heating and cooling [5].

Titanium can react with oxygen in air forming titanium dioxide (TiO_2), a n-type semiconductor that has gained great interest thanks to its remarkable properties including chemical stability and resistance to corrosion. Moreover, the crystalline forms of TiO_2 that can be synthesized by several routes provide a wide range of potential applications in gas sensing, water splitting, photo electrocatalysis and photovoltaic cells. It is also largely used in photocatalysis which is attracting much attention from both fundamental and practical viewpoints. It has been used in many others industrial areas including environmental purification, solar cell, gas sensors, pigments and cosmetics [6].

This oxide represents the major percentage of titanium that is utilized nowadays in practical applications, and it is also one of the most extensively utilized and studied among all transition metal oxides making it one of the most investigated compounds in material science. It exists in many different structures with slight differences between properties; the three principal allotropic forms for titanium dioxide are: anatase, rutile and brookite whose structures are presented in Figure 1.1.

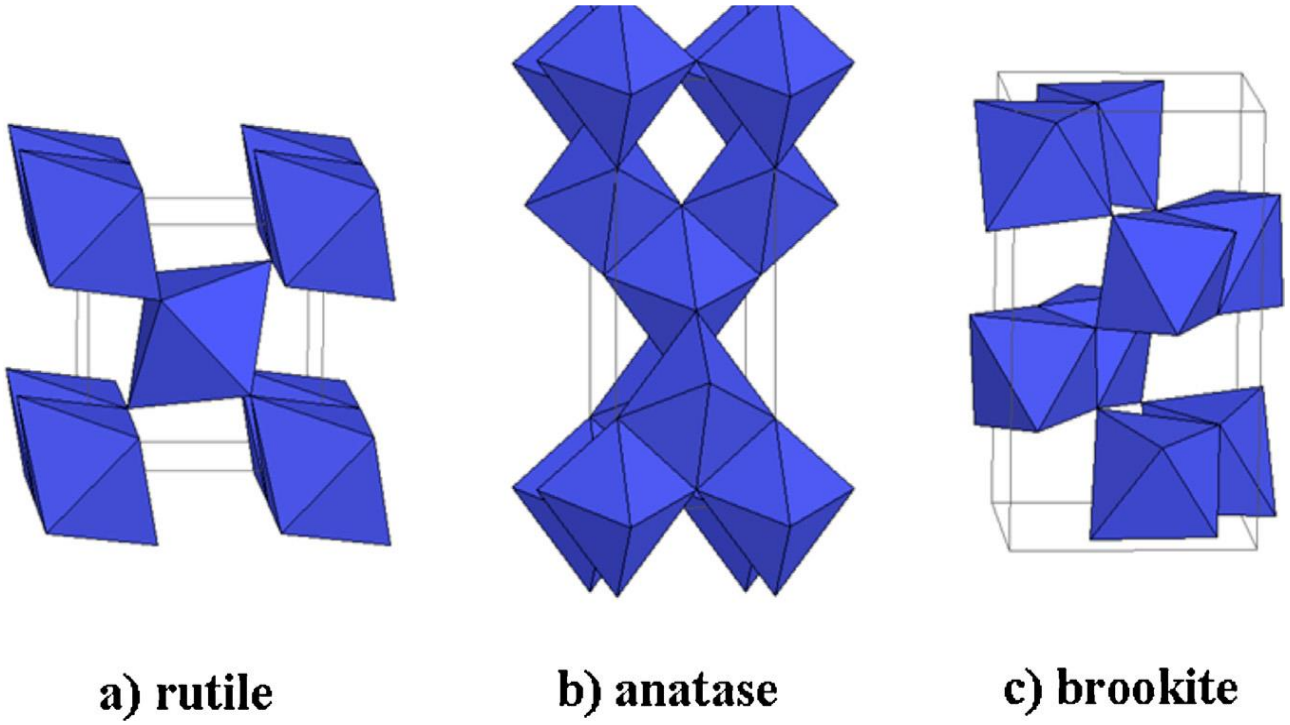

Figure 1.1. TiO_2 crystal structures: rutile (a), anatase (b) and brookite (c) [63]

Rutile is a stable form characterized by a tetragonal structure, anatase is also tetragonal but metastable form; among the crystalline forms of titania, anatase is generally recognized to be the most interesting for engineered applications as opposed to the rutile and brookite forms. Brookite instead presents an orthorhombic metastable structure which is very difficult to synthetize, consequently being the least studied and valuable one [7].
The main drawback is the band gap value of its crystal structures, equal to 3.02 eV for rutile and 3.20 eV for anatase, which correspond to the need for UV-A irradiation to activate its photocatalytic performances [8].

1.2 Titanium dioxide nanotubes

Titanium nanotubes can be obtained starting from TiO_2, also known as titanium (IV) oxide, that is the natural occurring oxide of titanium whose atomic alignment and structure can be seen in Figure 1.2.

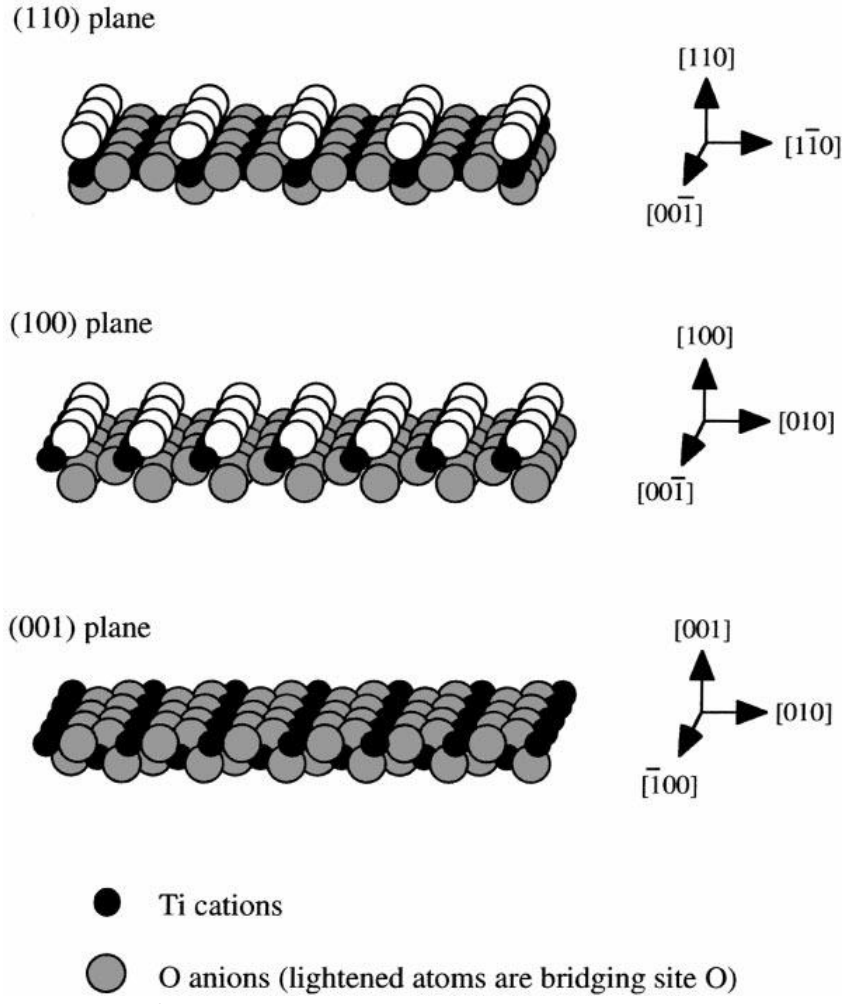

Figure 1.2. Schematic illustration of the atomic alignments on ideal TiO_2 (1 1 0), (1 0 0), and (0 0 1) single crystal faces [64]

Titanium dioxide morphology can be organized in the form of nanotubes using an appropriate synthesis method like: anodic oxidation, electrochemical lithography, photoelectrochemical etching, sol-gel processing, hydrothermal synthesis and template synthesis [9].

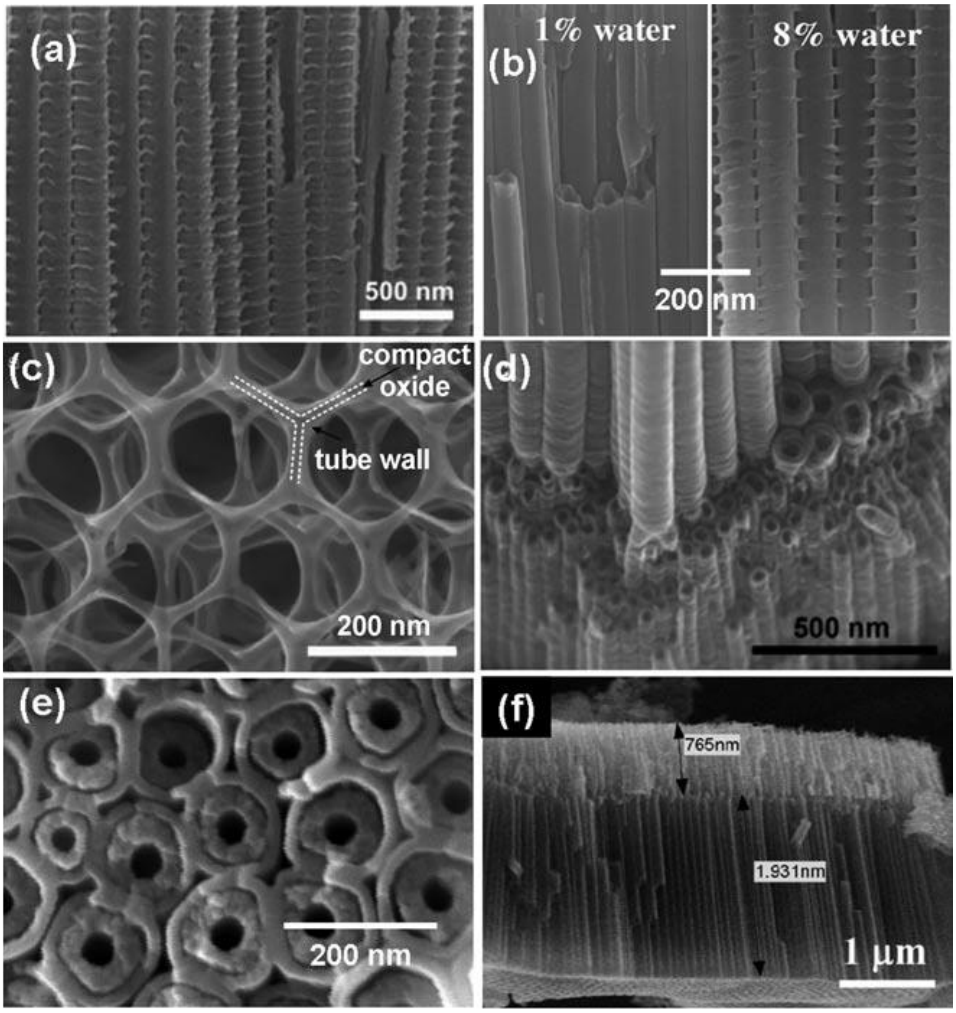

Figure 1.3. Advanced TiO_2 nanotube morphologies: a) Bamboo nanotubes fabricated by alternating voltage anodization, b) smooth to bamboo-tube transition induced by variation of H_2O content in the electrolyte, c) nano lace, d) branched nanotubes by voltage stepping, e) double-walled nanotubes, f) amphiphilic double-layer [10]

Little changes in the parameters of production of TiO_2 nanotubes will lead to a variety of different morphologies, and as can be seen in Figure 1.3 different structures can be obtained like: bamboo nanotubes, nano laces, branched nanotubes, double walled nanotubes, amphiphilic double-layers, etc [10].

Low-dimensional nanostructured materials have attracted considerable attention recently due to their unique physical properties compared to their bulk counterparts resulting from the larger surface area in a small geometrical area and fewer interfacial grain boundaries which can assist in promoting charge transport, for example TiO_2 nanowires possess a significantly higher photocatalytic activity than the standard titanium dioxide nanoparticles [11].

Talking about their potential applications in photocatalysis, nanoelectronics and optoelectronic nanodevices dimensionality is a crucial factor in determining the properties of nanomaterials, and the control of their size and shape is of great interest. Among the techniques employed for the realization of these structures anodization seems to be the more promising one, indeed with this technique nanotubes made by this oxide can be grown directly on titanium samples, at room temperature, guaranteeing a perfect adhesion to the substrate and an extremely controlled grown which is uniform and highly ordered [12].

Over the past decades, nanotubular geometries have been studied for a huge amount of applications and activities, which is evident from the over 100 000 papers published on "nanotubes" up to 2013. The main reason for this interest is the anticipated economic impact in the form of applications that are based on specific physical and chemical features of these structures.

Among the transition metal oxides the wide band gap of titanium dioxide, especially when it is in form of nanotubes, found immediate interest, mainly due to the perspective of using the structures to enhance the properties in Grätzel-type solar cells, whose representation can be seen in Figure 1.4, and other photocatalytic materials [13].

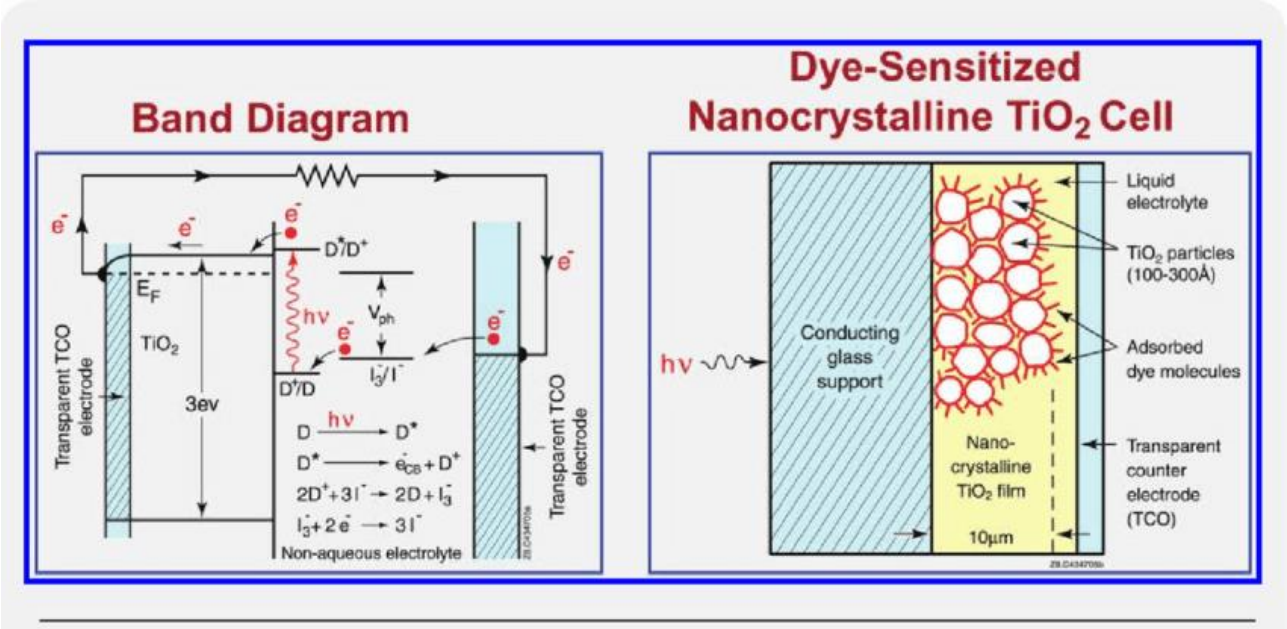

Figure 1.4. A schematic representation of the Grätzel-type solar cell [13]

The ability to control the architecture of titanium dioxide on a nanoscale level can be expected to positively impact a variety of economically important technologies, so now some of the principal fabrication methods that can be used for this purpose will be presented. Electrochemical lithography, whose scheme can be seen in Figure 1.5, works by transferring a pattern on a conductive mold to a target with an electrochemical reaction. This process is based on selective laser irradiation of an anodically formed oxide film following precise steps. At first an anodic oxidation of the titanium substrate in an anodizing electrolyte is needed, followed by the patterning of the oxide by an excimer laser irradiation in air. Now the process of electrochemical dissolution of the metal from the irradiated areas takes place in an electropolishing electrolyte and in the end an ultrasonic cleaning is performed to remove the protruding oxide film resulting from under-etching [14].

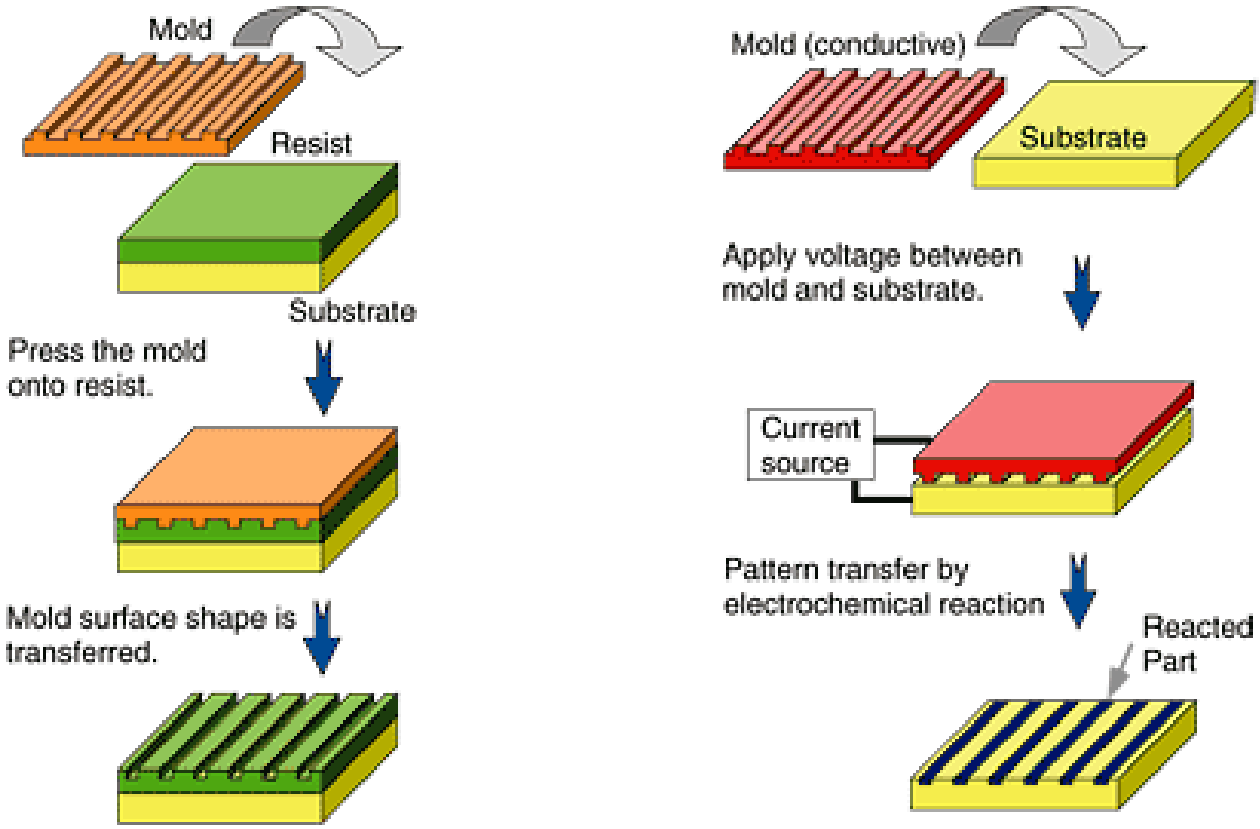

Figure 1.5. Concepts of conventional nanoimprint (left) and nanoelectrode lithography (right) [65]

There exist a lot of etching procedures that are extensively used for the production of semiconductor devices, because these processes are able to alter physical dimensions of the material providing holes and slices or cutting up semiconductor disks into individual chips. With advancing technology an improvement is needed in all etching procedures in which reactions are usually isotropic or preferential with respect to specific crystal planes limiting precision and resolution while the process advances in all directions. Photoetching instead limits the reaction in the part of the surface that is irradiated confining the etching reaction in a narrow area providing better resolution and precision resulting in anisotropic etching. In the photochemical process the semiconductor is in contact with an electrochemical solution and the area to be etched is illuminated by an electromagnetic radiation that will provide enough energy to excite electrons from the valence band to the conduction one. A time varying potential is applied between the semiconductor and a counter electrode dissolving the more electromagnetic element that is taken away by the solution used [15].

Another well-known method used for the production of TiO_2 nanostructures is the sol-gel process in which the initial system is represented by a solution where different polymerization and polycondensation processes lead to the gradual formation of the solid phase network.

The sol formed in this way is then subjected to a series of operations that are: gelling, drying, pressing, drawing and casting, which result in various structural and phase transformations. This is done to obtain powders, fibers, coatings and bulk monolithic products from the same initial composition.

This synthesis methods can be divided into three groups depending on the initial precursors that can be made by: aqueous solutions of metal salts, metal alkoxide solutions and mixed organic and inorganic precursors.

The sol-gel approach follows a simple scheme, reported in Figure 1.6, is a quite cheap technique that allows to obtain, even at low temperatures, a fine product whose chemical composition is well defined [16].

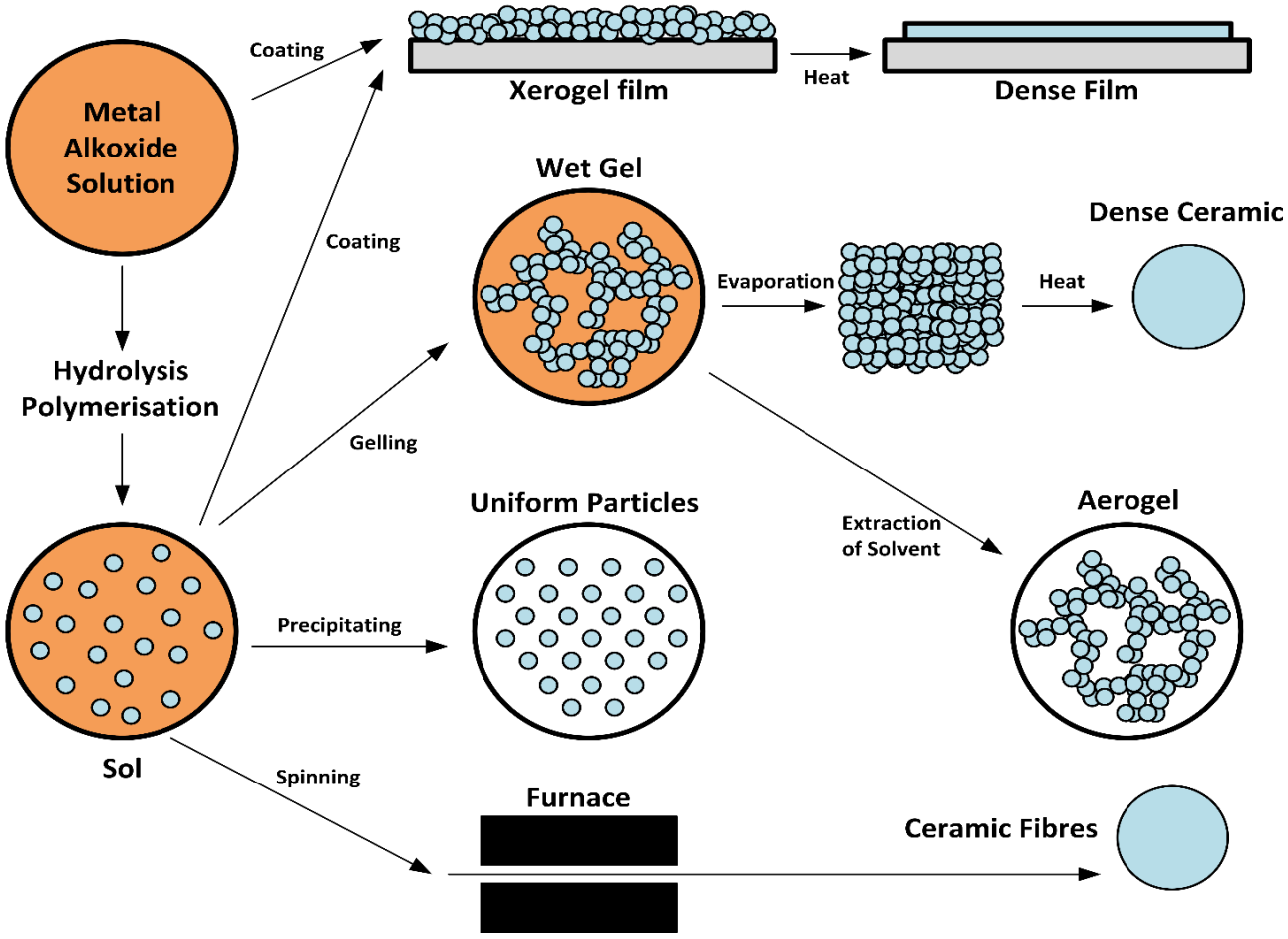

Figure 1.6. Sol-Gel technology scheme [66]

This process is used for the production of protective coatings, thin films and fibers, nanoscale powders and products for opto-mechanical and medical applications.
Right now the fabrication of TiO_2 nanotubes, with a well ordered structure and precise orientation, using this method is still a challenge because of the complexity of sol-gel chemistry [17].

Hydrothermal synthesis is also very used method because with this process it is possible to synthetize anatase, rutile, or a mixture of both TiO_2 phases at low temperature, without additives and this is very important from the scientific, economic and technological standpoints. The crystallographic phase in the particles seems to be essential for special applications, in fact anatase and rutile demonstrates better photocatalysis activity than does the single TiO_2 phase. However, the transformation of metastable anatase to thermodynamically stable rutile during heat treatment usually is associated with a reduction in the specific surface area of the particles, which decreases its catalytic capability. In Hydrothermal synthesis chemical reactions can occur in aqueous or organo-aqueous environments, under the simultaneous application of heat and pressure, permitting to prepare highly crystalline TiO_2 particles at lower temperatures, respect to other procedures. A monodisperse, spherical anatase phase can be prepared using this method at a temperature of only 250°C, and high sinterability has been demonstrated, even at 900°C. Nevertheless, anatase-to-rutile phase transformation did not occur up to 800°C [7].

There are different methods for performing this technique: temperature-difference, temperature-reduction and metastable-phase.

The most used one is the temperature difference method in which supersaturation is achieved by reducing the temperature in the crystal growth zone.

The nutrient is placed in the lower part of the autoclave, whose typical shape can be seen in Figure 1.7, filled with a specific amount of solvent then the autoclave is heated in order to create two temperatures zone.

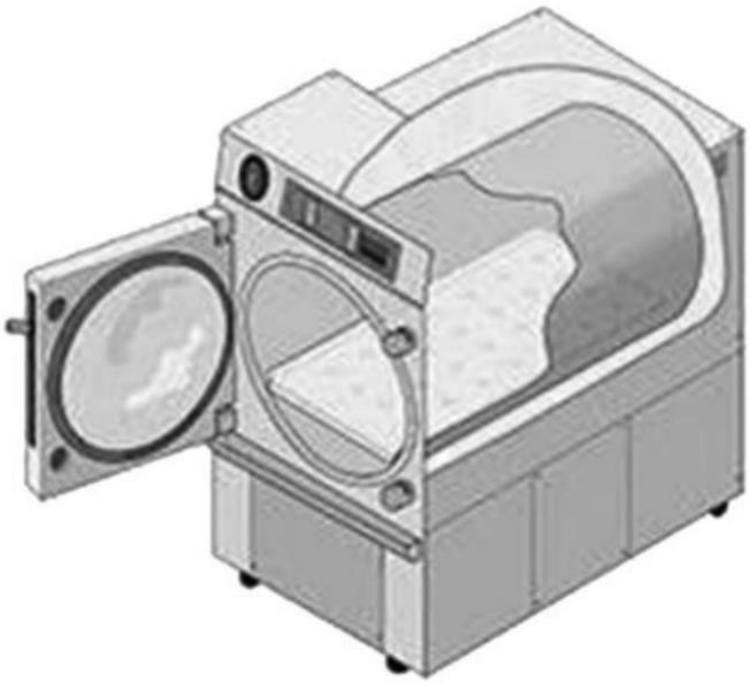

Figure 1.7. Cutaway illustration of a cylindrical-chamber autoclave [18]

The nutrient dissolves in the hotter zone while the saturated aqueous solution in the lower part is transported up by convective motion of the solution, at the same time the cooler and denser solution counterflows down in the autoclave so the solution becomes supersaturated in the upper part as the result of the reduction in temperature and crystallization sets in.

In the temperature reduction technique instead, the crystallization takes place without a temperature gradient between the growth and dissolution zones but the supersaturation in achieved by a gradual reduction in temperature of the solution in the autoclave. The disadvantage of this method is the difficulty in controlling the growth process and introducing seed crystals. The last technique is the metastable-phase one that is based on the difference in solubility between the phase to be grown and that serving as the starting material, so the nutrient is made by compounds that are thermodynamically unstable under the growth conditions, while the solubility of the metastable phase exceeds that of the stable one, and the latter crystallize due to the dissolution of the metastable phase [18].

Among these processes for preparing TiO_2 nanostructures, the electrochemical anodization of titanium in fluorinated electrolytes seems to be the most promising one because it is a relatively simple and high controllable method to synthesize porous or tubular structures. TiO_2 nanotubes fabricated by this method are highly ordered, have high-aspect ratios and are oriented perpendicular to the substrate; moreover the nanotube arrays have a well-defined pore size, wall thickness and tube length [19].

This technique will be described in detail in the following subchapter.

1.3 Anodizing

Anodization is an electrochemical process used to obtain a protective oxide film on a metallic surface which plays the role of the anode in an electrolytic cell.
Prior to anodizing an appropriate pretreatment of the surface is necessary which comprised of polishing, degreasing and pickling to produce a chemically clean surface ready to be anodized. During the process a thick oxide layer is grown by passing a direct current between the anode, i.e., the titanium piece to be oxidized, and a cathode, through an electrolytic solution which develops hydrogen gas at the cathode [20].
This process is used on different metals including magnesium, zinc, zirconium, tantalum, titanium and mostly on aluminum alloys.
This process is carried out for various applications, for example to provide decorative finishing as anodization on titanium under different conditions results in a range of stable attractive colors and it can be used to produce a decorative coating on the articles.
The passive film that covers this metal when exposed to the atmosphere, that is only a few nanometers thick, has no color; nevertheless, by increasing the thickness of the native oxide, the surface acquires particular colors, which are due to interference phenomena as can be seen in the paintings in Figure 1.8 [21].

Figure 1.8. Paintings on titanium: colors obtained by anodic oxidation (by Pietro Pedeferri) [67]

The formation of titanium dioxide nanotubes by potenziostatic anodization proceeds following a simple scheme. In the first step the water is electrolyzed at the Ti anode, though reaction (R1.1), and a layer of compact anodic oxide resulted:

$$Ti + 2H_2O - 4e^- \rightarrow TiO_2 + 4H^+ \qquad (R1.1)$$

Then, chemical dissolution of the oxide as soluble fluoride complexes began to compete with the anodic oxidation, and a direct complexation of the high-field transported Ti cations also occurred at the oxide/electrolyte interface:

$$Ti^{4+} + 6F^- \rightarrow [TiF_6]^{2-} \qquad (R1.2)$$

$$TiO_2 + 6F^- + 4H^+ \rightarrow [TiF_6]^{2-} + 2H_2O \qquad (R1.3)$$

After that a compact layer of titanium oxide is formed on the titanium surface through reaction (R1.4):

$$[TiF_6]^{2-} + 2H_2O \rightarrow TiO_2 + 6F^- \qquad (R1.4)$$

Pitting of the oxide layer provides preferential locations for the field assisted chemical dissolution of TiO_2 by fluoride ions through these equations. Nanotubes dimensions will change dependently on the current density applied during these reactions: as it can be seen from Figures 1.9 and 1.10 the greatest is the current density applied the largest will become nanotubes that are formed. The pits are chemically dissolved further into the oxide layer; the pits provide the least resistive route for the current, therefore the high dissolution rate forms the inside of the tubes from the pits [22].

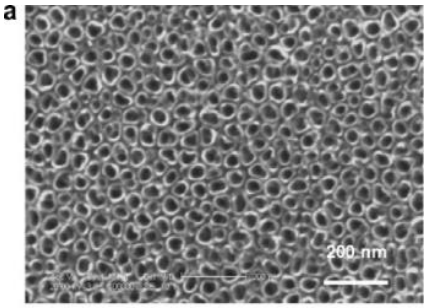

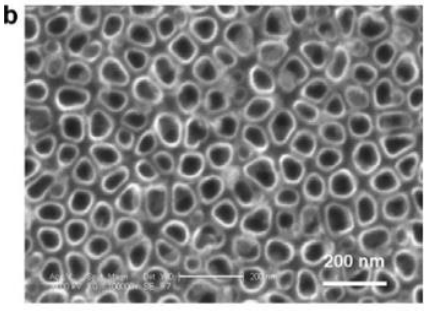

Figure 1.9. SEM images of the TiO_2 nanotubes obtained with different current densities: (a) 10 mA/cm^2, (b) 15 mA/cm^2 [19]

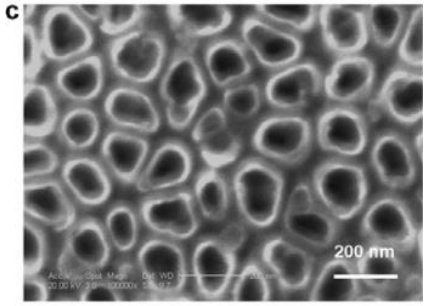

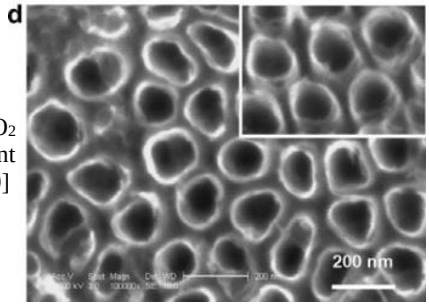

Figure 1.10. SEM images of the TiO_2 nanotubes obtained with different current densities: (c) 15 mA/cm^2, (d) 20 mA/cm^2 [19]

It is well known that titanium is a reactive metal that is rapidly attacked by atmospheric oxygen. Since anodizing provides a uniform stable protective film on the metal this process is also performed to reduce the friction on sliding surfaces, as an anodic film is generally harder than bare metal, it helps in reducing friction on moving parts. In addition, an anodic coating, owing to its porous nature, improves lubricity by providing a base for retention of lubricants or at contrary, again thanks to its porous nature, this process can be used to provide better adhesion for paints and glues [23].
For the purpose of this thesis the processes of anodization of titanium are of course of major importance; in Figure 1.11 a schematic set-up for these anodization experiments is presented.

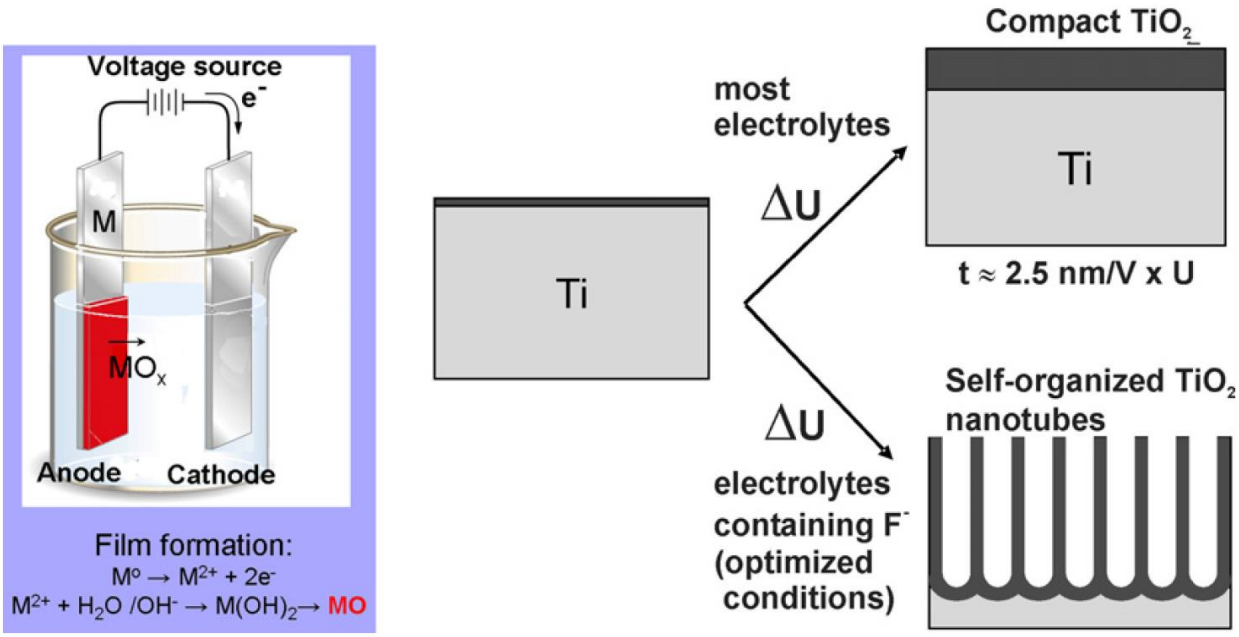

Figure 1.11. Schematic set-up for anodization experiments. Anodization leads to an oxidation of metal species that form a solid oxide on the metal surface [68]

Depending on the anodization conditions, mainly the voltage, the electrolyte composition and the temperature, the solid oxide layer shape can be controlled making it compact or even nanotubular. To achieve an ideal self-ordering of the nanotubes the use of the optimized anodization parameters is crucial. When compact films are produced, their thickness is linearly correlated to the applied voltage, which gives the possibility to extrapolate the oxide growth rate under certain conditions by measuring the oxide thickness obtained by optical methods, as reported in most literature works, or by coulometric or impedance measurements. However, only in the last few decades a correct control of the anodizing process has been achieved, which is of fundamental importance to the development of engineered TiO_2 surfaces.

An example of how the manipulation of anodizing parameters can be used to obtain different nanotubular morphologies is well represented by Figure 1.12 in which it can be seen that the use of neutral electrolytes, especially organic ones, can provide nanotubes lengths that are more than 100 µm thick while nanotubes obtained in an acidic media are only a few hundred nanometers thick [5].

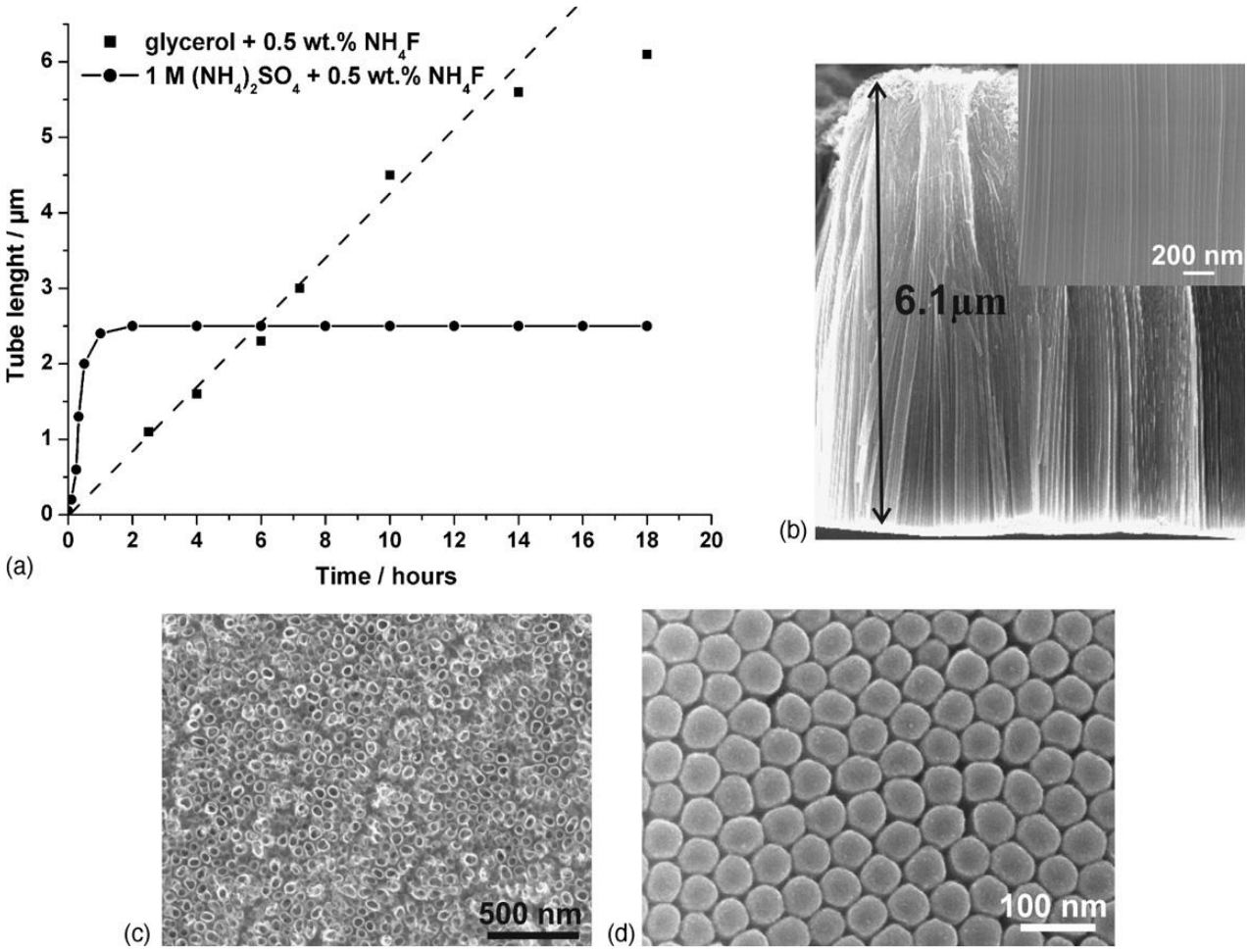

Figure 1.12. The tube length as a function of anodization time obtained directly from cross-section measurements of samples formed during different times in glycerol + 0.5 wt.% NH_4F and 1M $(NH_4)2SO_4$ + 0.5 wt.% NH_4F at 20V at 20◦C. Selected SEM cross-sectional (b), top-view (c) and bottom-view (d) images of self-organized TiO2 nanotubes with length of 6.1m formed during 18 h. An average nanotube diameter is approximately 50 nm and an average pore spacing is approximately 65 nm. The inset in (b) shows the smooth walls of the nanotubes at higher magnification [5]

In fact in aqueous acidic electrolytes a local thinning of the oxide barrier layer happens and random growing pore starts, causing a gradual increase in the current density, until it reaches a steady-state so there is no more thickness change in the oxide barrier layer and is at this stage that the nanotube formation takes place. However, in neutral organic electrolytes after an initial exponential decay, the current density smoothly decreases in a monotonic way until it reaches a quasi-steady state, without appearing a local minimum. It could be explained on the basis of the different anodic conditions employed, which lead to a less passivation of the Ti substrate, so that the nanotube

growth occurs without previously random pore formation, due to the less aggressive nature of the organic non-acidic electrolyte [24].
Before anodization usually a pre-treatment on titanium must be done to uniformize the surface, for example polishing treatment is used to remove the natural oxide layer that is formed on the titanium surface when exposed to air, that thin oxide layer of course has not the properties requested for these kind of applications and also it will prevent the formation of a more thick and nanostructured oxide layer through passivation mechanism. In Table 1.2 it can be seen how minimal changes in operational parameters, for example operational temperature and electrolyte parameters, can affect final results.

Table 1.2. Evaluation of charge density, porosity and current efficiency during anodization [25]

Evaluation of charge density, porosity and current efficiency during anodization

Electrolyte	T (°C)	Q (C cm^{-2})	Porosity (%)	Current efficiency (%)
Glycerol + 0.5 wt.% NH_4F	0	0.48	65–85	≈100
Glycerol + 0.5 wt.% NH_4F	20	0.715	60–80	≈100
Glycerol + 0.5 wt.% NH_4F	40	0.96	55–75	≈100
Ethylene Glycol + 0.5 wt.% NH_4F	20	0.565	65–85	<100
1 M $(NH_4)_2SO_4$ + 0.5 wt.% NH_4F	20	2.791	70–80	30–40
1 M H_2SO_4 + 0.15 wt.% HF	20	2.022	70–80	5–15

Recently, several properties of TiO_2 nanotubes build with this technique have already been explored. For instance, the nanotubes show a high photo-response, when annealed they show high sensitivity to hydrogen when used as gas-sensor, they can change their surface wettability, they show significant light conversion efficiencies when dye-sensitized, they can act as a catalyst support for methanol electrooxidation, or they can be N-doped by annealing in NH_3 or by N-ion implantation (in order to make a photocatalyst that is active even in the visible light). Additionally, they can serve as a very suitable substrate for hydroxyapatite growth in biomedical application. [25]

Among anodizing techniques there is also the Anodic spark deposition (ASD), also called microarc oxidation or plasma electrolytic oxidation; this technique diverges from traditional anodizing not in the procedure but in the process parameters necessary to produce the micro-plasma state, which are far more onerous than those required by the anodizing procedures described above. This advanced plasma-chemical electrochemical method can be used for forming ceramic like surfaces on anodic metal substrates of valve metals as titanium [26].

ASD-induced crystallization is caused by compressive stresses arising from electrostriction, exerted by the electric field within the film and typically higher than 106 V/cm$_2$. This leads initially to the formation of anatase nuclei, while at higher voltages anatase undergoes an allotropic transformation to rutile, probably induced both by the increase in crystal- lite dimensions with time during the process and by annealing effects, as can be seen in Figure 1.13 [5].

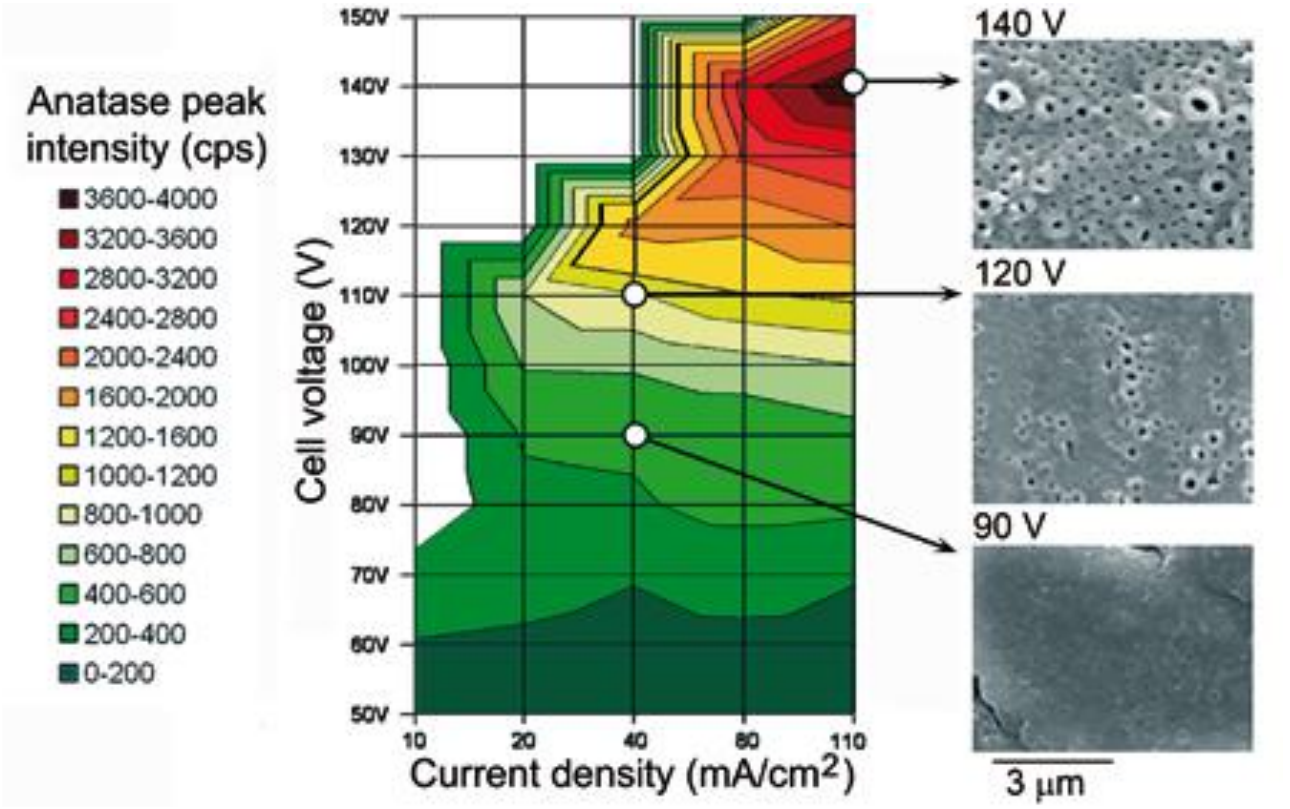

Figure 1.13. Map of anatase peak intensities as a function of applied cell voltage and current density for commercial purity titanium anodized in 0.5 M H_2SO_4, and surface morphology at 90 V, 110 V, and 140 V reproducing three different stages of the ASD process [5]

At first, a uniform oxide layer is formed on the titanium anode, whose thickness increases with increasing feeding voltage and creates a compact dielectric barrier that prevents ionic current from further flowing through the oxide itself. If the breakdown voltage of the oxide is exceeded the barrier is overcome and the oxide keeps growing and that is called dielectric breakdown.

The growing oxide is able to obstruct the current flow so all the available current is concentrated in the points where the oxide layer is weaker. At this points a localized micro-plasma state is created caused by atom ionization due to the extremely high values of the electric field concentrate, reaching temperatures up to 7700 °C.
Small electronic arcs, or sparks, are created moving along the surface due to the dielectric breakdown; these are characterized by cracking noises that becomes grater as the process move forward moving from one weak point to another also damaging adjacent oxide areas extending the process to the whole anodic surface.
Titanium and titanium alloys processed with this technique are broadly used in biomedical applications, like dental implants as can be seen in Figure 1.14 or orthopedic endoprostheses because of their good biocompatibility, resistance to corrosion, and their Young modulus, which is lower than stainless steel and cobalt-based alloys. The essential characteristic associated to this process is the increased cation mobility which causes ions from the electrolyte to be incorporated into the oxide during plasma quenching [5].

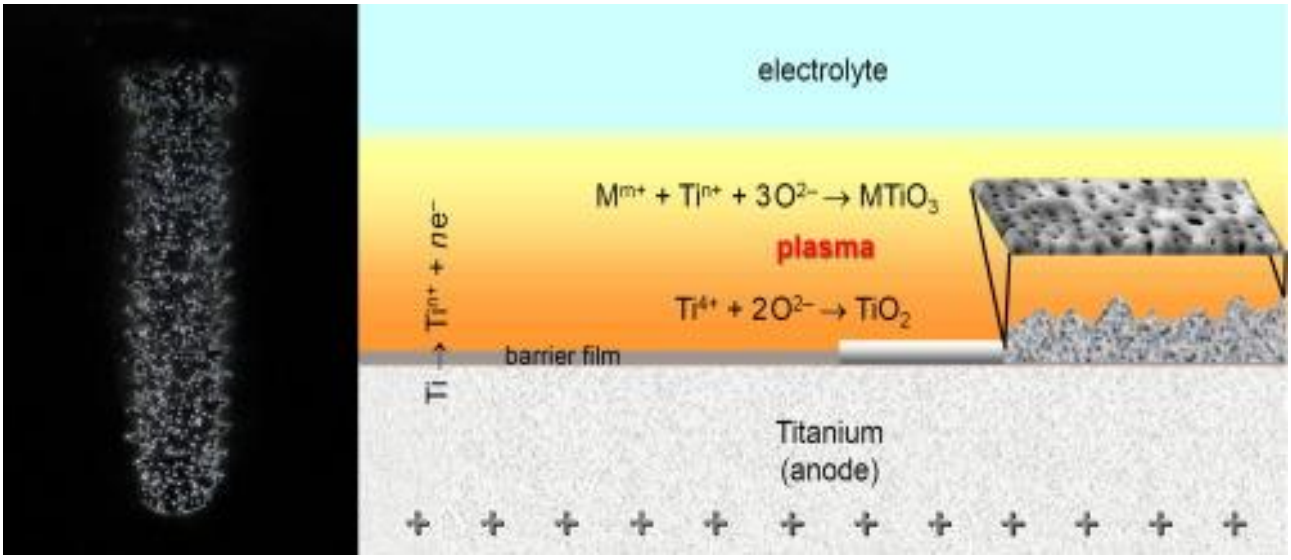

Figure 1.14. On the left is presented a visible micro plasma sparking at a Ti-dental implant as anode during ASD, on the right is presented the ASD process on the anode [26]

1.4 Photocatalysis

The term photocatalysis is defined as the acceleration of a photoreaction by the presence of a catalyst so it implies catalysis by light, while photoreaction is sometimes elaborated on as a "photoinduced" or "photoactivated" reaction, all to the same effect. In photogenerated catalysis, the photocatalytic activity depends on the ability of the catalyst to generate free radicals that can undergo secondary reactions. Thus, a photocatalyst is defined as a material that is able to absorb light, producing electron-hole pairs that enable chemical transformations of the reaction participants and regenerate its chemical composition after each cycle of such interactions [27].
There are two types of photocatalytic reactions: homogeneous and heterogeneous.
In the first one, reactants and the photocatalyst exist in the same phase, and the most commonly used homogeneous photocatalysts include ozone and photo-Fenton systems. In heterogeneous photocatalysis instead the catalyst is in a different phase from the reactants, this include a large variety of reactions: dehydrogenation, hydrogen transfer, mild and total oxidations, isotopic exchange, metal deposition and water detoxification which lead to a lot of practical applications as can be seen in Figure 1.15 [28].

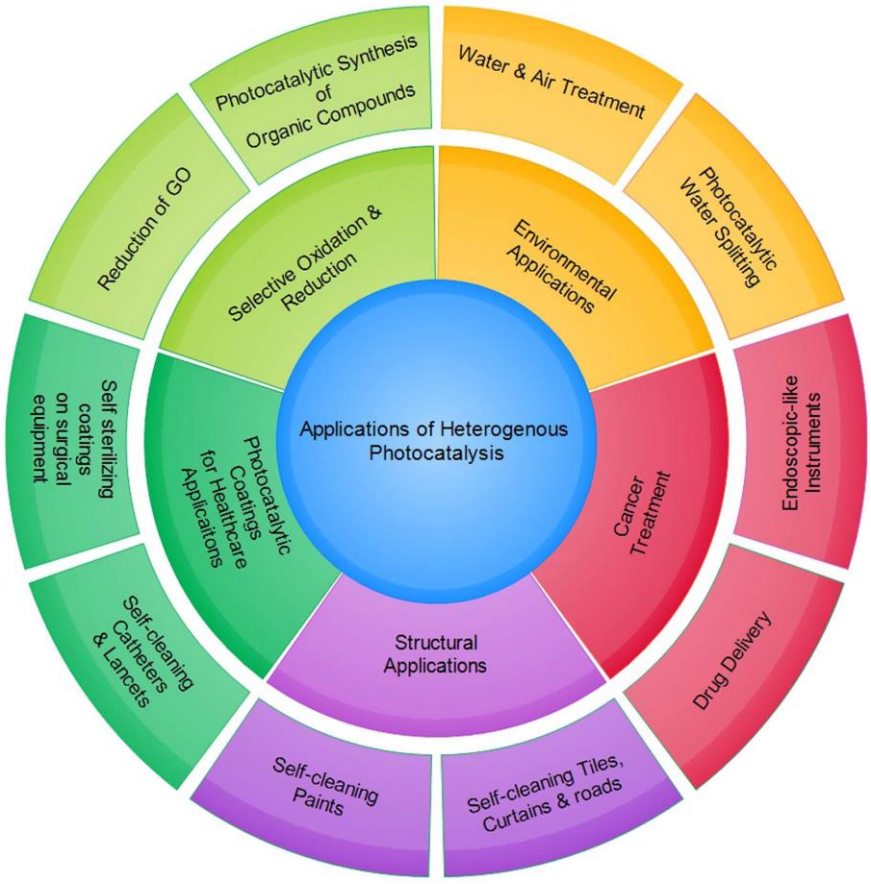

Figure 1.15. Applications of Heterogeneous Photocatalysis [30]

In this process, a semiconductor is activated with either ultraviolet light, visible light, or a combination of both, and photoexcited electrons are promoted from the valence band to the conduction band, forming an electron-hole pair. The photogenerated pair can reduce and/or oxidize a compound adsorbed on the photocatalyst surface. The photocatalytic activity of metal oxide comes from two sources: the generation of hydroxyl radicals by oxidation of hydroxyl anions (OH^-) or generation of oxygen radicals by reduction of molecular oxygen. Both the radicals and anions can react with pollutants to degrade or otherwise transform them to lesser harmful byproducts. Hence, the mechanism of heterogeneous photocatalysis involves a chain of oxidative and reductive reactions on the surface of the photocatalyst.
In a semiconductor, the lowest occupied and the highest unoccupied energy bands are divided by a bandgap. When light hits the semiconductor with a photon energy greater than or equal to electronic band gap of the semiconductor is illuminated on its surface, the electrons from the valence bands are photo-excited and promoted to conduction band in femtoseconds following the mechanisms that can be seen in Figure 1.16 [29].

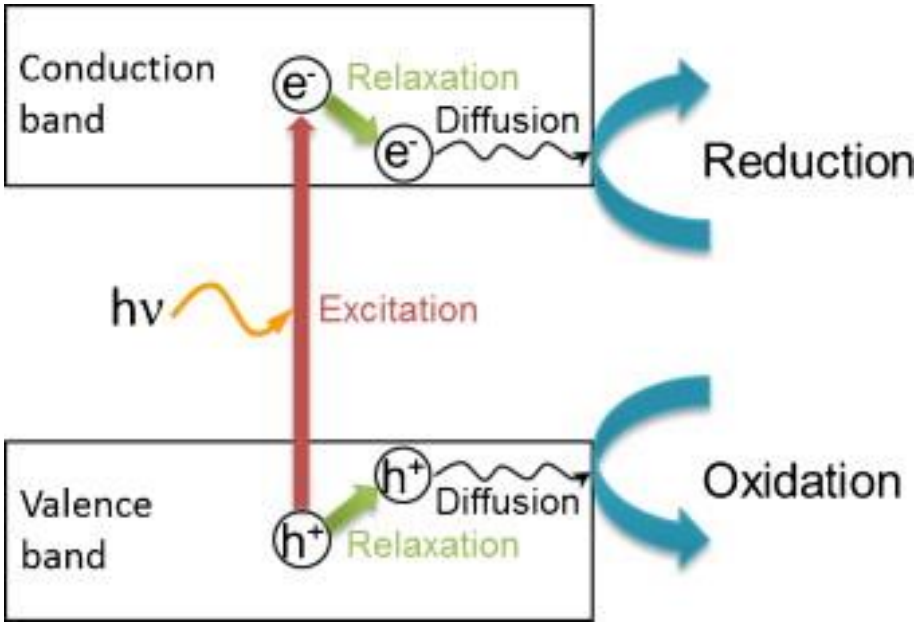

Figure 1.16. Schematic illustration of the formation of photogenerated charge carriers (hole and electron) upon absorption of ultraviolet (UV) light [29]

This leaves behind an unfilled valence band, called a hole, thus creating an electron–hole pair. If these electrons and holes are somehow trapped on the semiconductor surface and their recombination is prevented, this initiates a series of reactions postulated that can be seen in Figure 1.17.

$$\text{Photoexcitation: } TiO_2 + h\nu \rightarrow e^- + h^+, \quad (1)$$

$$\text{Entrapment of free electrons: } e^-_{CB} \rightarrow e^-_{TR}, \quad (2)$$

$$\text{Entrapment of holes: } h^+_{VB} \rightarrow h^+_{TR}, \quad (3)$$

$$\text{Charge carrier recombination: } e^-_{TR} + h^+_{VB} \rightarrow e^-_{CB} + \text{heat}, \quad (4)$$

$$\text{Photoexcited electron scavenging: } (O_2)_{ads} + e^- \rightarrow O_2^-, \quad (5)$$

$$\text{Oxidation of hydroxyls: } OH^- + h^+ \rightarrow OH\cdot, \quad (6)$$

$$\text{Photodegradation by } OH^- \text{ radicals: } R - H + OH\cdot \rightarrow R'\cdot + H_2O. \quad (7)$$

Figure 1.17. Classical scheme of reaction of a photocatalysis phenomenon [30]

The purpose of these photocatalysts design is to facilitate reactions between the excited electron with oxidants to produce reduced products and also reactions between holes and reductants to give oxidized products.

The OH· radicals generated in equation (6) reduces organic impurities into intermediate compounds, which are further degraded by the same reaction until CO_2 and water are released as by-products (equation (7)) [30].

The overall photocatalysis reaction as portrayed can be divided into five independent steps [31]:

I) Mass transfer of the organic pollutants or bacteria from the liquid phase to the TiO_2 surface.

II) Adsorption of organic contaminants into the photon activated photocatalyst surface.

III) The generation of OH· radicals and H_2O_2 followed by the chemical degradation of the contaminants.

IV) Desorption of the intermediate or final products from the surface of TiO_2.

V) Mass transfer of the intermediate from the interface to the bulk liquid phase.

In recent years a lot of researches has been developed for studying the behavior of different semiconductors for photodegradation experiments; the most utilized one is of course titanium dioxide, pure or doped with different materials. Table 1.3 presents an example of photocatalytic efficiency evaluation for TiO_2-based materials of different composition investigated in the degradation of different pollutants. Among them, organic dyes are often found, as they represent an easy-to-study target whose degradation can be followed in laboratory with simple equipment. For this reason, these pollutants will be the subject of the experimental part of this thesis.

Table 1.3. Various nanocomposites of TiO_2 for UV and Visible light photoactivity [30]

Composition	Light source	Pollutant	Experimental conditions	Dimensionality	PE
TiO_2	15 W UV	NO_x	$t_r = 16$ h	0D	25.4%
TiO_2 P25	250 W UV	Rhodamine B (10 mg l^{-1})	CL = 0.2 g l^{-1} $t_r = 60$ min	0D	55%
TiO_2	UV	Ammonia (700 mg l^{-1})	CL = N/A $t_r = 120$ min	0D	72%
TiO_2	125 W UV	*E. coli* (10^7 CFU/100 ml)	CL = 0.05-2 g l^{-1} $t_r = 10$ min	0D	72.22%–99.76%
N–TiO_2	300 W visible	Methylene blue	CL = 1 g l^{-1} $t_r = 240$ min	0D	~60%
Au doped TiO_2	24 W visible	Phenol (0.1 mM)	CL = 1 g l^{-1} $t_r = 240$ min	0D	74%
Al doped TiO_2	UV	Acid orange 7 (5 mg l^{-1})	CL = 0.5 g l^{-1} $t_r = 60$ min	0D	99%
S doped TiO_2	300 W UV	Methylene blue (10 mg l^{-1})	CL = 0.2 g l^{-1} $t_r = 12$ min	0D	95%
Ag doped TNH	UV–vis	Methylene Blue (30 mg l^{-1})	CL = 1 g l^{-1} $t_r = 15$ min	2D	~100%
N–TiO_2	Visible	*E. coli* (10^3 CFU ml^{-1})	CL = 0.5 g l^{-1} $t_r = 10$ min	3D	~100%
CdS-TNTA[a]	300 W visible	Rhodamine B (5 mg l^{-1})	CL = N/A $t_r = 300$ min	3D	68.14%
TiO_2 NRs-CNTs[b]	Sunlight	Methylene blue (5 mg l^{-1})	CL = 0.2 g l^{-1} $t_r = 180$ min	3D	97.5%

Note. PE = photodegradation efficiency.
CL = catalyst loading.
t_r = irradiation time.
TNH = TiO_2 nanoholes structure.
[a] TiO_2 nanotube arrays.
[b] TiO_2 nanoribbons and carbon nanotubes.

1.5 Organic dyes

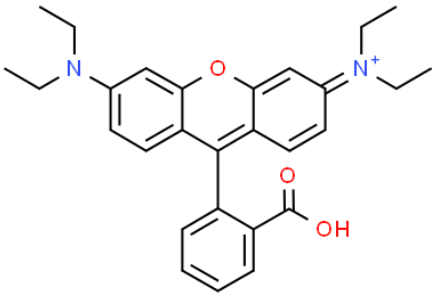

Figure 1.19. Rhodamine B molecule [70]

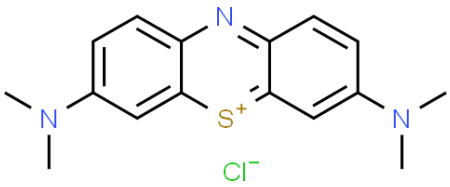

Figure 1.18. Methylene Blue molecule [69]

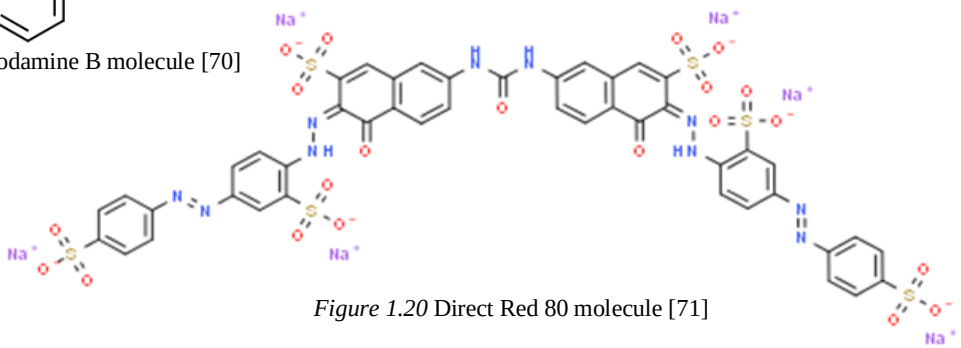

Figure 1.20 Direct Red 80 molecule [71]

Color is essential to the attractiveness and acceptability of most products used by modern society. As long ago as the 25th century BC man colored his surroundings and clothes using a limited range of natural colorants of both animal and vegetable origin. However, the preparation in 1856 of the first synthetic dyestuff, mauveine, by Perkin gave birth to the development of many other important sectors of the modern chemical industry. Compared with natural dyestuffs, synthetic colorants are better able to meet the increasingly rigorous technical demands of the present day in terms of stability and fastness. Color can add not only aesthetic appeal, but frequently provides an almost irreplaceable safety feature (traffic lights and signs, drug identification, control systems) [32].

For the purpose of this thesis work 3 organic dyes have been chosen for the evaluation of their degradation during photocatalytic experiments, namely Methylene Blue (MB), Rhodamine B (RhB) and Direct Red 80 (DR80) whose molecular structures can be seen in Figures 1.18, 1.19 and 1.20 respectively. Organic dyes can be defined as a group of organic substances that are able to strong color fibers, textiles and some other materials. There are different kinds of dyes that can be divided according to their source, like natural dyes (such as vegetable dyes, mineral dyes, animal dyes, etc.) or synthetic dyes that are created by molecular experiments in laboratory and then fabricated artificially. Dyes can also be discriminated by their molecular structure and so they are divided into: azo dyes, phthalocyanine dyes, nitro dyes, aromatic dyes and anthraquinone dyes.

The last classification can be done based on their application methods and so we will talk about: basic or acid dyes, sulfur dyes, reactive dyes, direct dyes, disperse dyes and so. The main property of dyes is of course the color that characterize them, but not all the substances that have a distinct color can be classified as a dye, indeed they must have a chromophore and an auxochrome group. The chromophore can be defined as a part of the molecule where the electronic band gap between two separated molecular orbitals falls within the range of the visible spectrum, so when the visible light hits the chromophore it can be absorbed by exciting an electron from its ground state to an excited one. By this definition it can be concluded that the color of a substance is just the wavelength spectrum of all the visible light that is not absorbed by the substance itself. Instead the auxochrome group is a group of atoms that is attached to a chromophore modifying its ability to absorb light. These groups are not able to produce the color themselves, but when they are present along with the chromophores in an organic compound, they act intensifying the color of the chromogen (which can be defined as a colorless chemical compound that can be converted into a dye or a pigment by suitable chemical reactions) [33].

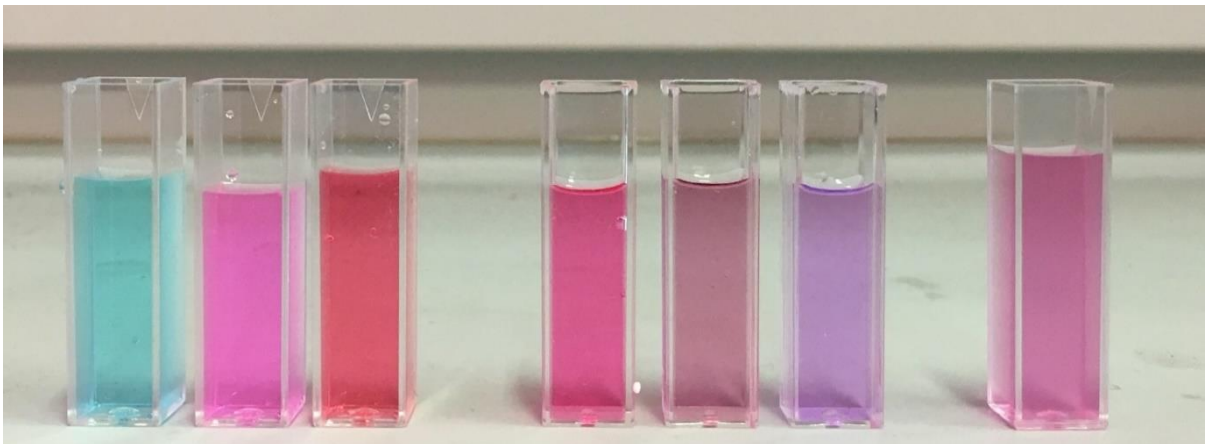

Figure 1.21. From left to right all the solutions of organic dyes utilized for photocatalysis reactions:
3 single-dye solutions of methylene blue, rhodamine B and direct red 80.
3 binary solutions: RHB + DR80, MB + DR80, MB + RHB.
1 ternary solution: MB + DR80 + RHB

Dyes and pigments are emitted into wastewaters from various industrial branches, mainly from the dye manufacturing and textile finishing. Wastewater streams from the textile dyeing operation contain a lot of different unused dyes for about 8–20% of the total pollution load and others auxiliary chemicals along with large amounts of water, for that reason the analysis of solutions in which more dyes were mixed together was of fundamental importance for better approximating industrial wastewater conditions. Samples of these binary and ternary solutions are presented in Figure 1.21 together with single dye ones. The presence of dyes in water reduces light penetration and has a derogatory effect on photosynthesis.

It is important to find a clean way to recover or degrade these compounds, but this is not simple due to the complex chemical structure of these dyes that are resistant to breakdown by chemical, physical and biological treatments. Furthermore, any degradation by physical, chemical or biological treatments may produce small amount of toxic and carcinogenic products [34].

1.6 Textile industry wastewaters composition and treatments

Most of the effluents produced by textile industries contain important quantities of synthetic organic dyes. The discharge of these colored compounds in the environment is a serious risk for the health of all the living creatures that drink or live in that water and also it causes non-aesthetic pollution. Since conventional wastewater treatment plants are still not able to totally degrade the majority of these pollutants, or can produce at the same time dangerous byproducts, powerful methods for the decontamination of dyes in wastewaters have received increasing attention over the past decade [35].

For that reason nowadays the demand of methods for the decolorization of industrial wastewaters is a top priority. This kind of waters may contain a huge amount of different color-causing compounds, so this task is hard to achieve. There are different methods for this purpose, which can be divided into physico-chemical, electrochemical, chemical, microbiological, enzymatic and advanced oxidation processes (AOPs) as is shown in Figure 1.22.

Among physicochemical techniques the most used are: coagulation, adsorption and membrane separation. In coagulation, the disperse dyes are removed from the electrostatic attraction between oppositely charged soluble dye and a polymer molecule. However, this approach has the problem to generate large amounts of sludge and high content of dissolved solids remains in the effluent. Adsorption, instead, allows good removal of dyes from the effluent, but the adsorbent regeneration is expensive and involves the loss of adsorbent. Finally, the use of appropriate membranes allows to remove all types of dyes, being a compact technology without generation of sludge. However, membrane separation can be very expensive since its equipment and membrane themselves are very costly, especially considering other limitations such as the lowered productivity with time due to fouling of the membrane and the disposal of concentrates [36].

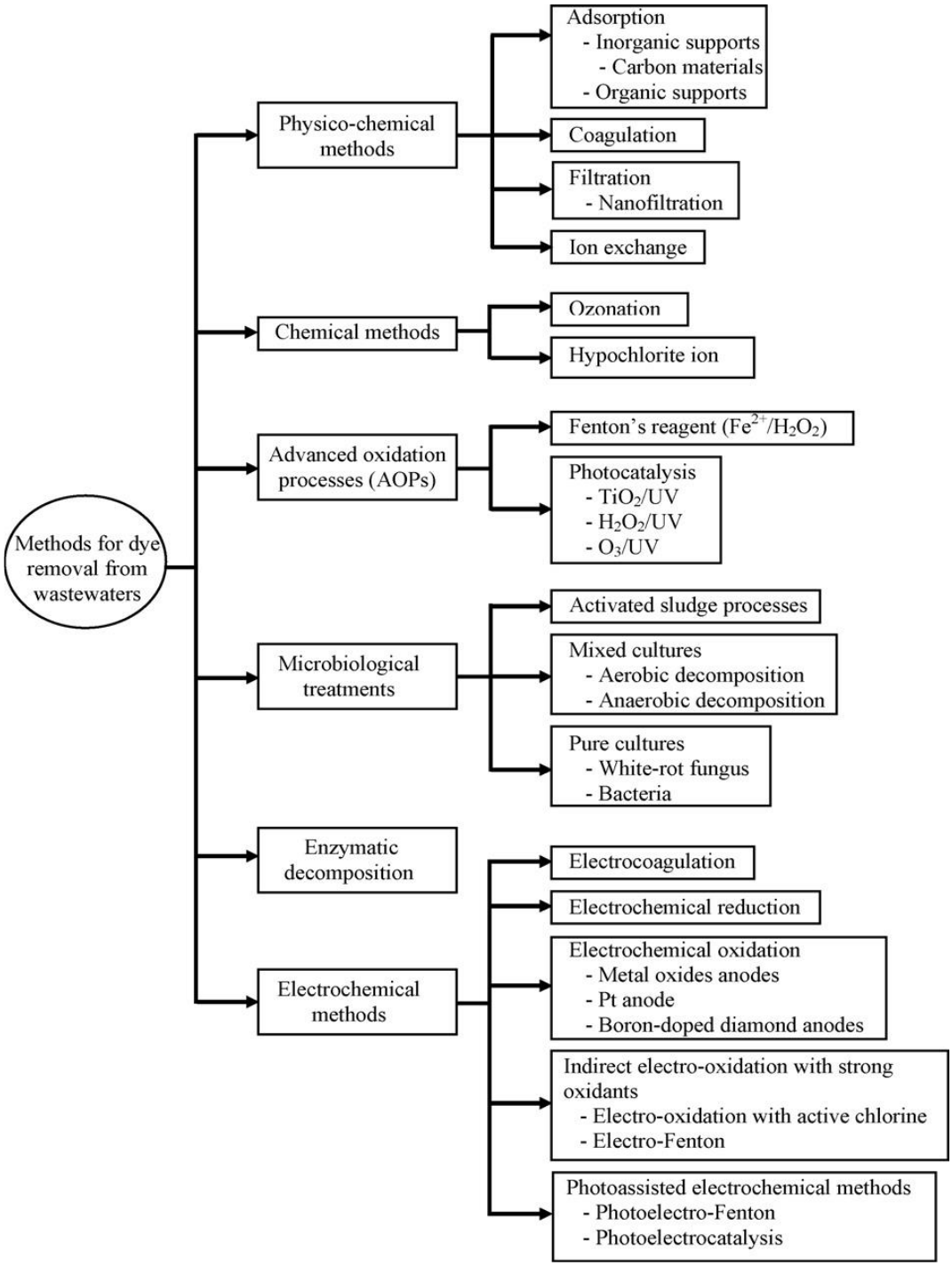

Figure 1.22. Main methods used for the removal of organic dyes from wastewaters [35]

Regarding biological treatments, anaerobic process, oxidation, trickling filters and activated sludge process have been intensively studied; in fact, microorganisms such as algae, fungi, bacteria and yeasts are capable to degrade certain type of dyes. Biological methods are environmentally friendly, produce less sludge than physicochemical systems and are relatively inexpensive. Nevertheless, their application is limited since biological treatment needs a large land area, has sensitivity toward toxicity of certain chemicals and treatment time is very high [37].

More powerful chemical methods such as ozonation and oxidation with hypochlorite can be exploited; particular attention has been given to advanced oxidation processes (AOPs), such as Fenton's reagent, in which a solution of hydrogen peroxide with iron sulfate as catalyst is used to oxidize contaminants, and photocatalytic systems that can provide fast decolorization and degradation of dyes. In fact, AOPs are environmentally friendly methods involving the onsite generation of highly reactive oxygen species, such as hydroxyl radicals, that control the degradation mechanism. Nevertheless, the use of these methods is not currently well accepted because they are quite expensive and have operational problems [38].
Lastly, electrochemical technologies have emerged as novel treatment technologies for the elimination of a broad range of organic contaminants from water; an example of photoinduced reactions involved in TiO2 photoelectrocatalysis is presented in Figure 1.23.

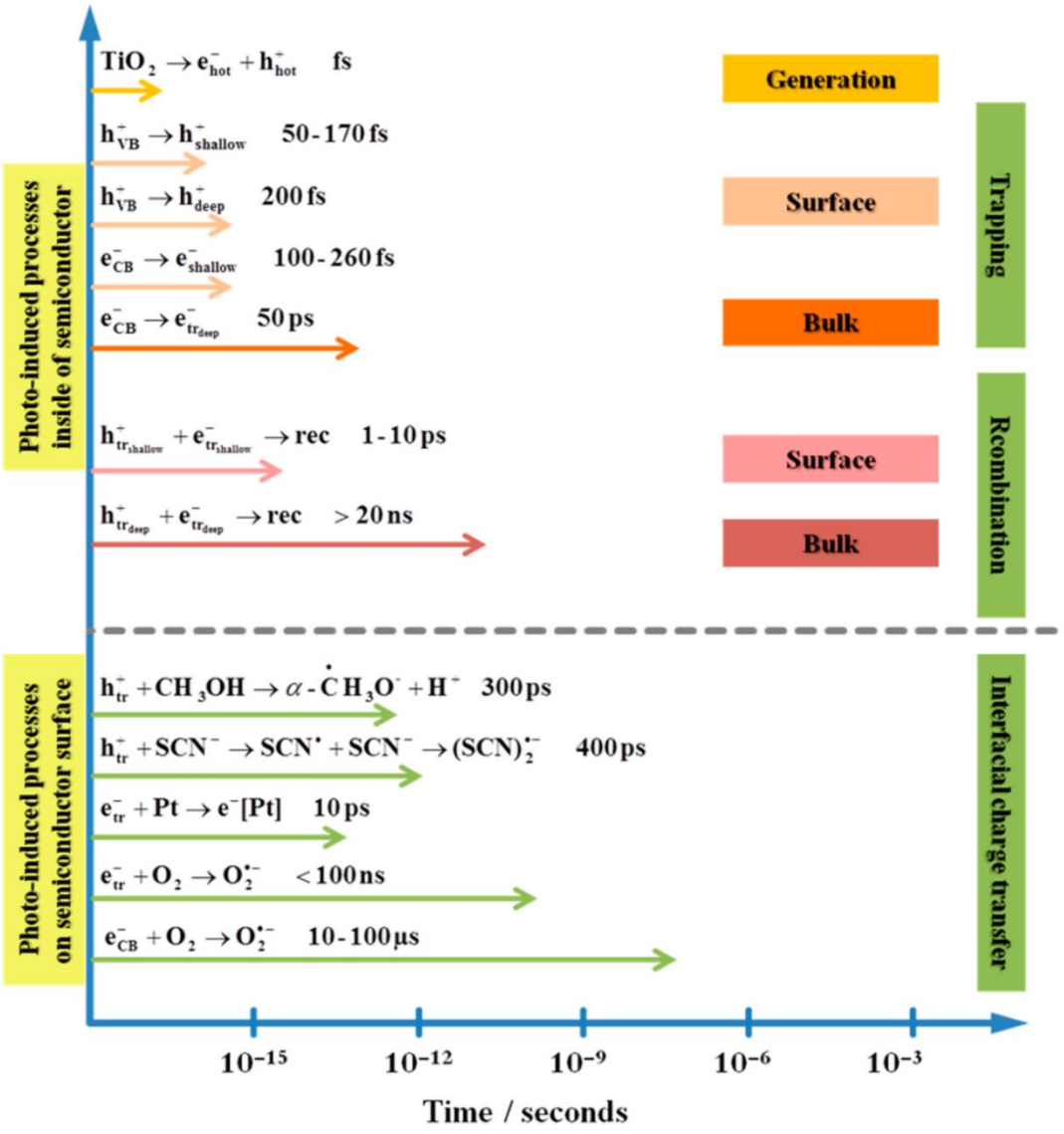

Figure 1.23. Photoinduced reactions in TiO2 photocatalysis and the corresponding time scales [72]

The environmental application of electrochemical approaches has been the topic of several books and reviews summarizing and discussing their use for the prevention and remediation of pollution problems. These techniques have several advantages including: higher energy efficiency with respect to other traditional processes, easy handling due to the simplicity of the required equipment, safety because they operate under mild conditions (ambient temperature and pressure) and versatility. Among all these technologies, electrochemical advanced oxidation processes have received great attention, although other electrochemical approaches can also be effectively used for treating industrial effluents. The strategies of electrochemical technologies include not only the treatment of effluents and wastes, but also the development of new processes or combined methods with less harmful effects, often denoted as process integrated environmental protection [35].

The choice between different schemes and techniques depends on economic and treatability factors such as chemical dosage used in the factory, sludge quantity produced, degree of inhibitory and non-biodegradable substances present as well as their type. For these reasons every process has its own constraints in terms of cost, feasibility, reliability, stability, practicability, environmental impact, sludge production, operation difficulty, pretreatment requirements, the extent of the organic removal and even potential toxic byproducts.

It is easy to understand why some processes are reported to be suitable for a successful decolorization of a particular wastewater but they may not be applicable to other types of colored wastewaters [39].

Moreover, each one of these processes, if not combined with other dye removal methods, is not able to satisfy the actual requirements for the disposal of wastewaters. These requirements are governed by the Directive 2013/39/EU of the European parliament, which amends Directives 2000/60/EC and 2008/105/EC as regards priority substances in the field of water policy; moreover the 2013 directive asserts that wastewater treatment today is very expensive, so that the development of innovative water treatment technologies must be encouraged in order to facilitate a cheaper and more cost-effective treatment [40].

Another problem not to be underestimated is both the formation of intermediates during decolorization processes, since these byproducts can even be more toxic than the parent compounds, and the interactions among dyes and other chemical compounds. In fact, these dyes and colors are present in wastewaters with other residual reagents, generally used for processing, impurities coming from raw materials and other hazardous substances employed in the finishing process (including polyvinyl alcohol, starches, surfactants, pesticides and biocides). These components can also exhibit low BOD/COD ratios (< 0.1) due to the low biodegradable nature of the dyes themselves.

The final effluent from textile wastewater treatment plants always exhibits a certain degree of color intensity as can be seen in Figure 1.24 [41].

Figure 1.24. Bangladesh mills ignore effluent treatment realizing colored wastewaters in local rivers [41]

The complicated nature of these compounds, as well as strict regulatory requirements, render the color elimination in wastewater treatment extremely difficult and costly. The discharge of colored waste to receiving waters is aesthetically displeasing and, although not all dyes are toxic compounds, some can produce hazardous aromatic amines; the characteristics of some wastewaters are summarized in Table 1.4.

Table 1.4. Wastewater characteristics derived from different combination of dyes, substrate and dyeing equipment [39]

No.	Dye class	Substrate	Method	ADMI* colour	Apparent ADMI	TOC (mg l^{-1})	BOD (mg l^{-1})	pH	Cl^- (mg l^{-1})	Suspended solids (mg l^{-1})	Dissolved solids (mg l^{-1})†
1	Vat	Cotton	Exhaust	1,910	–	265	294	12	190	41	3945
2	1:2 Pre-metallised	Polyester	Exhaust/Beck	370	–	400	570	7	nil	5	1750
3	Disperse	Polyester	Atmospheric/ Exhaust	315	–	300	234	8	33	39	914
4	After coppered direct	Cotton	Exhaust/Beck	525	1280	135	87	5	520	41	2763
5	Reactive	Cotton	Exhaust/Beck	3890	–	150	INT††	11	9800	32	12500
6	Disperse	Polyamide	Exhaust/Beck	100	–	130	78	8	28	14	395
7	Chrome	Wool	Exhaust/Beck	3200	–	210	135	4	33	9	1086
8	Basic	Polyacrylic	Exhaust/Beck	5600	12000	255	210	6	27	13	1469
9	Disperse	Polyester	Exhaust/Beck	215	315	240	159	7	27	101	771
10	Acid	Polyamide	Exhaust/Beck	4000	–	315	240	5	14	14	2028
11	Direct	Rayon	Exhaust/Beck	12500	–	140	15	7	61	26	2669
12	Developed	Rayon	Exhaust/Beck	2730	–	55	12	3	130	13	9,8
13	Disperse/ Acid/Basic	Polyamide	Exhaust/Beck	210	720	130	42	7	10	8	450
14	Disperse	Polyester	HT Exhaust	1245	–	360	198	10	1680	76	1700
15	Sulphur	Cotton	Continuous	450	–	400	990	4	42	34	2000
16	Reactive	Cotton	Continuous	1390	–	230	102	9	57	9	691
17	Vat/ Disperse	Cotton/ Polyester	Continuous	365	1100	350	360	10	167	27	2292
18	Basic	Polyester	Atmospheric/ Exhaust	1300	2040	1120	1470	5	17	4	1360
19	Disperse/ Acid/Basic	Polyamide	Continuous/ Kuster	<50	100	100	100	7	22	49	258
20	Azoic	Cotton	Exhaust/Package	2415	–	170	200	9	7630	387	10900

*ADMI = American Dye Manufacturers Institute †Mostly salt ††INT= High salt or reactive

Regarding dye removal, there is a clear distinction among decolorization, degradation, and mineralization of the dyes. The first one is simply the disappearance of the color without actually breaking apart complex dye molecules; as an example, the addition of a bleach to the wastewater solution leads to a decolorization, but the colorless waste may still contain organics complexes that could be more toxic than the original colored water. A reduction reaction, that could be done with a biological, chemical or photochemical process, presents the same problem. Even more, some compounds undergo color change, or even become colorless, in certain pH ranges. Thus, the disappearance of the color in wastewaters does not mean a complete degradation of the organic dye molecules, because it is sufficient to break the chromophore bond for achieving decolorization, meanwhile the major fragments of the original molecule could remain intact. Degradation is attained only if these molecules are broken down into their smaller parts, which could be easily separated from the solution with standard methods. Lastly, mineralization is a process in which organic substances are converted into inorganic ones, so that organic carbon atoms are converted into inorganic CO_2.

As mentioned above, dye removal processes are not able to obtain a purity degree sufficiently high to respect European standards if they are applied alone [39].

In order to achieve this goal a combination of more processes is needed, such as anaerobic coagulation pretreatment followed by aerobic biological oxidation, one of the most common technique used for decolorizing wastewaters. It seems quite clear that the pretreatment step is fundamental since it renders the effluent more amenable to subsequent aerobic treatment. An example of a typical stages used in wastewater treatment are reported in the scheme above in Figure 1.25.

In this work the evaluation of the three dyes selected for photocatalytic experiments has been performed not only for single-dye solution, but even for solutions in which these dyes are mixed together in binary and ternary solutions for better approximating the behavior of industrial wastewaters.

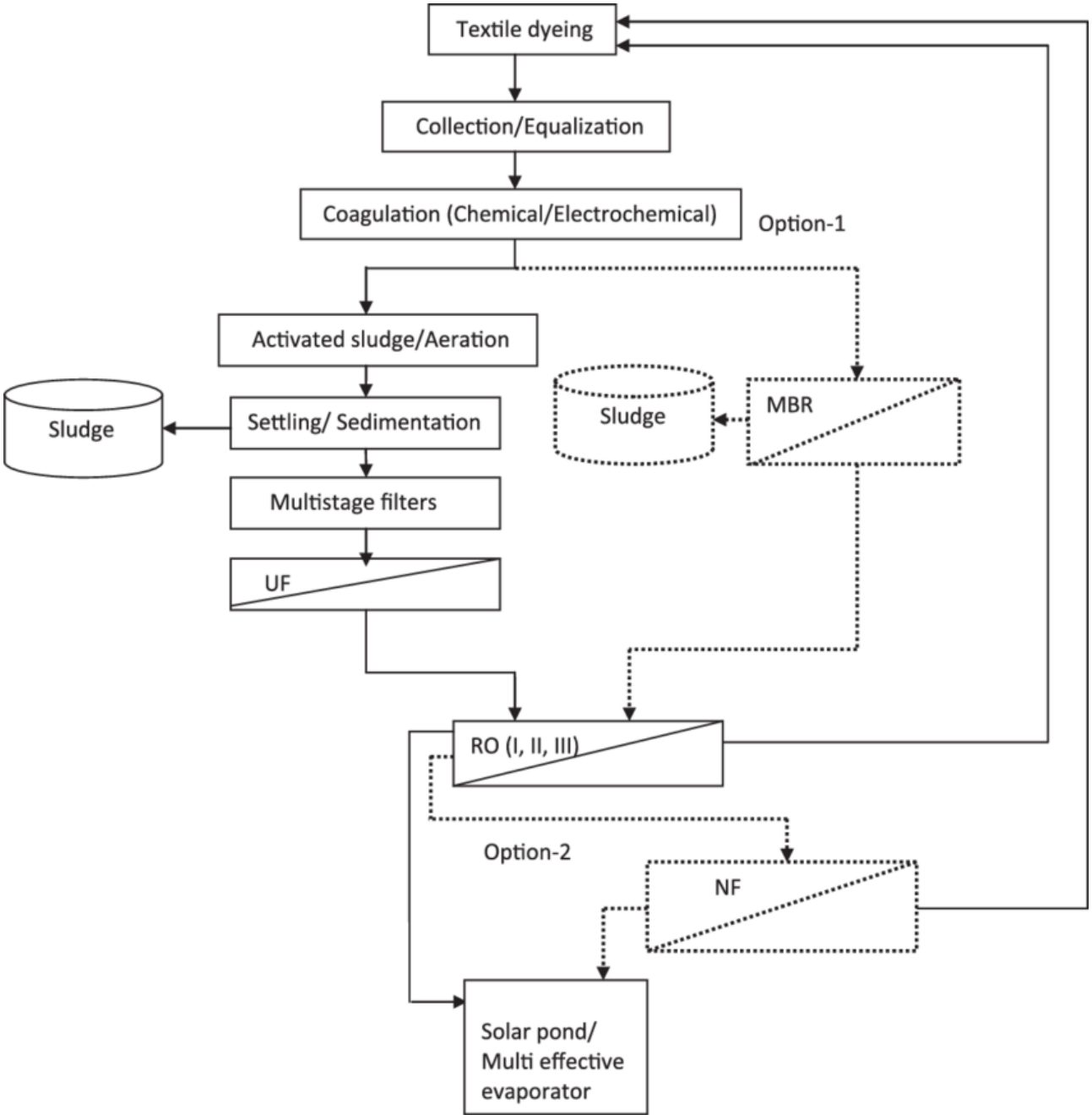

Figure 1.25. Typical stages generally used in textile wastewater treatment plant [39]

1.7 Quantification of dyes in binary and ternary solutions

In recent years, considerable information has been collected for the degradation of single dye solutions through photocatalytic processes, but most of the industries emit wastewaters that contain a mixture of several dyes, like textile industries, and limited data is available on multi-component dye photodegradation. That's because the simultaneous analysis of a multi-component dye mixtures is a very complex problem in analytical chemistry due to spectral interferences, which results in widely overlapped absorption bands [42].

For that reason, different methods have been studied for the simultaneous determination of two or more compounds in the same solution.

There are a lot of analytical methods such as visible spectrophotometry, mass spectrophotometry, differential pulse polarography, capillary electrophoresis and high-performance liquid chromatography. Among them, there are also derivative techniques and multivariate calibration methods that are very common approaches to resolve two-dyes and ternary mixtures with spectral overlapping without previous chemical separation. Several spectrophotometric methods have been applied for the simultaneous determination of dyes: hybrid linear analysis, partial least squares, ratio derivative method, first and second order derivative spectrophotometry [43].

Derivative spectrophotometry has been utilized for a lot of researches, due to its greater selectivity respect to normal spectrophotometry, because it decreases spectral overlap and allows a better resolution, so that mixtures of compounds with highly overlapped spectra can be resolved by using multicomponent analysis programs [44].

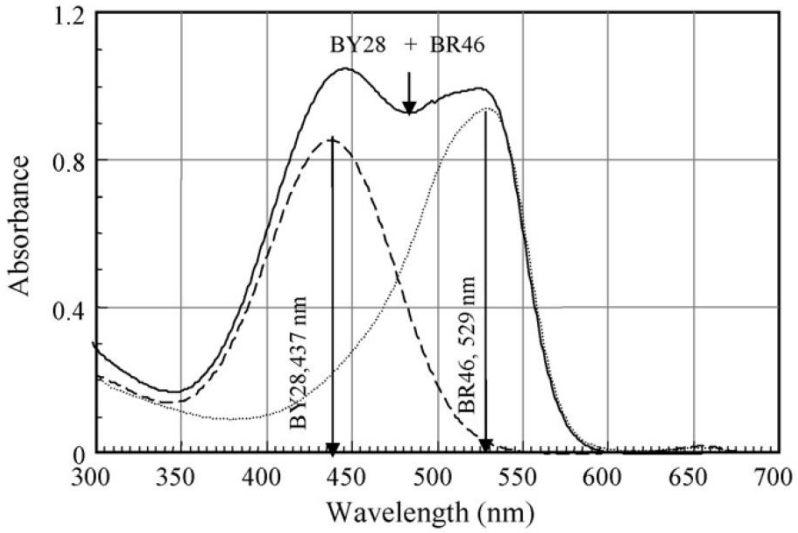

Figure 1.26. Spectra of Basic Yellow 28 (BY28) and Basic Red 46 (BR46) in single and binary solutions [46]

Among these methods zero-crossing first order derivative spectrophotometry has demonstrated a good applicability for resolving binary mixtures with overlapping spectra, whose example is reported in Figure 1.26, being one of the most advanced modern spectrophotometric techniques. It is based on the mathematical derivation of derivative spectra which are generated from parent zero-order ones. The derivatization of zero-order spectrum can lead to a separation of overlapped signals, removing the background caused by presence of other compounds in a sample. The mentioned properties can allow the quantification of each analyte without initial separation or purification. Nowadays this technique has found application in many fields of analysis, especially in pharmaceutical, clinical and biochemical as well as in inorganic or organic analysis [45].

For the calculation of the first derivative all data as to be collected with a sampling interval of $\Delta\lambda$, which size depends on the natural bandwidth of the instrument used to generate data; the literature reports a range of usable $\Delta\lambda$ values between 4 nm and 10 nm. This permits the building of new absorbance spectra like the ones presented in Figure 1.27.

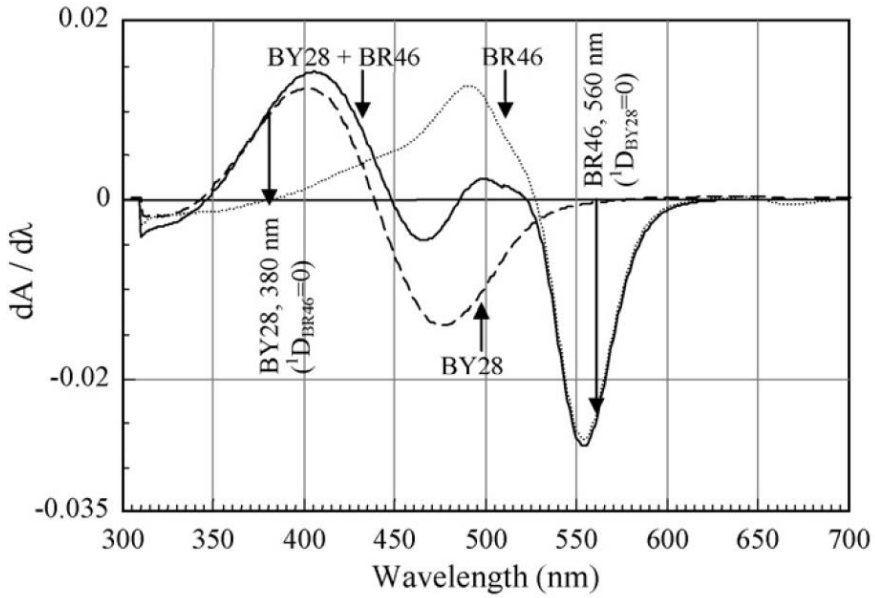

Figure 1.27. First order derivative spectra of Basic Yellow 28 (BY28) and Basic Red 46 (BR46) in single and binary solutions [46]

It can be noticed notice that there are certain wavelength values in which the derivative absorbance of one dye is zero, while the derivative of both the other dye and the binary solution one have a non-zero value. These are the working wavelengths in which it is possible to analyze the contribution of each compound with zero-crossing first order derivative spectrophotometry, since they correspond to points where the measured derivative absorbance is correlated only to the contribute of one dye, thus respecting the Beer-Lambert law [46].

The advantages that characterize mathematical techniques, like this one, are that derivative spectra may be easily calculated with different parameters, and smoothing techniques may be used to improve the signal-to-noise ratio. This renders that method quicker and easier if compared to alternative methods, such as high-performance liquid chromatography or gas chromatography, since the only machine needed is a spectrophotometer to collect absorbances data for building up an absorption spectrum [47].

Alternatively, for more precise methods (such as in the pharmaceutical field), more complex instruments can be used, like the optical technique that uses wavelength modulation that follow the scheme visible in Figure 1.28, where the wavelength of incident light is rapidly modulated over a narrow wavelength range by an electromechanical device.

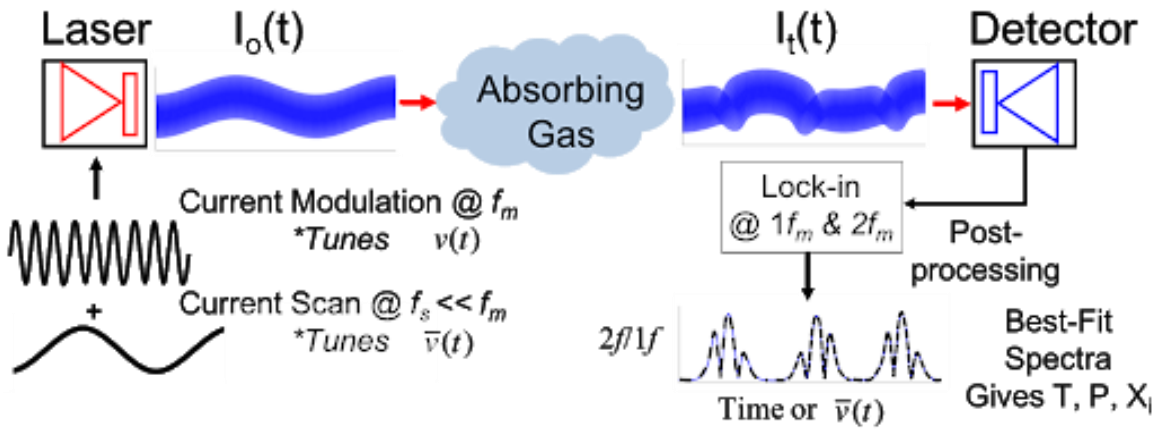

Figure 1.28. Basic operating principles of Wavelength-modulation spectroscopy sensors [73]

The first and second derivatives may be easily obtained by this way using dedicated spectrophotometers, like a dual wavelength spectrophotometer that generates a derivative spectrum by scanning with each monochromator two different wavelengths separated by a small constant difference. First and high order derivatives can also be generated using analog resistance capacitive devices. These generate the derivative as a function of time as the spectrum is scanned at constant speed, but this electronic method suffers from the disadvantage that the amplitude and wavelength shift of the derivatives varies with scan speed, slit width and resistance-capacitance gain factor [48].

Instead for the analysis of ternary mixtures with overlapping spectra, whose example has been reported in Figure 1.29, a different mathematical method is required; one of the most promising one, that has been chosen for this work, is double divisor-ratio spectra derivative spectrophotometry.

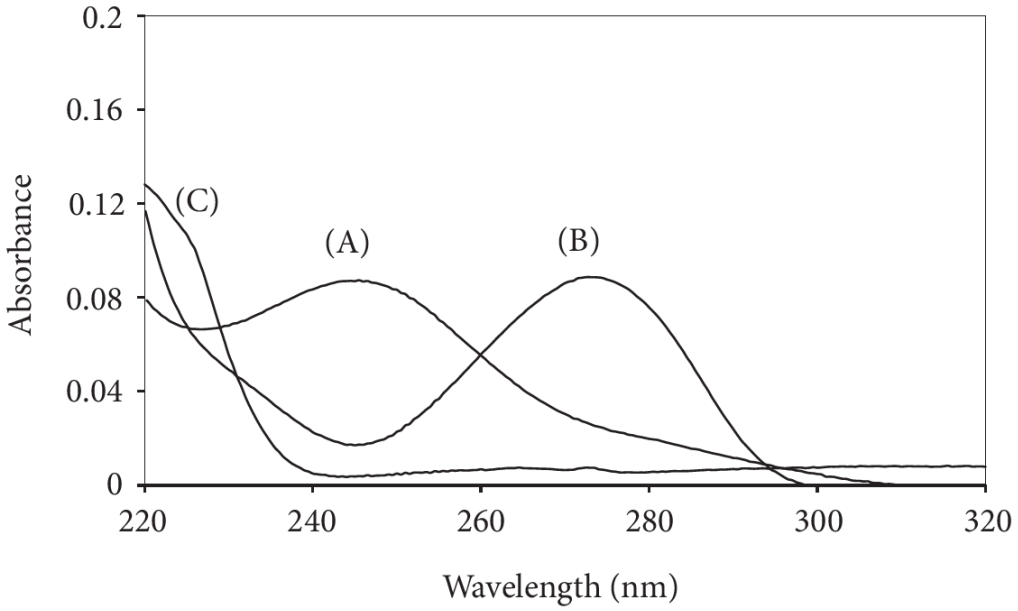

Figure 1.29. The absorption spectra of: aspirin 50 μmol/L (A); caffeine 20 μmol/L (B); paracetamol 20 μmol/L (C) [55]

The method is based on the use of the coincident spectra of the derivative of the ratio spectra obtained by using a 'double divisor' (sum of two spectra) and the measurements at either the maximum or minimum wavelengths. To achieve this the spectrum of a single compound in a ternary mixture is divided by the double divisor, made by the binary solution of the others, obtaining new spectra like the ones presented in Figure 1.30.

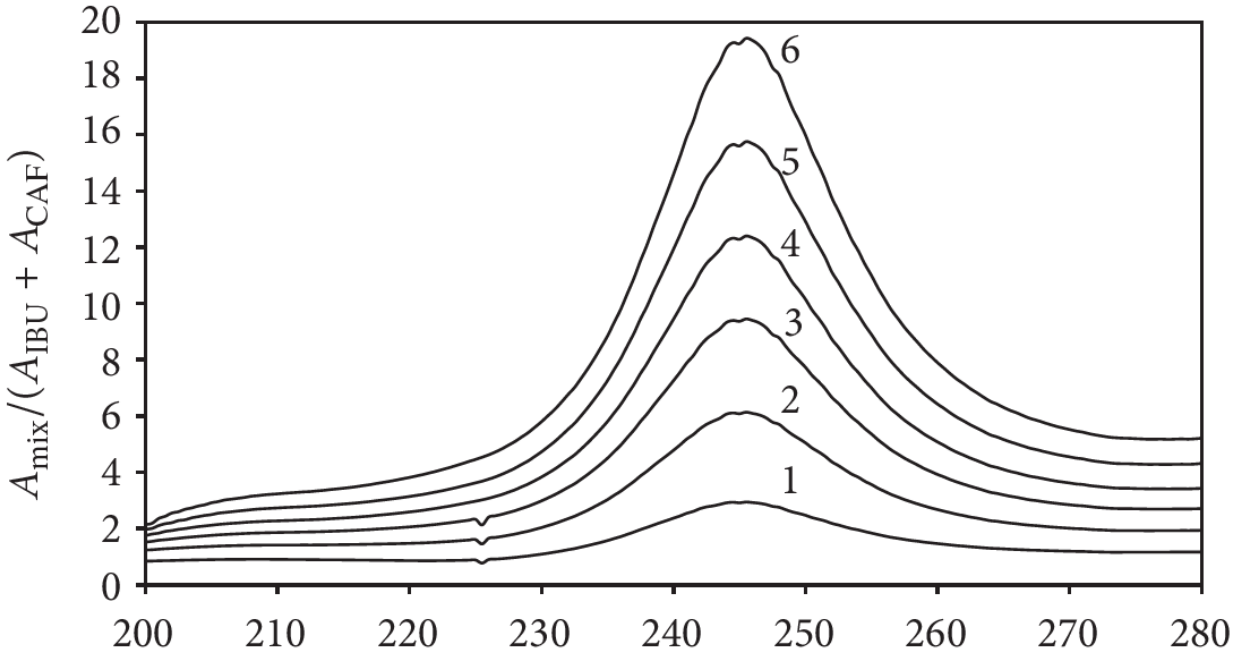

Figure 1.30. Set of 6 ternary spectra that have been divided by their double divisor for a ternary mixture of aspirin, caffeine, and paracetamol [55]

Now the first derivative of these spectra has to be calculated, finally resulting in the double divisor-ratio spectra for a ternary mixture; an example of these spectra is presented in in Figure 1.31.

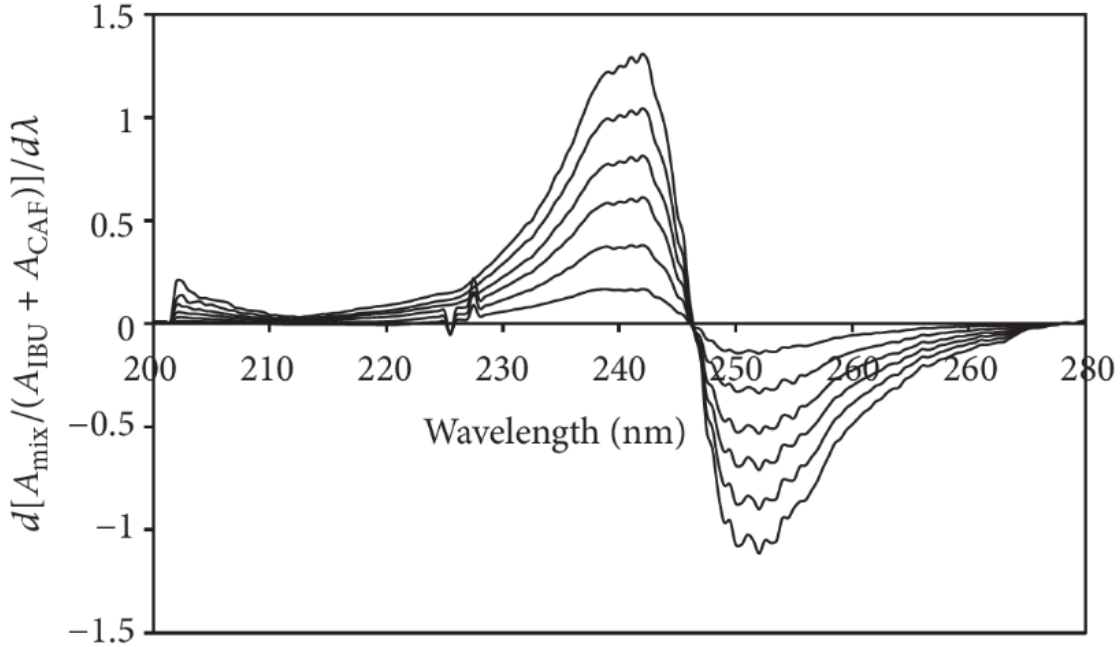

Figure 1.31. First-derivative double divisor-ratio spectra for a ternary mixture of aspirin, caffeine, and paracetamol [55]

From the analysis of these spectra coincident points ca be found on the first derivative signals of the ratio spectra. These are the points in which derivative signals of the compound in its single-dye mixture and in the ternary mixture with the others coincide, when these points reaches a maximum or a minimum it is possible to find the proper working wavelength in which data has to be collected for a discrete evaluation of one dye in a ternary mixture. If it is not possible to find these coincident points, an higher order derivative spectrophotometric approach can be tried [49].

The double divisor-ratio spectra derivative method has resulted to be less expensive with respect to other methods, its advantage is that it does not require separation procedures or sophisticated instrumentation, and it is even more easily exploitable than the derivative ratio spectrum zero-crossing method since it does not request the mandatory use of zero-crossing points [47].

The evaluation of the dye concentration allows to evaluate the reaction rate of the photocatalytic process. All photocatalytic reaction that has been studied during this work, in fact, are apparently following a pseudo-first order kinetic in agreement with a generally observed Langmuir–Hinshelwood mechanism, with the rate r being proportional to the coverage θ which becomes proportional to C at low concentrations, as show in equation (3.3) [50]:

$$r = k\theta = \frac{kKC}{1+KC} \approx kKC = K_{app}C \quad (3.3)$$

From a mechanistic point of view, it is well known that the photoexcitation of a semiconductor surfaces induces the formation of an electron-hole pair:

$$TiO_2 + {h_{VB}}^+ \rightarrow TiO_2({e_{CB}}^- + {h_{VB}}^+) \quad (3.4)$$

While some electron-hole pairs are recombined, the remaining holes contribute to the oxidation reactions by generating $\bullet OH$ radicals, either by the decomposition of water

$$H_2O + {h_{VB}}^+ \rightarrow H^+ + \bullet OH \quad (3.5)$$

Or by the reaction of the hole with adsorbed OH^-

$${h_{VB}}^+ + OH^- \rightarrow \bullet OH \quad (3.6)$$

The hydroxyl radical species alone is an extremely strong oxidant for the partial or complete mineralization of organic chemicals:

$$dye + \bullet OH \rightarrow oxidation\ products \quad (3.7)$$

The high oxidative potential of the hole (${h_{VB}}^+$) may lead also to the direct oxidation of adsorbed dye:

$$dye + {h_{VB}}^+ + dye\bullet^+ \rightarrow oxidation\ products \quad (3.8)$$

Meanwhile, on the surface of the catalyst, oxygen is reduced as an electron acceptor to superoxide and this leads to production of $HOO\bullet$ radical, which eventually play a strong oxidant role [51].

$${e_{CB}}^- + O_2 \rightarrow {O_2}^- + H^+ \rightarrow HO_2\bullet \quad (3.9)$$

$$HO_2\bullet + {O_2}^- + H^+ \rightarrow H_2O_2 + O_2 \quad (3.10)$$

$$H_2O_2 + {e_{CB}}^- \rightarrow OH^- + \bullet OH \quad (3.11)$$

Chapter 2 : Materials and methods

2.1 Titanium samples preparation

The anodization procedure that was utilized to growth well-ordered and control sized TiO_2 nanotubes with a crystalline structure on titanium samples was always the same and rigorously followed precise steps.
Firstly 14 samples were cut from a titanium sheet into squares of 3 cm X 3 cm, with thickness of 0.5 mm, then they were mechanically polished using a grinder equipped with a P600 SiC paper. This step allows to remove the very thin oxide film that naturally grows (without a nanotubular structure) when titanium is exposed to air and that protects the metal from further oxidation an example of a titanium sample pre-polishing is presented in Figure 2.1.

Figure 2.1. Titanium sample 3 cm x 3 cm pre-polishing.

Figure 2.2. Titanium sample 3 cm X 3 cm after polishing

The surface treatment applied on titanium samples can strongly influence the growing process of nanotubular structures, the polishing procedure has been preferred over pickling because of results obtained by previous studies.
With polishing the amorphous oxide layer is removed leaving a homogeneous titanium structure ready to be used for the growth of a new nanotubular oxide layer by means of anodization. After the polishing procedure the samples were cleaned using a sonication machine for 5 minutes in ethanol and then washed with distilled water to remove every residue of silicon carbide or other contaminants; an example of a titanium sample after polishing and sonication is presented in Figure 2.2.

2.2 Anodization

After the polishing and the sonication, the samples were subjected to anodization procedure that was carried out in a machine that has been provided by LTC-Caoduro, whose image can be seen in Figure 2.3.

Figure 2.3. Anodization Machine made by LTC-Caoduro.

The electrolytic cell, that has been built ad-hoc for this procedure, is placed inside this machine, with the titanium sample immersed in the center of it. This cell is made of a plastic beaker containing the electrode, the anode and the electrolyte; at its bottom some weights have been glued so that it can be immersed in a water jacket made by a bigger beaker filled with distilled water, in order to avoid an excessive overheating of the electrolyte during the anodization procedure.

Moreover, the cell is characterized by a titanium net placed at the walls of the plastic beaker acting as a cathode surrounding the titanium sample, that is the anode, and it is kept well immersed in the electrolytic solution sustained by a special conductive plier that can be seen in Figure 2.4.

Figure 2.4. Zoom on the plier holding the sample.

Figure 2.5. Control panel of the anodizing machine

It is preferable to have a cathodic surface area huger than the anodic one in order to favor the passage of current, overcome surges and promote the growth of the oxide. Another important condition that must be fixed is the distance between the sample and the titanium net, the ideal configuration is to keep the sample in the exact center of the cylinder made by this net. The solution is made by an ethylene glycol-based electrolyte containing 0.2 M of NH_4F, that favors the growth of a nanotubular oxide layer, and 2 M of water. The entire configuration of the electrolytic cell, already placed in the anodizing machine, and the position of the sample immersed in the ethylene glycol-based electrolyte are presented in Figures 2.6 and 2.7.

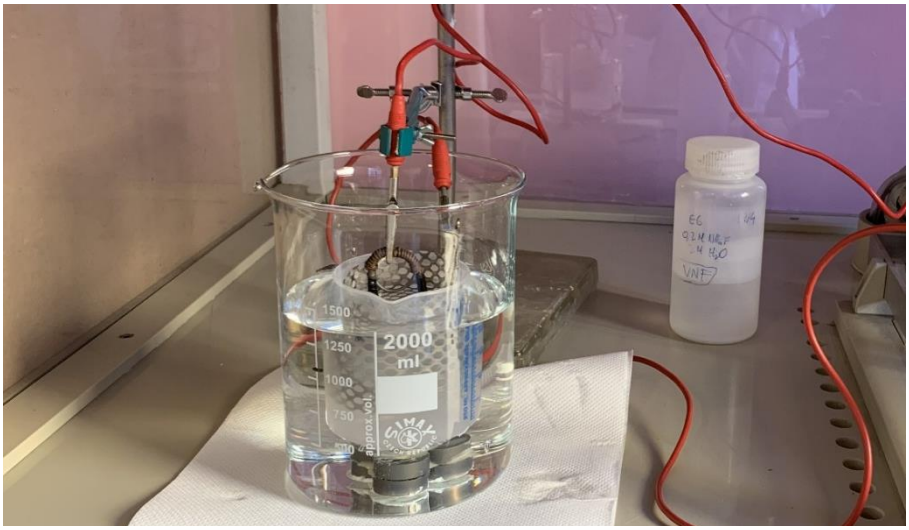

Figure 2.6. All the equipment necessary for the anodization procedure assembled and ready to start.

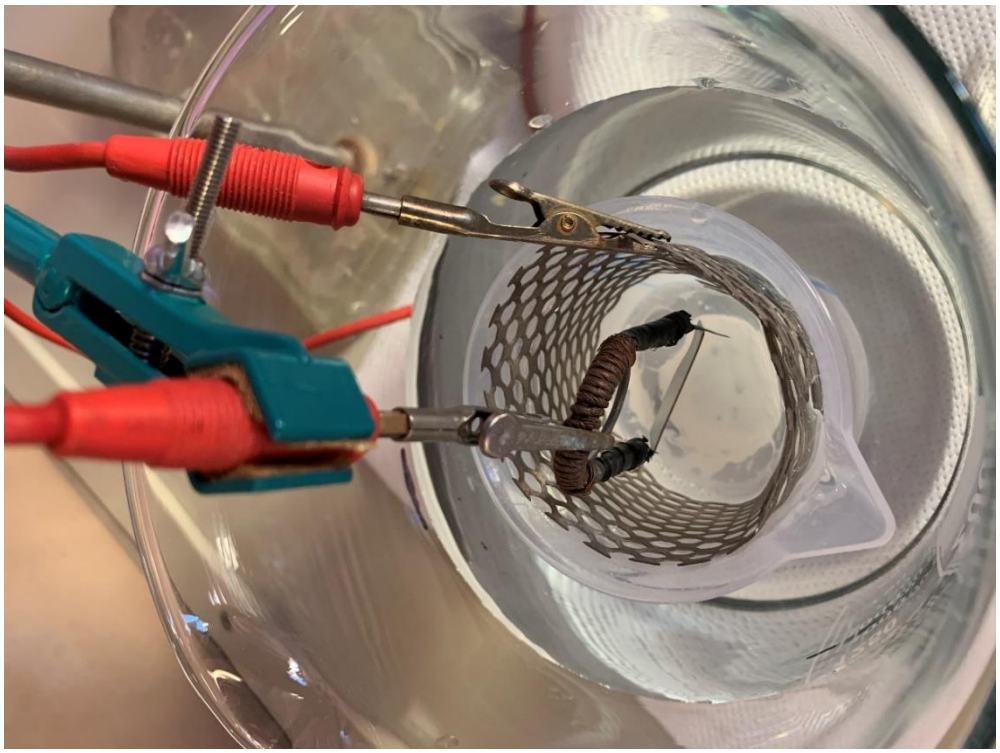

Figure 2.7. Titanium sample position respect to the net, seen from above.

Once all the preparation steps have been done the anodization procedure can be started, for titanium samples it has been find out that the best configuration is to keep the current at 45 V for 30 minutes. The anodizing plant allows to work in voltage ramp, setting a precise time for reaching the desired voltage, from the control panel visible in Figure 2.5, and then a precise maintenance time, at the end of which the plant automatically stops. The obtained nanotubes must be carefully rinsed one last time, to remove all possible traces of the electrolyte, using distilled water and finally dried using compressed air at a very low pressure. To verify the results provided by anodization a characterization of the samples surface has been provided via scanning electrode microscopy analysis. SEM has been performed using a Cambridge Instruments Stereoscan 360, with an EHT value of 20.0 kV, for checking the thickness and the morphology of the oxide layer built during the anodizing procedure.

2.3 Annealing

Annealing is the last step for the preparation of the samples, this procedure is carried out in a Gefran 1200 oven, presented in Figure 2.8, at 500 °C for 2 hours.

Figure 2.8. Gefran 1200 oven set to 500 °C going in temperature.

The goal of this process is to obtain the ideal ratio between rutile and anatase phases for photocatalytic efficiency. In Figure 2.9 and 2.10 the difference of the sample before and after the annealing procedure can be seen, the sample presents a yellowish color typical of voltages involved, using an appropriate annealing procedure a single titanium oxide phase structure or a mixture of anatase and rutile can be obtained. To verify results provided by the annealing process a characterization of the samples surface has been provided via X-ray diffraction analysis.
For XRD the Panaltical Empyrean diffractometer, with copper material as anode and 40 mA and 40 kV as generator settings, has been used to check if the correct anatase/rutile ratio was obtained during the annealing process.

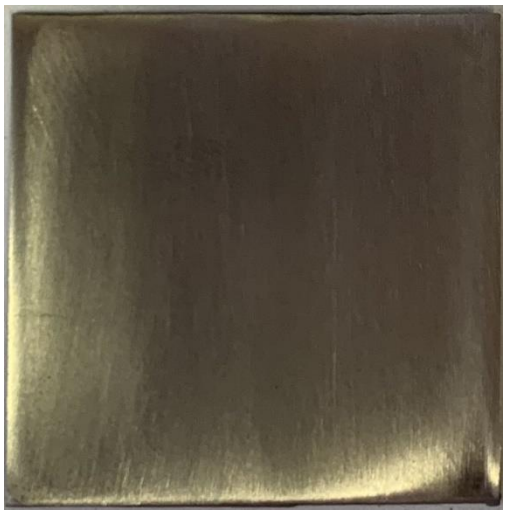

Figure 2.9. Titanium sample pre-annealing.

Figure 2.10. Titanium sample post annealing.

2.4 Photocatalytic experiments with UV-LEDs

Once that all the calibration curves have been characterized for each dye in the evaluated solutions, photocatalytic experiments have been performed. These experiments lasted for 6 hours; it has been noticed that this is the time in which even the strongest of the dyes reached 0 values of absorbance at its peak.
For this purpose mini-batch type reactors have been built: these are made by a 100 ml beaker, containing 40 ml of solution, with a titanium net in the middle, made to sustain the sample immersed in the solution keeping it a fixed distance (3.5 cm) from the UV-LED that is placed on top of the beaker. These reactors are placed on a stirrer, with a magnet inside to keep the solution mixed during the reaction, in fact the sample support is used to allow the magnet to rotate freely (at a speed of 300 rpm). By stirring the solution is homogenized, making sure that there is always a part of the dye, that is not attacked by radicals, which is in contact with the nanotubular oxide. In this way concentration gradients are avoided and also the presence of oxygen is promoted, which, from the free surface, enters the solution and then comes in contact with the titanium oxide. The LED is sustained by a plastic support, that has been 3D printed ad hoc for these experiments, able to keep the LED centered on the top of the beaker isolating at the same time the solution from the environment (this will prevent the solution from evaporating due to the heat released from the LED itself). In Figure 2.11 the UV-LED attached to its plastic support can be seen.

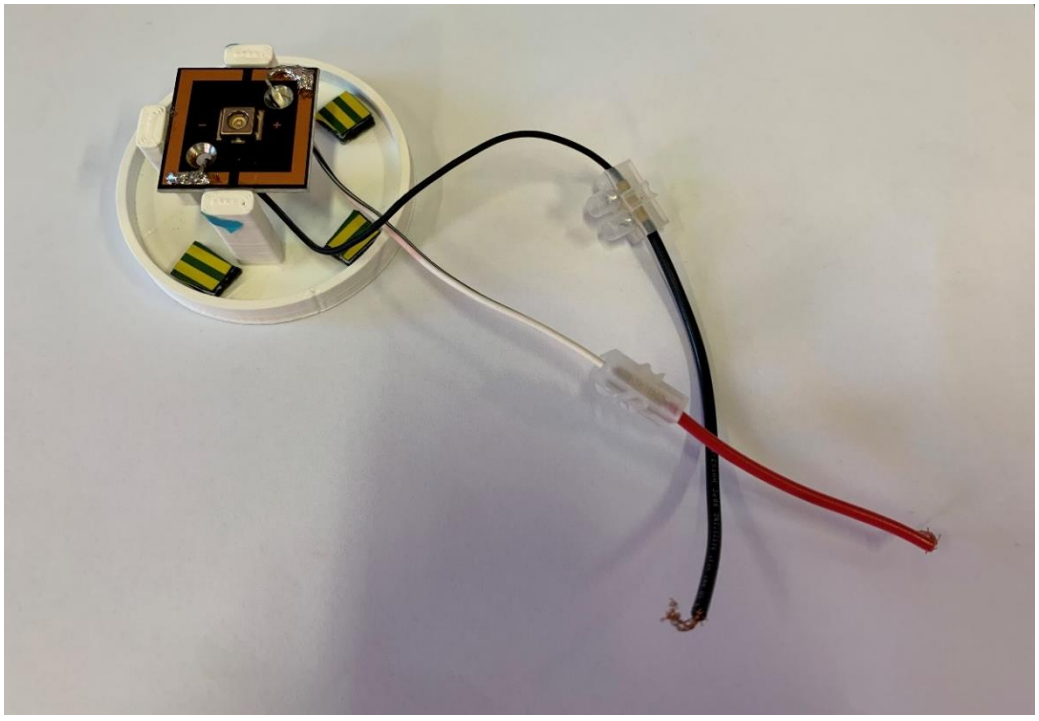

Figure 2.11. Plastic support with the UV-LED ready to be putted on the reactor.

UV source is given by the Nichia NCSU033B UV SMD-LED; whose emission spectrum can be seen in Figure 2.12. Led working conditions were set at 3.8 V and 500 mA, which are provided by an AIM PLH120 generator through welding joints at the poles. During all the tests measurements with the spectrophotometer have been performed once every 30 minutes in the firsts 3 hours of testing and then once every hour for the remaining 3, till reaching 6 hours of photocatalytic test.

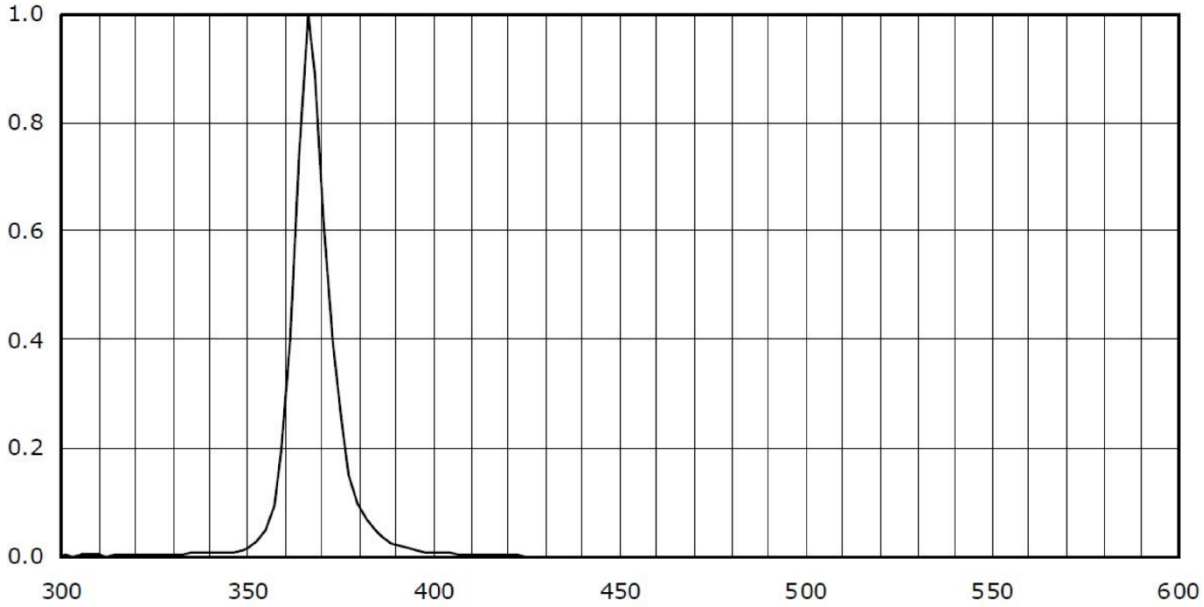

Figure 2.12. Emission spectrum of the UV-LED.

The absorbance analysis has been done with a SPECTROSONIC 200 spectrophotometer; whose image can be seen in Figure 2.13.

Figure 2.13. Spectrophotometer Spectronic 200.

This apparatus is characterized by a fixed beam of emitted light (I_0) in the range 340-1000 nm; this beam pass through a FISHER cuvette, that is filled with a little amount of the solution. Then it correlates this value with the intensity of the same beam of emitted light measured from a sensor positioned after the cuvette (I). The ratio of these two values corresponds to the amount of light that has been absorbed by the solution, at certain wavelengths. For these analysis values going from 400 nm to 700 nm has been considered, which almost corresponds to the range of wavelengths of visible light. The values that have been obtained by this way are called absorbance and corresponds to this quantity: $A = -log\, I/I_0$. This result can be then correlated to the degradation process with the application of the Lambert-Beer law equation: $A = l * C * \varepsilon$. Calibration curves can easily be obtained knowing the two parameters l and ε (the first is constant, in fact it depends only on the instrument, while the other one is depending on the type of the dye, so it will change for every dye involved). For every solution that has been taken in analysis (being it single, binary or ternary) 3 different tests have been performed. The first is the photocatalytic test that has been performed following the scheme just explained and has a 3 times repeatability. These experiments were done changing every time the titanium sample, to evaluate possible differences between samples. A photography of these tests at different times can be seen in Figure 2.14.

Figure 2.14. From left to right are presented 2 tests on methylene blue, the first one just started while the second has been going on for 3 hours.

The other 2 kinds of tests have been performed for every solution are photolysis and absorbance tests. The first one was done without the titanium sample, in order to evaluate the presence of photolysis reactions, while the second one was performed in a dark room (of course even without the UV-LED), to verify the occurrence of adsorption of the dyes on the TiO_2 surface. These two values must be taken into account in order to verify which phenomenon is effectively responsible for the degradation of the dyes giving greater reliability to results obtained with photocatalytic experiments.

2.5 Photocatalytic experiments with White LEDs

The same tests that have been performed using UV-LEDs were also repeated using white LEDs, but only on single dye solutions. These tests have been performed following the same procedure lasting for 6 hours, differently from UV-LEDs tests, during this time even the most labile of the dyes did not reached 0 values of absorbance at its peak. The same mini-batch type reactors have been used as always placed on a stirrer, with a magnet inside to keep the solution mixed during the reaction. Even the white LED is sustained by a plastic support, that has been 3D printed ad hoc for these experiments, this support is able to keep the LED centered on the top of the beaker isolating at the same time the solution from the environment.
In Figure 2.15 the white LED can be seen already attached to its plastic support.

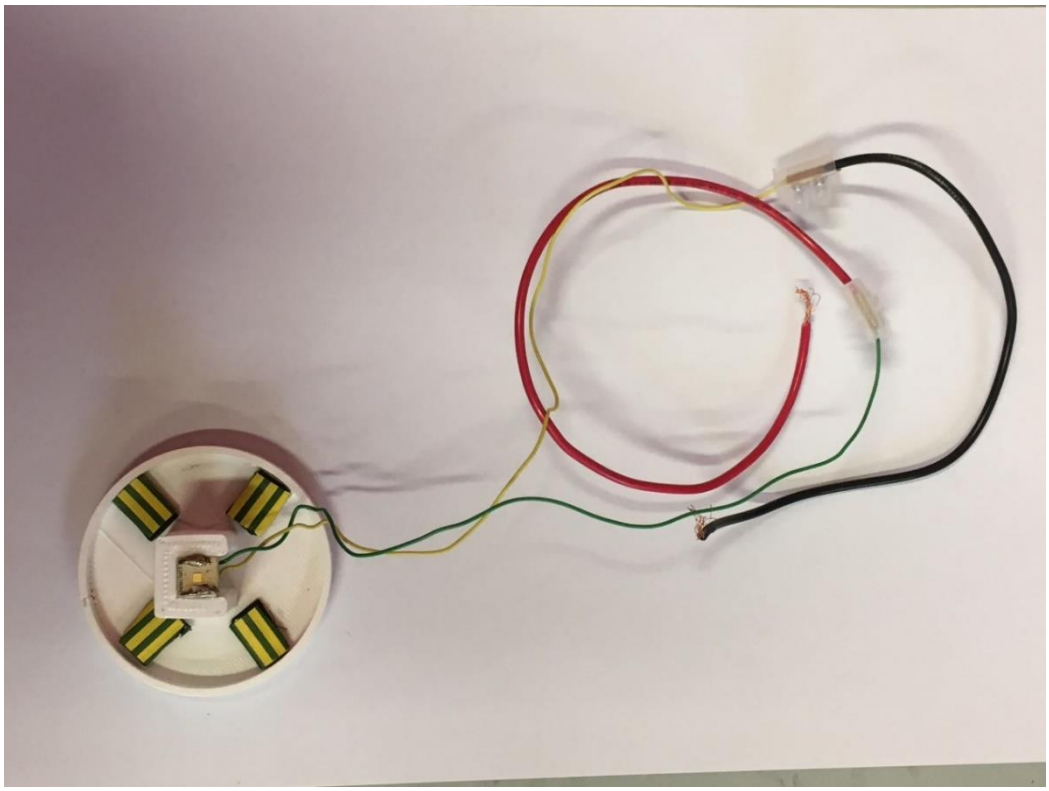

Figure 2.15. Plastic support and the white LED ready to be putted on the reactor.

Light source is given by Nichia NVSWE21AT and emits in the continuous of visible light, its emission spectrum can be seen in Figure 2.16. Its working conditions were set to 3 V and 700 mA provided by an AIM PLH120 generator through welding joints at the poles. During all the tests measurements with the spectrophotometer have been performed once every 30 minutes in the firsts 3 hours of testing and then once every hour for the remaining 3, till reaching 6 hours of photocatalytic test.

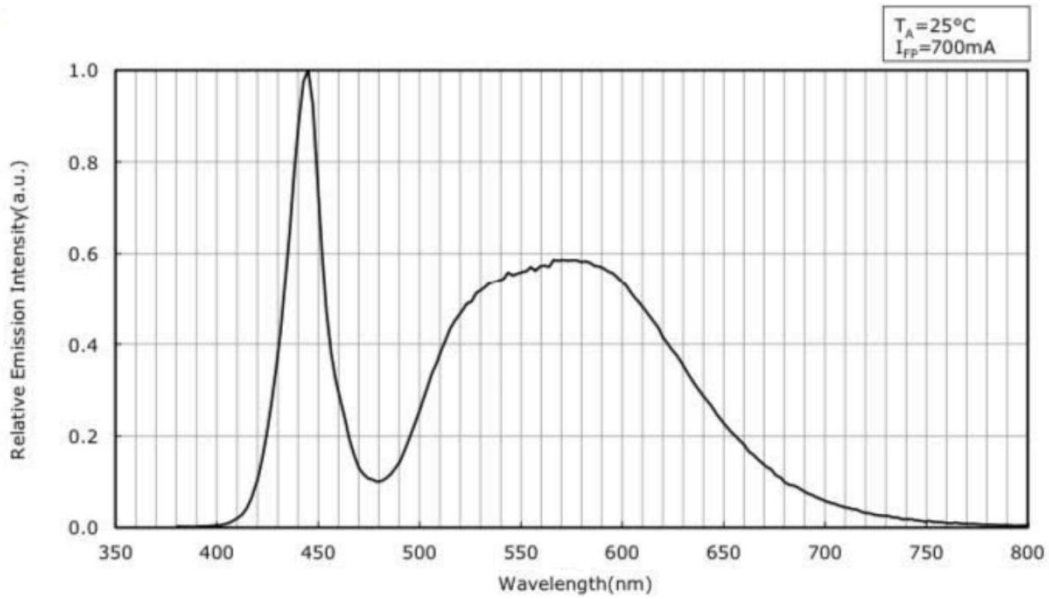

Figure 2.16. Emission spectrum of the white led.

As before the absorbances analysis has been done with a SPECTROSONIC 200 spectrophotometer. For every solution 3 different kinds of test have been performed.

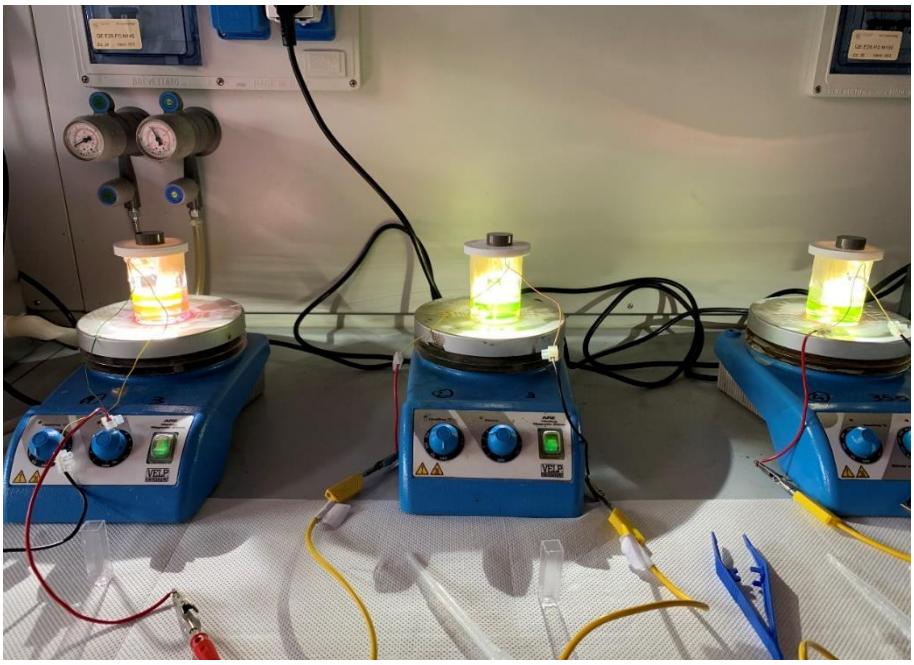

Figure 2.17. Three photocatalytic tests performed on rhodamine B single solution using white LEDs.

The first is the photocatalytic test, with repeatability of three, following the same simple scheme of UV-tests; a photography of these tests can be seen in Figure 2.17. The other 2 kinds of tests that have been performed are again photolysis and absorption tests. The first one was performed without the titanium sample, in order to evaluate the presence of photolysis reactions, while the second one was done in a dark room (of course even without the white LED), to verify the occurrence of adsorption of the dyes on the TiO_2 surface. These two values must be taken into account to verify which phenomenon is effectively responsible for the degradation of the dyes giving greater reliability to results obtained with photocatalytic experiments.

2.6 Dyes solutions

The photocatalytic experiments were carried out on different solutions made by distilled water and dyes, initially all tests were done on single dye solutions, then on binary solutions and lastly on the ternary solution. It has been decided to use 3 different organic dyes for performing these experiments that are Methylene Blue (MB), Rhodamine B (RhB) and Direct Red 80 (DR80); for each one a solution in distilled water concentrated at $10 * 10^{-6}$ M has been prepared, as shown in Figure 2.18.

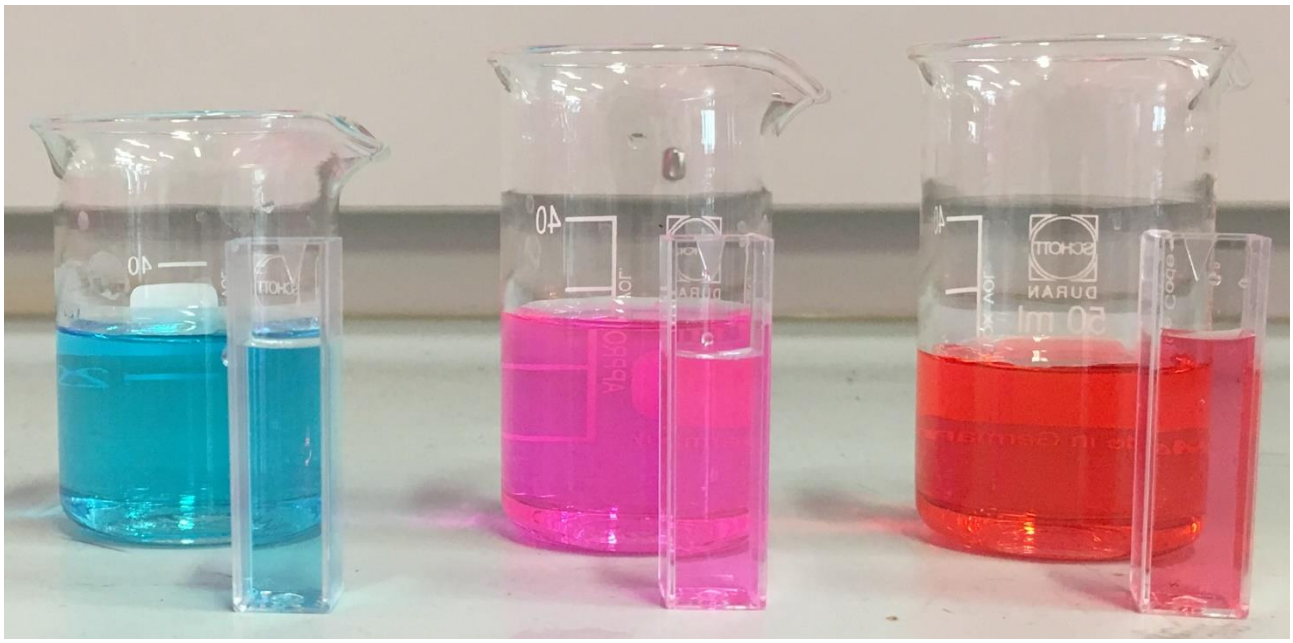

Figure 2.18. From left to right: Methylene Blue, Rhodamine B and Direct red 80.

For these kind of experiments it is impossible to use dyes that are to highly concentrated because they can easily screen the UV-light going from the LED to the samples, so all the initial solutions were made with a concentration of the dye, in the single color solution, of 10^{-5} M. The concentration of the single dye, in binary solutions, was instead of $5 * 10^{-6}$ M, in fact 20 ml of one dye were mixed with 20 ml of the other one, all the 3 combinations of these dyes in binary solutions can be seen in Figure 2.19.

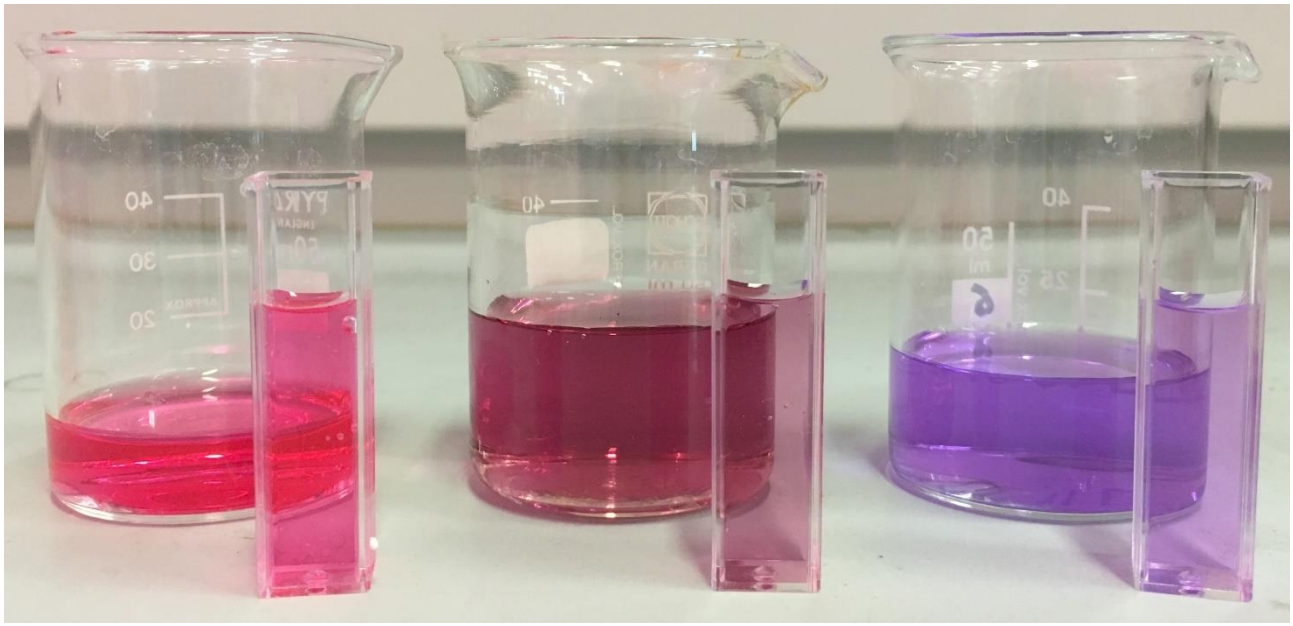

Figure 2.19. From left to right: DR80 + RhB, DR80 + MB and RhB + MB.

The only possible ternary solution were made by all dyes mixed together, it can be seen in Figure 2.20, that solution was always prepared starting from the same dyes concentrated at 10^{-5} M mixed in a solution of 39 ml made by 13 ml of each one reaching a final concentration of $3.33 * 10^{-6}$ M for every dye. For that reason another study on single dye solutions were carried out on solutions made by 13 ml of one dye and 26 ml of distilled water, that was done to obtain the same concentration of the single dye, in the ternary solution, using only one colorant. This is fundamental because it is very important to know how the behavior of a dye in a single solution will differ from the behavior of that same dye in a ternary one to highlight if there are interactions between one dye and the others and how much this phenomenon can interfere with final results.

Figure 2.20. Ternary solution.

Dyes concentrations were monitored by spectrophotometry. To do so, the correlation between concentration and absorbance was needed: therefore, preliminary spectrophotometric tests were performed on a set of dyes samples with different concentrations to build calibration curves, to identify the dye maximum absorbance peak *A* and using it as representative of its concentration *C*, through the application of Beer-Lambert law:

$$A = l * C * \varepsilon \qquad (2.1)$$

In which A represents the absorbance, l corresponds to the optical path length (that depends on the experimental apparatus involved for the measurements) and ε is the molar attenuation coefficient, or absorptivity, of the attenuating species (that depends only on the type of the dye).

A brief characterization of the dyes involved in the experiments and also their behavior in combination with other dyes in binary or ternary solutions is now presented:

Methylene Blue: Methylene blue is a heterocyclic aromatic chemical compound with the molecular formula of $C_{16}H_{18}N_3SCl$ and molecular weight of 319.85 g/mol that is also used for medical purposes. It appears as a dark green powder is solid form while when solved in water it gives to the solution the characteristic blue color. In medicine this molecule is counted in the World Health Organization's list of essential medicines and it is used to treat methemoglobinemia and the Varadi-Papp syndrome and it is also used as a dye in chromoendoscopy, its absorbance spectrum and molecular structure are presented in Figure 2.21 [52].

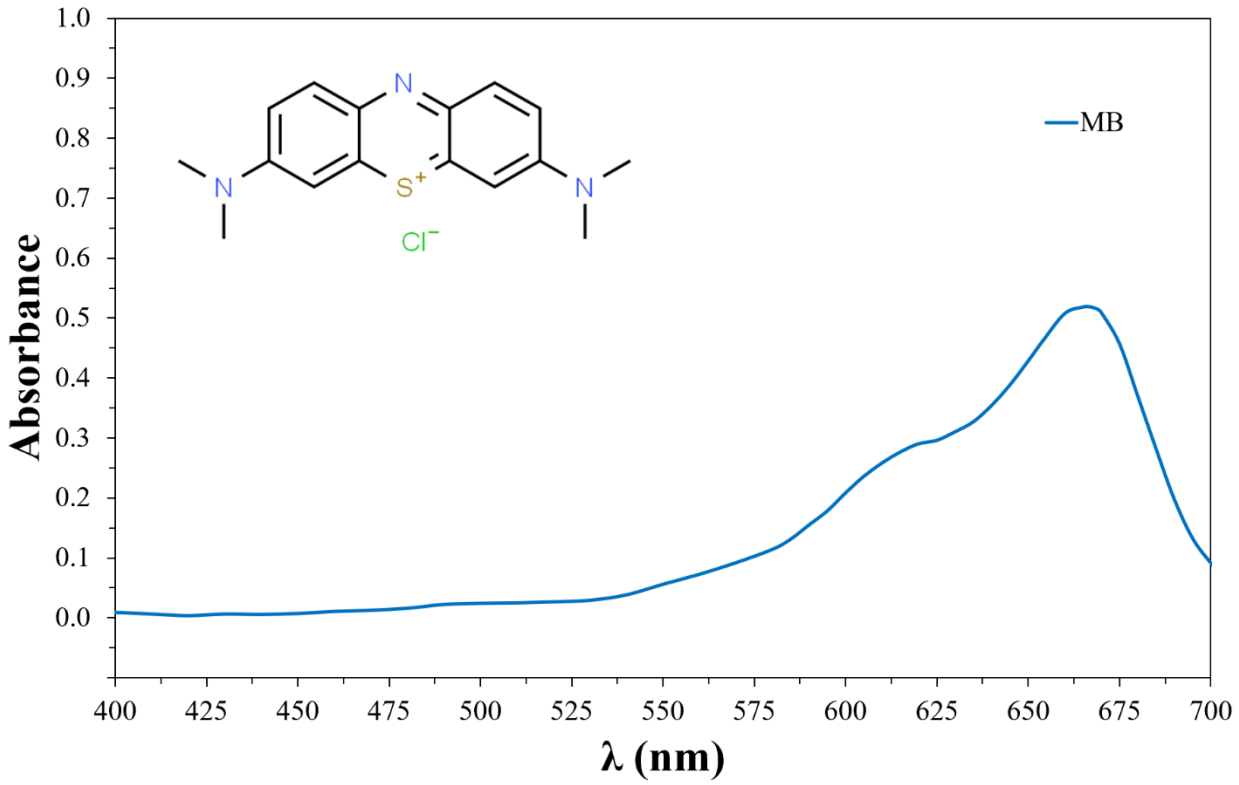

Figure 2.21. Methylene blue absorbance spectrum and molecular structure.

Rhodamine B: Rhodamine B is a xanthene dye whose chemical formula is $C_{28}H_{31}ClN_2O_3$ and has a molecular weight of 479.02 g/mol. This molecule is used as a water tracer fluorescent and also as a colorant in textiles and food industries, it can be quite dangerous if not treated carefully causing eye, skin and respiratory tract irritation. It is also used as a biomarker in oral rabies vaccine, its absorbance spectrum and molecular structure are presented in Figure 2.22 [53].

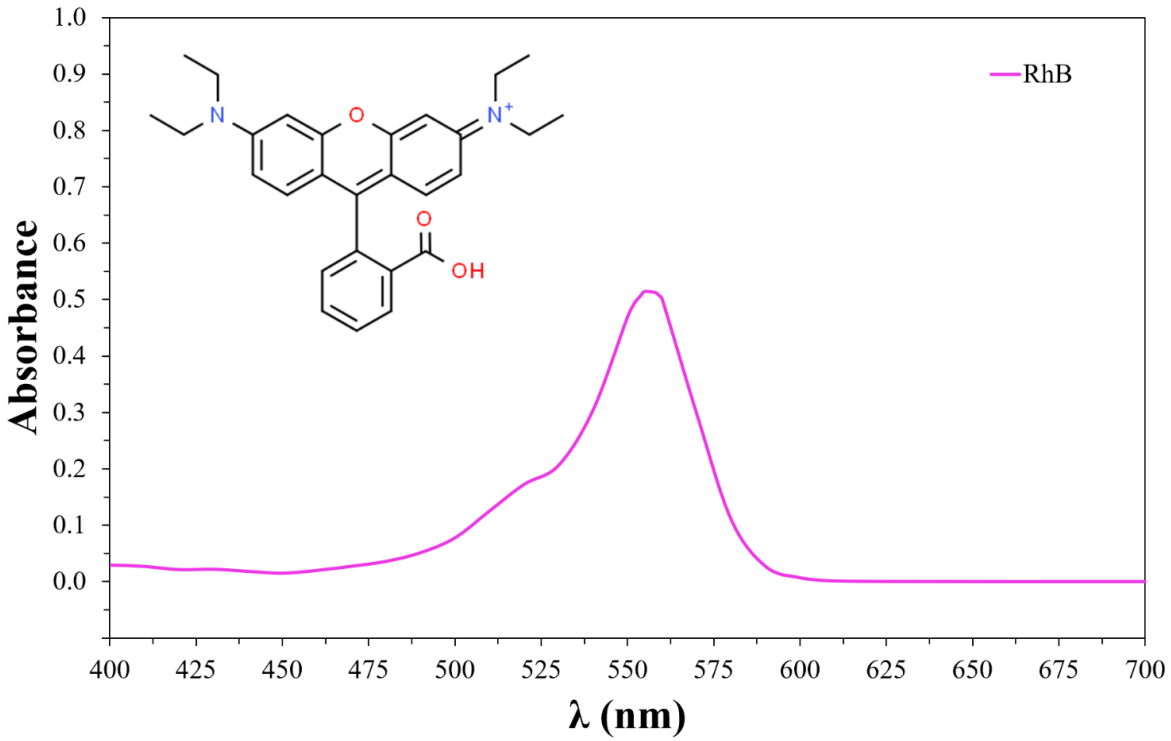

Figure 2.22. Rhodamine B absorbance spectrum and molecular structure.

Direct red 80: Direct red 80 is an organic dye whose chemical formula is $C_{45}H_{26}N_{10}Na_6O_{21}S_6$ and has a molecular weight of 1373.07 g/mol. It is used as an ingredient in the preparation of saturated picric acid for immunohistochemical detection and quantitation of collagen in liver tissues. It has also been used in the staining for collagen, his absorbance spectrum and molecular structure are shown in Figure 2.23. [54]

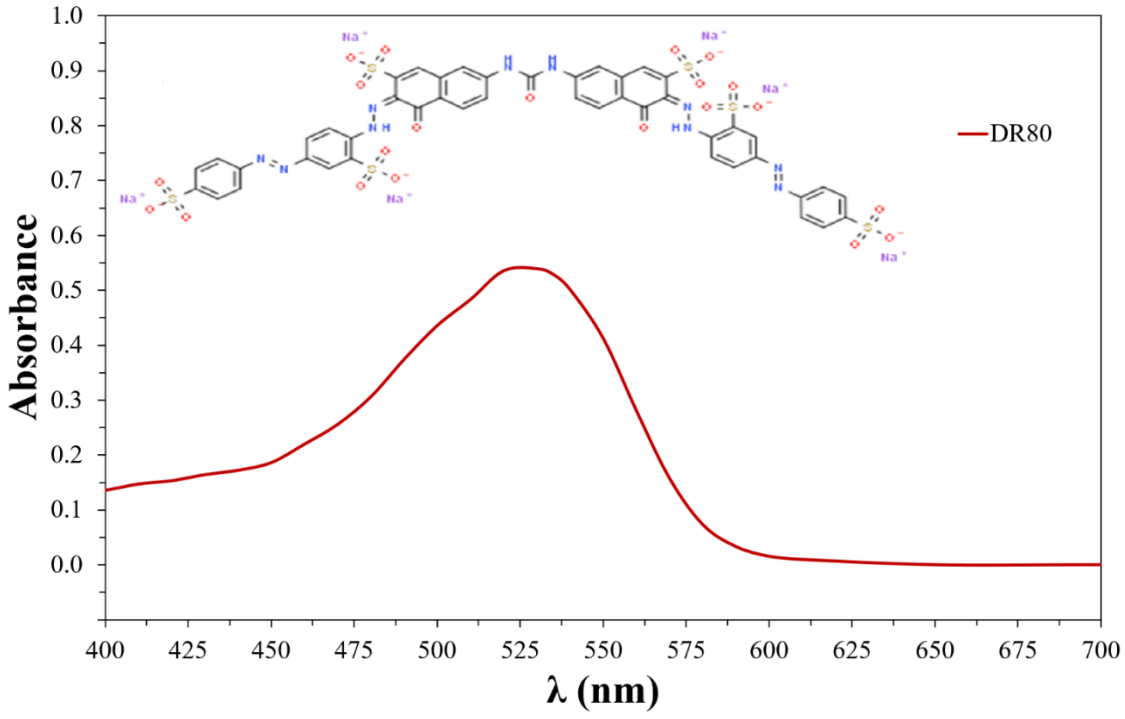

Figure 2.23. Direct red 80 absorbance spectrum and molecular structure.

Binary solutions: The three binary solutions made by the combination of the three single dye solutions were obtained by mixing the same amount in volume of the two dyes selected (20ml + 20ml). Starting from two dyes whose concentrations were $10^{-5}\,M$ a solution has been obtained in which each dye has half the starting concertation that corresponds to $5 * 10^{-6}\,M$, so that the total dye concentration is always equal to $10^{-5}\,M$. All their absorbance spectra can be seen in Figure 2.24.

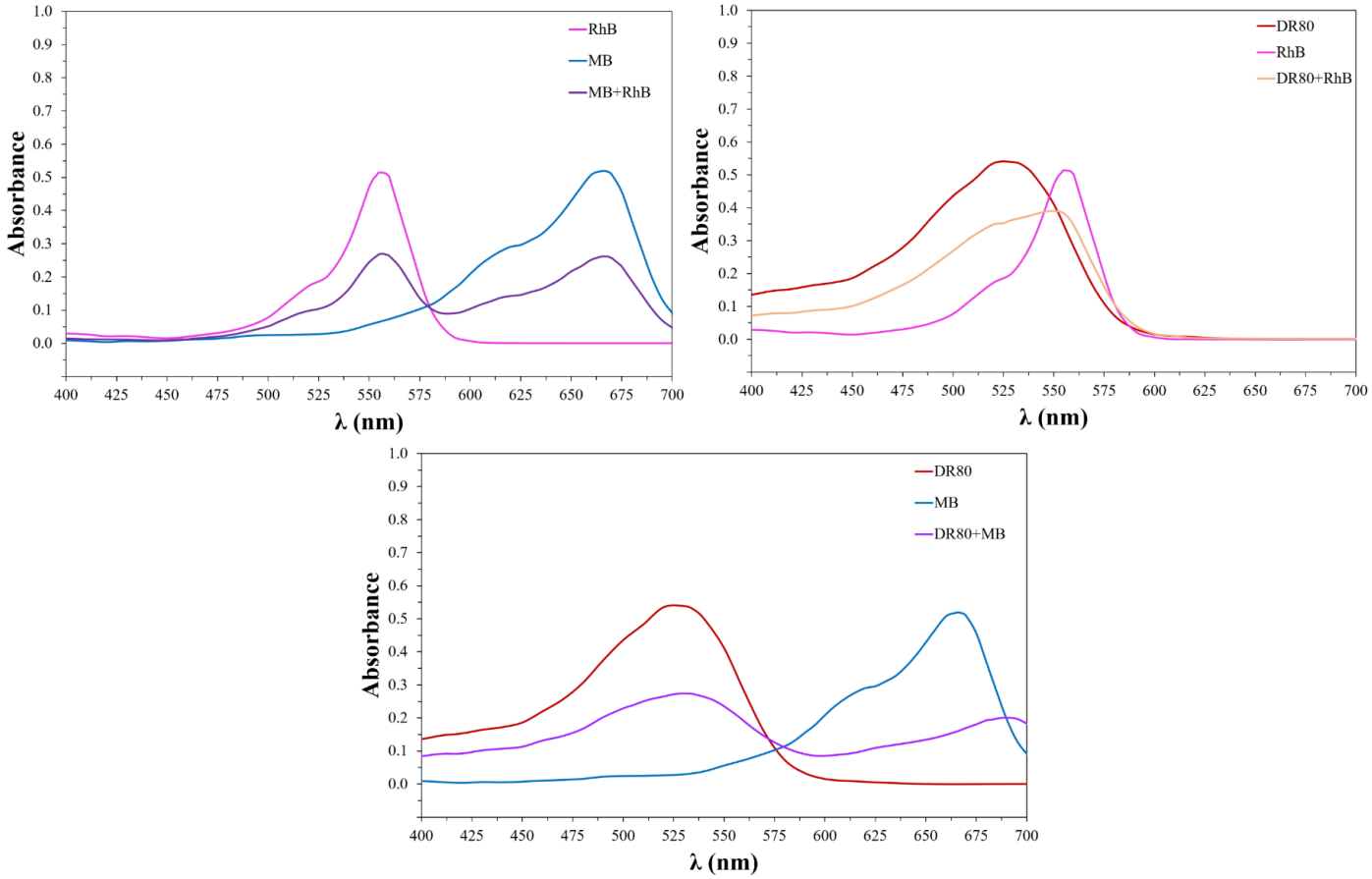

Figure 2.24. MB+RHB, DR80+RHB and DR80+MB binary solutions absorbance spectra.

From these plots some particularities can be noticed, for example in the case of the DR80 + RhB solution there is only a single peak because the two peaks of these two dyes are quite near leading to an overlapping of the two signals. Instead in the other two cases, which are DR80 + MB and MB +RhB, the binary solution presents two peaks because the difference between the single peaks of their components is sufficiently high. Anyway even these two binary solutions had shown a huge difference in their behavior, in fact in the DR80 + MB solution the peak of DR80 remains placed at 527 nm, whereas there is a shift on the MB peak, from 666 nm to 690 nm, due to a possible electrostatic interaction between these two dyes. Instead in the solution made by MB + RhB the two peaks of the binary solution simply correspond to the peaks of the two single-dye solutions, that are 555 nm for RhB and 666 nm for MB.

The problem of overlapping of spectra does not allow to make a discrete analysis of the absorbance of dyes present, so for the analysis of binary solutions the application of a mathematical method has proven to be fundamental. This method is zero-crossing first order derivative spectrophotometry that consist in the conversion of a normal spectra into its first derivative spectra. This allows to determine the right wavelengths that should be chosen to evaluate the exact concentration evolution during photocatalysis, without spectra interference. Moreover, this method is quicker and easier if compared to alternative methods, such as HPLC or GC, since it does not require neither sophisticated instrumentation or any separation tests. [47]
For the final development of this new model some mathematical passages must be done starting from the Beer-Lambert law in which the concentrations of the X component (A_X) and respectively of the Y component (A_Y) can be described by equations (2.2) and (2.3):

$$A_{X,\lambda_i} = \alpha_{X,\lambda_i} C_X \tag{2.2}$$

$$A_{Y,\lambda_i} = \beta_{Y,\lambda_i} C_Y \tag{2.3}$$

Where A_{X,λ_i} and A_{Y,λ_i} corresponds to the absorbance of the 2 compounds X and Y, recorded at a certain wavelength λ_i, while α_{X,λ_i} and α_{Y,λ_i} are the absorptivity of the components of concentrations C_X and C_Y. In a binary solution made by the combination of these 2 components the absorbance value of the mixture can be expressed by equation (2.4):

$$A_{m,\lambda_i} = \alpha_{X,\lambda_i} C_X + \beta_{Y,\lambda_i} C_Y \tag{2.4}$$

Diving equation (2.4) with the absorbance of the singular component X equation (2.5) can be obtained:

$$\frac{A_{m,\lambda_i}}{\alpha_{X,\lambda_i} C_X} = 1 + \frac{\beta_{Y,\lambda_i} C_Y}{\alpha_{X,\lambda_i} C_X} \tag{2.5}$$

Deriving with respect to the wavelength will lead to equation (2.6):

$$\frac{d}{d\lambda}\left[\frac{A_{m,\lambda_i}}{\alpha_{X,\lambda_i} C_X}\right] = \frac{d}{d\lambda}\left[\frac{\beta_{Y,\lambda_i}}{\alpha_{X,\lambda_i} C_X}\right] C_Y \tag{2.6}$$

From equation (2.6) it can be noticed that the derivative spectra of the binary mixture depend on the concentration C_Y, when fixing the concentration of the X component and vice versa. With this method it is possible to evaluate what is the right wavelength that has to be chosen to measure the concentration of one single component in a binary mixture obtaining finally the right calibration curve. This method is based on the fact

that in a binary mixture there are certain wavelengths for which the derivative absorbance of one dye is zero, while the derivate absorbance of the ore dye has a non-zero value. These wavelengths can be taken into account as possible candidates to be studied to obtain the calibration curve, because in these points the measured absorbance derives only from one the two dyes and thus respecting the Lambert-Beer law.
This can be mathematically demonstrated with the development of the quotient rule on equation (2.6), that will provide equation (2.7):

$$\frac{d}{d\lambda}\left[\frac{A_{m,\lambda_i}}{\alpha_{X,\lambda_i}C_X}\right] = \frac{d}{d\lambda}\left[A_{m,\lambda_i}\right]\frac{\alpha_{X,\lambda_i}C_X}{(\alpha_{X,\lambda_i}C_X)^2} - \frac{A_{m,\lambda_i}}{(\alpha_{X,\lambda_i}C_X)^2}\frac{d}{d\lambda}\left[\alpha_{X,\lambda_i}C_X\right] \qquad (2.7)$$

Some terms of the equations (2.6) and (2.7) can be renamed by this way:

$$\frac{\alpha_{X,\lambda_i}C_X}{(\alpha_{X,\lambda_i}C_X)^2} = \sigma \qquad \frac{A_{m,\lambda_i}}{(\alpha_{X,\lambda_i}C_X)^2}\frac{d}{d\lambda}\left[\alpha_{X,\lambda_i}C_X\right] = \tau \qquad \frac{d}{d\lambda}\left[\frac{\beta_{Y,\lambda_i}}{\alpha_{X,\lambda_i}C_X}\right] = \omega$$

Leading to equation (2.8): $$\frac{d}{d\lambda}\left[\frac{A_{m,\lambda_i}}{\alpha_{X,\lambda_i}C_X}\right] = \frac{\omega}{\sigma}C_Y + \frac{\tau}{\sigma} \qquad (2.8)$$

Which has the same form of a linear equation: $y = mx + q$
It has also to be mentioned that the ratio between ω and σ, for a specific wavelength, is constant and does not depend on C_X and C_Y since:

$$\frac{\omega}{\sigma} = \frac{\alpha_{X,\lambda_i}\frac{d}{d\lambda}\left[\beta_{Y,\lambda_i}\right] - \beta_{Y,\lambda_i}\frac{d}{d\lambda}\left[\alpha_{X,\lambda_i}\right]}{\alpha_{X,\lambda_i}} \qquad (2.9)$$

Conclusively the Lambert-Beer law has the form of $y = mx + q$ and the attention must be put on wavelength values were the value q (corresponding to the ratio $\frac{\omega}{\sigma}$) is equal to zero. It has been noticed that in general for binary solutions there are two points that respect this characteristic and that the most correct value of wavelength that has to be taken into account corresponds to the one that presents the higher value of dA/dλ. For calculating derivatives it has been found on literature a range of Δλ values between 4 nm and 10 nm. This value must be chosen based on the sensitivity of instruments involved for making measurements; during this work preliminary tests with two different Δλ values, namely 5 nm and 10 nm, were performed in order to choose the best one. Making calculation of derivates with a Δλ of 10 nm has provided results that are very similar to the ones obtained with a Δλ of 5 nm, consequently, to better approximate the definition of incremental limit ratio, it has been decided to take the

lowest difference value. For this work it was no possible to use a Δλ value below the threshold of 5 nm, this would lead to values for ΔA that are lower than the experimental error, providing not reliable data ([55], [47], [49], [44]).

Ternary solutions: The ternary solution has been made by mixing all the 3 organic dyes in equal parts per volume (13 ml of RhB + 13 ml of MB + 13 ml of DR80). Since all the organic dyes were starting from a concentration of $10^{-5}\ M$ a solution in which every single dye had 1/3 of its initial concentration has been obtained, resulting in a concentration of $3{,}33 * 10^{-6}\ M$ for each dye; even in this case the total dye concentration is equal to $10 * 10^{-6}\ M$. The absorbance spectrum of this solution can be seen in Figure 2.25, looking at the graph some features can be noticed: the ternary solution presents all the 3 peaks of single dyes solutions but the one corresponding to the rhodamine B value, at 555 nm, is more accentuated because there is a partial overlapping with the peak corresponding to direct red 80 that is nearly located at 527 nm. Regarding the peak of methylene blue, it can be seen that it follows the same behavior presented in the binary solution made by MB + DR80, confirming the hypothesis that there is an interaction between these two dyes that acts
shifting this peak from 666 nm to 690 nm. Even in this case the MB spectrum, at its peak, overlaps neither with DR80 or with RhB.

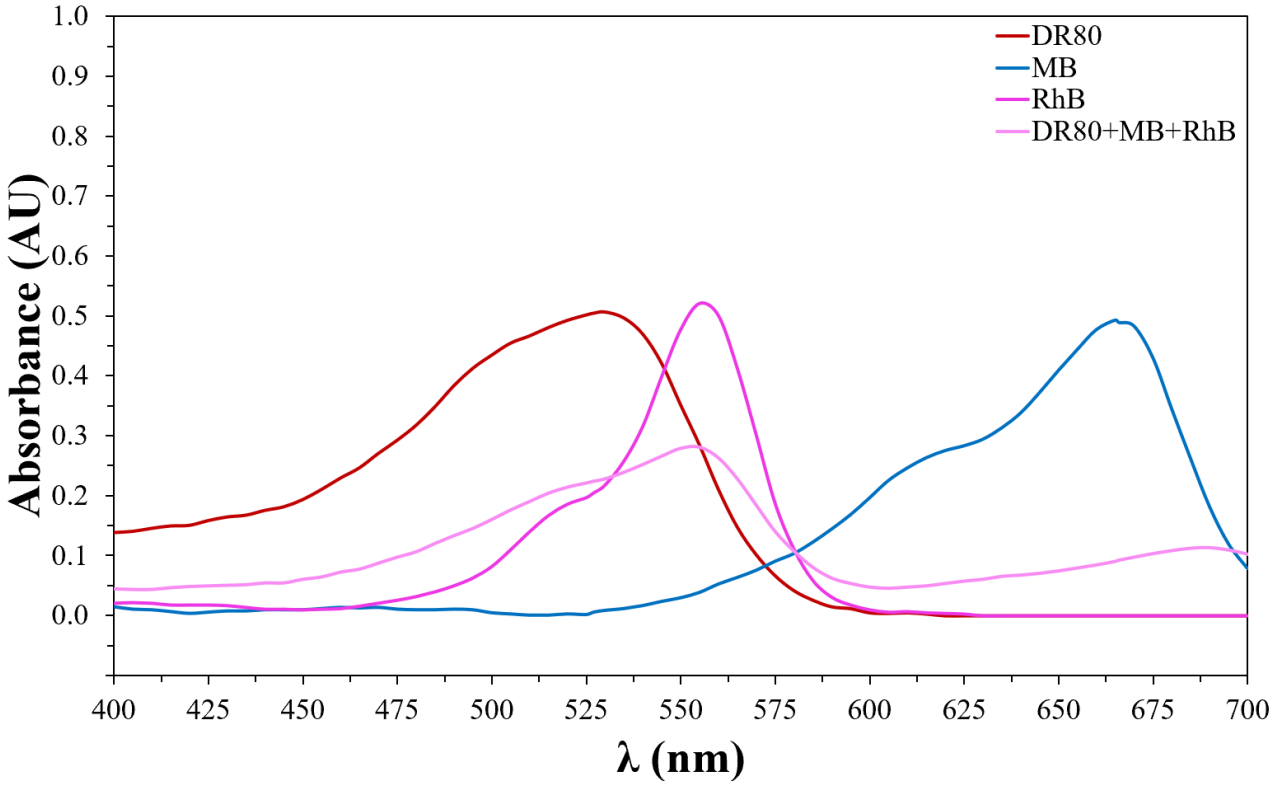

Figure 2.25. Ternary solution absorbance spectrum presented with single-dye solutions absorbance spectra.

Even for ternary solutions the overlapping of spectra does not allow to make a discrete analysis of the absorbance of dyes present, again for the analysis of these solutions the application of a mathematical method has proven to be fundamental. For ternary mixtures the method chosen is double divisor-ratio spectra derivative spectrophotometry in which for a ternary mixture (made for example by three components X, Y and Z) to determine one component like X the spectra of X+Y+Z are divided by the sum of the spectra of Y and Z as "double divisor" and their ratio spectra are obtained. From the resulting ratio spectra, the first derivative of the ratio spectra is traced. Once that the first derivative of the ratio spectra of a pure compound and its ternary mixture have been obtained these spectra can be plotted together to see where there is an overlapping in correspondence of a maximum point, or a minimum point, of the wavelength. These coinciding points of the derivative of the ratio spectra can be selected as working wavelengths for the determinations of the subject compounds in the ternary mixture.
Mathematically speaking if a ternary mixture made by three components called X, Y and Z, for simplicity, is considered and if all the components obey the Beer-Lambert law the UV-VIS spectrum of a ternary mixture, at a wavelength corresponding to λ_i, can be given by equation (2.10):

$$A_{M,\lambda_i} = \alpha_{X,\lambda_i} C_X + \beta_{Y,\lambda_i} C_Y + \gamma_{Z,\lambda_i} C_Z \qquad (2.10)$$

Where A_{M,λ_i} corresponds to the absorbance of the ternary mixture at λ_i, while α_{X,λ_i}, β_{Y,λ_i} and γ_{Z,λ_i} are the absorbances of X, Y and Z, respectively.
The double divisor corresponds to the absorbance of two compounds in a ternary mixture and can be written with a similar expression:

$$A_{M,\lambda_i} = \alpha_{X,\lambda_i} C_X + \beta_{Y,\lambda_i} C_Y \qquad (2.11)$$

Now dividing equation (2.10) with equation (2.11) the resulting expression for the ratio of spectra will be given as equation (2.12):

$$\frac{A_{M,\lambda_i}}{\alpha_{X,\lambda_i} C_X^0 + \beta_{Y,\lambda_i} C_Y^0} = \frac{\alpha_{X,\lambda_i} C_X + \beta_{Y,\lambda_i} C_Y}{\alpha_{X,\lambda_i} C_X^0 + \beta_{Y,\lambda_i} C_Y^0} + \frac{\gamma_{Z,\lambda_i} C_Z}{\alpha_{X,\lambda_i} C_X^0 + \beta_{Y,\lambda_i} C_Y^0} \qquad (2.12)$$

The first ratio $\frac{\alpha_{X,\lambda_i}C_X+\beta_{Y,\lambda_i}C_Y}{\alpha_{X,\lambda_i}C_X^0+\beta_{Y,\lambda_i}C_Y^0}$ is equal to a constant (K), or very close to 1, with respect to λ_i in a certain range of wavelength and if the K constant is replaced in equation (2.12) the equation (2.13) can be obtained:

$$\frac{A_{M,\lambda_i}}{\alpha_{X,\lambda_i}C_X^0+\beta_{Y,\lambda_i}C_Y^0} = K + \frac{\gamma_{Z,\lambda_i}C_Z}{\alpha_{X,\lambda_i}C_X^0+\beta_{Y,\lambda_i}C_Y^0} \quad (2.13)$$

In the double divisor procedure the two concentrations C_X^0 and C_Y^0 are equal or at least very close to each other so: $\alpha_{X,\lambda_i}C_X^0 + \beta_{Y,\lambda_i}C_Y^0 \cong (\alpha_{X,\lambda_i} + \beta_{Y,\lambda_i})C_X^0$ (2.14)

Substituting equation (2.14) in equation (2.13) will provide equation (2.15):

$$\frac{A_{M,\lambda_i}}{(\alpha_{X,\lambda_i}+\beta_{Y,\lambda_i})C_X^0} = K + \frac{\gamma_{Z,\lambda_i}C_Z}{(\alpha_{X,\lambda_i}+\beta_{Y,\lambda_i})C_X^0} \quad (2.15)$$

The first, or high order, derivation of equation (2.15) can be taken with respect to λ_i in the selected region wavelength, remembering that the derivation of a constant, like K, will give 0 as result providing equation (2.16):

$$\frac{d}{d\lambda}\left[\frac{A_{M,\lambda_i}}{(\alpha_{X,\lambda_i}+\beta_{Y,\lambda_i})C_X^0}\right] = \frac{d}{d\lambda}\left[\frac{\gamma_{Z,\lambda_i}C_Z}{(\alpha_{X,\lambda_i}+\beta_{Y,\lambda_i})C_X^0}\right]\frac{C_Z}{C_X^0} \quad (2.16)$$

This derivative signal of Z is depending exclusively on C_Z and C_X^0 and is independent on the concentrations C_X and C_Y in ternary mixtures, while the concentration C_Z is proportional to the derivative signal in the points corresponding to the maximum and the minimum of wavelengths for pure Z and its ternary mixture with X and Y.

The same procedure can be applied to obtain C_X and C_Y making the appropriate settings, the final equation represents the expression of double divisor-ratio spectra derivative method for the resolution of a generic ternary mixture. When applying this method an accurate choice of standard double divisor concentration is mandatory, since it can strongly influence the results. [44]

Indeed first derivative signals are proportionally decreased if the concentration of the standard solution (the divisor) increases, and vice versa, even if the maxima and

minima positions are still fixed at the same wavelengths. As a consequence, the slope of the resulting calibration curve for the evaluation of the Z compound decreases as the standard double divisor concentrations (C_X^0 and C_Y^0) increase, this could lead to a poor data differentiation ([55], [44], [56]).

On the other hand, too low standard double divisor concentrations could lead to an increase of signal-to-noise ratio, augmenting the derivative of the ratio $\frac{A_{M,\lambda_i}}{\alpha_{X,\lambda_i}C_X^0+\beta_{Y,\lambda_i}C_Y^0}$, consequently increasing the standard error for these estimations. [57]

For the evaluation of the standard concentration for the ternary mixture analyzed in this work, made by DR80 + MB + RhB, seven different double divisors have been tested. The best ones were found by choosing three equimolar double divisors, leading to an equivalent concentration for each dye equal to $2.5 * 10^{-6}\ M$. This decision has been taken because it represents the best balance among data differentiation, linearity range and experimental errors.

Lastly, has for zero-crossing first order derivative spectrophotometry, the determination of working wavelengths for the determination of the subject compounds has to be done. To do this the first derivative of the ratio spectra of a pure compound have to be plotted together with the ratio spectra of its ternary mixture. In these plots there here would be points coinciding in the spectral region corresponding to a maximum point or a minimum point of the wavelength. These points of the derivative of the ratio spectra can be selected as working wavelengths. As for binary solutions during the building of calibration curves all the derivatives have been calculated using a $\Delta\lambda$ of 5 nm and 10 nm, again results obtained were very similar, so the value of 5 nm has been selected because it can approximate better the incremental ratio limit without compromising ΔA values reliability.

Chapter 3 : Results and Discussions

3.1 Analysis of Anodization and Annealing procedures

The final goal of this thesis is to evaluate the photodegradation of three different organic dyes performing tests on single-dye, binary and ternary solutions, in which the total concentration of dyes is always equivalent to 10^{-5} M. Even if the 14 samples have been prepared in the same way, the presence of defects could affect their behavior providing different results. In order to check the behavior of each sample and the repeatability and reproducibility of the synthesis of the photocatalyst, each photocatalytic test has been performed three times. These photocatalytic tests have been performed on different samples, reproduced identically, to analyze repeatability and discard variability in the measurement related to sample preparation; indeed, results showed a very similar behavior for all samples, with variations smaller than the differences actually observed in the tests discussed afterwards. This can grant a high reproducibility to all the tests performed, which is a key parameter for this kind of experimental analyses. Before starting with photodegradation experiments, the characterization of the samples has been performed, through SEM and XDR analyses, in order to evaluate both the effective formation of nanotubular structures by means of anodization and the formation of the proper crystalline structure with annealing.

Figures 3.1 and 3.2 show the homogeneous, nanotubular oxide layer obtained via anodization on one of the samples involved for photocatalytic experiments.

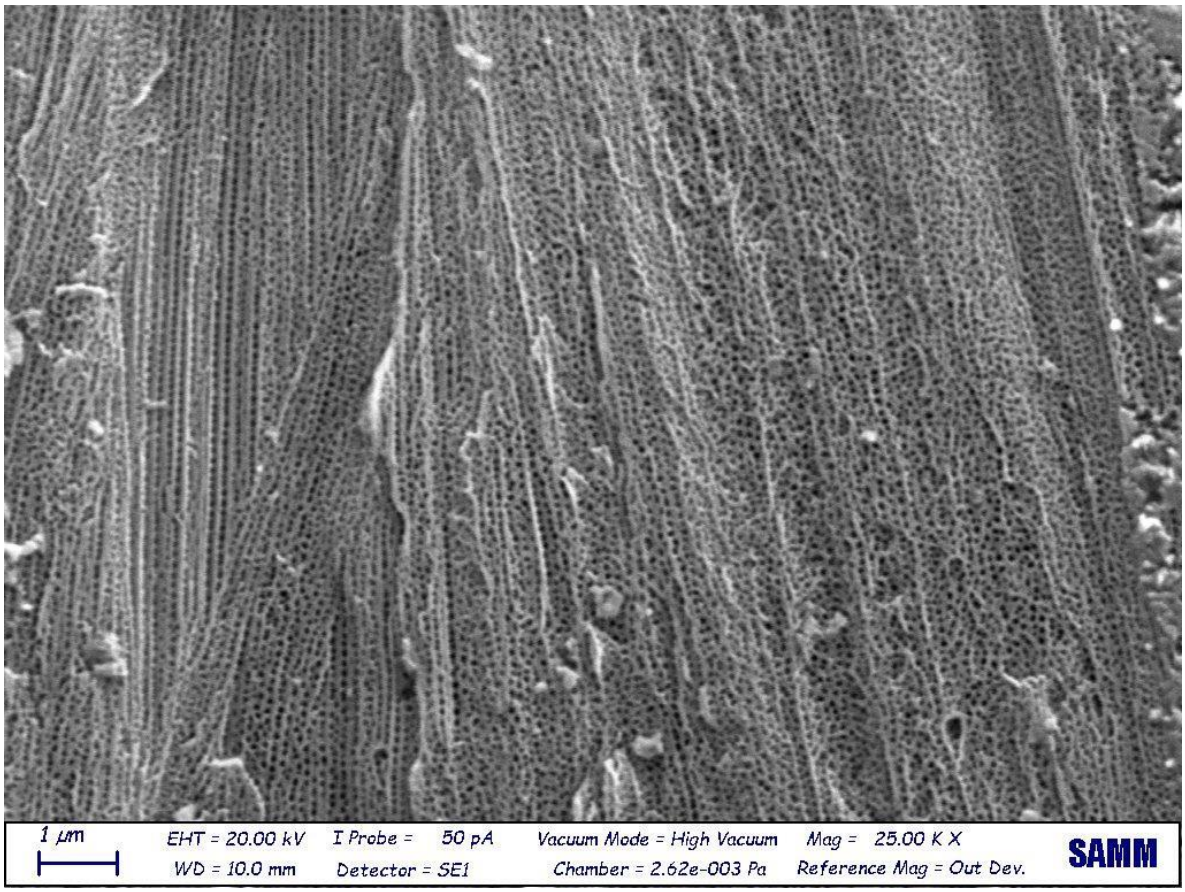

Figure 3.1. Scanning electron microscope image of the nanotubular TiO_2 structure present on one sample.

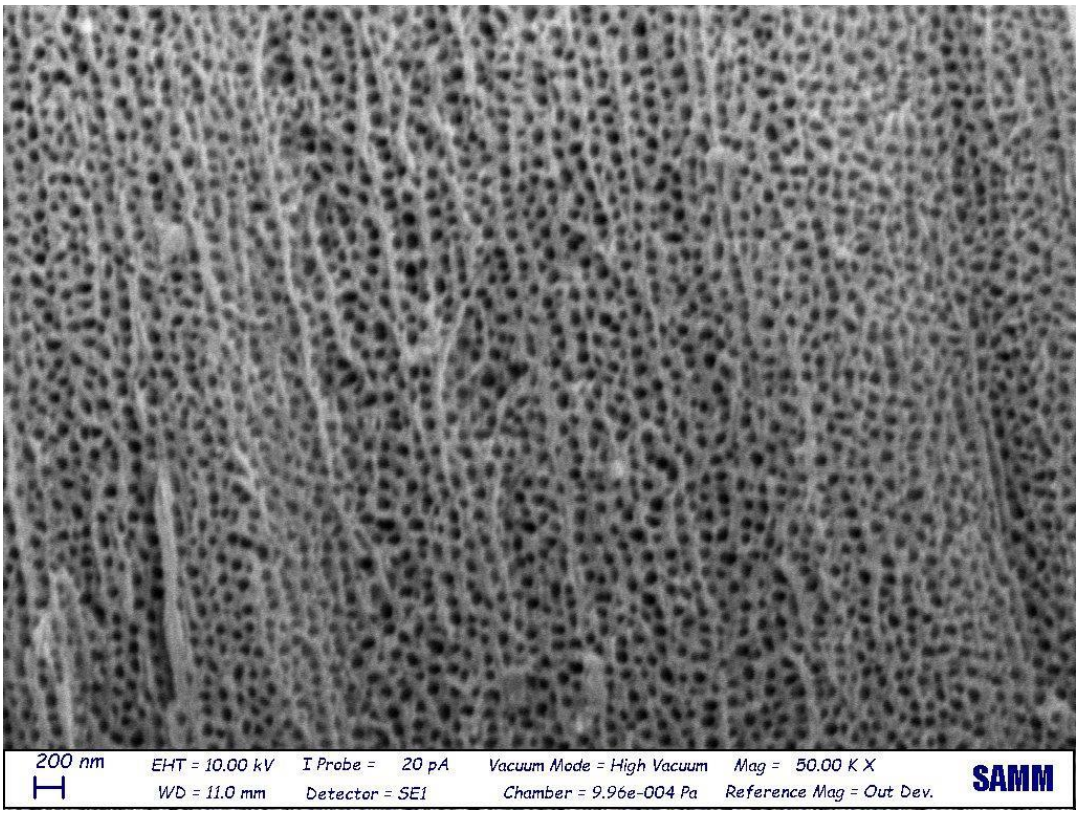

Figure 3.2. Scanning electron microscope zoomed image of the nanotubular TiO_2 structure present on one sample.

Moreover, XRD analysis has been done on the same sample (Figure 3.3): the typical peaks of titanium appear after the anodizing process only, while different peaks appear after the annealing process, corresponding to the growth of the anatase and rutile phases which are fundamental to obtain an high photocatalytic efficiency.

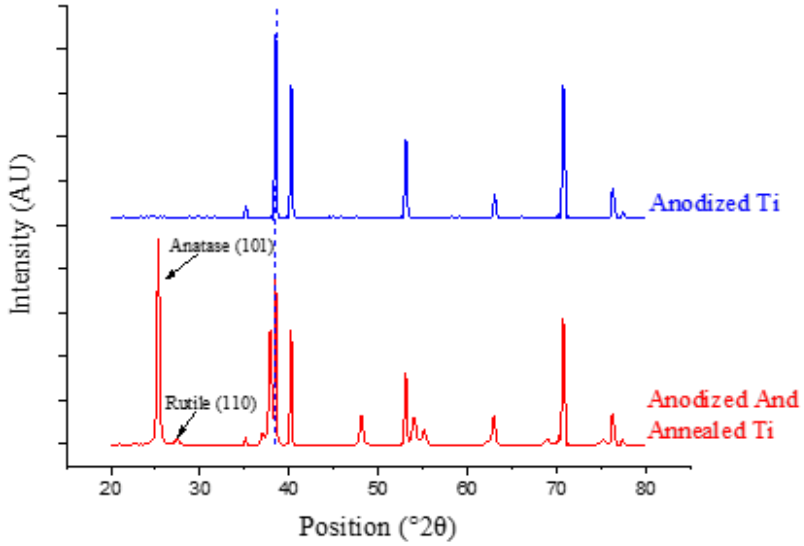

Figure 3.3. X- ray diffraction analyses performed on a titanium sample before and after annealing.

It has been demonstrated that annealing processes must be performed in a temperature range comprised between 500 °C and 600 °C, from previous investigation it has been seen that the composition of these two phases can strongly influence photocatalytic activity. For the analysis of anatase-rutile mixtures, it has been used a function of the intensities that is approximately equal to the weight fraction x_A of anatase present:

$$x_A \approx f = \frac{1}{1+1.26*\frac{I_R}{I_A}} \qquad (3.1)$$

In which I_R/I_A is the ratio of the intensity of the strongest rutile reflection to the intensity of the strongest anatase reflection [58].

The ideal mass fractions of rutile and anatase, that has been reported in literature, corresponds to anatase at 78% in mass fraction and rutile at 22%. During the analysis of our sample different mass fractions has been founded, which corresponds to 3% rutile and 97% anatase. Among literature there is a huge discrepancy about the argument of the “ideal ratio”; indeed, despite this huge difference respect to ideal theoretical values, very good results have been provided during photocatalytic experiments, as can be seen in following subchapters. At lower temperatures there is a too weak crystallization of the samples, while at higher temperatures there is a too high conversion of anatase into rutile phase, which has the lowest photocatalytic activity among three different crystalline phases of TiO_2, and also a rupture of nanotubular structures can occur [59].

3.2 Calibration Curves

Before starting with photocatalytic tests another important step must be done that is the building of calibration curves. As it has already been mentioned to evaluate the effective degradation of the organic dyes (in single-dye, binary and ternary solutions) all the tests have been stopped every 30 minutes in order to evaluate the absorbance variation through spectrophotometric analyses. It is possible to trace the concentration values of the dyes form the absorbance values using simply the Lambert-Beer law:

$$A = l * C * \varepsilon \qquad (3.2)$$

In equation (3.2) l corresponds to the optical path length (that depends only on the experimental apparatus used for the measurements) and ε corresponds to the molar attenuation coefficient or absorptivity of the attenuating species (that depends only on the type of the dye). If the concentration-absorbance correlation is known, as given by a calibration curve, it is possible to obtain concentration values directly from absorbance ones.

Depending on the evaluated solutions, different calibration curves have been built.

Single solutions: All the calibration curves for each single-dye solution were built experimentally. Starting from a solution of known concentration four others were obtained by dilution with distilled water, remaining in the range of 0 - 1.6 Abs (that is the range in which the spectrophotometer works). The absorbance values obtained from the spectrophotometer were measured and a linear regression was made leading to the plots visible in Figures 3.4, 3.5 and 3.6.

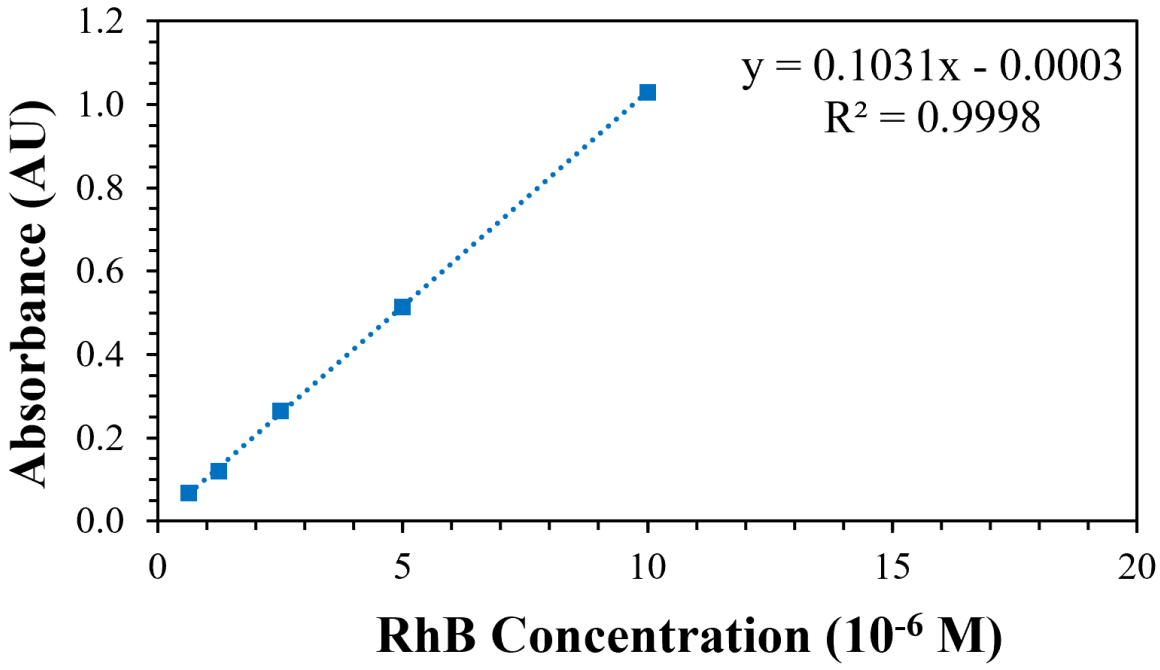

Figure 3.4. Rhodamine B calibration curve.

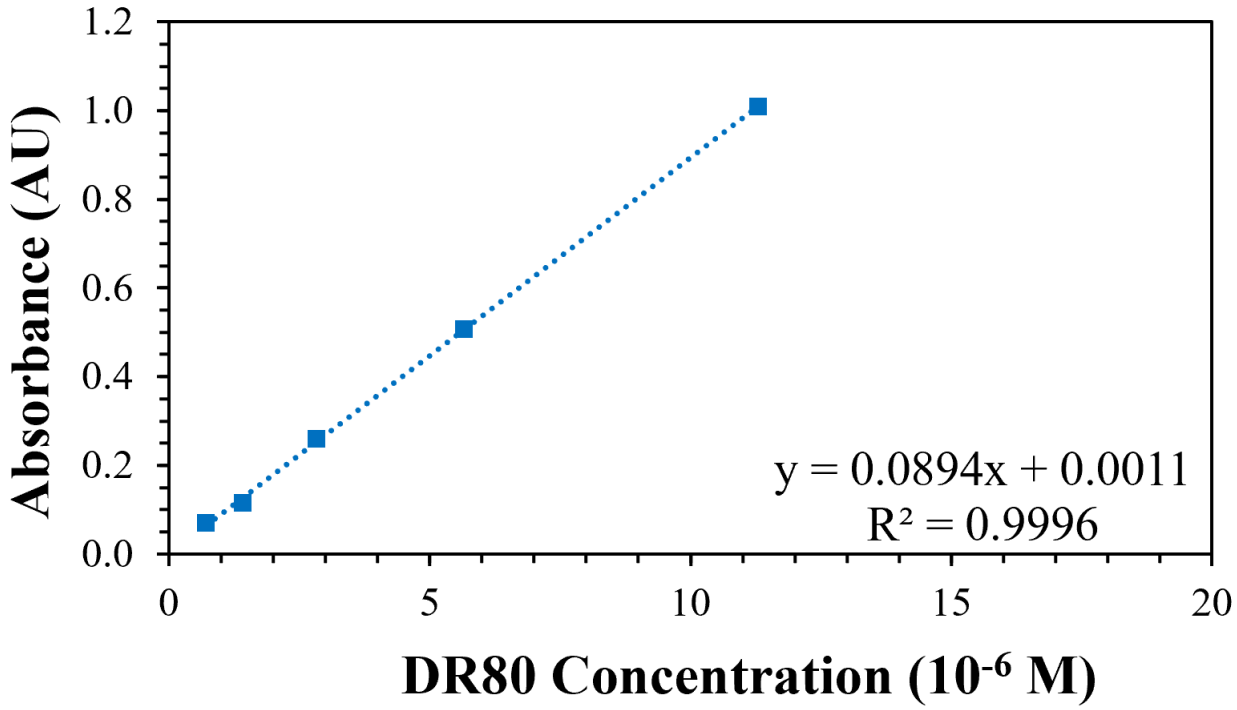

Figure 3.5. Direct red 80 calibration curve.

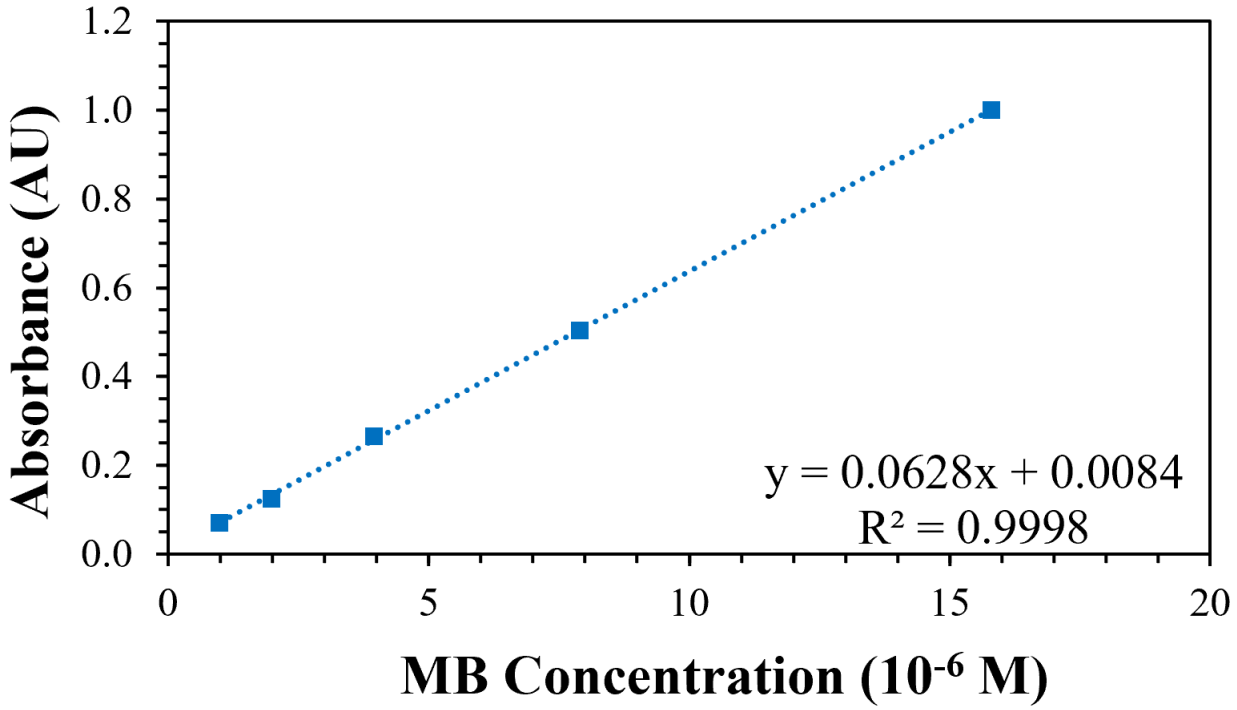

Figure 3.6. Methylene blue calibration curve.

These curves are showing a high linearity between absorbance and concentration, as can be seen from R^2 values that are always higher than 0.999. Moreover, intercept values with absorbance axis are always negligible, which is a key parameter for the reliability of these curves (indeed if the concentration of the dye is null also its absorbance value must be null, according to Beer-Lambert law).

It has to be mentioned that the slopes of the curves changes as a function of the dye studied and therefore ε also changes.
Calibration curves have also been built for binary and ternary solutions but using different methods, that have been already mentioned in the previous chapters, for solving the problem of overlapping of the spectra.

Binary solutions: Binary solutions are obtained by mixing 2 dyes in a volume ratio of 50/50 (with 20 ml of each dye). For the building of calibration curves different solutions have been prepared varying every time the concentration of one of the two dyes, while of course maintaining constant the concentration of the other one, obtaining different concentration ratios. After that the same procedure has been applied in reverse changing the concentration of the other dye, while keeping constant the concentration of the dye that was varying the first time, resulting in the solutions that can be seen in Table 3.1.

Table 3.1. Concentration of dyes in all binary solutions studied for the building of calibration curves.

MB+RhB		
Name	Concentration MB	Concentration RhB
MB+RhB - 1	3.95	2.50
MB+RhB - 2	0.00	2.50
MB+RhB - 3	0.79	2.50
MB+RhB - 4	1.58	2.50
MB+RhB - 5	2.37	2.50
MB+RhB - 6	3.16	2.50
MB+RhB - 7	5.93	2.50
MB+RhB - 8	7.90	2.50
MB+RhB - 9	3.95	0.00
MB+RhB - 10	3.95	0.50
MB+RhB - 11	3.95	1.00
MB+RhB - 12	3.95	1.50
MB+RhB - 13	3.95	2.00
MB+RhB - 14	3.95	3.75
MB+RhB - 15	3.95	5.00
	$\cdot 10^{-6}$ M	$\cdot 10^{-6}$ M

DR80+MB		
Name	Concentration DR80	Concentration MB
DR80+MB - 1	2.83	3.95
DR80+MB - 2	0.00	3.95
DR80+MB - 3	0.57	3.95
DR80+MB - 4	1.13	3.95
DR80+MB - 5	1.70	3.95
DR80+MB - 6	2.26	3.95
DR80+MB - 7	4.24	3.95
DR80+MB - 8	5.65	3.95
DR80+MB - 9	2.83	0.00
DR80+MB - 10	2.83	0.79
DR80+MB - 11	2.83	1.58
DR80+MB - 12	2.83	2.37
DR80+MB - 13	2.83	3.16
DR80+MB - 14	2.83	5.93
DR80+MB - 15	2.83	7.90
	$\cdot 10^{-6}$ M	$\cdot 10^{-6}$ M

DR80+RhB		
Name	Concentration DR80	Concentration RhB
DR80+RhB - 1	2.83	2.50
DR80+RhB - 2	0.00	2.50
DR80+RhB - 3	0.57	2.50
DR80+RhB - 4	1.13	2.50
DR80+RhB - 5	1.70	2.50
DR80+RhB - 6	2.26	2.50
DR80+RhB - 7	4.24	2.50
DR80+RhB - 8	5.65	2.50
DR80+RhB - 9	2.83	0.00
DR80+RhB - 10	2.83	0.50
DR80+RhB - 11	2.83	1.00
DR80+RhB - 12	2.83	1.50
DR80+RhB - 13	2.83	2.00
DR80+RhB - 14	2.83	3.75
DR80+RhB - 15	2.83	5.00
	$\cdot 10^{-6}$ M	$\cdot 10^{-6}$ M

From the analysis of these data, and their spectra, calibration curves for every dye in all binary solutions has been obtained; these are presented in Figure 3.7, 3.8 and 3.9 (blue lines) together with calibration curves obtained previously for single-dye solutions (red lines) for a rapid comparison.

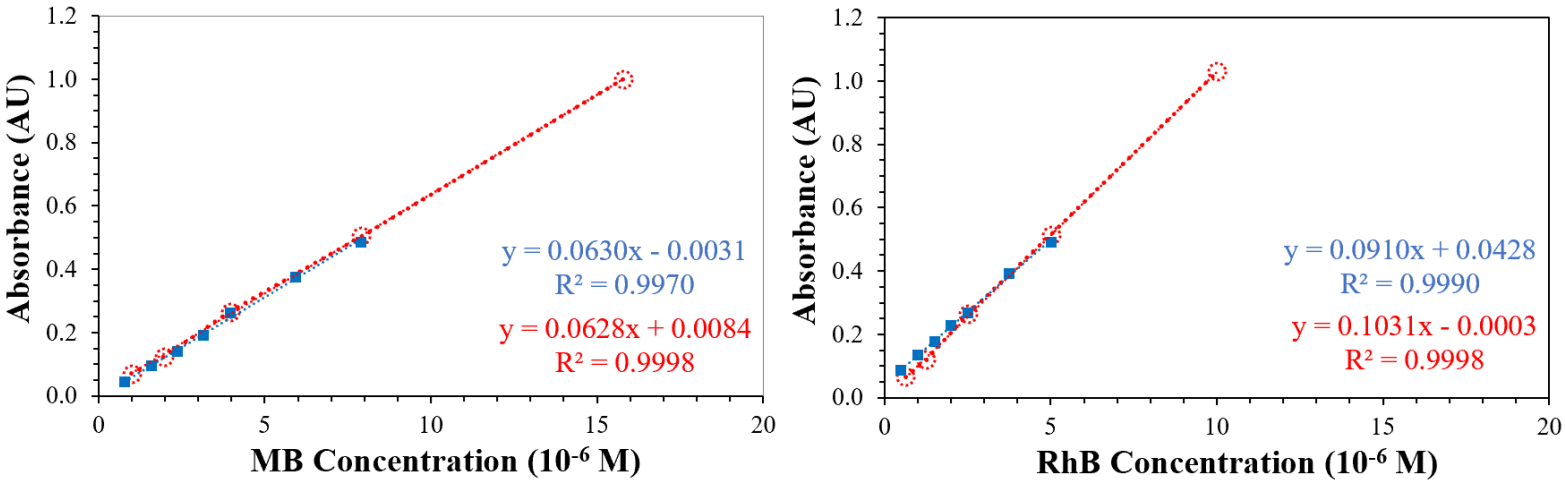

Figure 3.7. MB and RhB calibration curves obtained from the study of their binary solution.

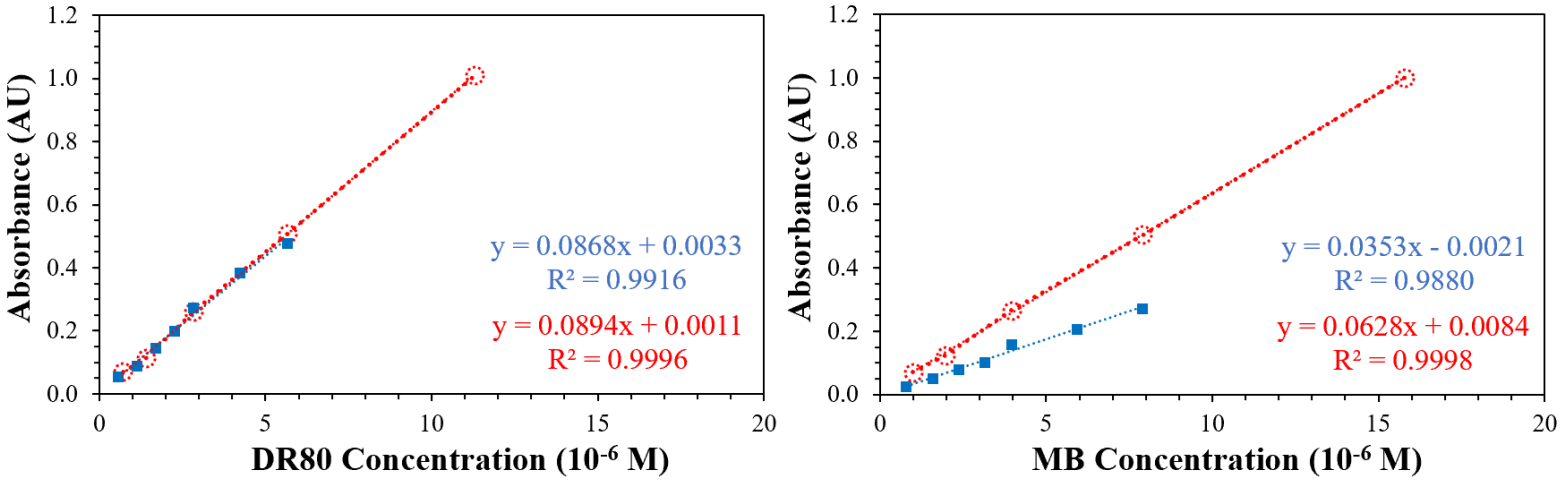

Figure 3.8. DR80 and MB calibration curves obtained from the study of their binary solution.

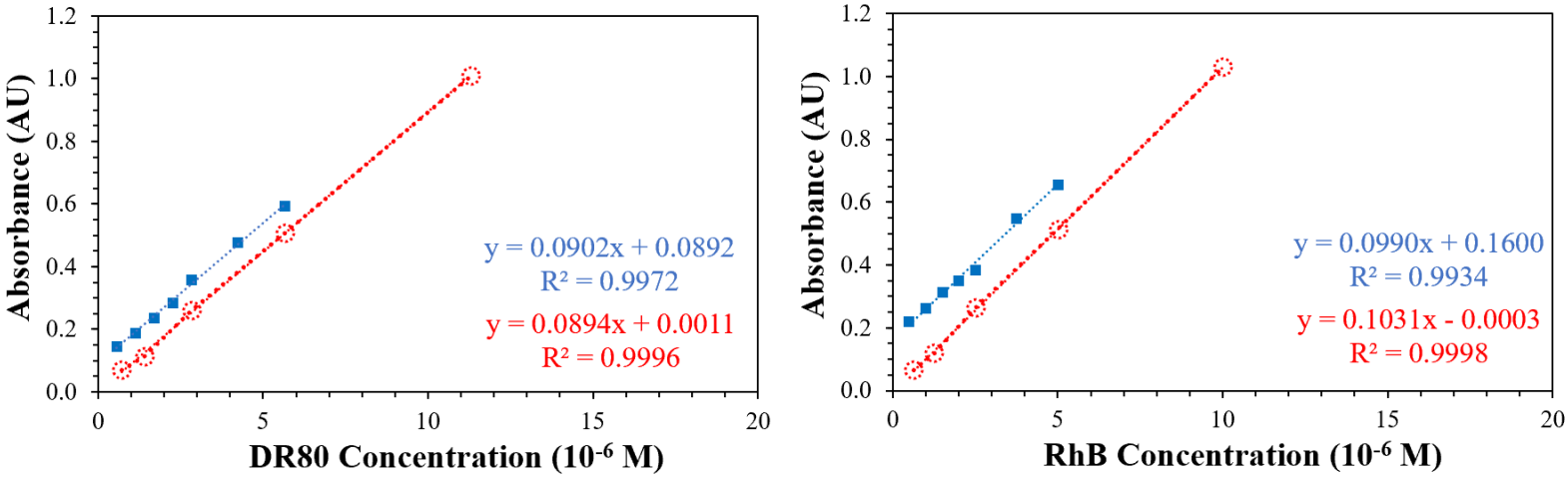

Figure 3.9. DR80 and RhB calibration curves obtained from the study of their binary solution.

Starting from MB + RhB solutions it can be seen that there is a very good similarity between MB's calibration curves obtained analyzing these binary solutions (blue lines) and calibration curves obtained from single-dye solutions (red lines), indeed these curves are showing very similar angular coefficients. Differently for RhB there is a difference of about 13% between the slope of its calibration curve for single-dye mixtures and that of ternary ones, from which it can be concluded that RhB can be slightly influenced by the presence of MB. Anyways, these calibration curves are showing a too high value of their intercept with absorbance axis, which makes the Beer-Lambert law no longer valid (in fact, according to this law, 0 values of the absorbance must correspond to 0 values of the concertation). A totally different behavior has been shown by DR80 + MB solutions, certainly the calibration curve obtained for DR80 is very similar to the one corresponding to its single-dye solution, but for MB calibration curves are very different. In this case there is a reduction of about 50% between its single-dye calibration curve angular coefficient and the binary one. For experiments performed with a constant path length this could only mean that there is a change in MB's molar attenuation coefficient that is leading to different absorbances values. There could be an electrostatic interaction between these two dyes that can alter MB molar attenuation coefficient, this is confirmed by the analysis of spectra of these solutions in which there is a clear shifting of the MB peak from 666 nm to 690 nm, as can be seen in Figure 3.10.

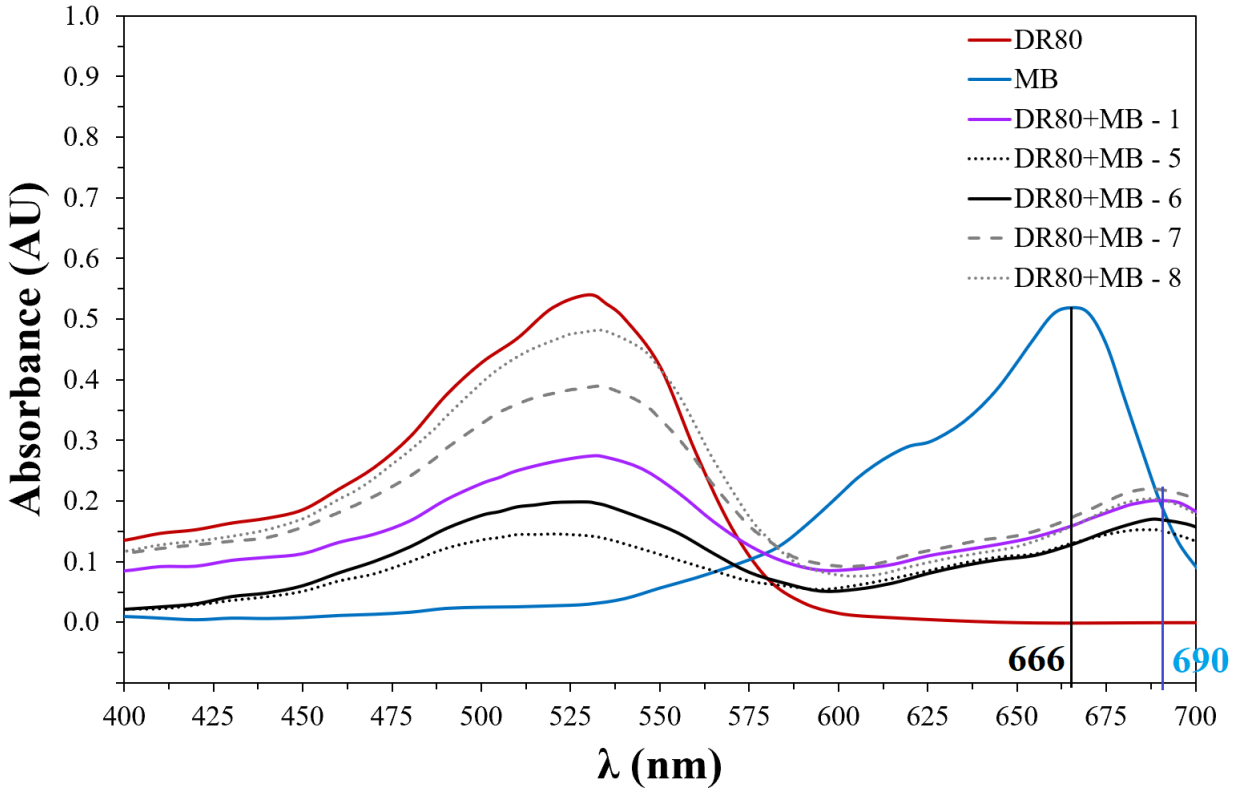

Figure 3.10. Spectra for DR80 + MB binary solutions analyzed during the building of calibration curves.

Also for the curves of this binary solution there are non-negligible y-intercept values, so it is not possible to clearly distinguish the contribution of each dye inside the binary mixture.

Moreover, also considering DR80 + RhB solutions, and evaluating their calibration curves, it can be noticed that there is an inconsistency with Beer-Lambert law. For DR80 and RhB dyes in this solution it can be seen that the values of angular coefficients are very similar between calibration curves obtained respectively from the analysis of binary and single-dye solutions, which suggests that they are not affected by each other's presence. Anyway, calibration curves of this binary solution are shifted up and there is a drastic increase in y-intercept values, which again makes the Beer-Lambert law no longer valid, and therefore it is not possible to know discretely the concentration of a single dye in this mixture. From these data it can be concluded that the simple application of the Beer-Lambert law is not enough to know the exact concentration of individual dyes in these mixtures. Consequently, this could affect results lowering the accuracy and the precision of data obtained using calibration curves obtained by this way, this phenomenon is due to the overlapping of spectra of the two components present, so a more advanced analysis is necessary. It has been found out that the zero-crossing first order derivative spectrophotometry method appears to be valid alternative for a correct interpretation of the spectrophotometer's data. This analytical technique allows the determination of right wavelengths that should be chosen to evaluate the exact concentration evolution during photocatalysis without spectra interference, by this way more precise calibration curves can be obtained for individual dyes in binary solutions. The absorption spectra for binary solutions and their respective first order derivative curves are presented in Figures 3.11, 3.12 and 3.13.

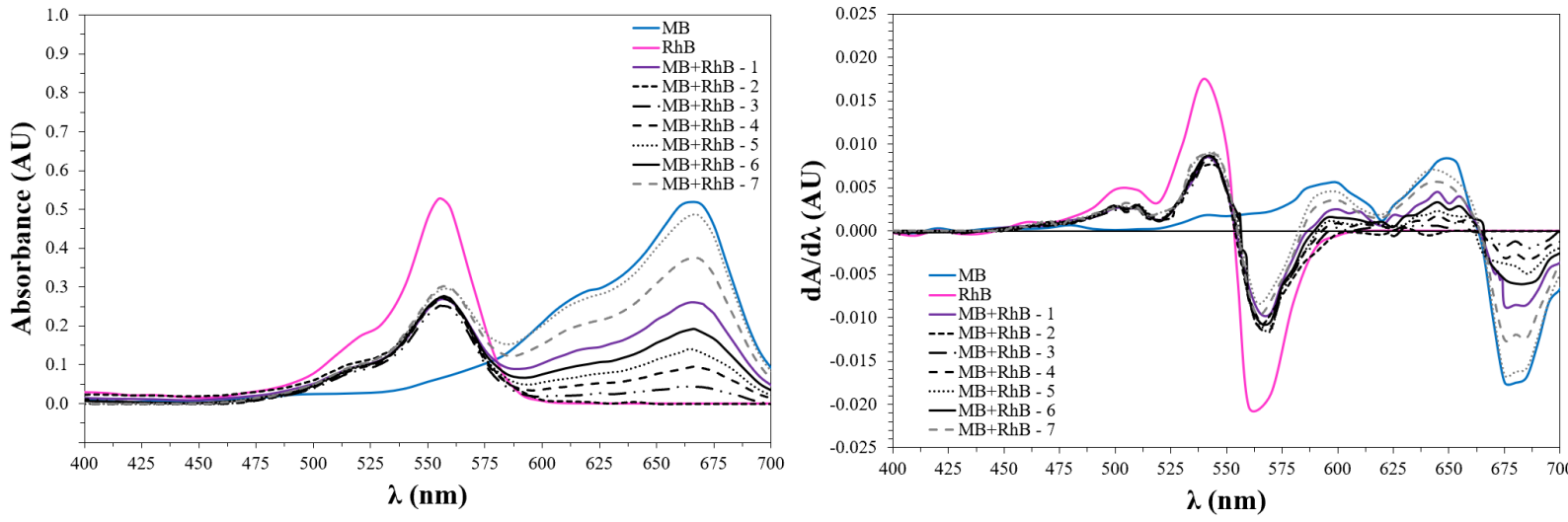

Figure 3.11. Plots of both absorbance curves and the corresponding first derivative plots for MB, RhB and MB + RhB solutions.

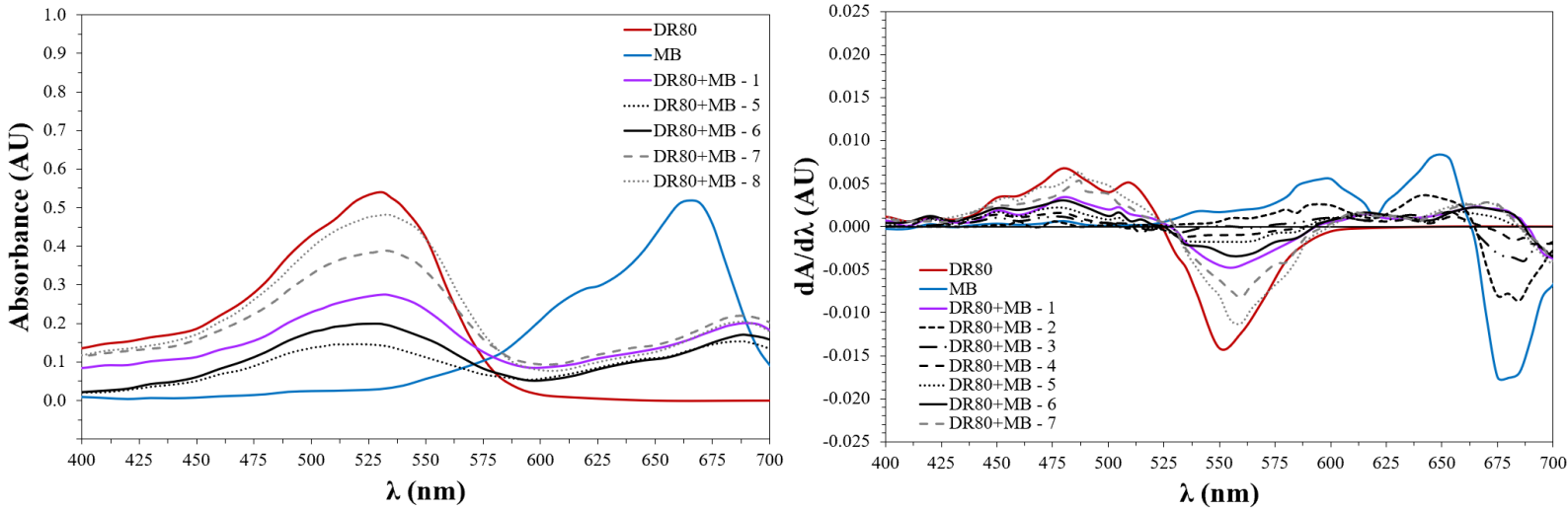

Figure 3.12. Plots of both absorbance curves and the corresponding first derivative plots for DR80, MB and DR80 + MB solutions.

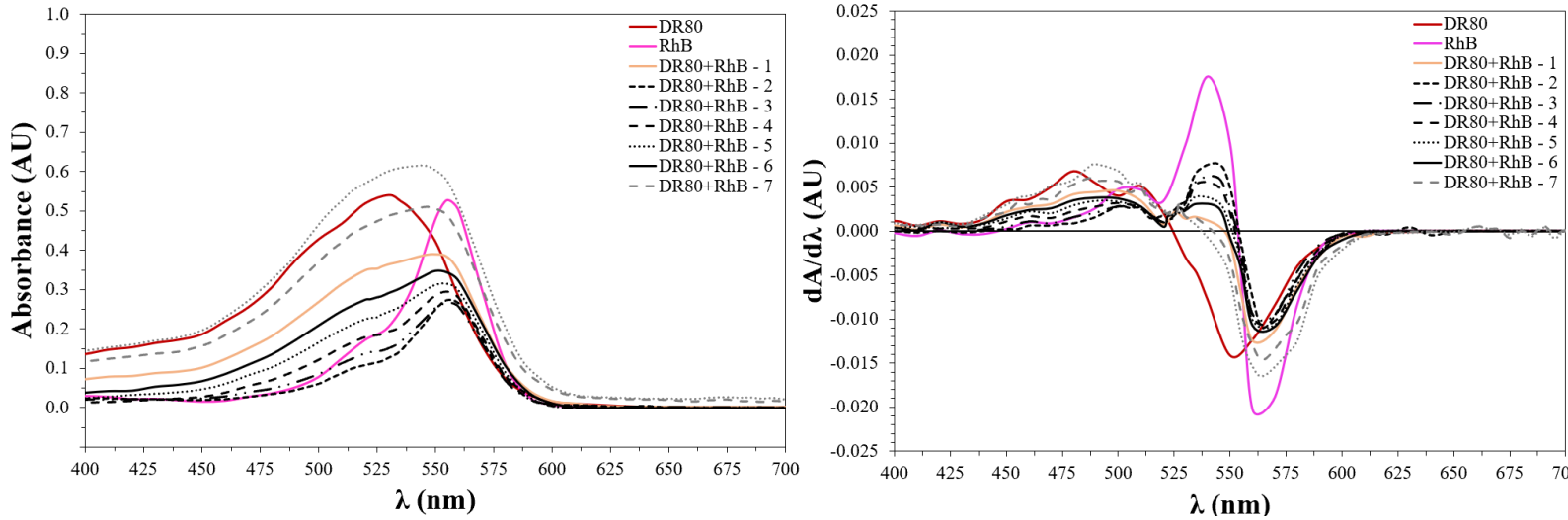

Figure 3.13. Plots of both absorbance curves and the corresponding first derivative plots for DR80, RhB and DR80 + RhB solutions.

From these plots it can be noticed that thanks to the analysis of derivative spectra well-defined peaks can be identified, even in presence of a strong overlap. Moreover, it can be seen that there are certain wavelength values in which the derivative absorbance of one dye is zero, while the derivative of the binary solution and of the other dye have a value which is different from zero. These values can be defined as working wavelengths in which it is possible to analyze discretely the contribution of one compound, since they correspond to points where the derivative absorbance is correlated to the contribute of one dye independently from the other, thus respecting the Beer-Lambert law.

In Table 3.2 all the new peaks that have been chosen thanks to zero-crossing first order derivative spectrophotometry can be seen.

Table 3.2. New peaks values obtained applying first order derivative spectrophotometric evaluation.

MB + RhB		DR80+MB		DR80+RhB	
Colorante	**λ**	**Colorante**	**λ**	**Colorante**	**λ**
MB	685 nm	DR80	505 nm	DR80	555 nm
RhB	505 nm	MB	675 nm	RhB	525 nm

With these new data it is now possible to build new calibration curves, these ones will of course be more accurate and more consistent with the theory, considering that now the absorbance values have been taken at wavelengths in which the contribute of the other dye is negligible and the values of the intercept in equation line are low enough to be also considered negligible. All the new calibration curves for binary solutions, built using this method, can be seen in Figures 3.14, 3.15 and 3.16, respectively for MB + RhB, DR80 + MB and DR80 + RhB solutions.

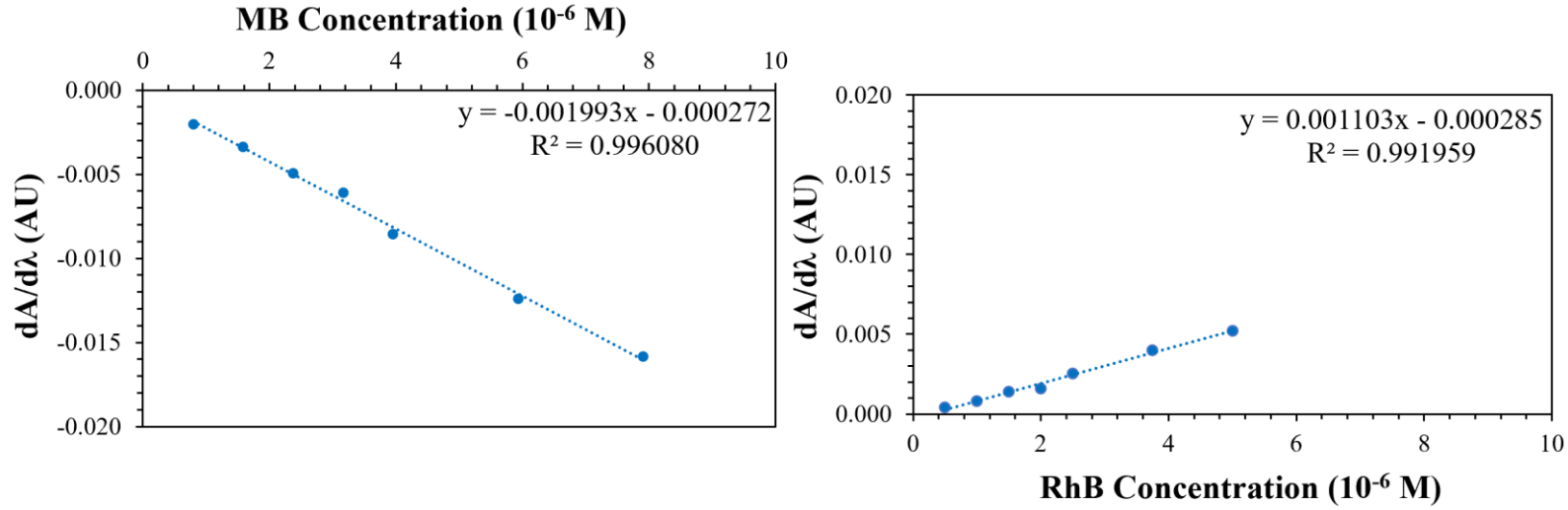

Figure 3.14 Calibration curves of the binary solutions obtained via zero-crossing first order derivative approach for MB and RhB in MB + RhB mixture.

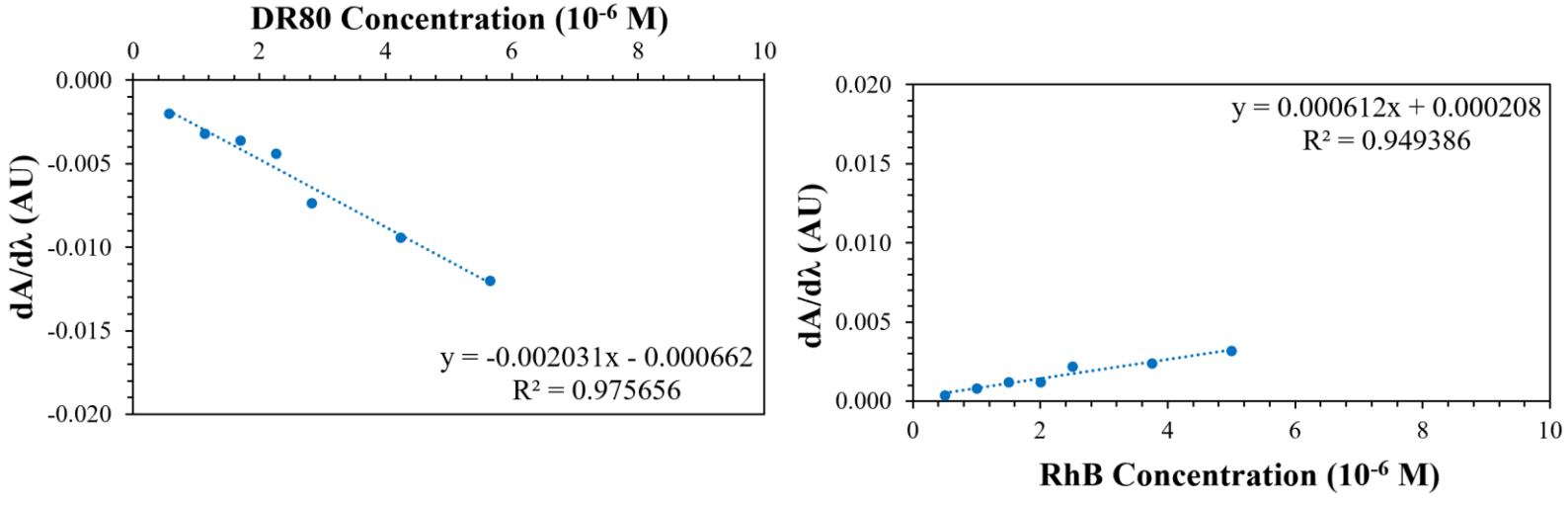

Figure 3.15. Calibration curves of the binary solutions obtained via zero-crossing first order derivative approach for DR80 and RhB in DR80+RhB mixture.

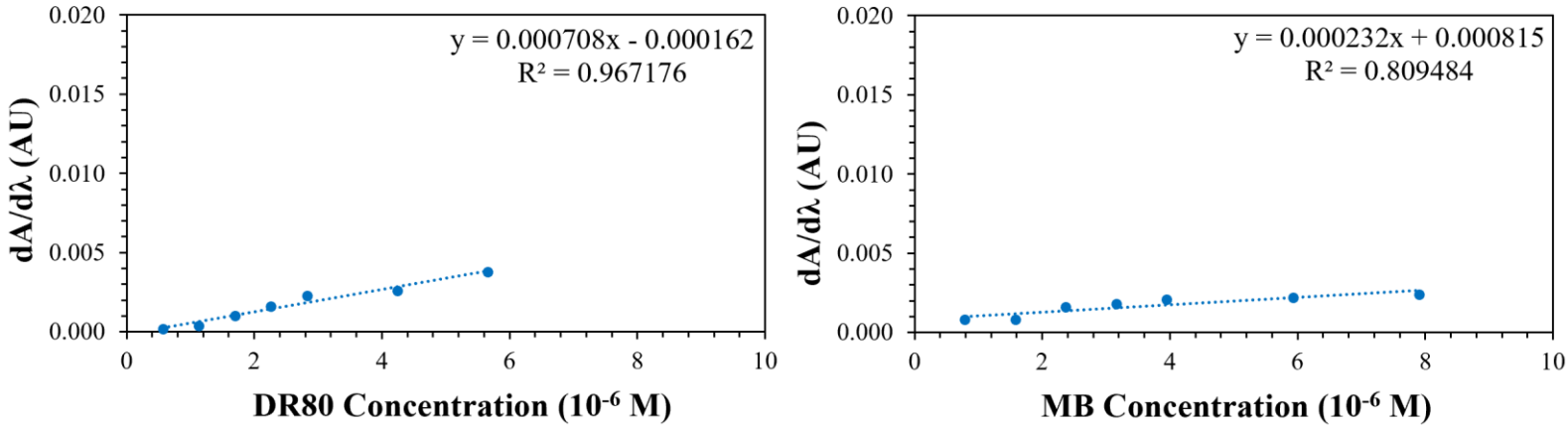

Figure 3.16. Calibration curves of the binary solutions obtained via zero-crossing first order derivative approach for DR80 and MB in DR80+MB mixture.

This time all calibration curves are showing intercept values with absorbance axis that can be considered negligible, making possible to apply Beer-Lambert law with its new formulation $dA/d\lambda \propto C$. Calibration curves calculated for MB + RhB solution are certainly the best ones, these curves are showing a very high linearity between absorbance and concentration, characterized from R^2 values that are always higher than 0.99. These calibration curves are also characterized by the lowest q values (q represents the y-axis intercept) specially if correlated to m values (m is the angular coefficient), the smaller is the q/m ratio the more the curve has a negligible intercept. It can be also noticed that for MB in MB + RhB and for DR80 in DR80 + RhB the calibration curves are showing a negative trend: this must not be seen as an "unphysical" phenomena, since the curves evaluate the absorbance derivative, which can be positive or negative depending on the shape of the absorbance spectrum. Curves obtained for the solution made by DR80 + RhB are still showing a good linearity, characterized by R^2 values higher than 0,94, and also quite low q/m ratios, with an average valor of 0.332. Curves obtained for the DR80 + MB solution are certainly the hardest one to be evaluated. The calibration curve that have been obtained for DR80, in this solution, has shown a quite good linearity, a very low value for its intercept with absorbance axis and also a low q/m ratio of only 0.228. Instead the evaluation of the MB calibration curve has shown the worst linearity, with an R^2 value of only 0.809, the highest intercept value, and also the highest q/m ratio (3.513 which is more than 10 times the others). This phenomenon is probably due to an electrostatic interaction between these two dyes, whose principal effect is to move the peak of methylene blue from 666 nm to 690 nm. It has to be said that a more direct comparison between calibration curves of the same dye, in different binary solutions, cannot be performed, this is due to the fact that all dyes are studied at different wavelengths, depending on their mixture (no wonder, for example , if the DR80 in DR80 + MB has a positive calibration curve while DR80 in DR80 + RhB has a negative one).

Ternary solutions: Ternary solutions were obtained by mixing together all the dyes in equal parts in volume, corresponding to 13 ml of RhB + 13 ml of MB + 13 ml of DR80, leading to a concentration for each dye of $3{,}33 * 10^{-6}$ M and total dyes' concentration of $10^{-5}\,M$. As it has been done for binary solutions, different solutions have been prepared varying every time the concentration of one of the three dyes, while maintaining constant the concentration of the others, obtaining different concentration ratios. After that the same procedure has been applied in reverse changing the concentration of another dye, while of course keeping the concentration of the others constant. All the solutions obtained by this way can be seen in Table 3.3.

Table 3.3. Concentrations of every dye in ternary solutions studied for the building of calibration curves.

DR80+MB+RhB			
Name	Concentration DR80	Concentration MB	Concentration RhB
DR80+MB+RhB - 1 (DR80)	1.88	2.63	1.67
DR80+MB+RhB - 1 (MB)	1.88	2.63	1.67
DR80+MB+RhB - 1 (RhB)	1.88	2.63	1.67
DR80+MB+RhB - 2	0.00	2.63	1.67
DR80+MB+RhB - 3	0.38	2.63	1.67
DR80+MB+RhB - 4	0.75	2.63	1.67
DR80+MB+RhB - 5	1.13	2.63	1.67
DR80+MB+RhB - 6	1.51	2.63	1.67
DR80+MB+RhB - 7	2.83	2.63	1.67
DR80+MB+RhB - 8	3.77	2.63	1.67
DR80+MB+RhB - 9	1.88	0.00	1.67
DR80+MB+RhB - 10	1.88	0.53	1.67
DR80+MB+RhB - 11	1.88	1.05	1.67
DR80+MB+RhB - 12	1.88	1.58	1.67
DR80+MB+RhB - 13	1.88	2.11	1.67
DR80+MB+RhB - 14	1.88	3.95	1.67
DR80+MB+RhB - 15	1.88	5.27	1.67
DR80+MB+RhB - 16	1.88	2.63	0.00
DR80+MB+RhB - 17	1.88	2.63	0.33
DR80+MB+RhB - 18	1.88	2.63	0.67
DR80+MB+RhB - 19	1.88	2.63	1.00
DR80+MB+RhB - 20	1.88	2.63	1.33
DR80+MB+RhB - 21	1.88	2.63	2.50
DR80+MB+RhB - 22	1.88	2.63	3.33
	$\cdot 10^{-6}$ M	**$\cdot 10^{-6}$ M**	**$\cdot 10^{-6}$ M**

All the spectra analyzed for the characterization of these solutions are presented in Figures 3.17, 3.18 and 3.19, together with the spectra of single-dye solutions and even the standard ternary solution for a better comparison.

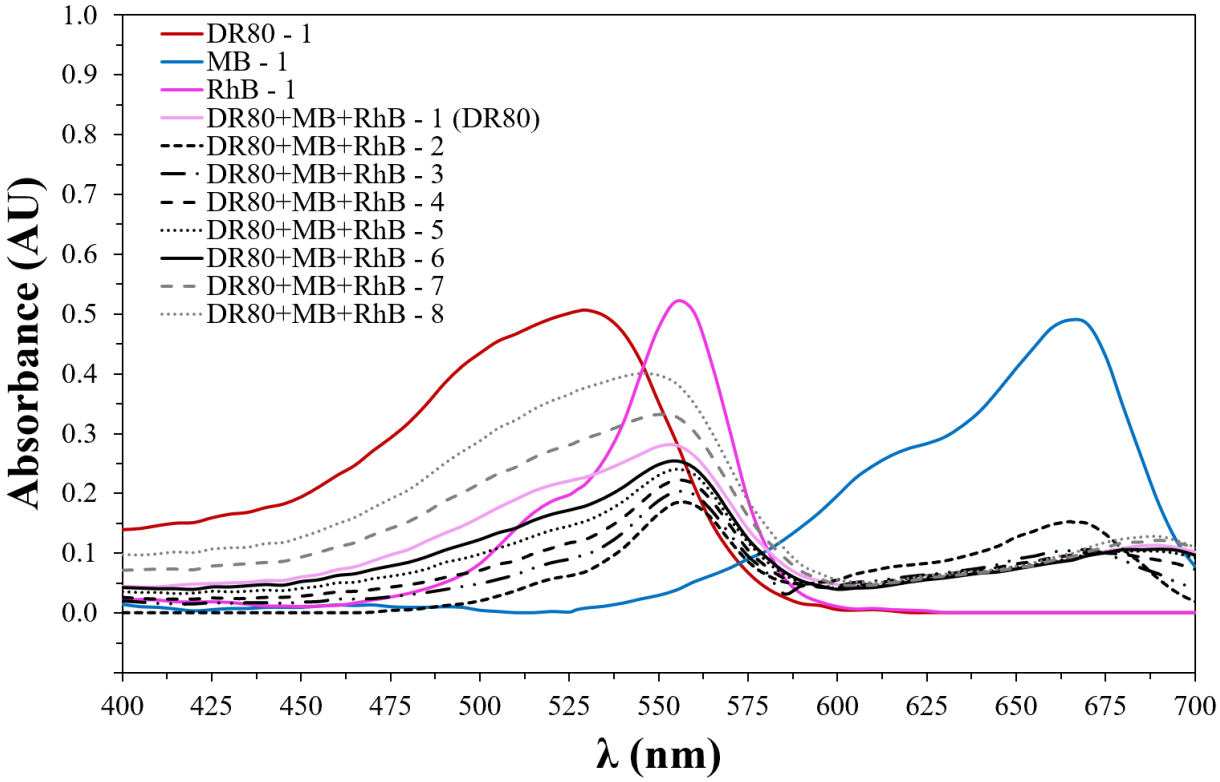

Figure 3.17. Spectra of ternary solutions built varying the concentration of DR80.

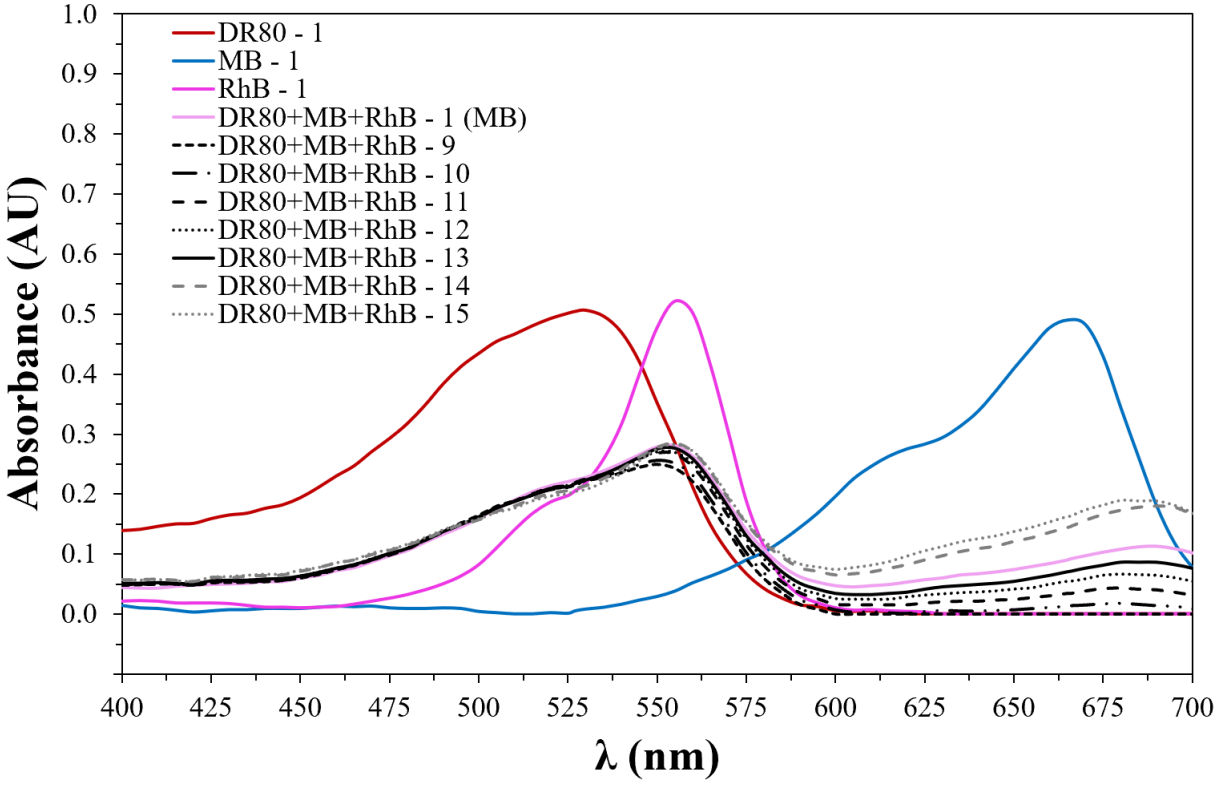

Figure 3.18. Spectra of ternary solutions built varying the concentration of MB.

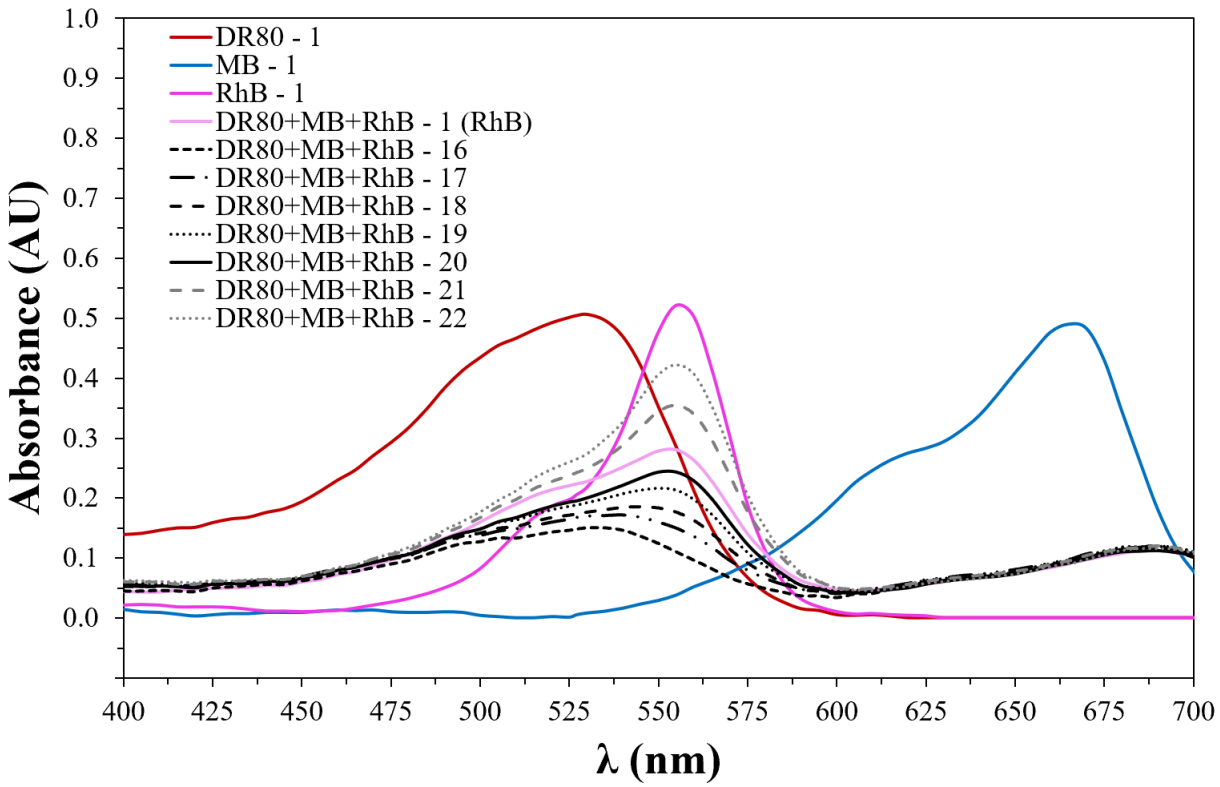

Figure 3.19. Spectra of ternary solutions built varying the concentration of RhB.

The analysis of these curve has led to the building of calibration curves that are presented in Figures 3.20, 3.21 and 3.22. These calibration curves (blue lines) are plotted together with calibration curves of their respective single-dye solution (red lines) for an easy comparison.

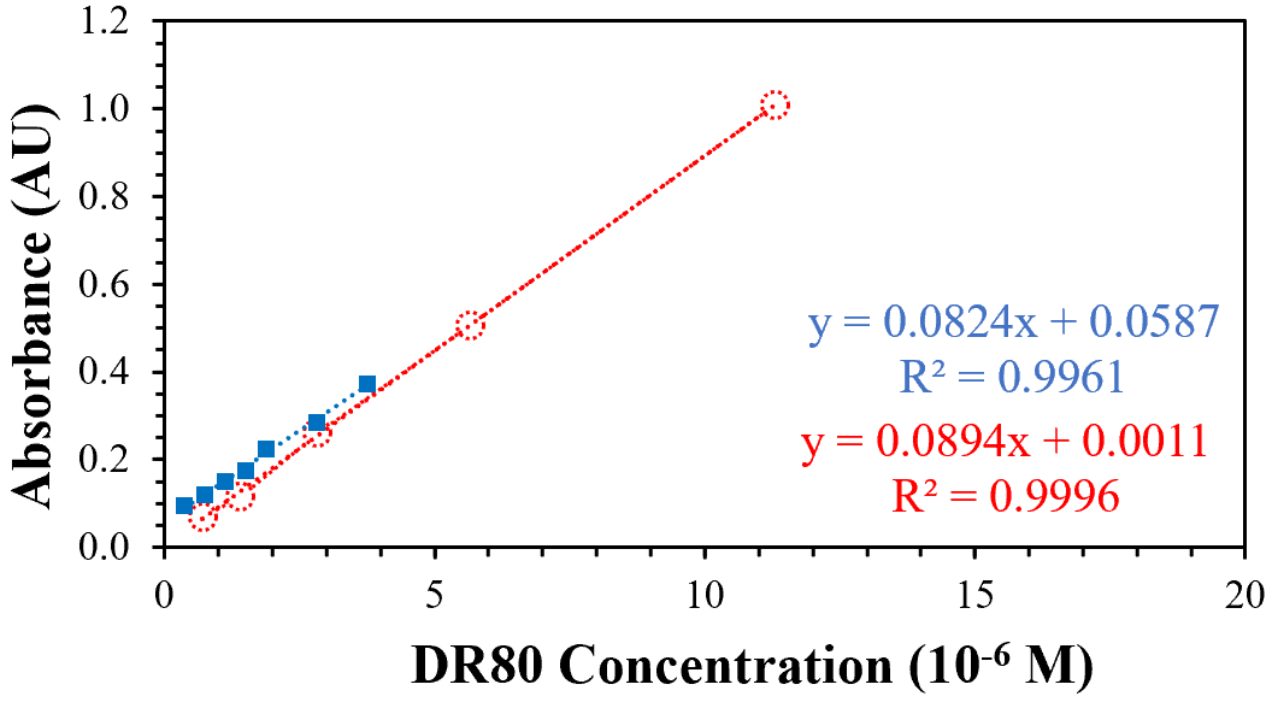

Figure 3.20. Calibration curves of DR80 obtained from the study of ternary solutions (blue line) and single-dye solutions (red line).

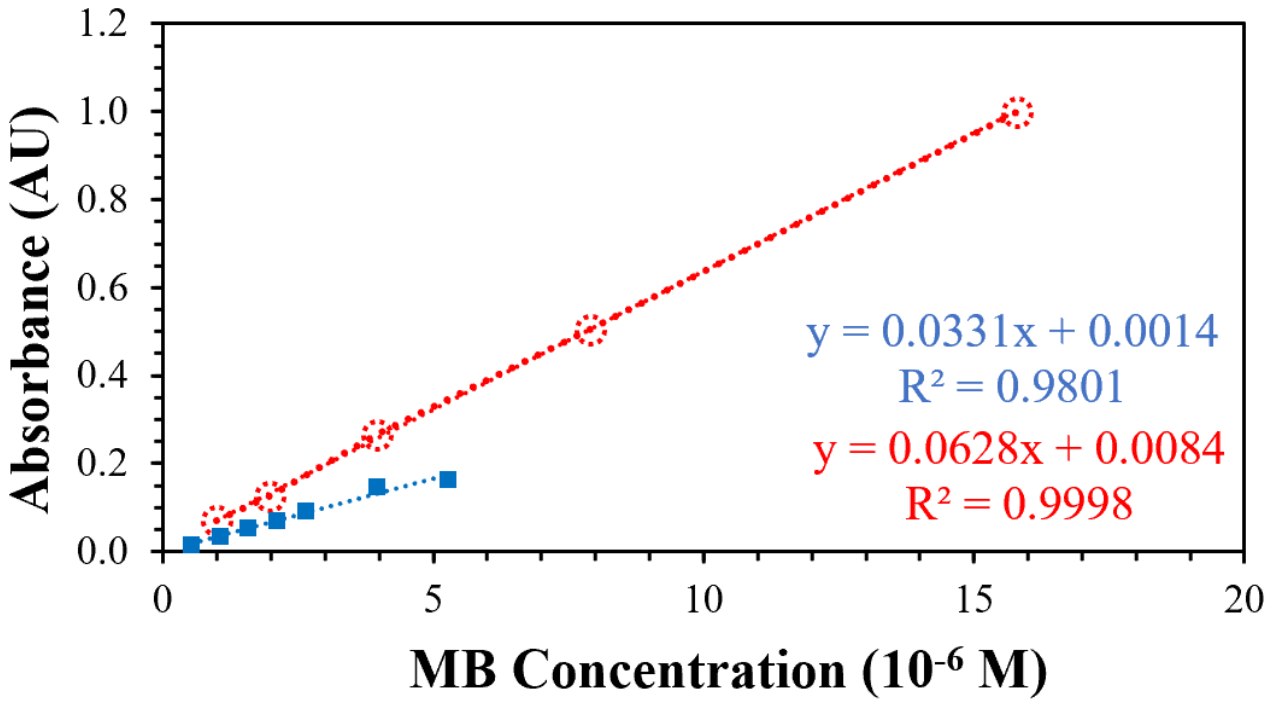

Figure 3.21. Calibration curves of MB obtained from the study of ternary solutions (blue line) and single-dye solutions (red line).

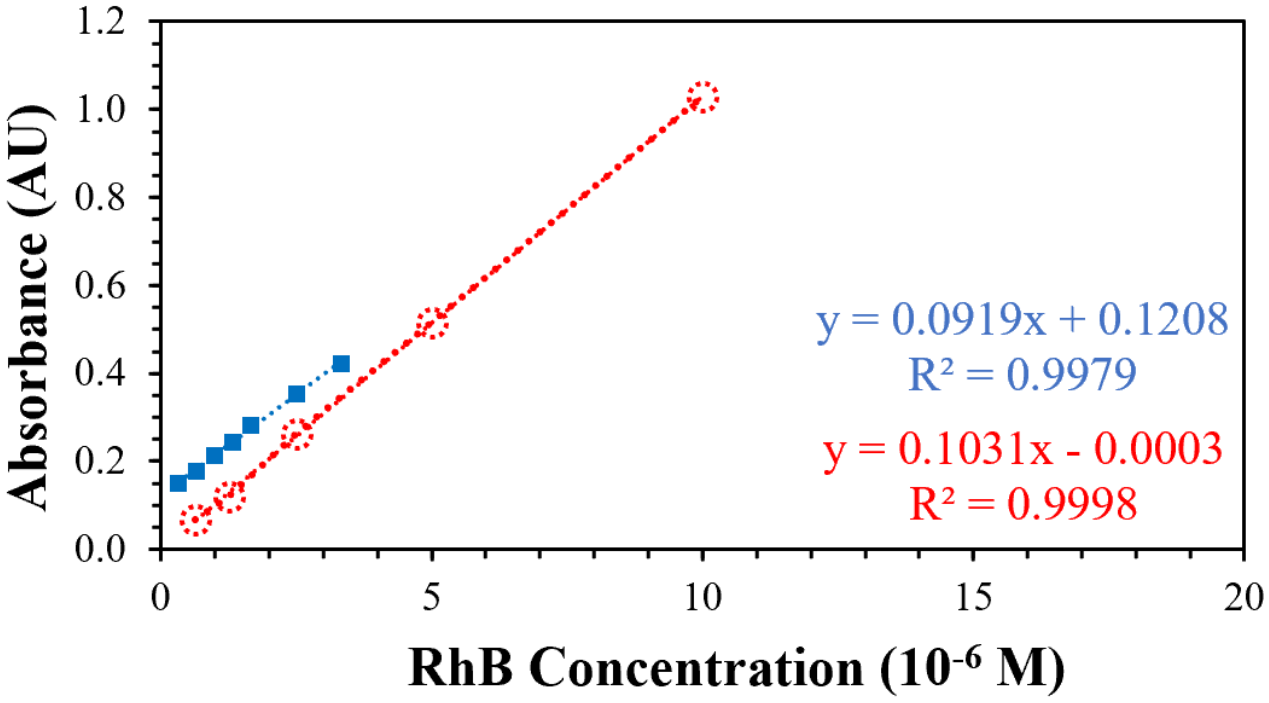

Figure 3.22. Calibration curves of RhB obtained from the study of ternary solutions (blue line) and single-dye solutions (red line).

As it happened for binary solutions these calibration curves are showing a too high value of their intercept with absorbance axis, which makes the Beer-Lambert law no longer valid, which is again due to overlapping of spectra. It can also be notice that the calibration curve obtained for MB in ternary solutions is showing a huge difference respect to its single-dye calibration curve (there is a difference of about 50% between these calibration curves' angular coefficients). Again, this could be due to a possible electrostatic interaction between MB and DR80, whose principal effect is to move its peak from 666 nm to 690 nm as it can be seen in previous spectra Figures 3.17, 3.18 and 3.19. Instead there is a good similarity between calibration curves obtained from the study between ternary and single-dye solutions for DR80 and RhB. This could mean that the behaviors of these two dyes are not highly affected by the presence of the others in the solution, since similar angular coefficients implies similar molar attenuation coefficients. As it is not possible to discriminate the concentration of single dyes inside their ternary mixture, the application of a mathematical method is required as it has been done for binary solutions. For the analysis of ternary solutions the method chosen is double divisor-ratio spectra derivative spectrophotometry, that has been deeply explained in the previous chapter. Another important evaluation has been performed for the evaluation of the so obtained in the ternary solutions. This consist into the analysis of new single-dye solutions in which 13 ml the dye selected were mixed with 26 ml of distilled water to obtain the same volume ratio that this dye had in ternary solutions, corresponding to 1/3, but using only one dye. These analyses have been performed to see if the calibration curve of a dye in its single-dye solution coincides with the one obtained in its ternary solutions, if this is true it means that it is possible to evaluate the concentration of each dye by excluding the contribution of the other two. To analyze these solutions the same method applied for binary and ternary solution has been used; preparing different solutions varying every time the concentration of the dye selected to obtain different volume ratios. All the solutions obtained by this way can be seen in Table 3.4.

Table 3.4. Concentrations of every dye in single solutions studied for the building of calibration curves.

DR80		**MB**		**RhB**	
Name	Concentration DR80	Name	Concentration MB	Name	Concentration RhB
DR80 - 1	5.65	MB - 1	7.90	RhB - 1	5.00
DR80 - 2	1.88	MB - 2	2.63	RhB - 2	1.67
DR80 - 3	11.30	MB - 3	15.80	RhB - 3	10.00
DR80 - 4	3.77	MB - 4	5.27	RhB - 4	3.33
DR80 - 5	1.13	MB - 5	0.00	RhB - 5	0.00
DR80 - 6	2.26	MB - 6	0.00	RhB - 6	0.00
DR80 - 7	0.75	MB - 7	1.05	RhB - 7	0.67
DR80 - 8	3.39	MB - 8	0.00	RhB - 8	0.00
DR80 - 9	4.52	MB - 9	0.00	RhB - 9	0.00
DR80 - 10	8.48	MB - 10	11.85	RhB - 10	7.50
	$\cdot 10^{-6}$ M		**$\cdot 10^{-6}$ M**		**$\cdot 10^{-6}$ M**

All the spectra analyzed for the characterization of these solutions are presented in Figures 3.23, 3.24 and 3.25.

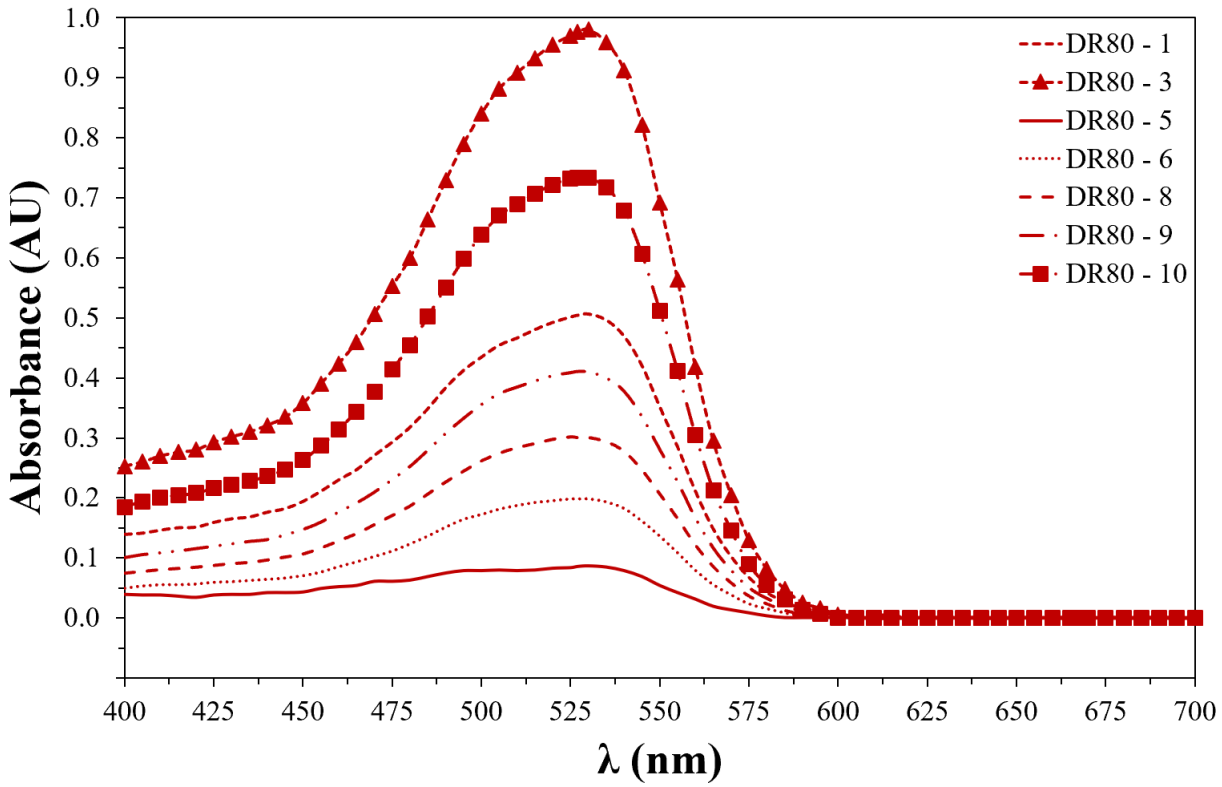

Figure 3.23. Spectra of single solutions built varying the concentration of DR80.

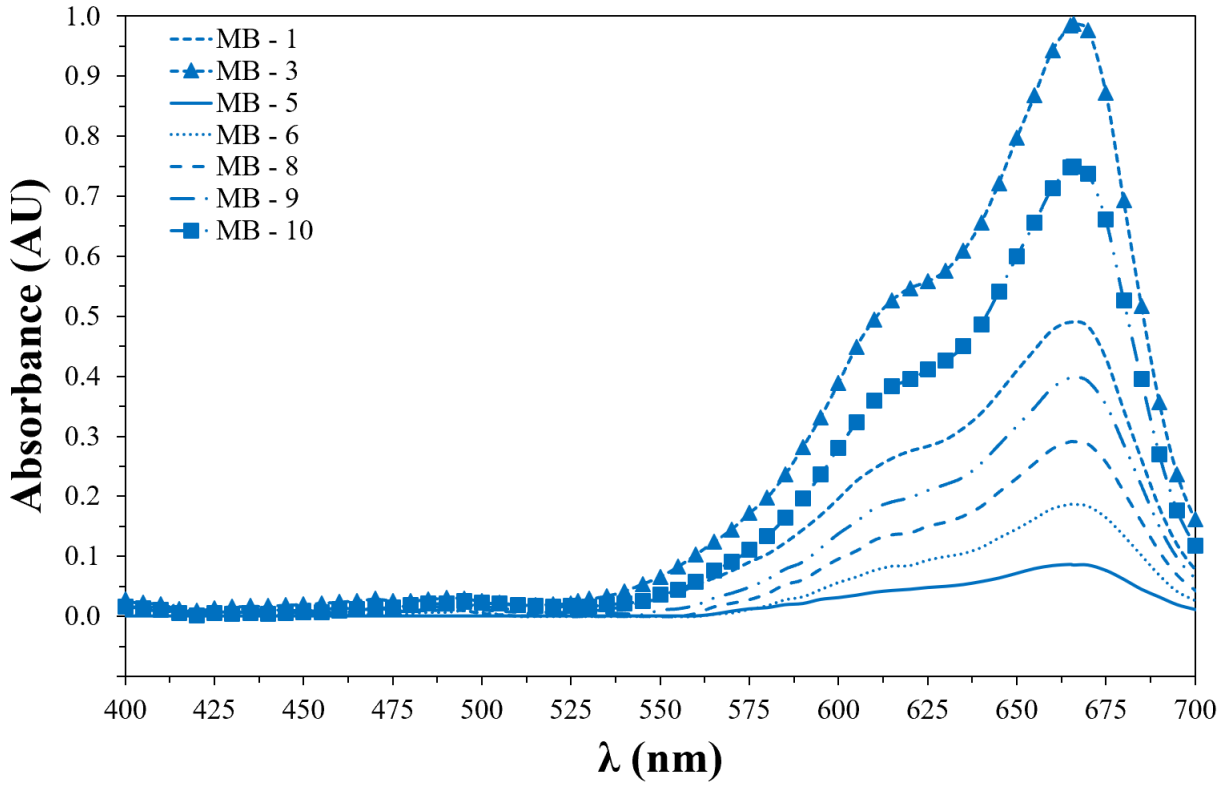

Figure 3.24. Spectra of single solutions built varying the concentration of MB.

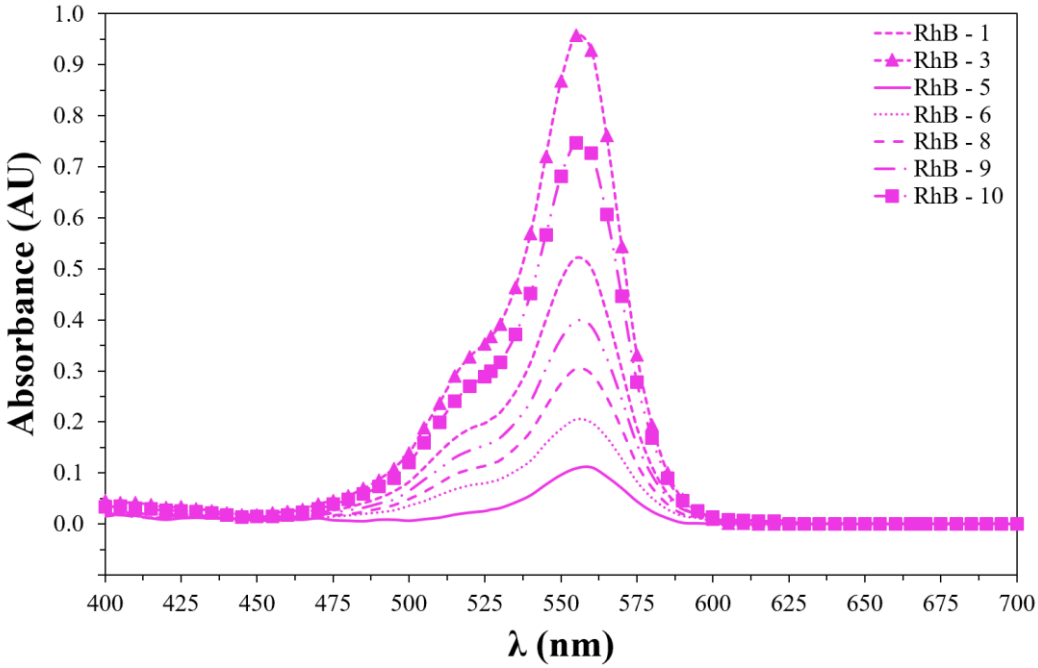

Figure 3.25. Spectra of single solutions built varying the concentration of RhB.

Finally, double divisor-ratio spectra derivative spectrophotometry has been used for the analysis of both ternary and new single-dye solutions. Once that the first derivative of the ratio spectra of a pure compound and its ternary mixture have been obtained these spectra can be plotted together to see where there is an overlapping in correspondence of a maximum point, or a minimum point, of the wavelength. These coinciding points of the derivative of the ratio spectra can be selected as working wavelengths for the determinations of the subject compounds in the ternary mixture. The spectra of ternary solutions (presented on the left of Figures 3.26, 3.27 and 3.28) has been used for selecting working wavelengths, while spectra of new single-dye solutions (presented on right of same Figures) are presented for a fast comparison between the behavior of these dyes in single-dye solutions and ternary ones.

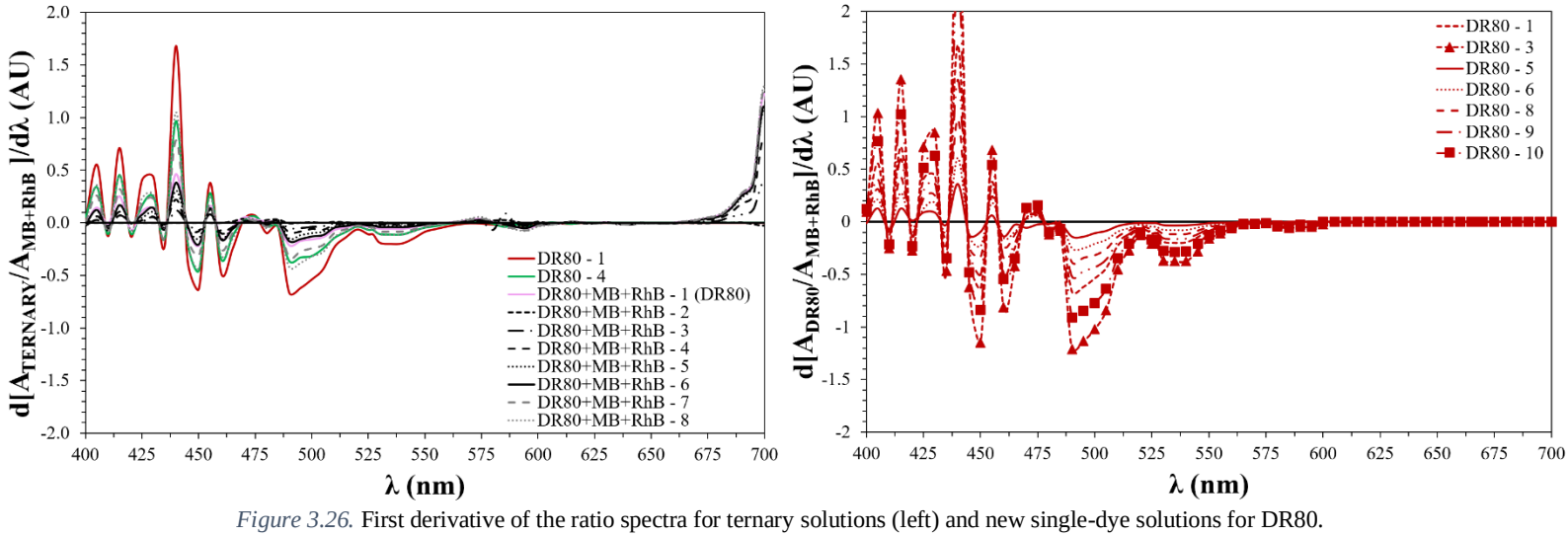

Figure 3.26. First derivative of the ratio spectra for ternary solutions (left) and new single-dye solutions for DR80.

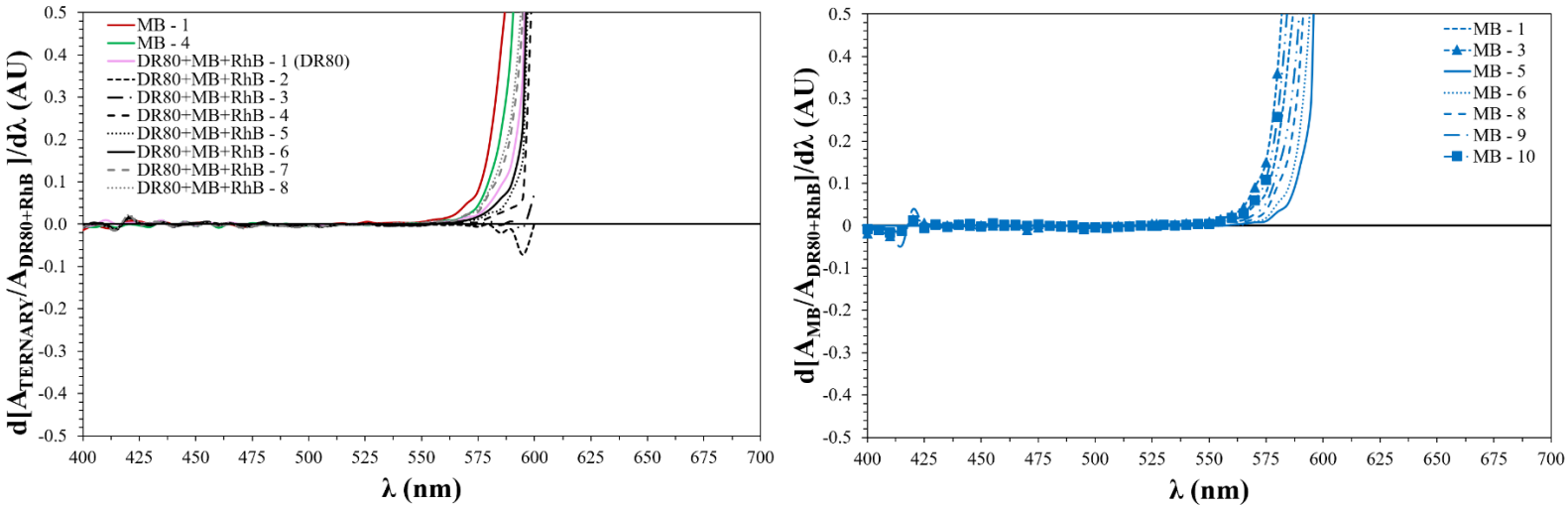

Figure 3.27. First derivative of the ratio spectra for ternary solutions (left) and new single-dye solutions (right) for MB.

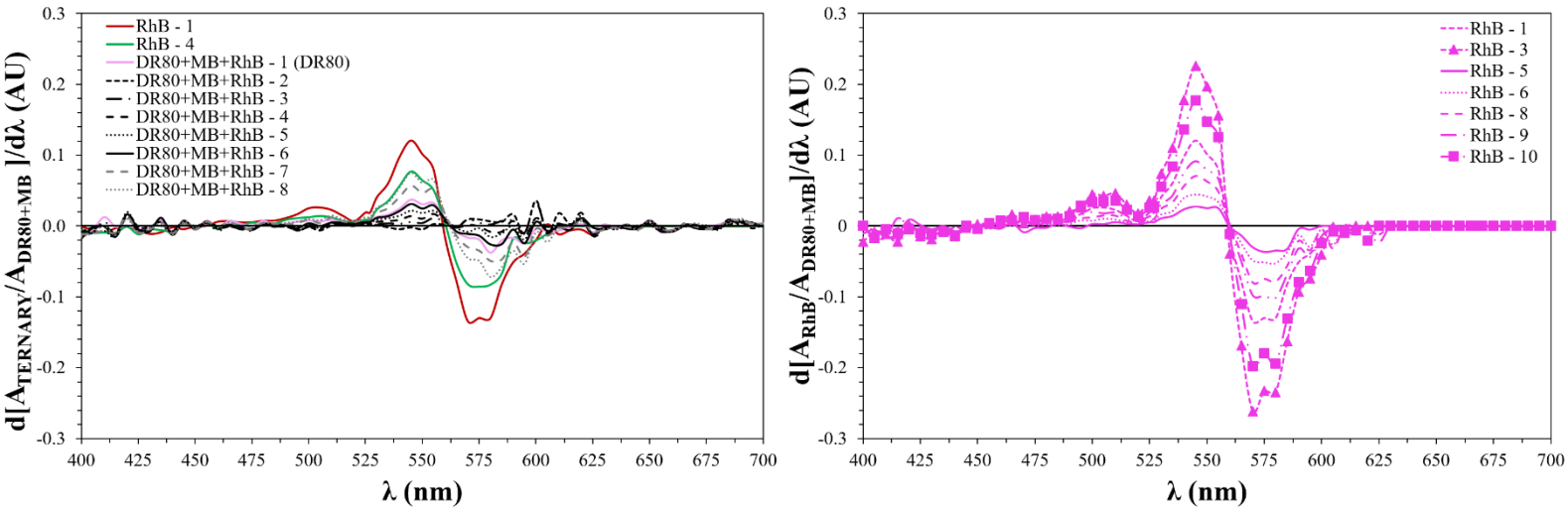

Figure 3.28. First derivative of the ratio spectra for ternary solutions (left) and new single-dye solutions (right) for RhB.

From all these plots it can be seen that all dyes in these new single-dye solutions are always showing a very similar behavior respect to the same dye in ternary solutions. For RhB and DR80, thanks to these graphs, new wavelength values have been detected for making the measurements of photocatalytic experiments, corresponding to 500 nm for DR80 and 550 nm for RhB. It can also be seen that this mathematical method cannot be used for MB, in fact its spectra are showing absorbance values that tends to infinity, because the double divisor DR80 + RhB has a null absorbance over 600 nm, where MB reaches its maximum, indeed the coincident points on the first derivative signals of the ratio spectra were not observed. In order to find these coincident points a higher order derivative spectrophotometer approach has been tried. Higher order derivative spectra can be used when the coincident points on the first derivative signals cannot be found or when this derivative provide a too high level of noise.

This does not permit to obtain a good calibration curve due to large errors introduced in the measurement of the compound concentrations. Instead higher order derivatives allow to select more appropriate working wavelengths from a greater range of possibilities. [49]
However, in this case higher-order ratio spectra derivative signals are not useful, since derivation at higher order provides signals similar to the ones shown in Figure 3.27, as can be seen in the fifth derivative of the ratio spectra in Figure 3.29.

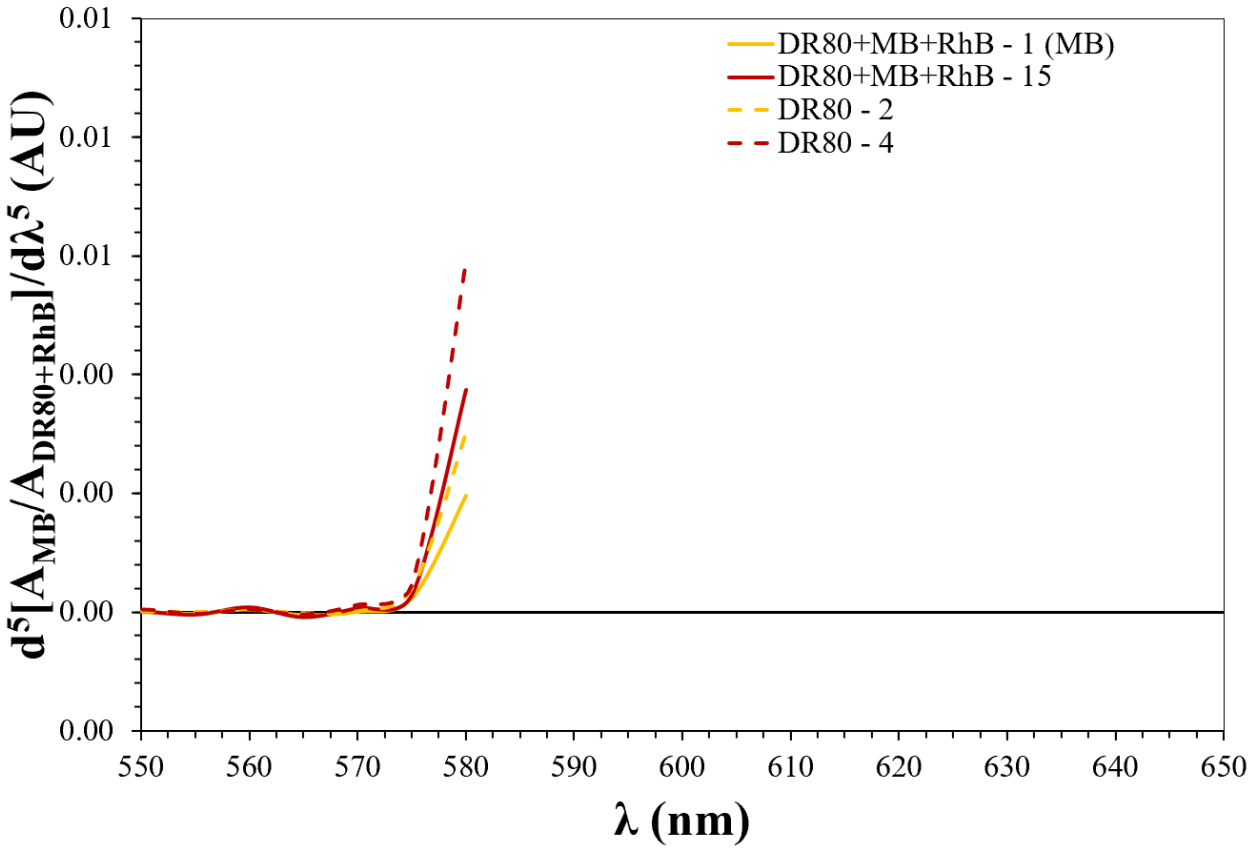

Figure 3.29. Fifth derivative of the ratio spectra of MB in single-dye solutions (- - -) and in ternary solutions having the same molarity of single-dye ones (——).

For the evaluation of methylene blue it has been decided to adopt the same method utilized for its original single-dye solution, making measurements at its peak. This is possible because the overlapping between MB and DR80 + RhB is very low, that is the reason why their ratio tends to infinity. This time, however, the peak of MB has been taken at 690 nm remembering the fact that probably there is an electrostatic interaction, between MB and DR80, that acts moving the MB's peak from 666 nm to 690 nm.
The new calibration curves calculated with the double divisor-ratio spectra derivative spectrophotometry method, for DR80 and RhB, are shown in Figures 3.30, 3.31. Calibration curves obtained from the study of ternary solutions (left) have been presented together with calibration curves obtained from the study of new single-dye solutions (right) for a better comparison.

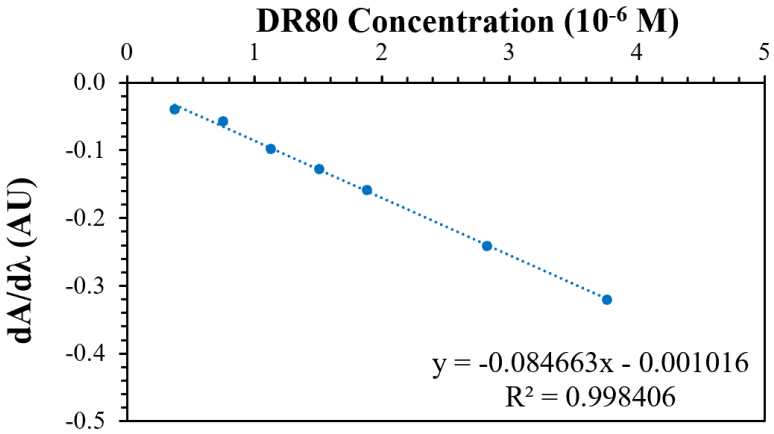

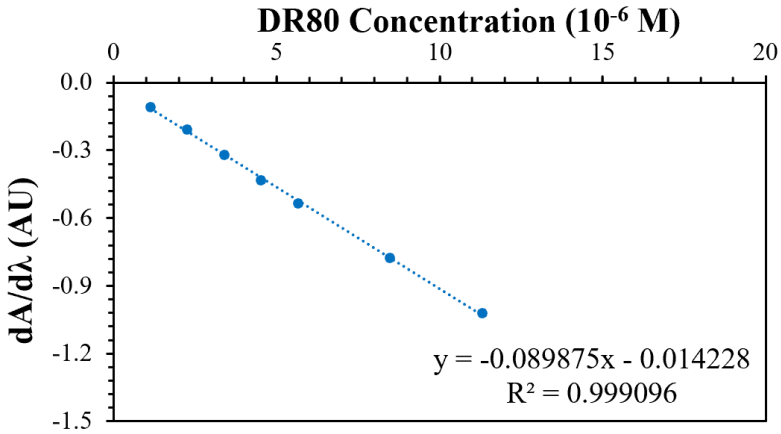

Figure 3.30. Calibration curves obtained from the study of ternary solutions (left) and new single-dye solutions (right) for DR80.

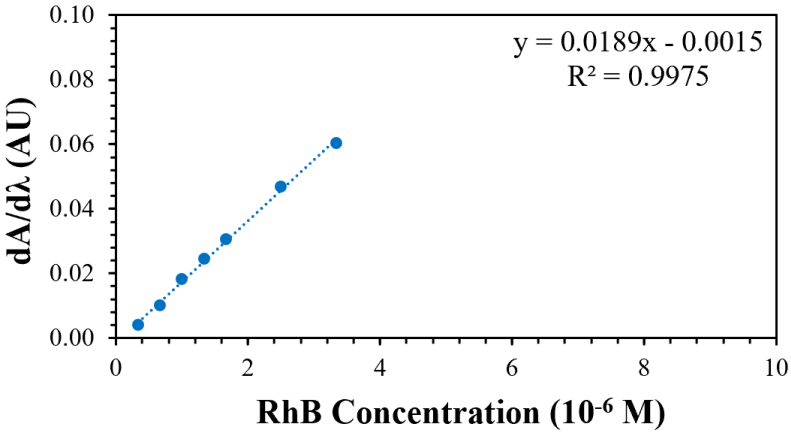

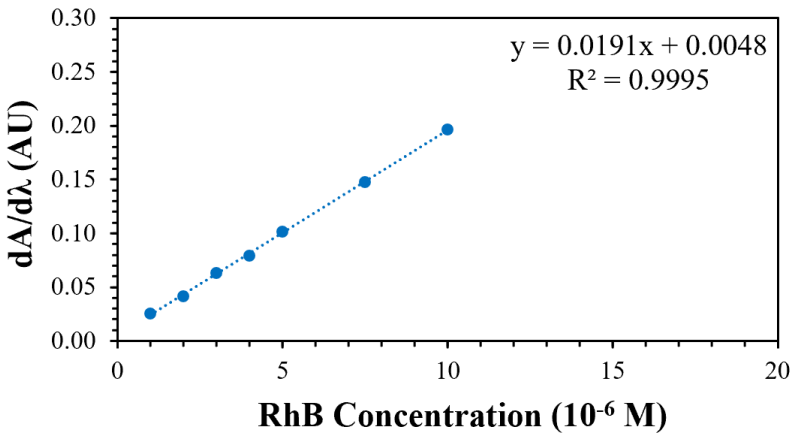

Figure 3.31. Calibration curves obtained from the study of ternary solutions (left) and new single-dye solutions (right) for RhB.

As it can be seen from these plots calibration curves obtained for DR80 and RhB in ternary mixtures are showing a high linearity between absorbance and concentration, with R^2 values that are always higher than 0.99. Moreover, their intercept values with y-axis are much lower, as the ratio between these intercepts and the slopes (q/m), respect to previous calibration curves (represented in Figures 3.20 and 3.22) and now they can be considered negligible. In this way the direct proportionality between absorbance and concertation is confirmed, in accordance to Beer-Lambert law. It can also be noticed that calibration curves obtained from the analysis of ternary solutions (left) are very similar to the ones obtained from the study of new-single dye solutions (right).

This confirms that this method is suitable for the discrete evaluation of a single dye in a ternary mixture, avoiding the undesirable effects due to overlapping of spectra.
Has it has already been said the calibration curve obtained for MB have been calculated simply applying the Beer-Lambert law; that curve is shown in Figure 3.32.

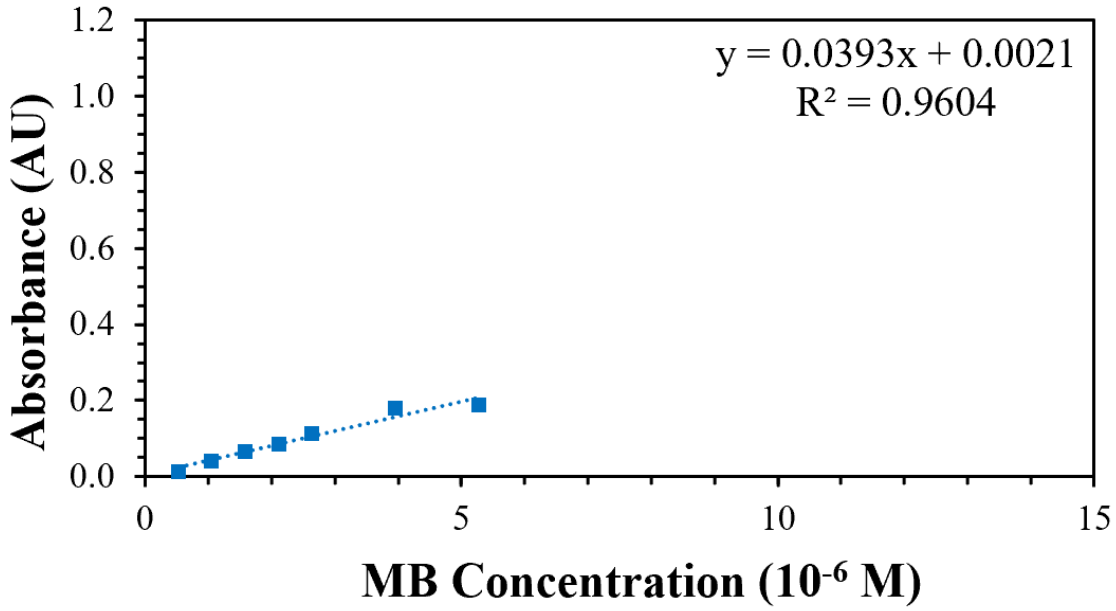

Figure 3.32. Calibration curve obtained from the study of MB in ternary solutions, simply using Beer-Lambert law.

As expected, this calibration curve is less accurate respect to RhB and DR80 ones, but it is showing a good linearity between absorbance and concentration, characterized by an R^2 value higher of 0.96. More important even the value of intercept with absorbance axis of this calibration curve is low enough to be considered negligible, as its q/m value, making even this curve useful for spectrophotometric measurements. This confirms that, at this wavelength, the overlapping between MB and DR80 + RhB binary solution is very low and can be considered negligible, leading to a good accuracy and reliability of data that will be collected using this calibration curve.

3.3 Photocatalytic Tests with UV-LEDs

After the setting-up of the calibration curves, photocatalytic tests have been performed. The procedure of these tests has been maintained the same for all the different kinds of solutions: these experiments had a total duration of 6 hours in which data were taken during the first 3 hours at regular intervals of half an hour and once every hour for the remaining 3. Given the high efficiency of the photocatalytic process, whose yield reached more than 90% in short time, data collected during the last 3 hours of testing presented differences between absorbance values that were too low for the correct evaluation of reaction rate constants, since they were, in most of the cases, lower than the spectrophotometer effective accuracy. Hence, data collected during the last 3 hours of testing were useful to understand when the solution would effectively lose every trace of the dyes. These photocatalytic reactions are apparently following a pseudo-first order kinetic in agreement with a generally observed Langmuir–Hinshelwood mechanism.
For all the solutions that have been studied in this work three different kinds of experiments have been performed; together with photocatalytic tests, having a 3 times repeatability, other two experiments have been performed, namely photolysis and absorption tests. The first one is performed without the titanium sample to verify the possibility of a photolysis reaction, while the second one is performed without any source of light to quantify the possible adsorption of dyes on the sample surface.

Single-Dye Solutions: Data collected for each solution are the average of absorbance values and the logarithm of the ratio between the final and the initial value. The effective repeatability of tests performed for single-dye solutions has been studied by analyzing the plots representing absorbance vs time curves for each dye, as shown in Figures 3.33, 3.34 and 3.35. From these curves it can be seen that these tests have a very high repeatability, because of the very good overlapping between curves. It can also be noticed the reason why data collected after the third our of testing are not considered for the calculation of reaction rate constants, in fact these value are too low being in the range of the maximum accuracy of the spectrophotometer.

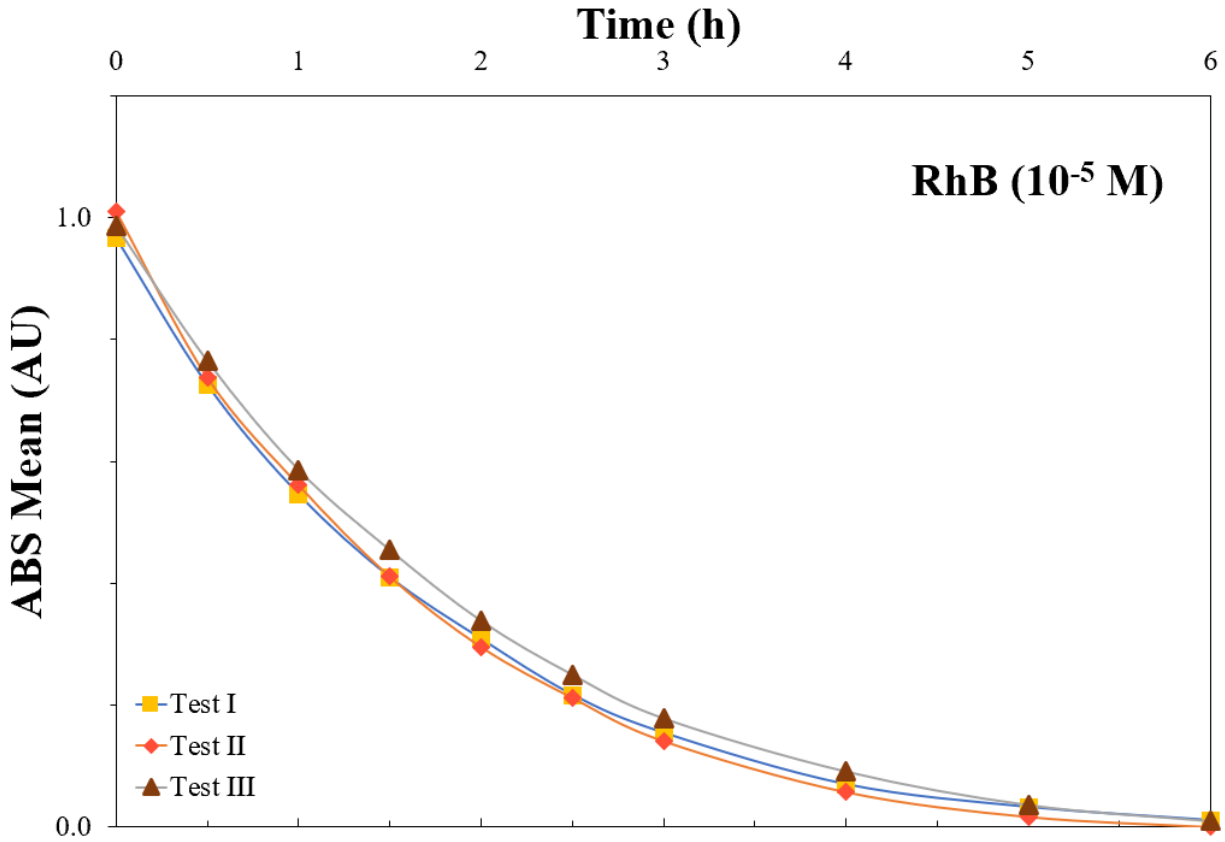

Figure 3.33. Absorbance vs time curves for photocatalytic tests performed on RhB single-dye solutions.

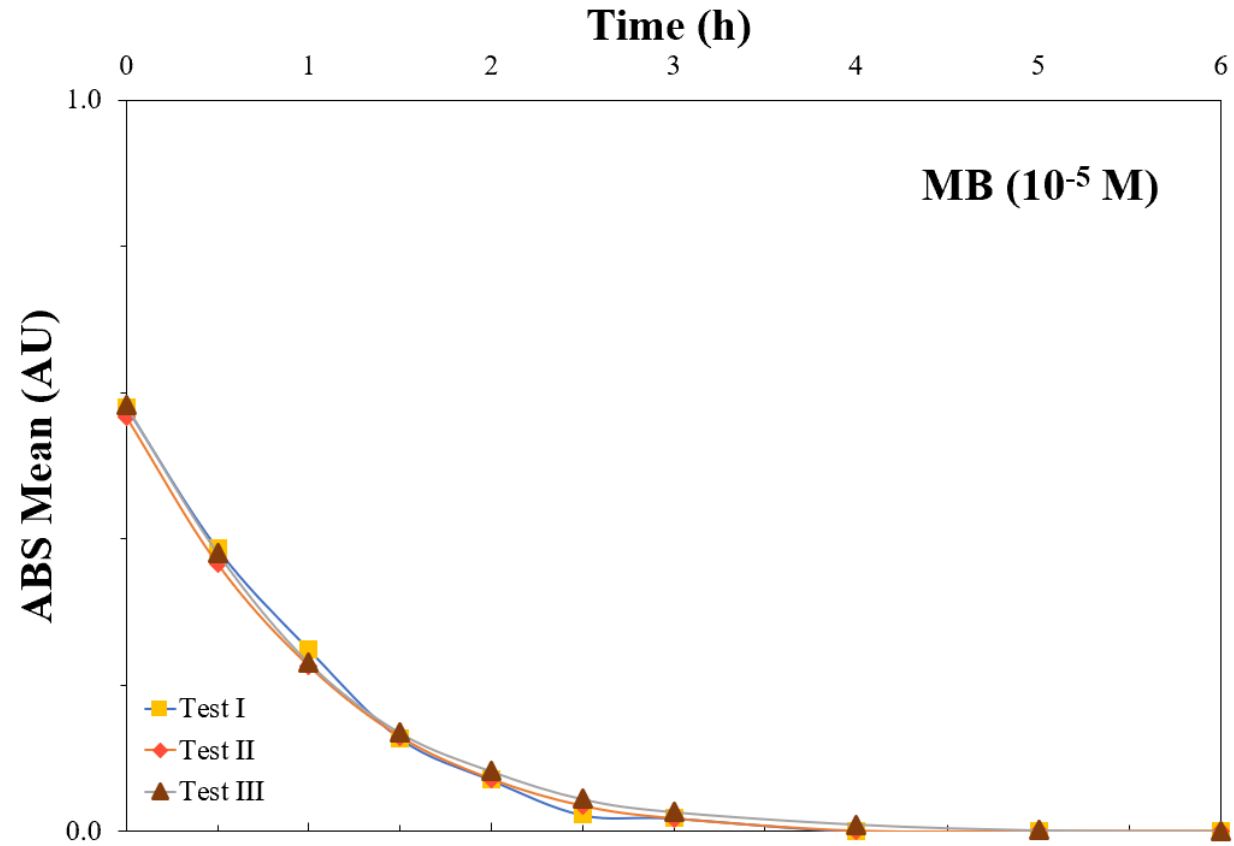

Figure 3.34. Absorbance vs time curves for photocatalytic tests performed on MB single-dye solutions.

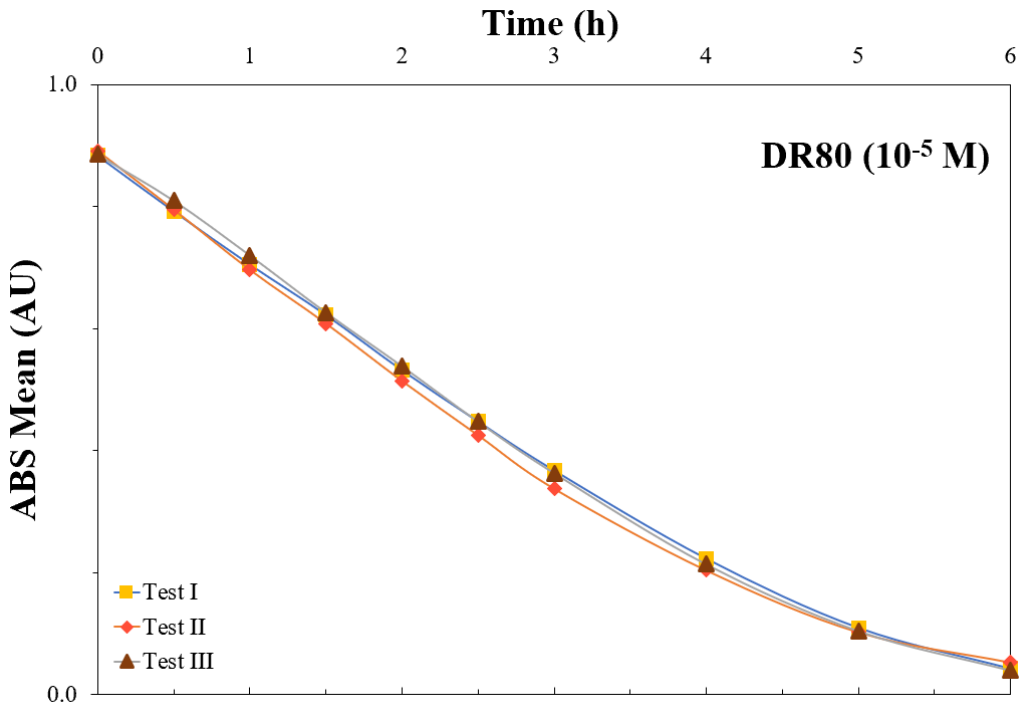

Figure 3.35. Absorbance vs time curves for photocatalytic tests performed on DR80 single-dye solutions.

Thanks to calibration curves these data has been processed leading to the building of $\ln(C/C_0)$ vs time curves from which a linear trend can be observed, confirming the pseudo-first order kinetic for the mechanism of these reactions. These curves can be seen in Figures 3.36, 3.37 and 3.38.

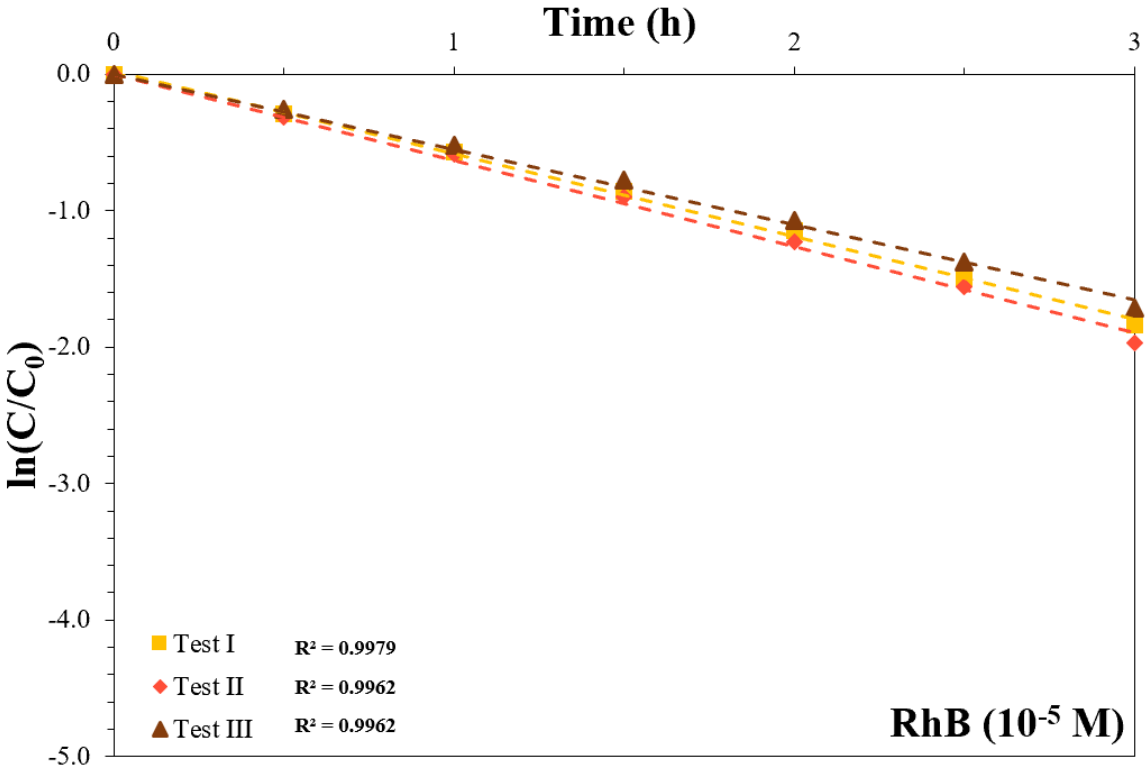

Figure 3.36. $\ln(C/C_0)$ vs time curves for photocatalytic tests performed on RhB single-dye solutions.

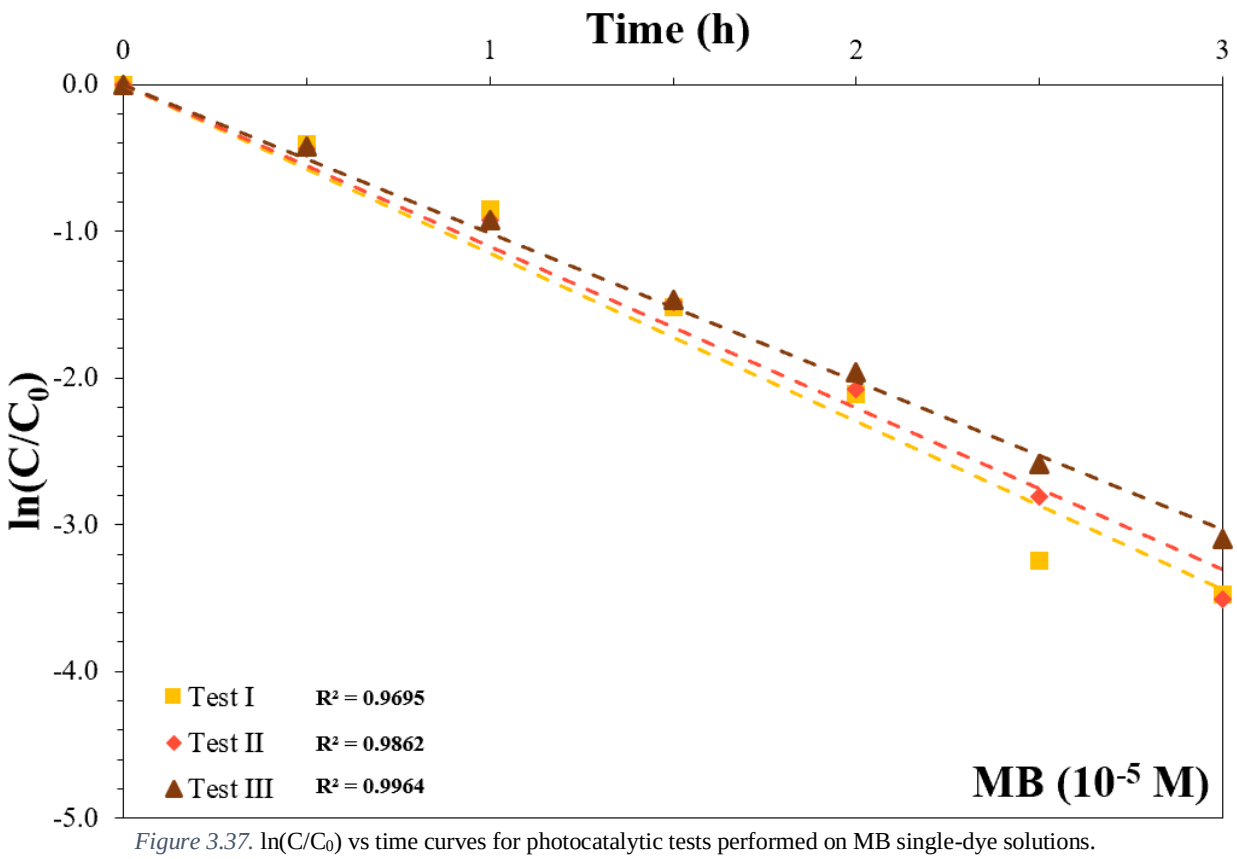

Figure 3.37. ln(C/C₀) vs time curves for photocatalytic tests performed on MB single-dye solutions.

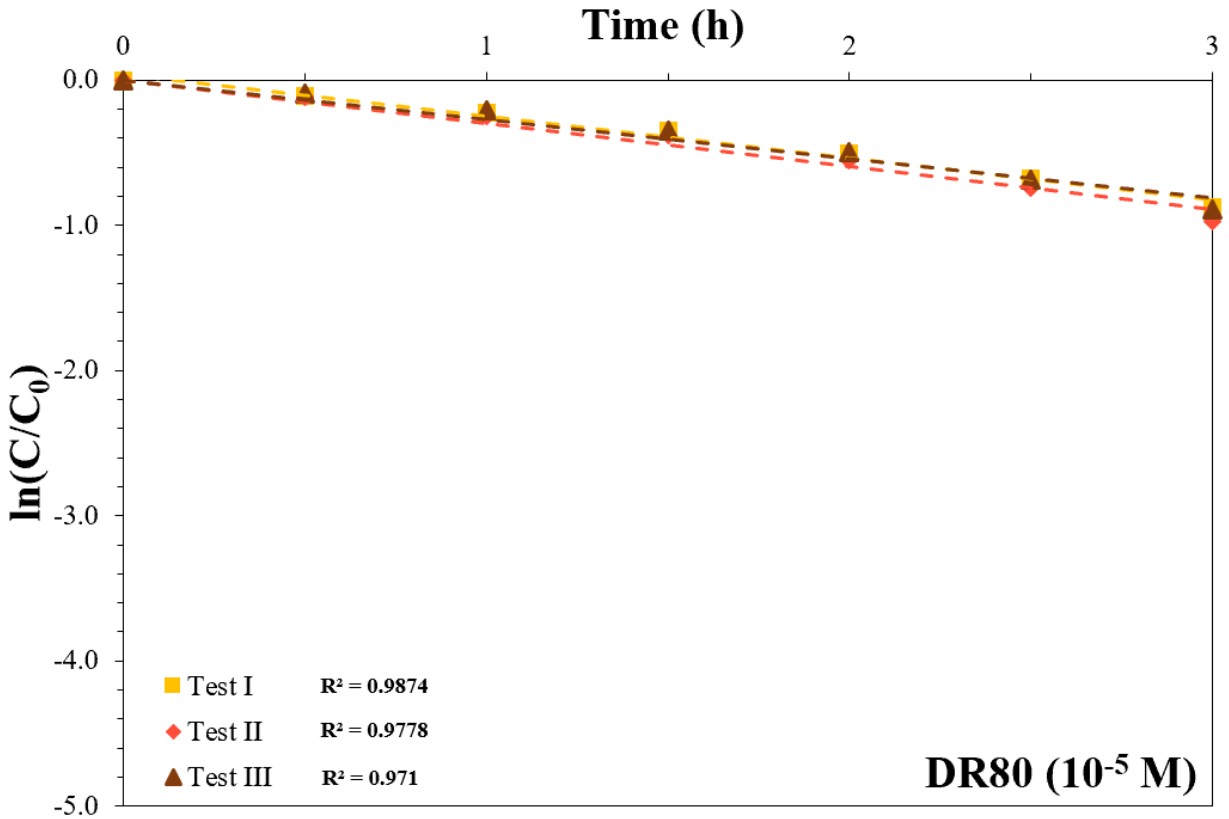

Figure 3.38. ln(C/C₀) vs time curves for photocatalytic tests performed on DR80 single-dye solutions.

From these plots it is possible to see the principal characteristic and the behavior of all the 3 dyes, in single-dye solutions, during photocatalytic tests. The tests performed on Rhodamine B clearly show the higher repeatability,confirmed by a very good overlapping, and even the higher linearity (in logarithmic scale), in fact all the tests have a R^2 value that is higher than 0,99. Methylene Blue instead is surely the hardest dye to be evaluated, even if all tests are characterized by a high R^2 value there was a higher variation in terms of maximum degradation extent and reaction rate constant calculated. It has been founded a difference of 12% between MB's max reaction rate constant value (1.146) and its minimum one (1.011). Still this variation was in a relatively small range. Lastly also experiments for Direct Red 80 have shown a quite high repeatability, indeed there is a very good overlapping of all the 3 curves corresponding to the 3 tests performed, leading to very similar results for $\ln(C/C_0)$. These tests have also shown a high linearity, in fact they all have an R^2 value that is higher than 0,97. The high linearity shown between the logarithm of the ratio between the final and the initial value of concentration and time is a key parameter, beacause it is confirming the applicability of Beer-Lambert law fot these kinf of experiments and also the realiability of calibration curves. From this data the corresponding reaction rate constant has been calculated from the regression analysis of the linear photodegradation curves leading to the values that can be seen in Figure 3.39.

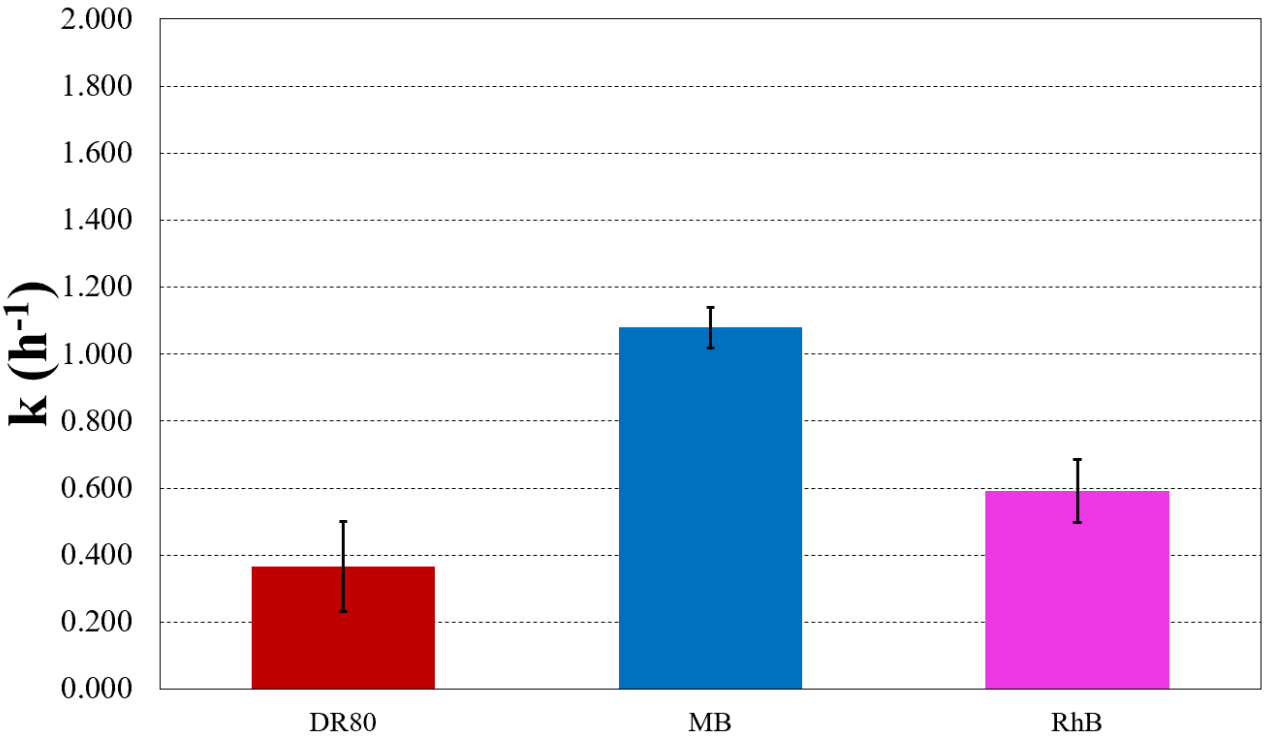

Figure 3.39. Comparison between reaction rate constants obtained for the three single-dye solutions during photocatalytic tests.

It is clearly visible that Methylene Blue has the highest reactivity during photocatalytic tests, followed by Rhodamine B and lastly Direct Red 80. These results were expected, in fact DR80 is surely the heaviest (1373.07 g/mol) and most complicated molecule, characterized by a huge number of double bonds (39) that can be attacked by radicals during photocatalytic reactions. Especially its four N=N double bonds are the most active sites for oxidation attack and are also the ones that requires more time to be broken, this means that increasing the azo groups in the dye structure increases the discoloration time [60]. The second double bonds for activity are N=C of aromatic rings that instead can be quite easily opened [61]. RhB is faster than DR80 because it is much lighter (479.02 g/mol) and has a lower number of double bonds (11). In this case the N=C double bound is the more active one and also the first to be broken, then this is followed by the rupture of aromatic rings [62]. MB is even faster than RhB, in fact this is the lighter molecule (319.85 g/mol) and has the lowest number of double bonds (7). Moreover, MB has two very active double bonds, that are N=C and an S=C, that are both very easy to be broken accelerating his discoloration. The electrophilic attack of OH• concerned the free doublet of heteroatom S. However, the passage from C–S^{+}=C to C–S(=O)–C requires the conservation of the double bond conjugation, which induces the opening of the central aromatic ring containing both heteroatoms, S and N. The origin of H atoms necessary to C–H and N–H bond formation can be proposed from the proton reduction by photogenerated electrons [50].

The other two kinds of tests, that are photolysis and absorption tests, have been performed following the procedure explained previously. Their resulting absorbance vs time curves can be seen in the plot in Figure 3.40, respectively for photolysis test (blue) and absorption test (orange) performed on the RhB single-dye solution.

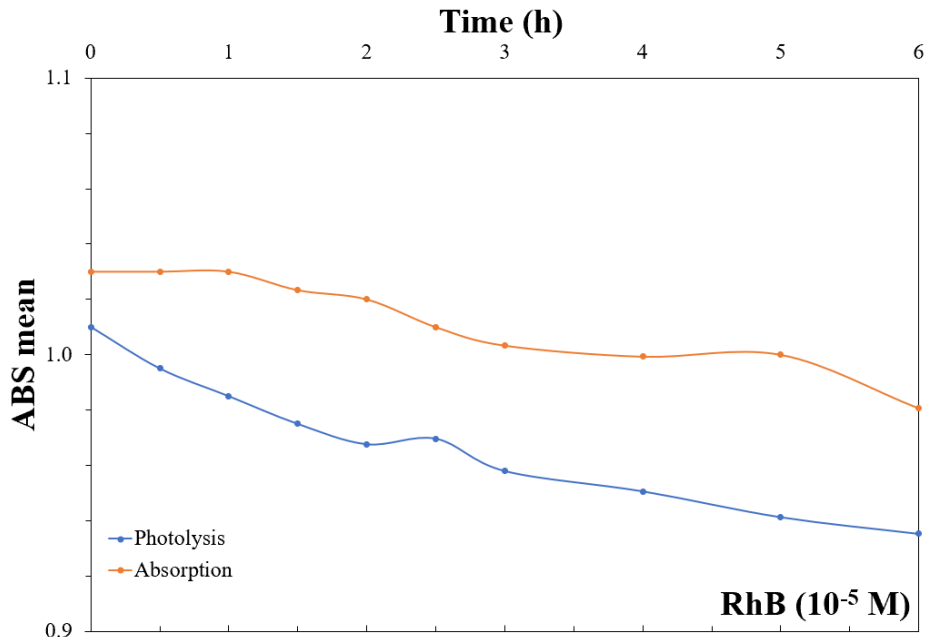

Figure 3.40. Absorbance vs time curves for photolysis and absorption tests performed on RhB single-dye solutions.

As in can be seen the variation of absorbance during these test is so low to not be considered reliable, in fact it is in the range of the spectrophotometer's accurancy. From this kind of curves it can be seen that this phenomena are negligible, particularly respect to photocatalytic ones. Anyway, even during these tests for each solution the average of absorbance values and the logarithm of the ratio between the final and the initial value has been collected. From this data the corresponding reaction rate constant has been calculated from the regression analysis of the linear photodegradation curves leading to the values that can be seen in Figure 3.41, presented toghether with reaction rate constants of photocatalytic test for a better comparison.

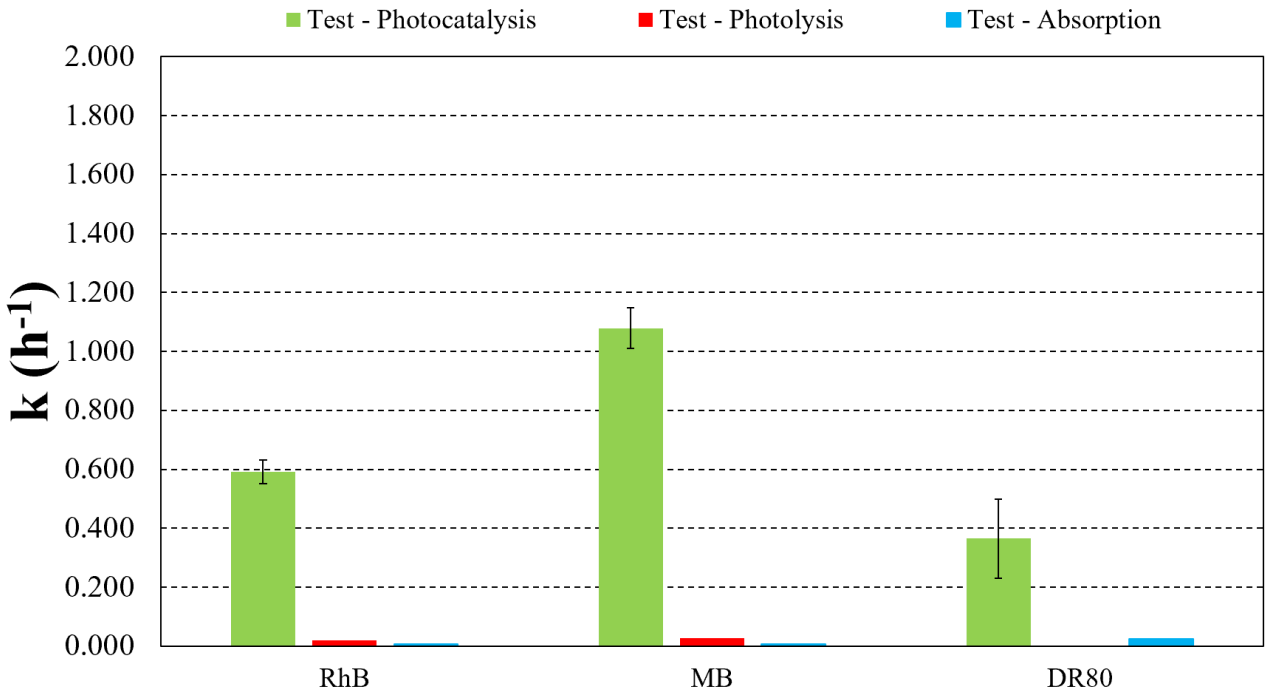

Figure 3.41. Comparison between reaction rate constants obtained for photocatalysis tests (green), photolysis tests (red) and absorption tests (light blue) for each single-dye solution.

All the reaction constants obtained by photolysis and absorption tests are very low, specially if compared to the ones obtained with photocatalytic experiments, so they can be considered negligible as the contribute of these reactions during these photocatalytic experiments.

Binary Solutions: Binary solutions have been prepared mixing 2 dyes in equal parts per volume, 20 ml of each dye, obtaining 3 binary solutions: MB + RhB, DR80 + RhB and DR80 + MB. Once again for each binary solution three different kinds of tests have been performed: photocatalysis tests, photolysis tests and absorption tests. Data collected for each solution are the average of absorbance values and the logarithm of the ratio between the final and the initial value. In Figure 3.42 concentration vs time curves for RhB and MB in their binary solutions are presented as an example to see which are typical trends of these curves.

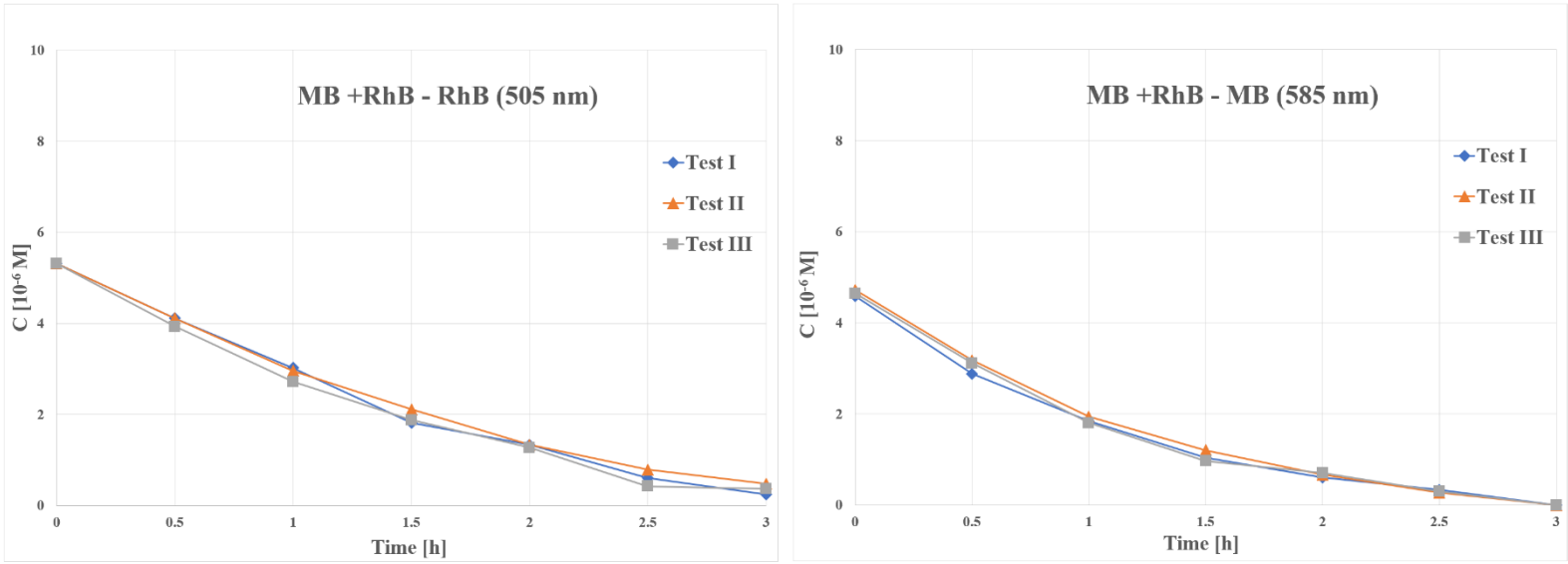

Figure 3.42. Concentration vs time curves for RhB and MB in their binary solutions.

There is an exponential trend for the degradation of dyes in binary solutions, like it happens in single-dye solutions, hence it is possible to pass to a logarithmic representation. Moreover, values calculated at the third hour are very low, like in single-dye solutions, so once again subsequent data can be ignored for the calculation of reaction rate constants. These data have to be processed using the zero-crossing first order derivative spectrophotometry method, that has been explained in the previous chapter.

The resulting $\ln(C/C_0)$ vs time curves, calculated for each component in all binary solutions, can be seen in Figures 3.43, 3.44 and 3.45.

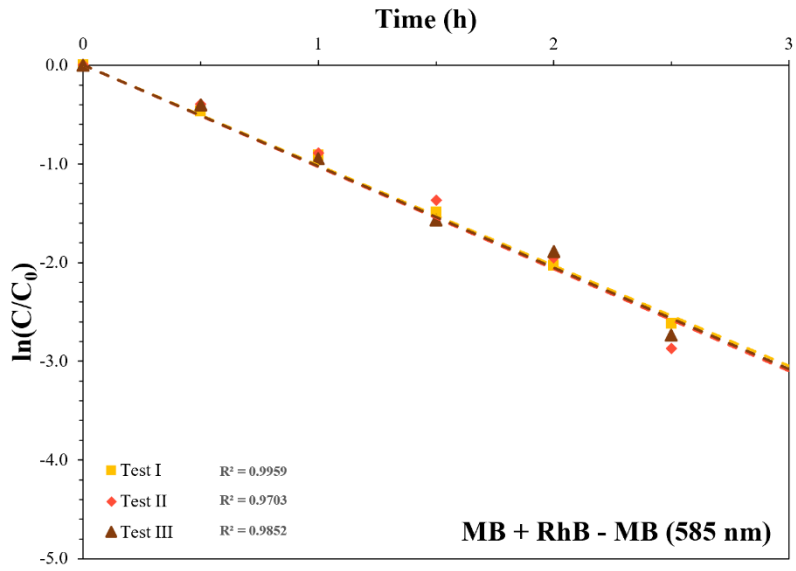

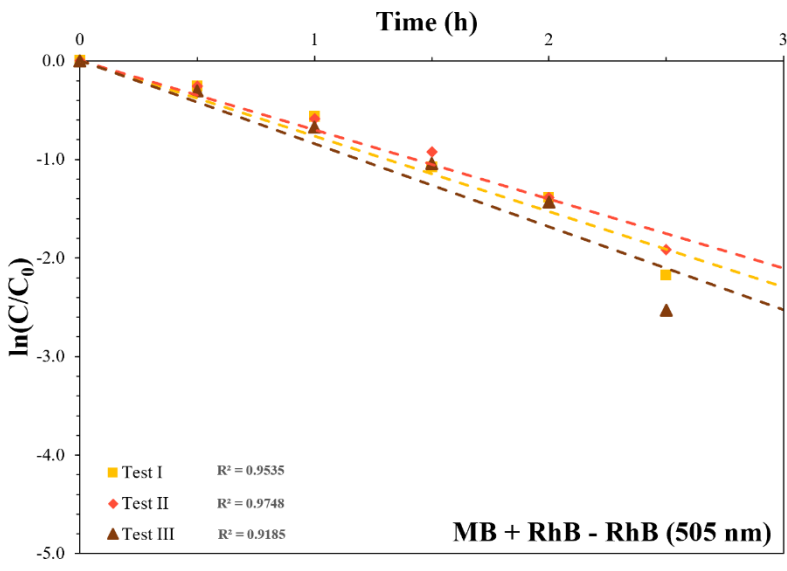

Figure 3.43. ln(C/C₀) vs time curves of photocatalytic tests performed on MB + RhB binary solutions.

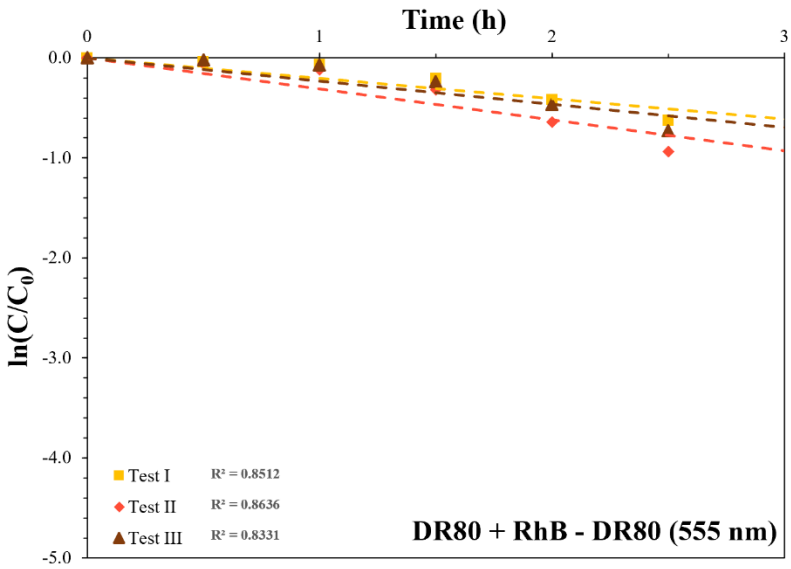

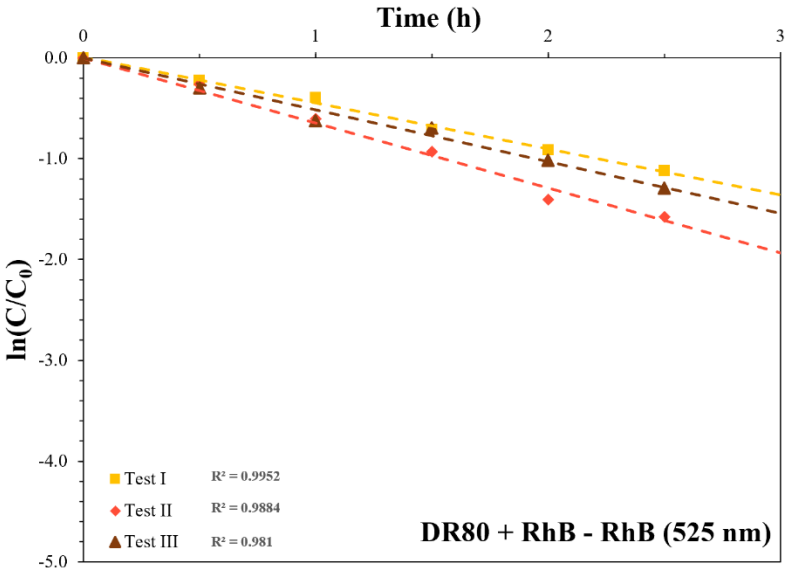

Figure 3.44. ln(C/C₀) vs time curves of photocatalytic tests performed on DR80 + RhB binary

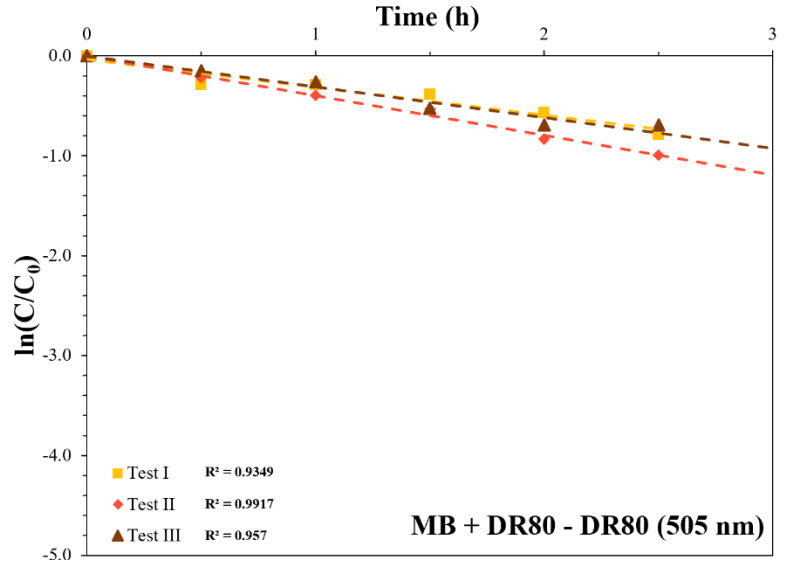

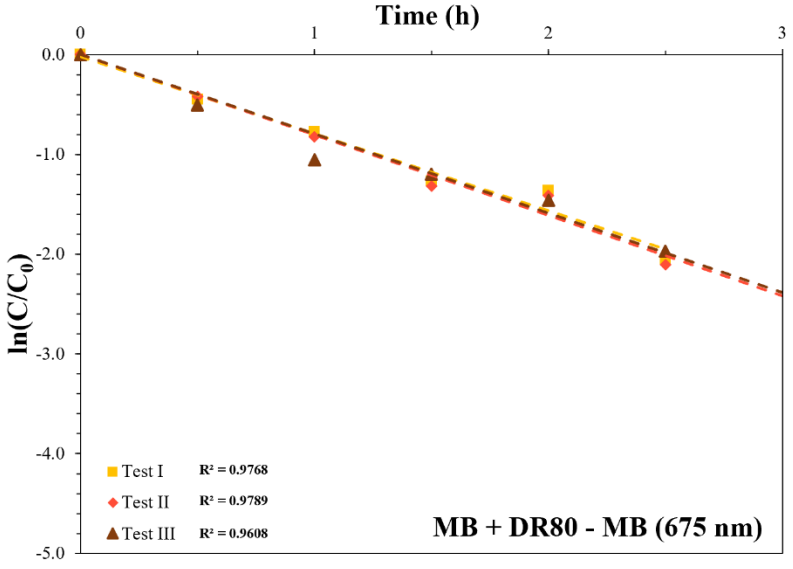

Figure 3.45. ln(C/C₀) vs time curves of photocatalytic tests performed on DR80 + MB binary solutions

All photocatalytic tests performed on binary solutions are showing a good repeatability, as can be seen from the overlapping of curves. Moreover, there is generally a good linearity between $\ln(C/C_0)$ and time confirming the applicability of Beer-Lambert law. The only exception is represented by DR80 in DR80 + RhB solutions, that presents a more exponential than linear trend, this phenomenon is probably due to the fact there is an interaction between these two dyes that act accelerating the disappearance of DR80 over time. RhB, on contrary, seems to not be influenced by DR80 showing always high values for R^2. MB + RhB binary solutions' curves are probably the best ones, MB's curves in these solutions are showing an almost perfect overlapping and very high R^2 values and also RhB's curves are well overlapping and presents a good linearity. This is probably due to the fact that spectra of these single-dye solutions are almost never overlapping, in fact their peaks are quite far away, and also they are not reacting with each other in anyway. Tests for DR80 + MB binary solutions has also shown a quite good linearity and a very good repeatability, even in this case their peaks are quite far away.

For each solution the corresponding reaction rate constant has been calculated from the regression analysis of the linear photodegradation curves leading to the values that can be seen in Figure 3.46, presented together with single-dye solutions' constants for a fast comparison.

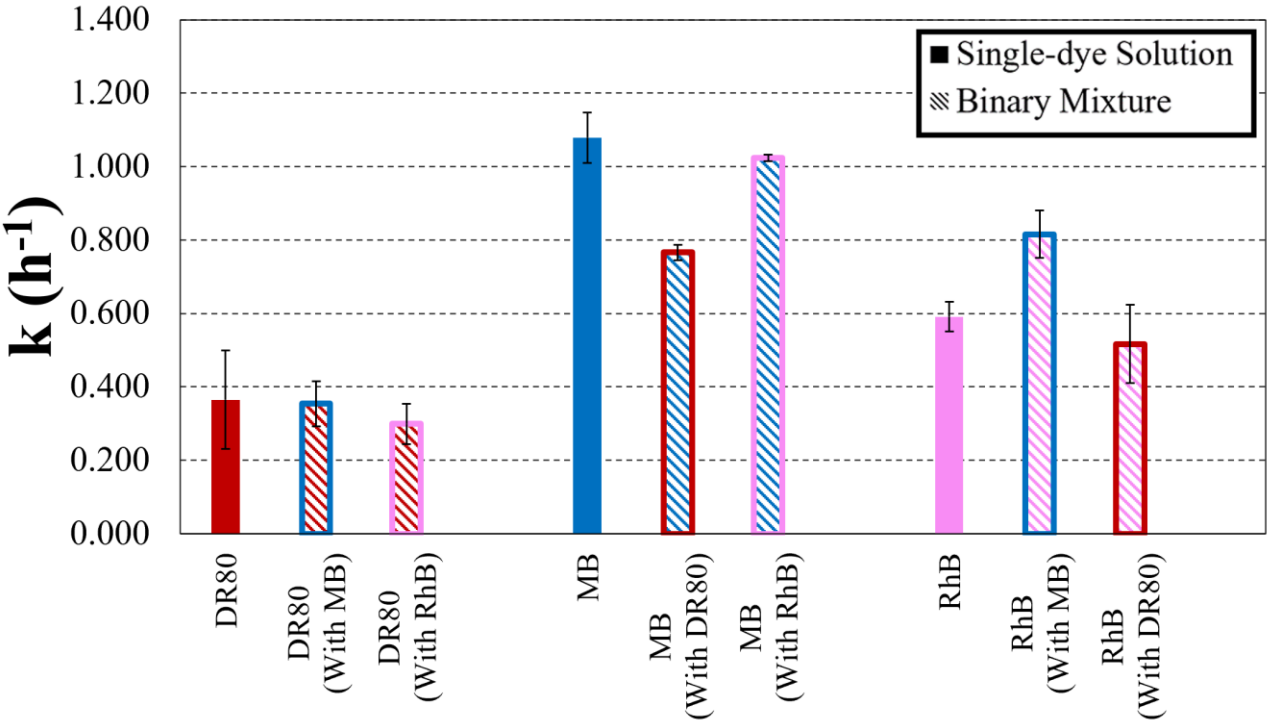

Figure 3.46. Comparison between reaction rate constants obtained for binary solutions and single-dye solutions.

From this data some considerations must be done, it is clear that the MB + RhB binary solution is the fastest one to be degraded, in fact it presents the highest reaction rate constants, among binary solutions. Moreover, RhB in this solution has a reaction rate constant that is 27% higher than the one presented in its single-dye solution, being the only component that has an higher reaction rate constant in a binary solution respect to the one of its single dye solution. Probably there is an interaction between RhB and MB that acts accelerating is degradation in these solutions. In fact, RhB in its binary solution with DR80 has a reaction rate constant that is more similar to the one of its single-dye solution. DR80 has presented the lowest values among all for reaction rate constants in its binary solutions, which are always a little lower respect to the one presented in its single-dye solution. Once again this is probably due to its heavy and complicated nature. MB has demonstrated to be the faster component to be degraded even in binary solutions, indeed this is the smaller molecule, even if its reaction rate constant in the DR80 + MB binary solution is 29% lower respect to the one of its single-dye solution. This confirm the possibility of occurrence of an electrostatic interaction between these two dyes that can affect MB's absorptivity, visible from the fact that there is a translation of the MB peak from 666 nm to 690 nm. DR80 instead seems to not be influenced by MB in anyway.
Results for reaction rate constant values obtained by photolysis and absorption tests, performed on binary solutions, are presented in Figure 3.47, in comparison with photocatalytic constant values aforementioned.

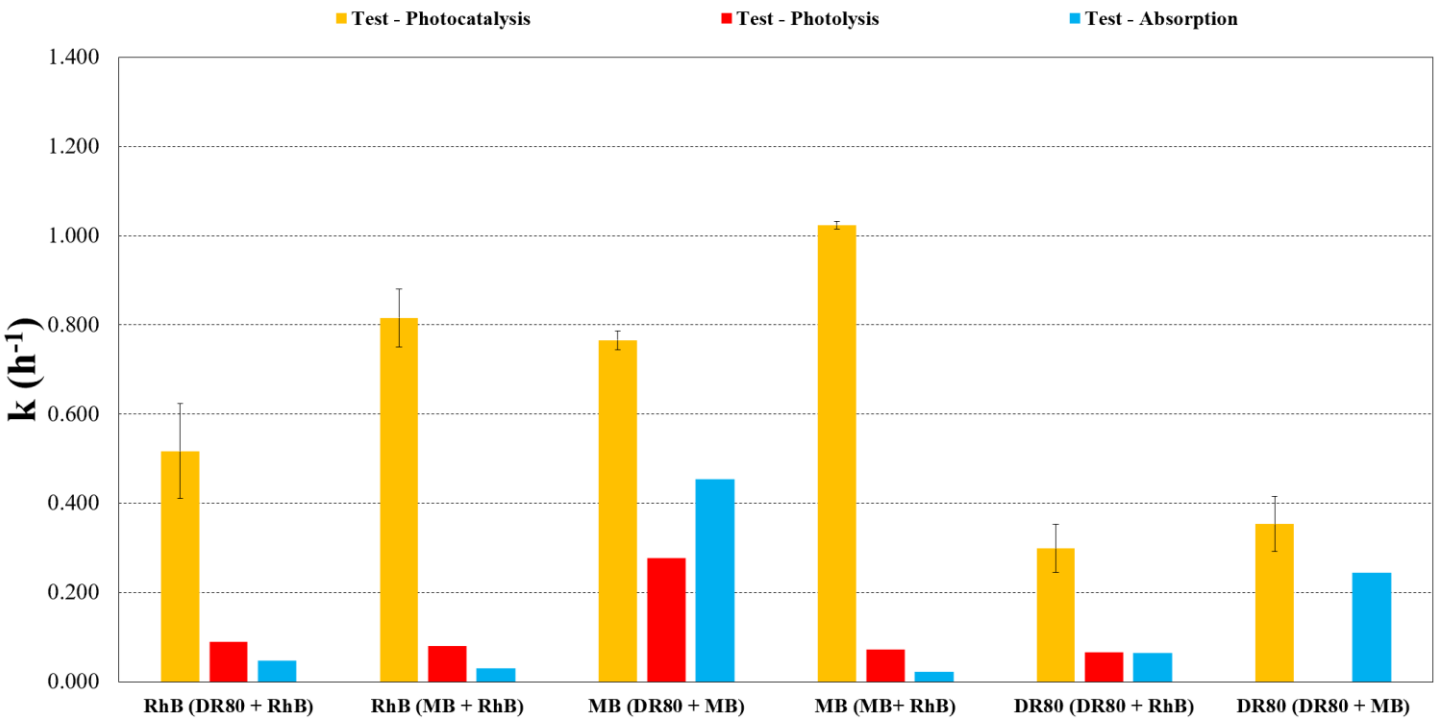

Figure 3.47. Comparison between reaction rate constants obtained for photocatalysis tests (orange), photolysis tests (red) and absorption tests (light blue) for each binary solution.

This time the reaction constants obtained by photolysis and absorbance tests are not low enough to be considered negligible, particularly in the case of DR80 + MB binary solutions. These too high values are due to an experimental error, in fact it has been noticed that, the calculation of derivative during the application of zero-crossing first order derivative spectrophotometry can lead, in cases of very low variations between absorbances, to a magnification of the discrepancies in the results leading to inappropriate observations. This problem, added to the interactions between DR80 and MB, has altered the results of these tests, leading to these too high values. This does not mean that this method has to be avoided, it is still a very useful trick that allows to make a discrete analysis of absorbances in binary mixtures. Therefore, it has to be used to monitor the degradation of dyes only for photocatalysis tests, where the degradation percentages are very high and the experimental error is negligible. Consequently, the measurements for photolysis and absorption tests have been repeated applying simply the Beer-Lambert law, as it has been done for single-dye solutions. The results obtained it this way are abundantly lower, as can been seen in Figure 3.48 in which these new data have been compared with previous ones.

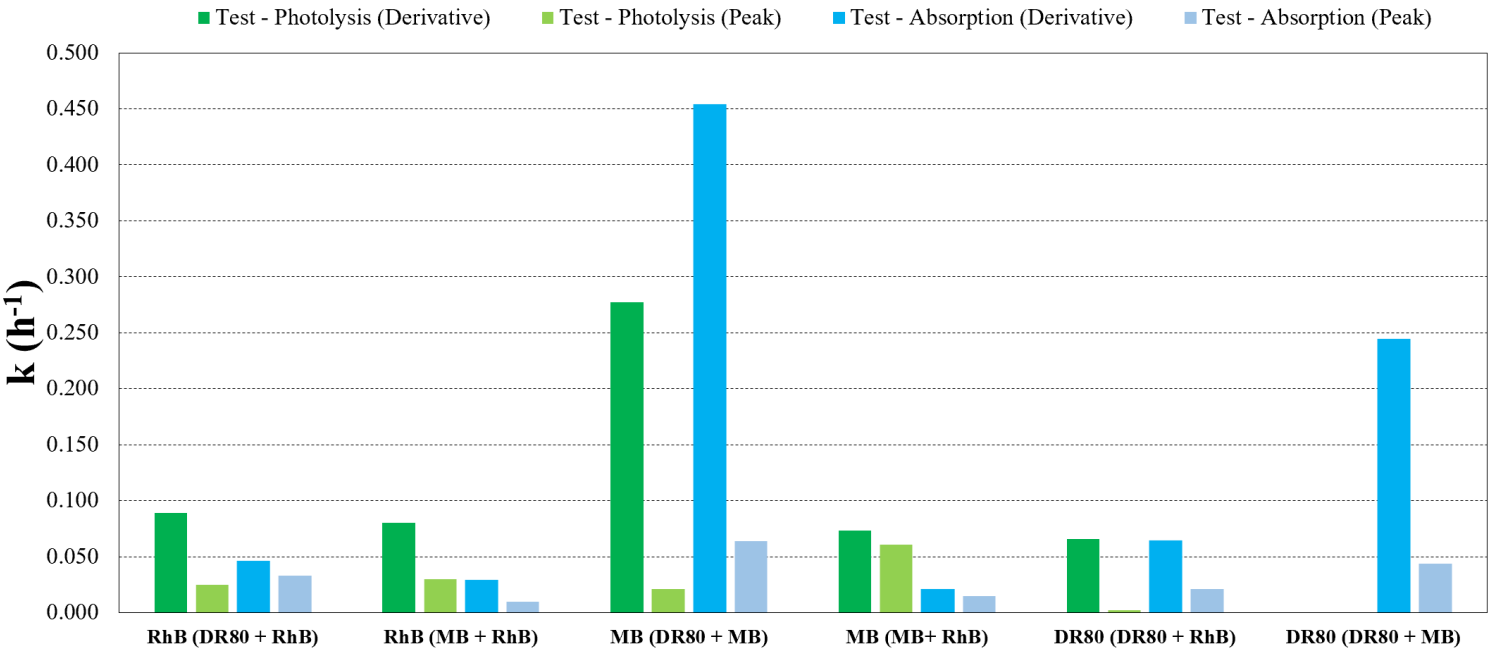

Figure 3.48. Comparison between reaction rate constants obtained with zero-crossing first order derivative spectrophotometry and simply applying Beer-Lambert law for photolysis tests (green) and absorption tests (light blue) on binary solutions.

As it can be noticed the values obtained simply applying Beer-Lambert law are abundantly lower with respect to the ones obtained with zero-crossing first order derivative spectrophotometry.

Particularly in the case of DR80 + MB binary solution, in which values calculated for MB have been reduced by 92% and 86%, respectively for photolysis tests and absorption tests, and by 82% for DR80 in absorption tests. Finally all these values are low enough to consider their contribution to photocatalytic tests negligible.

Ternary Solutions: Lastly the same three kinds of experiments have performed also on the ternary solution made by the combination of all the three organic dyes, in equal parts in volume (13.3 ml RhB + 13.3 ml MB + 13.3 ml DR80). As before the first tests performed are photocatalytic tests, with a 3 times repeatability, the analysis of the repeatability for this solution has been done following the same scheme utilized for binary and single dye solutions, an example of concentration data collected for DR80 (blue) and RhB (orange) during these tests have been reported in Figure 3.49.

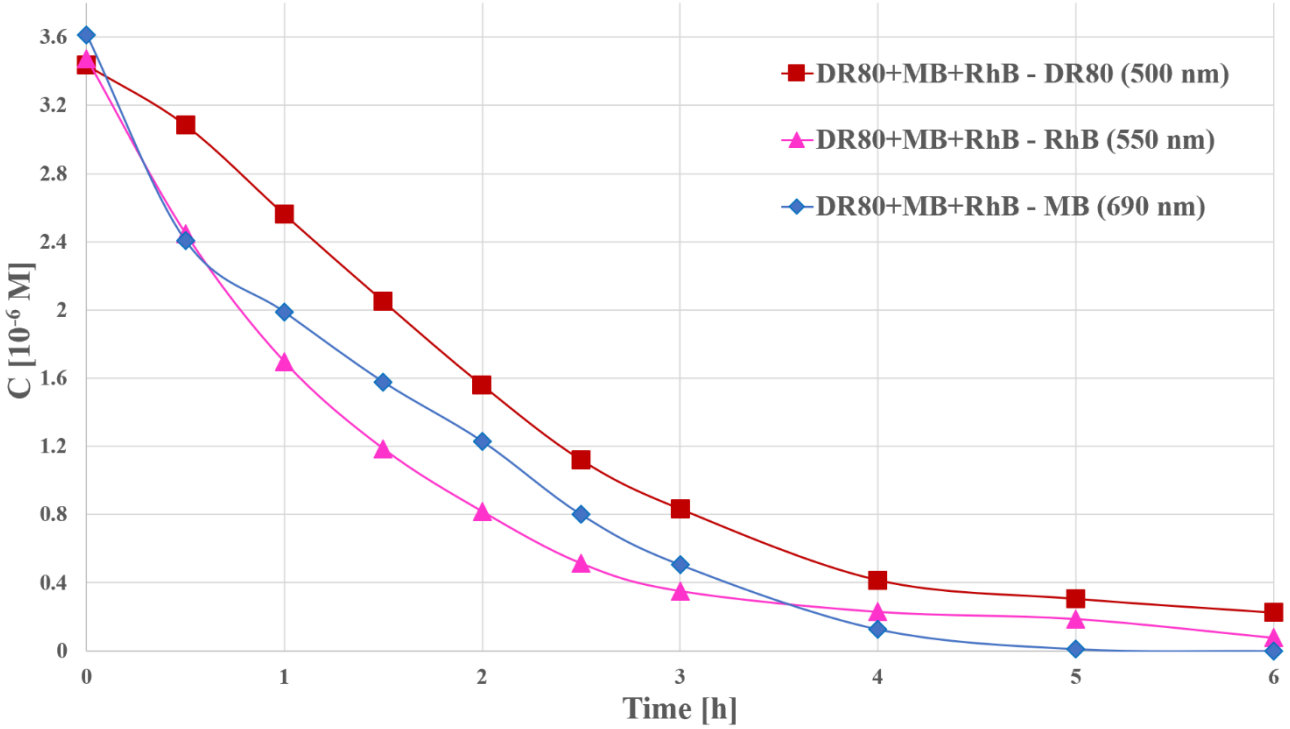

Figure 3.49. Concentration vs time curves for DR80 (red), RhB (pink)and MB (blue) in ternary solutions.

Once again, these plots are used to check if there is an exponential trend for the degradation of dyes in ternary solutions, like it happens in single-dye solutions. It can also be seen that values calculated after the third hour are very low, again like in single-dye solutions, so these data can be ignored for the calculation of reaction rate constants. These data have to be processed using the double divisor-ratio spectra derivative spectrophotometry method, as it has been explained in the previous chapter.

The resulting $\ln(C/C_0)$ vs time curves can be seen in Figures 3.50, 3.51 and 3.52.

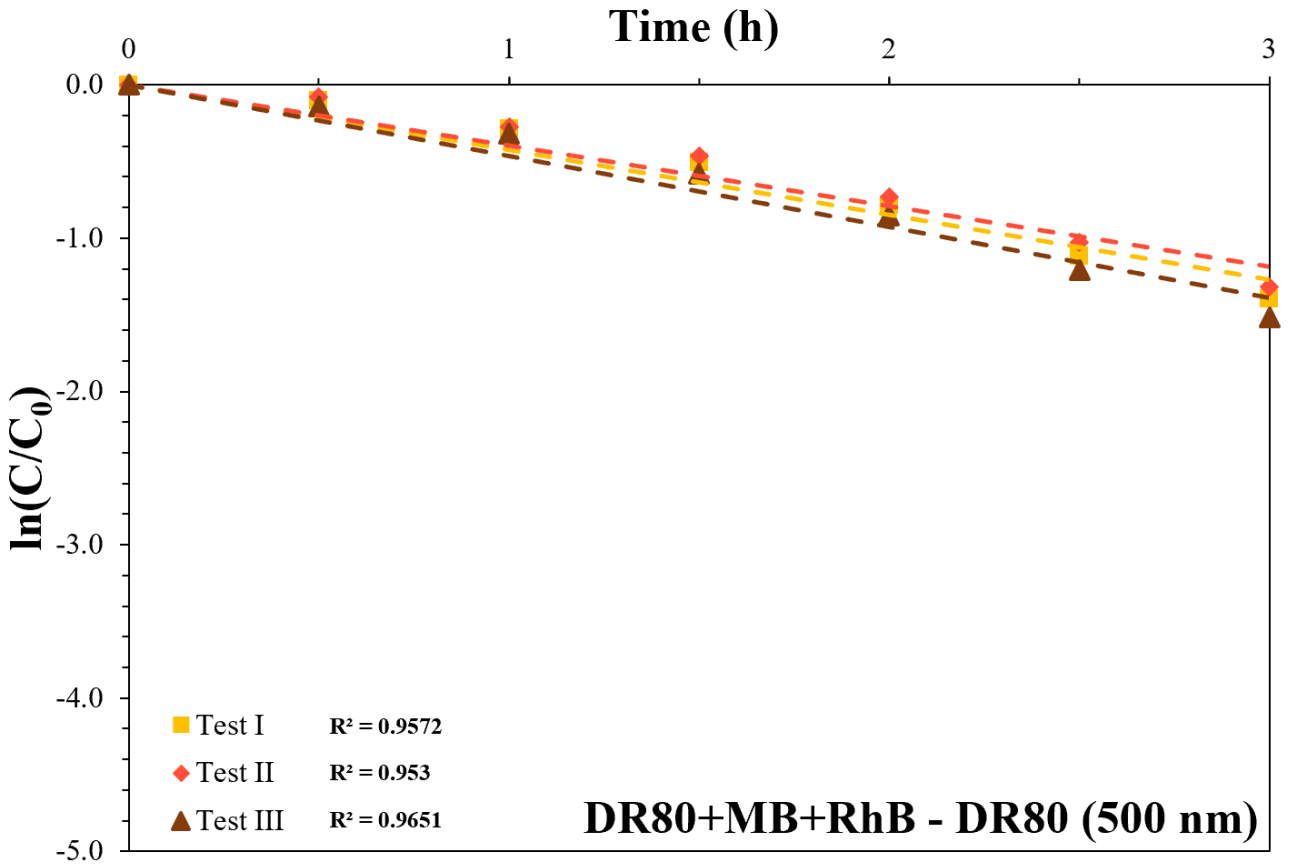

Figure 3.50. ln(C/C₀) vs time curves for DR80 in photocatalytic tests performed on ternary solutions.

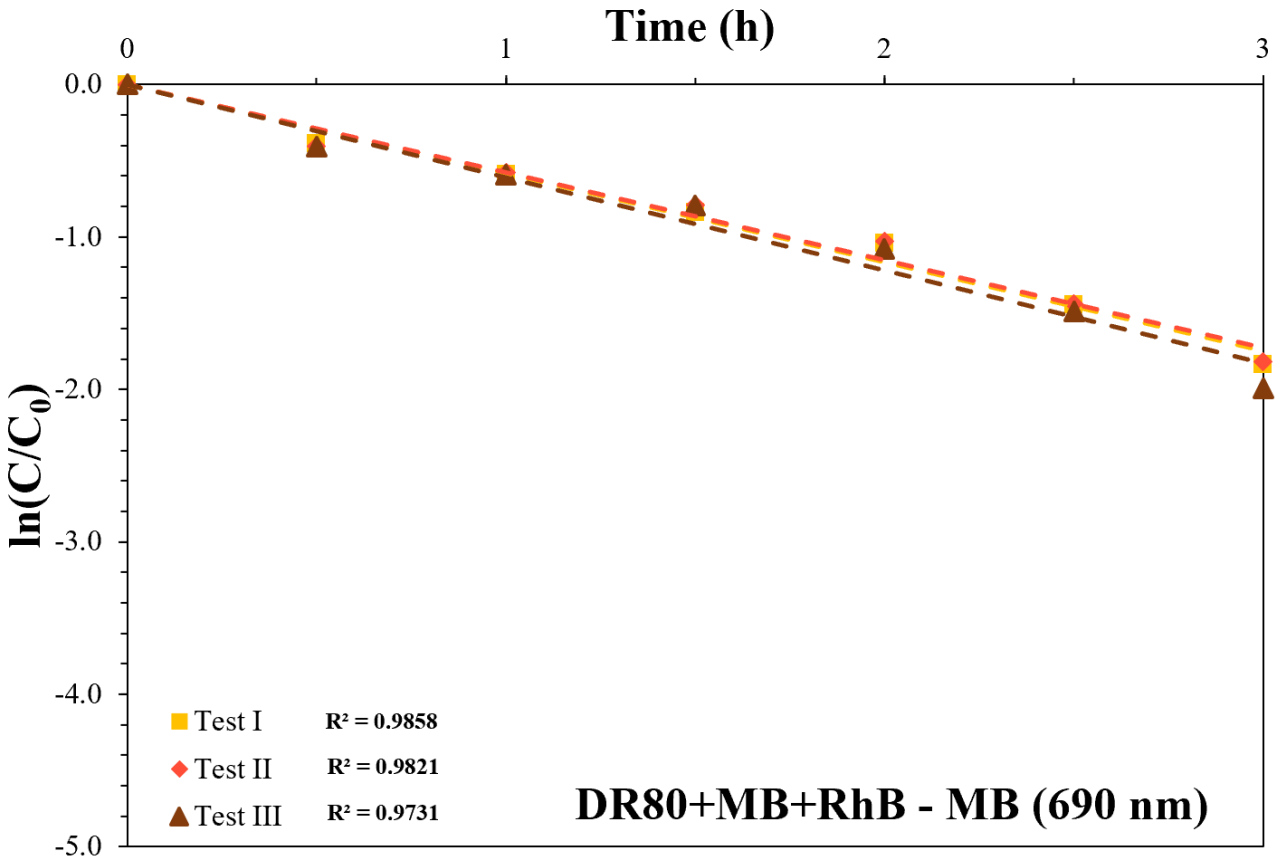

Figure 3.51. ln(C/C₀) vs time curves for MB in photocatalytic tests performed on ternary solutions.

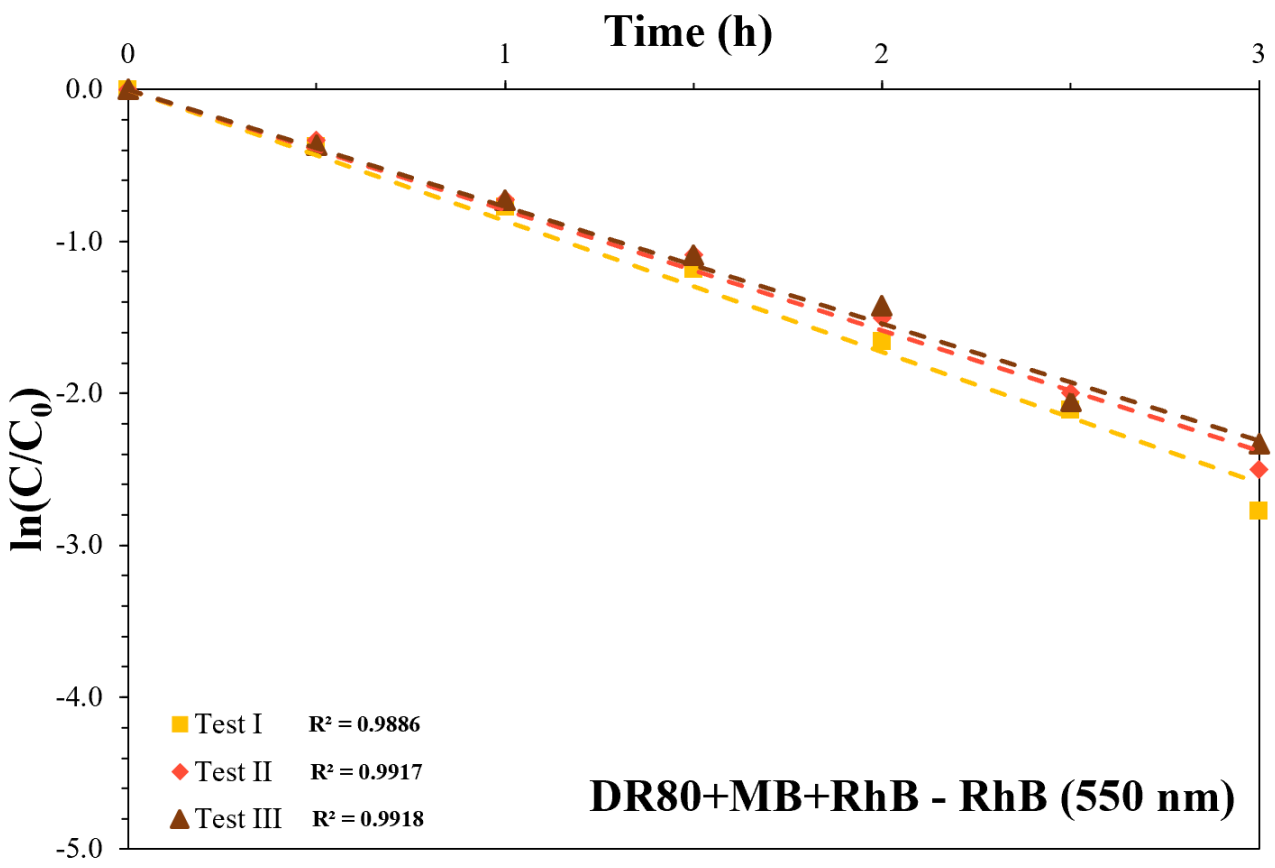

Figure 3.52. ln(C/C$_0$) vs time curves for RhB in photocatalytic tests performed on ternary solutions.

From these graphs it is clear that also tests performed on the ternary solution have a very high repeatability, demonstrated by a very good overlapping between curves for all the dyes in ternary solutions' analysis. These curves are also showing a quite good linearity (in logarithmic scale) with R^2 values that are always equal or higher than 0,953, confirming the applicability of Beer-Lambert law for these evaluations. The curves of DR80 are the ones presenting the worst linearity, even if only slightly indeed its R^2 are always higher than 0.95. RhB curves on the contrary are showing the best linearity, with R^2 values that are always higher than 0,988, confirming that this dye is the one that is lesser influenced by any kind of interaction. Even data collected for MB has shown a very good linearity confirming that absorbance measurements for this dye must be collected at 690 nm, instead of 666 nm, this could be again due to an electrostatic interaction between this dye and DR80. For each solution the corresponding reaction rate constant has been calculated from the regression analysis of the linear photodegradation curves leading to the final reaction rate constant values that can be seen in Figure 3.53, together with the reaction rate constants obtained for all single-dye and binary solutions.

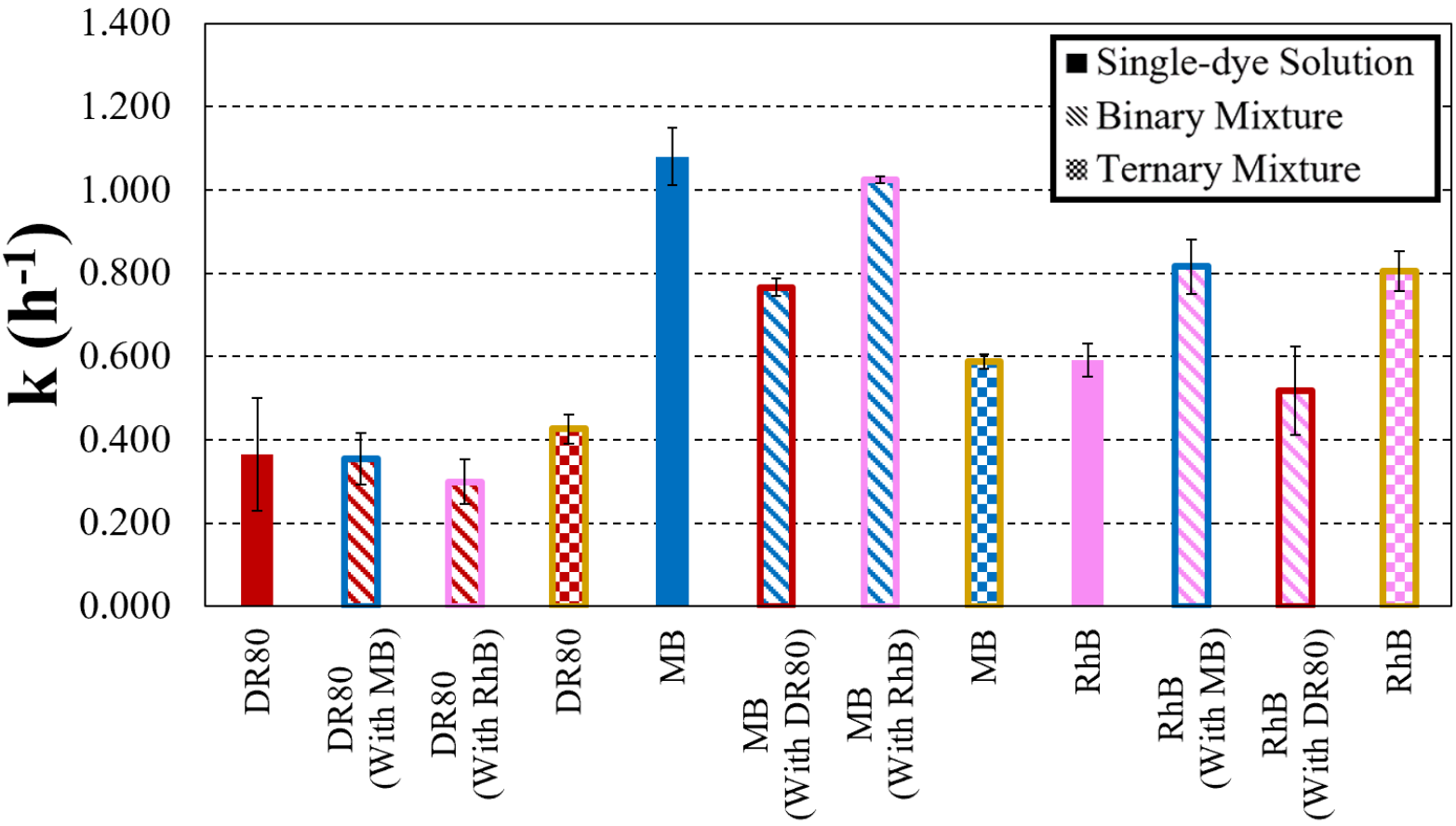

Figure 3.53. Comparison between reaction rate constant values for every solution analyzed.

From new data it can be noticed that reaction rate constants are showing a different trend, respect to binary and single-dye solutions. In fact, the fastest compound to be reduced is no longer MB but RhB that is 27% faster with respect to MB and 47% faster with respect to DR80. Once again, DR80 has been the slowest component to be degraded confirming the same trend presented in single-dye and binary solutions, with kinetics similar in all environments (only slight differences within the experimental error of tests made in single dye solutions). Even RhB has presented a higher reaction rate constant value with respect to the one of its single dye solution (36% higher), being very similar to the one obtained in the MB + RhB binary solution, indicating a beneficial effect of MB presence on RhB degradation. MB instead degrades slowly, being actually 46% lower respect to the one obtained for its single-dye solution.
Lastly photolysis and adsorption tests has been performed even on ternary solutions, leading to the results that are presented in Figure 3.54, once again in comparison with data obtained from photocatalytic experiments for an easy comparison.

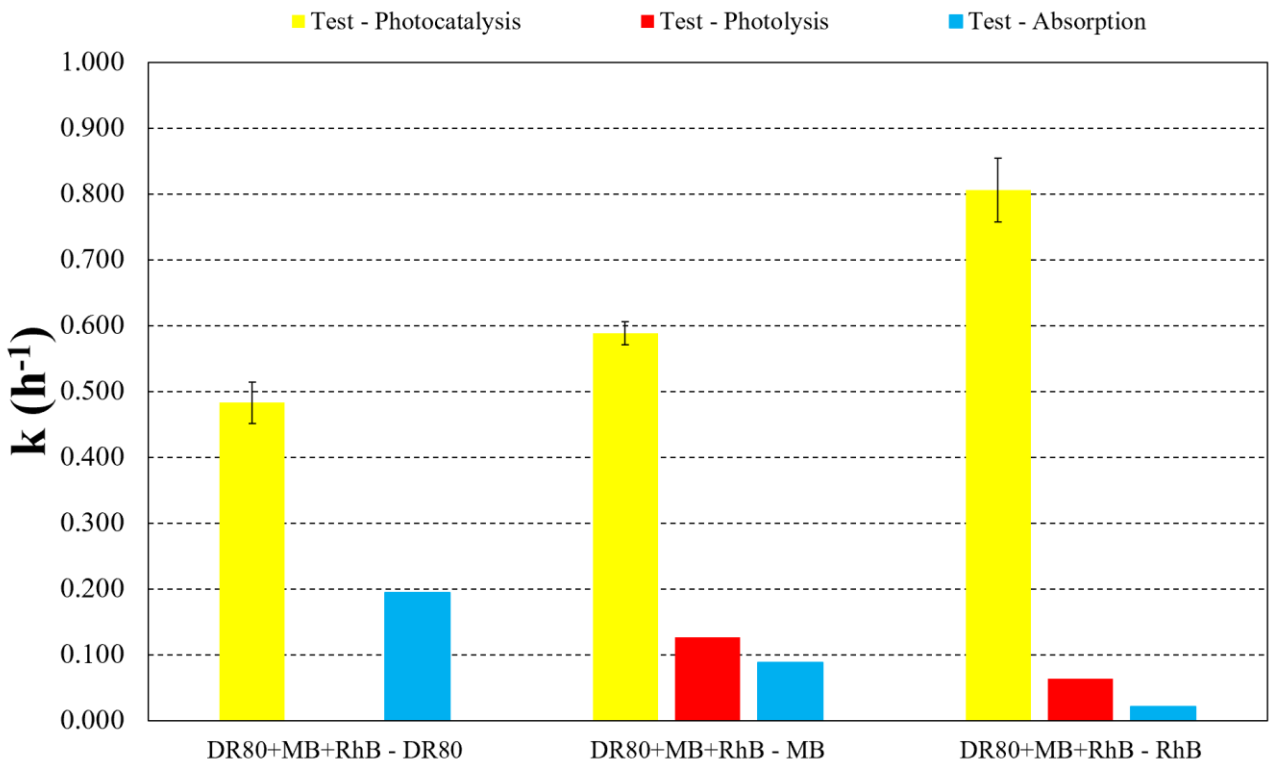

Figure 3.54. Comparison between reaction rate constants obtained photocatalysis tests (yellow), photolysis tests (red) and absorption tests (light blue) performed on ternary solutions.

The same problem, that occurred during the evaluation of reaction rate constants for photolysis and adsorption tests performed on binary solutions, has happened during the evaluation of ternary ones. Indeed, the calculation of derivative during the application of double divisor-ratio spectra derivative spectrophotometry can lead, in cases of very low variations between absorbances, to a magnification of discrepancies in the results leading to inappropriate observations. This problem, added to the interactions between DR80 and MB, has altered the results leading to these too high values, indeed it is not a case that values calculated for RhB are the ones that are less influenced by this effects, being RhB the less reactive component. This does not mean that this method has to be avoided, it is still a very useful way to make a discrete analysis of absorbances in ternary mixtures. Therefore, it has to be used to monitor the degradation of dyes only for photocatalysis tests, where the degradation percentages are very high and the experimental error is negligible. Consequently, the measurements for photolysis and adsorption tests have been repeated using the simpler peaks method, as it has been done for binary solutions. Such results are abundantly lower for DR80 and RhB, as can been seen in Figure 3.55 in which these data have been compared with previous ones.

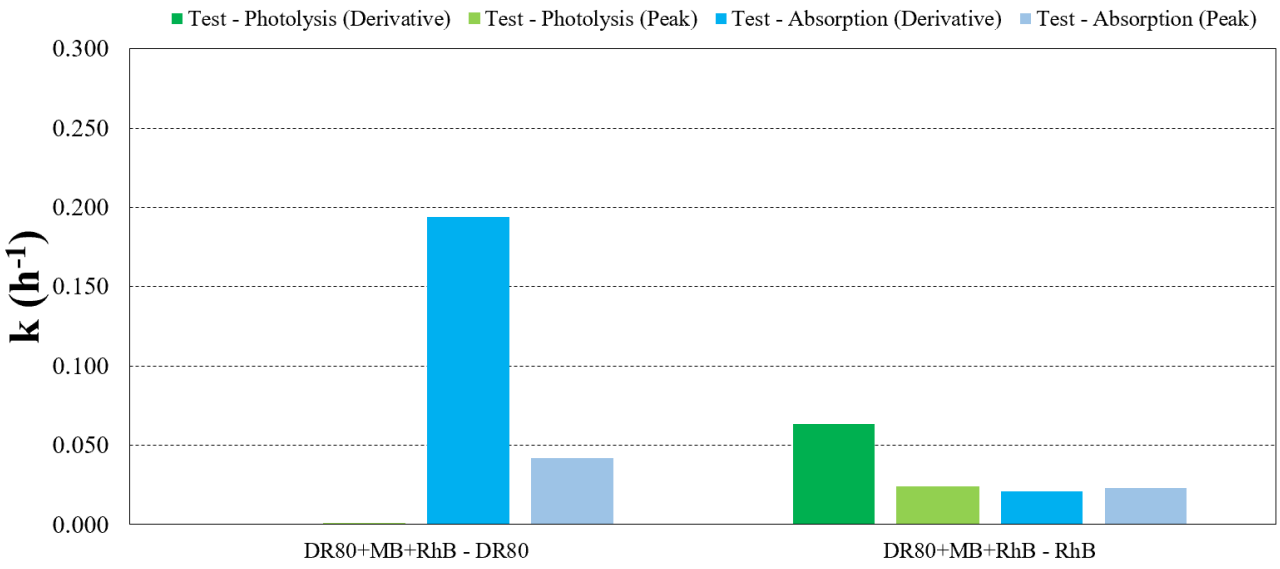

Figure 3.55. Comparison between reaction rate constants obtained with double divisor-ratio spectra derivative spectrophotometry and simply applying Beer-Lambert law for photolysis tests (green) and absorption tests (light blue) performed on ternary solutions.

With this data it is easy to understand why the reaction rate constant value obtained previously for DR80 during absorption tests is not to be considered reliable, indeed there is a reduction of about 78% for this value, simply applying Beer-Lambert law, leading to a totally negligible value. As expected, it has not been noticed a high variation in data obtained for RhB, but they were already low enough to be considered negligible. For the purpose of this thesis even data obtained previously for MB can be considered negligible, as their valor is probably due to the electrostatic interaction aforementioned. Because of that it has been decided that even in the case of ternary solution the contributions of photolysis and absorption reactions can be neglected leading to the conclusion that photocatalytic reactions are the only ones responsible for the mineralization of dyes.

3.4 Photocatalytic Tests with White LEDs

The same photocatalytic tests, with a 3 times repeatability, that have been performed using UV-LEDs, has been then repeated using white LEDs, but only for single dye solutions. These experiments have been done to evaluate the possibility of using natural light instead of UV-radiations for the mineralization of organic dyes in the same solutions already studied. Single dye solutions have been prepared following the same procedure of mixing the dye with distilled water to reach a final concentration of the dye of $10^{-5}\ M$. The absorbance vs time curves for these tests have been reported for all single-dyes solutions in Figures 3.56, 3.57 and 3.58.

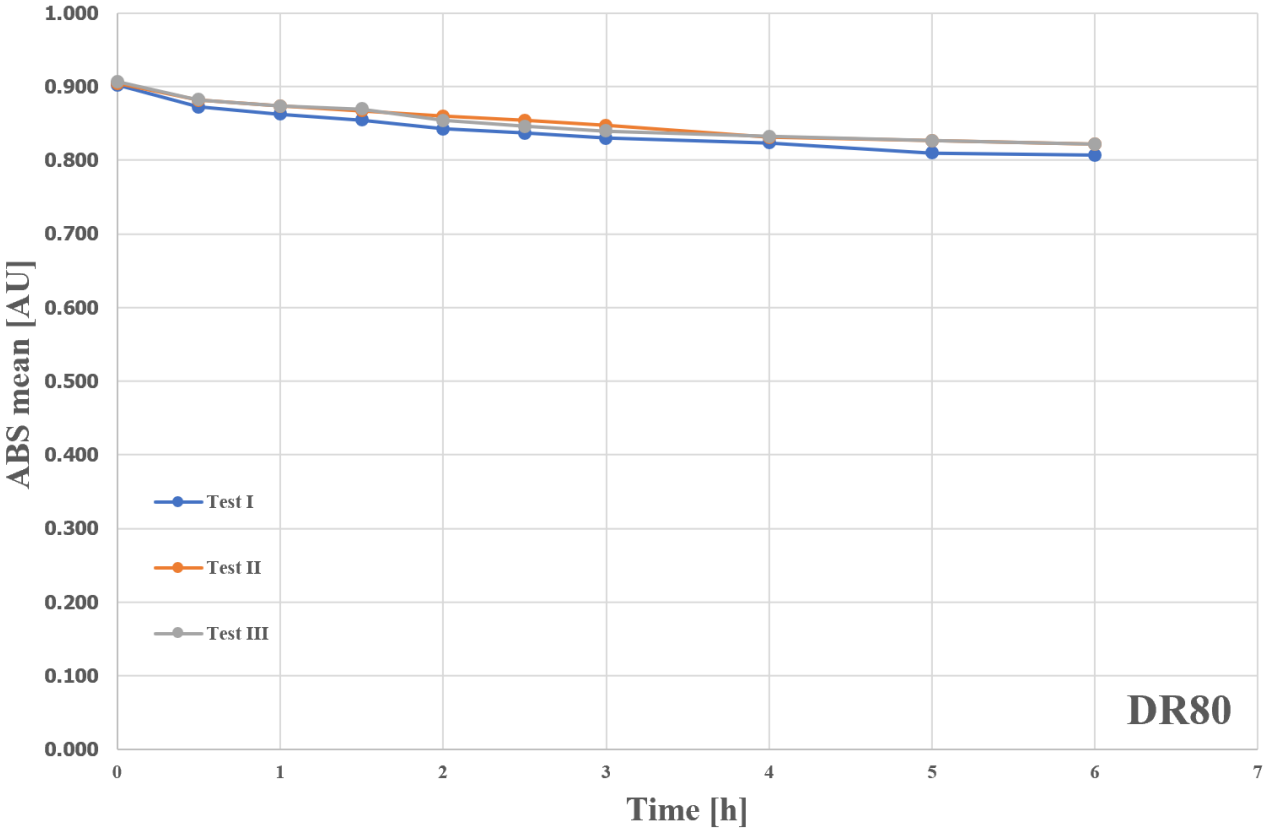

Figure 3.56. Absorbance vs time curves for photocatalytic tests performed on DR80, using white LEDs.

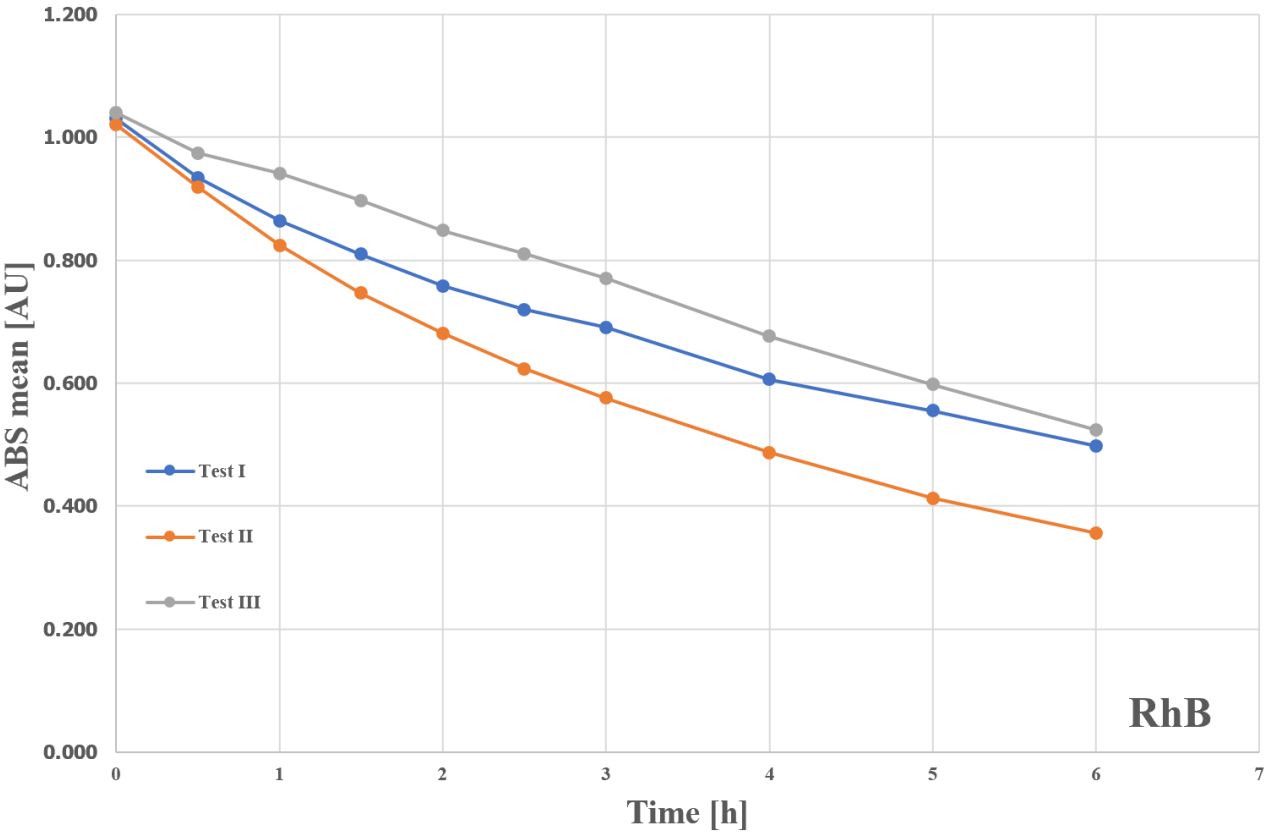

Figure 3.57. Absorbance vs time curves for photocatalytic tests performed on RhB, using white LEDs.

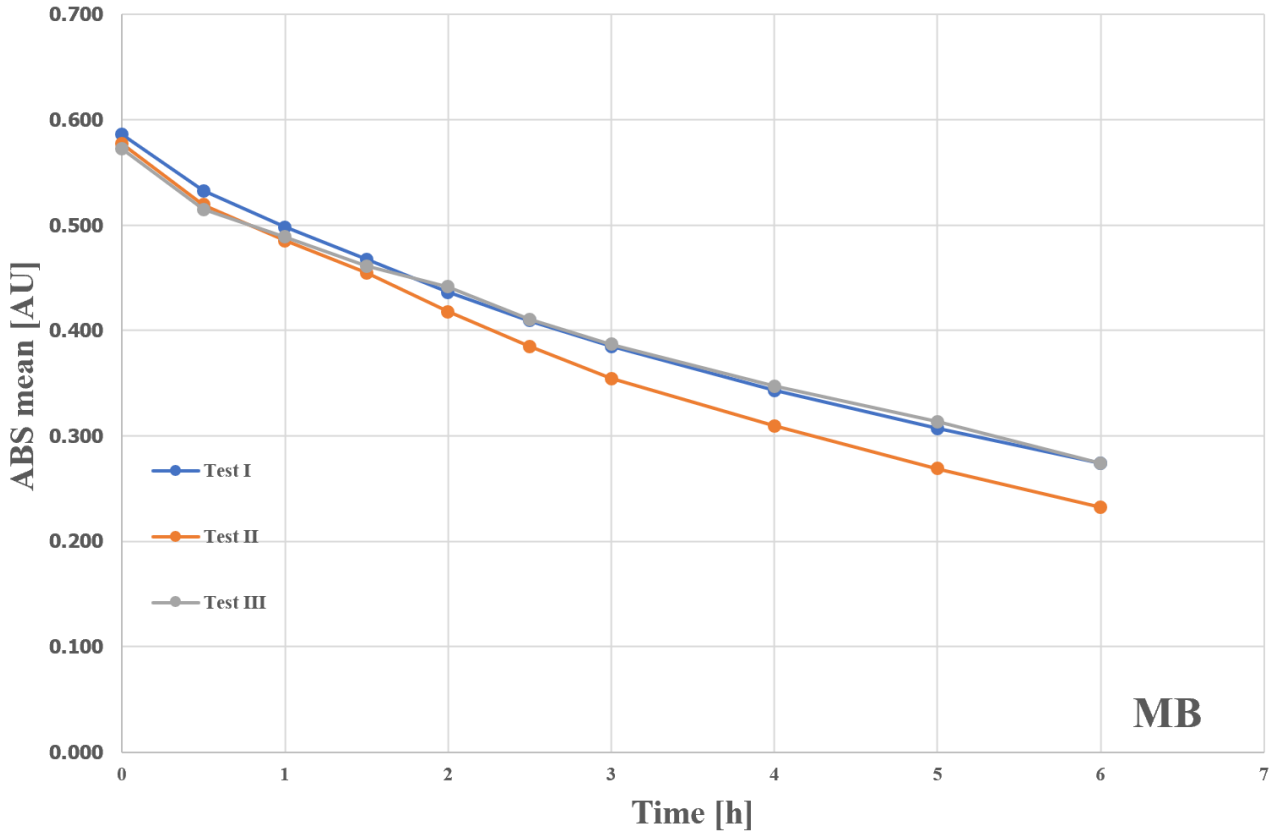

Figure 3.58. Absorbance vs time curves for photocatalytic tests performed on MB, using white LEDs.

Thanks to calibration curves, these data has been processed leading to the building of $\ln(C/C_0)$ vs time curves from which a linear trend can be observed, confirming the pseudo-first order kinetic even for the mechanism of these reactions. These curves can be seen in Figures 3.59, 3.60 and 3.61, from which the effective repeatability of these tests can be evaluated.

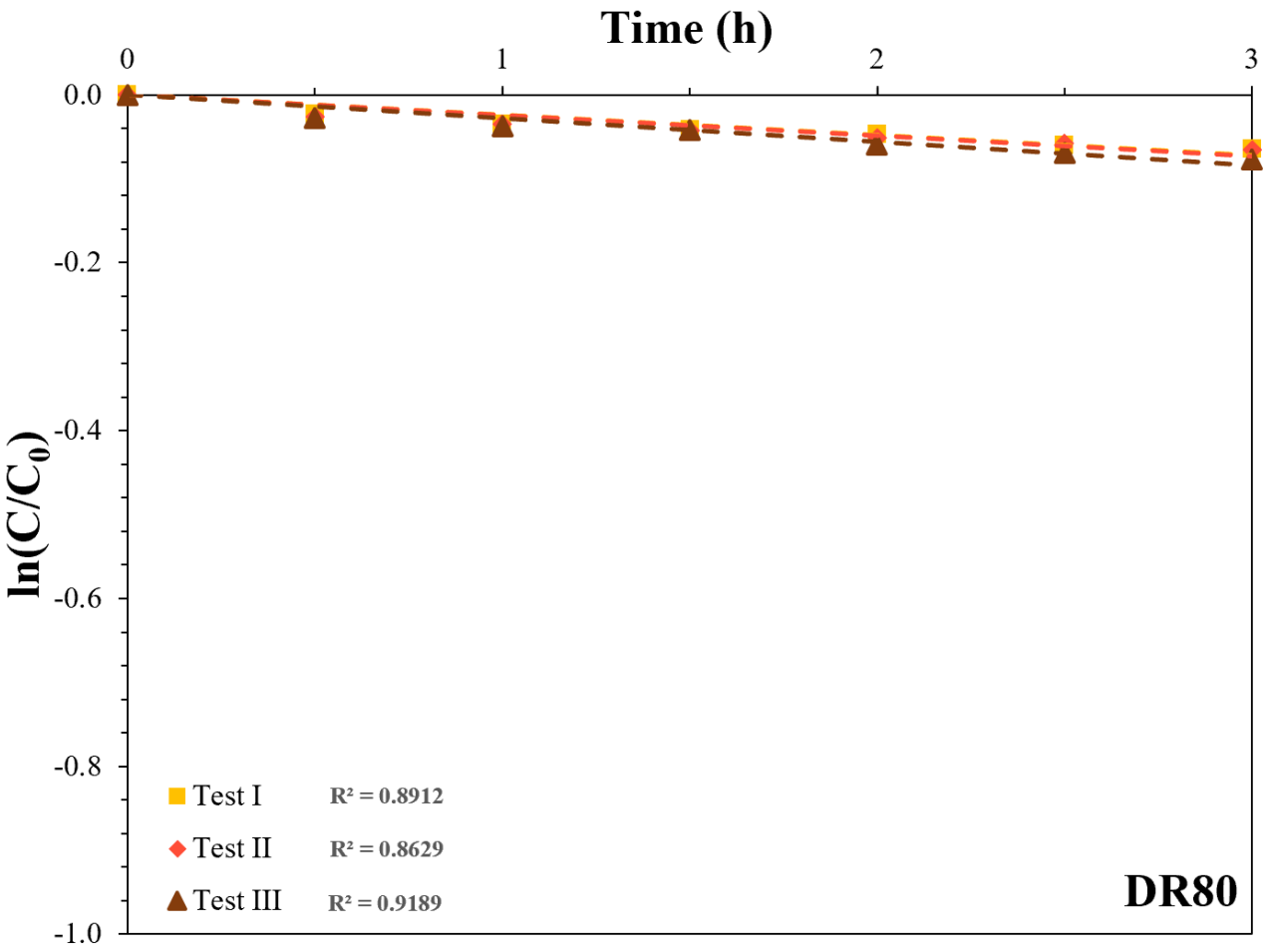

Figure 3.59. $\ln(C/C_0)$ vs time curves for photocatalytic tests performed on DR80, using white LEDs.

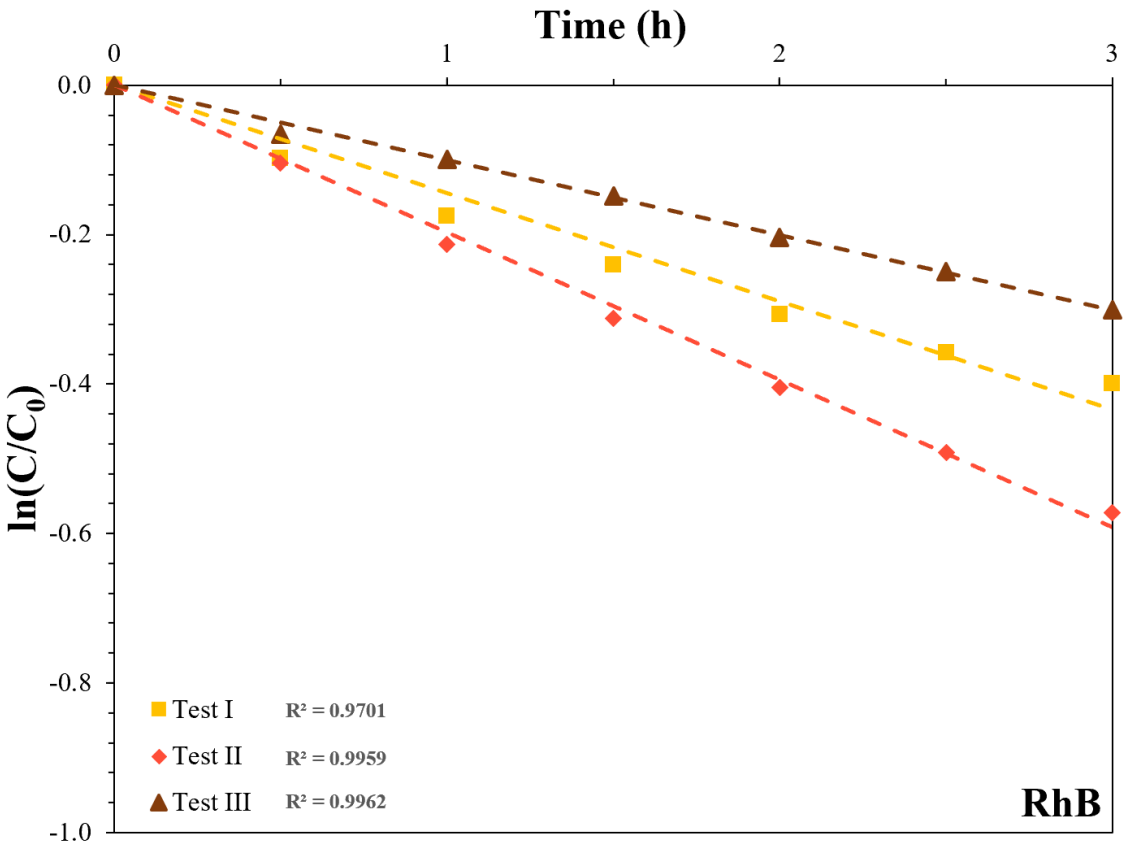

Figure 3.60. ln(C/C₀) vs time curves for photocatalytic tests performed on RhB, using white LEDs.

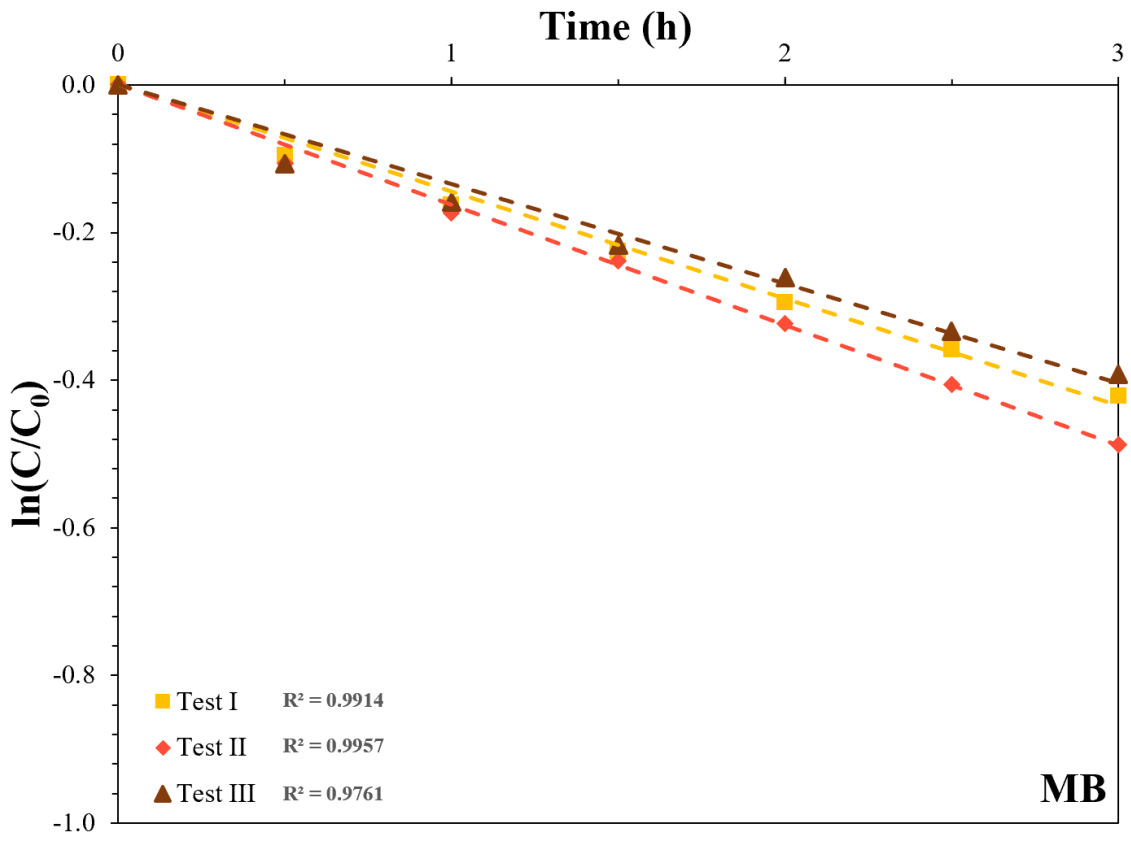

Figure 3.61. ln(C/C₀) vs time curves for photocatalytic tests performed on MB, using white LEDs.

From data plotted in these graphs it is clear that even with white LEDs the degradation phenomena are still following a pseudo-first order kinetics, as evidenced by a linear trend (in logarithmic scale), particularly for tests performed on MB and RhB whose R^2 values are always higher than 0.97. A little deviation is observed by tests performed on DR80, whose R^2 values are quite low, anyway this result was expected as this dye has demonstrated to be the hardest one to be mineralized even using UV-LEDs. The effective three-time repeatability of these tests is almost respected, this is demonstrated by a good overlapping for curves of DR80 and MB. The case of RhB is a little harder to be evaluated, indeed its curves are not showing a good overlapping, even if the linearity trend has been well respected. In fact, this dye has shown a very strange behavior during these tests; it has been noticed that the typical magenta color of its solution has changed during time leading to a fluorescent green final color, instead of simply becoming more transparent. From the analysis of the RhB spectrum, in has been noticed the formation of a new peak at 505 nm. This phenomenon was ascribed to the sequential loss of the four RhB ethyl groups, giving as last decomposition compound the de-ethylated molecule rhodamine, that is precisely characterized by a green fluorescence. [8]
Data collected with measurements at 505 nm for RhB solutions has been reported in the following plot, in Figure 3.62.

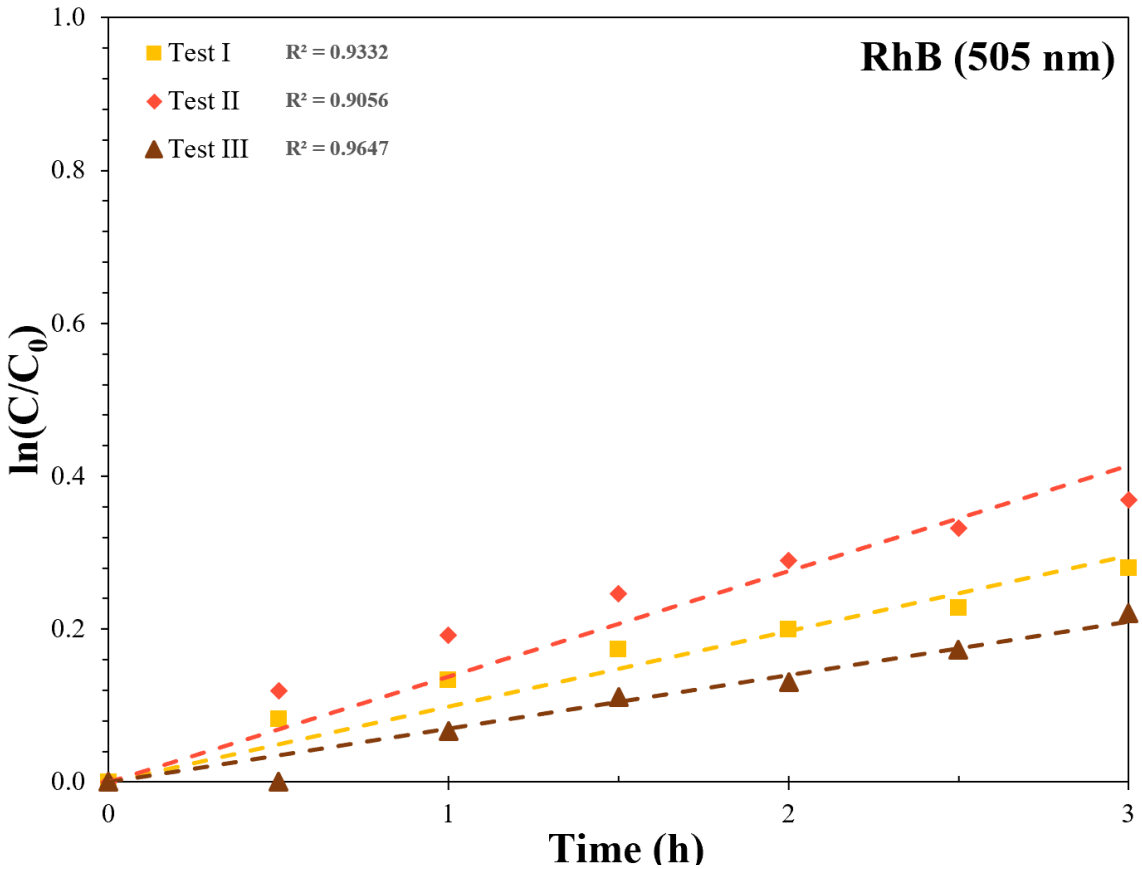

Figure 3.62. ln(C/C₀) vs time curves for data collected at 505 nm during photocatalytic tests performed on RhB, using white LEDs.

From all these data the corresponding reaction rate constant has been calculated from the regression analysis of the linear photodegradation curves leading to the final reaction rate constant values that can be seen in Figure 3.63. these are presented together with reaction rate constant values obtained with photolysis and absorption tests, that also in this case has been performed.

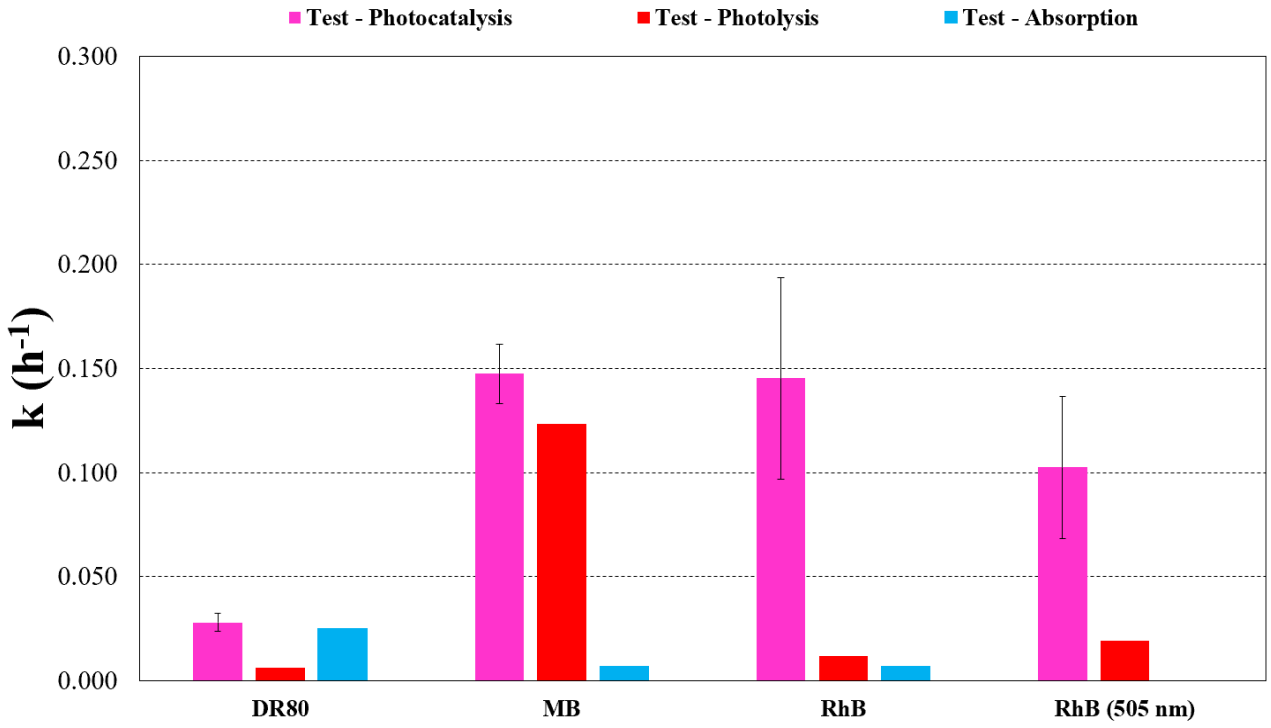

Figure 3.63. Comparison between reaction rate constant values obtained with photocatalysis tests using white LEDs (pink), photolysis tests using white LEDs (red) and absorption tests (light blue) performed on all single dye solutions.

As expected reaction kinetics obtained with white LEDs are much slower than the ones obtained using UV-LEDs and also they are comparable with reaction rate constants values that have been obtained with photolysis and absorption tests, making impossible to consider negligible the contribution of these reactions, particularly for MB and DR80. For MB it can be seen that its reaction rate constant value obtained for photocatalysis is only 16% higher than the one obtained with photolysis experiments, while for DR80 the reaction rate constant value measured with photocatalysis is only 11% higher respect to the one measured during absorption tests. For these experiments all values have been obtained simply using Beer-Lambert law so in this case there is an effective degradation of the dye due to the photolysis and absorption reactions and not to photocatalytic effects. Anyway, DR80 it is practically not degraded during photocatalytic experiments, with white LEDs, due to its heavy and complicated nature. While MB and RhB have been partially mineralized, even if very slowly.

One last consideration has to be done; even if these two dyes are characterized by very similar reaction rate constant values, from these data it can be noticed that their degradation mechanisms are due to very different effects.
Indeed, MB's mineralization is mostly due to the photolysis reaction, that has occurred during photocatalytic experiments, while RhB's mineralization is principally due to its conversion into rhodamine green (RhG). In fact, the reaction rate constant value measured for the formation of RhG is almost the 72% of the value obtained for the degradation of RhB. These final consideration leads to the conclusion that visible light cannot be used to achieve an effective mineralization of these organic dyes using nanotubular titanium dioxide for photocatalytic degradation.

Chapter 4 : Conclusions

The purpose of this thesis was the evaluation of the photocatalytic degradation of three different organic dyes in their single, binary and ternary solutions to assess the effective applicability of photocatalytic purification treatments on textile industrial wastewaters, in which many components are mixed together. The titanium samples involved during these experiments have been anodized, to build up nanotubular structures on their surfaces that can provide the highest ratio between surface area and volume, and annealed, to obtain the ideal ratio between rutile and anatase phases for photocatalytic experiments. Moreover, the samples have been characterized in order to verify the proper morphology and crystalline structure through SEM and XRD, respectively.

Later on, all the organic dyes solutions have been studied to obtain calibration curves correlating spectrophotometric measurements and dye concentration, using different methods to overcome the problem of possible overlapping of spectra, leading to more reliable and precise results. From these curves a linear correlation between absorbance and concentration of organic compounds has been observed in all cases, even if in some cases the interaction between different dyes has made more difficult the interpretation of data.

The results obtained with photocatalytic experiments, using UV-LEDs, fit very well with a first order kinetics, so that it is possible to assess that each solution has been degraded after three hours with a photocatalytic efficiency always higher than 70%. Even more, experiments for the evaluation of possible contributions of photolysis reactions or adsorption of dyes on titanium samples surfaces have been performed for each analyzed condition, leading to very low kinetic constant values; this allows to say that only photocatalytic degradation was responsible for the decreased concentration of the organic components in the solutions.

Methylene Blue has demonstrated to be the most susceptible dye for photocatalytic degradation phenomena for single and binary solutions, while Rhodamine B has shown very high reaction rate constant value only in presence of MB, both in binary and ternary solutions; Direct Red 80, instead, seems to be the most recalcitrant dye in all the conditions involved, and its behavior does not seem influenced by the presence of the other two dyes. However, it must be mentioned that an interaction has been observed between Methylene Blue and Direct Red 80 that acts moving the peak of MB from 666 nm to 690 nm; this interaction causes a drastic lowering of MB reaction rate when DR80 is present in the solution.

Regarding the photocatalytic tests that have been performed using visible light LEDs, very poor reaction rates have been recorded, leading to the conclusion that it is still impossible to perform a photodegradation on these solutions using visible light instead of UV radiation.

All the results presented in this work represents a good analysis of photocatalytic processes that can be used for the treatment of textile wastewaters. Also the mathematical methods involved for the building of calibration curves have demonstrated to be very useful in overcoming the problems occurred due to the overlapping of spectra in multi-dye solutions, but for the correct analysis in cases with very low differences between absorbances, for example photolysis and absorption tests performed on interacting solutions (like the ones with Direct Red 80 and Methylene Blue present at the same time) some precautions must be taken.

Further analyses are required in order to better understand the nature of the interactions among the different dyes.

Bibliography

[1] "Greta Thunberg Listen To Us Speech In Assemblee Nationale | LYBIO.NET Discover New Reading Content." [Online]. Available: https://lybio.net/greta-thunberg-listen-to-us-speech-in-assemblee-nationale/speeches/. [Accessed: 17-Jan-2020].

[2] D. K. Gardiner and B. J. Borne, "Textile Waste Waters: Treatment and Environmental Effects," *J. Soc. Dye. Colour.*, vol. 94, no. 8, pp. 339–348, 1978, doi: 10.1111/j.1478-4408.1978.tb03420.x.

[3] L. Qin *et al.*, "Effect of anodization parameters on morphology and photocatalysis properties of TiO2 nanotube arrays," *J. Mater. Sci. Technol.*, vol. 31, no. 10, pp. 1059–1064, 2015, doi: 10.1016/j.jmst.2015.07.012.

[4] X. Liu, P. K. Chu, and C. Ding, "Surface modification of titanium, titanium alloys, and related materials for biomedical applications," *Materials Science and Engineering R: Reports*. 2004, doi: 10.1016/j.mser.2004.11.001.

[5] M. V. Diamanti, B. del Curto, and M. Pedeferri, "Anodic oxidation of titanium: From technical aspects to biomedical applications," *J. Appl. Biomater. Biomech.*, vol. 9, no. 1, pp. 55–69, 2011, doi: 10.5301/JABB.2011.7429.

[6] Z. Y. Yuan and B. L. Su, "Titanium oxide nanotubes, nanofibers and nanowires," in *Colloids and Surfaces A: Physicochemical and Engineering Aspects*, 2004, doi: 10.1016/j.colsurfa.2004.04.030.

[7] H. Hayashi and K. Torii, "Hydrothermal synthesis of titania photocatalyst under subcritical and supercritical water conditions," *J. Mater. Chem.*, vol. 12, no. 12, pp. 3671–3676, 2002, doi: 10.1039/b207052a.

[8] M. V. Diamanti, M. Ormellese, E. Marin, A. Lanzutti, A. Mele, and M. P. Pedeferri, "Anodic titanium oxide as immobilized photocatalyst in UV or visible light devices," *J. Hazard. Mater.*, vol. 186, no. 2–3, pp. 2103–2109, 2011, doi: 10.1016/j.jhazmat.2010.12.128.

[9] H. H. Ou and S. L. Lo, "Review of titania nanotubes synthesized via the hydrothermal treatment: Fabrication, modification, and application," *Sep. Purif. Technol.*, 2007, doi: 10.1016/j.seppur.2007.07.017.

[10] I. Paramasivam, H. Jha, N. Liu, and P. Schmuki, "A review of photocatalysis using self-organized TiO 2 nanotubes and other ordered oxide nanostructures," *Small*, vol. 8, no. 20, pp. 3073–3103, 2012, doi: 10.1002/smll.201200564.

[11] G. K. Mor, O. K. Varghese, M. Paulose, N. Mukherjee, and C. A. Grimes, "Fabrication of tapered, conical-shaped titania nanotubes," *J. Mater. Res.*, vol. 18, no. 11, pp. 2588–2593, 2003, doi: 10.1557/JMR.2003.0362.

[12] L. Y. Chin, Z. Zainal, M. Z. Hussein, and T. W. Tee, "Fabrication of highly ordered TiO 2 nanotubes from fluoride containing aqueous electrolyte by anodic oxidation and their photoelectrochemical response," *J. Nanosci. Nanotechnol.*, vol. 11, no. 6, pp. 4900–4909, 2011, doi: 10.1166/jnn.2011.4108.

[13] K. Lee, A. Mazare, and P. Schmuki, "One-dimensional titanium dioxide nanomaterials: Nanotubes," *Chem. Rev.*, vol. 114, no. 19, pp. 9385–9454, 2014, doi: 10.1021/cr500061m.

[14] P. F. Chauvy, P. Hoffmann, and D. Landolt, "Electrochemical micromachining of titanium using laser oxide film lithography: Excimer laser irradiation of anodic oxide," *Appl. Surf. Sci.*, 2003, doi: 10.1016/S0169-4332(03)00256-3.

[15] I. Photoetching and S. P. Technical, "United States Patent (19)," no. 19, 1983.

[16] Y. Dimitriev, Y. Ivanova, and R. Iordanova, "ChemInform Abstract: History of Sol-Gel Science and Technology," *ChemInform*, vol. 40, no. 12, pp. 181–192, 2009, doi: 10.1002/chin.200912249.

[17] K. Wang, M. Wei, M. A. Morris, H. Zhou, and J. D. Holmes, "Mesoporous titania nanotubes: Their preparation and application as electrode materials for rechargeable lithium batteries," *Adv. Mater.*, vol. 19, no. 19, pp. 3016–3020, 2007, doi: 10.1002/adma.200602189.

[18] "Chemical Analysis and Material Characterization by Spectrophotometry - 1st Edition." [Online]. Available: https://www.elsevier.com/books/chemical-analysis-and-material-characterization-by-spectrophotometry/kafle/978-0-12-814866-2. [Accessed: 10-Feb-2020].

[19] S. Kaneco, Y. Chen, P. Westerhoff, and J. C. Crittenden, "Fabrication of uniform size titanium oxide nanotubes: Impact of current density and solution conditions," *Scr. Mater.*, vol. 56, no. 5, pp. 373–376, 2007, doi: 10.1016/j.scriptamat.2006.11.001.

[20] M. Shahzad, M. Chaussumier, R. Chieragatti, C. Mabru, and F. Rezai-Aria, “Surface characterization and influence of anodizing process on fatigue life of Al 7050 alloy,” *Mater. Des.*, 2011, doi: 10.1016/j.matdes.2011.02.027.
[21] M. V. Diamanti, B. Del Curto, and M. P. Pedeferri, “Interference colors of thin oxide layers on titanium,” *Color Res. Appl.*, vol. 33, no. 3, pp. 221–228, 2008, doi: 10.1002/col.20403.
[22] A. Haring, A. Morris, and M. Hu, “Controlling morphological parameters of anodized titania nanotubes for optimized solar energy applications,” *Materials (Basel).*, vol. 5, no. 10, pp. 1890–1909, 2012, doi: 10.3390/ma5101890.
[23] A. K. Sharma, “Anodizing titanium for space applications,” *Thin Solid Films*, vol. 208, no. 1, pp. 48–54, 1992, doi: 10.1016/0040-6090(92)90946-9.
[24] V. Vega *et al.*, “Electrolyte influence on the anodic synthesis of TiO2 nanotube arrays,” *J. Non. Cryst. Solids*, vol. 354, no. 47–51, pp. 5233–5235, 2008, doi: 10.1016/j.jnoncrysol.2008.05.073.
[25] J. M. Macak and P. Schmuki, “Anodic growth of self-organized anodic TiO2 nanotubes in viscous electrolytes,” *Electrochim. Acta*, vol. 52, no. 3, pp. 1258–1264, 2006, doi: 10.1016/j.electacta.2006.07.021.
[26] M. R. Kaluđerović, J. P. Schreckenbach, and H. L. Graf, “Titanium dental implant surfaces obtained by anodic spark deposition – From the past to the future,” *Materials Science and Engineering C*. 2016, doi: 10.1016/j.msec.2016.07.068.
[27] J. L. H, “International Commission on Atomic Weights,” *Science (80-.).*, vol. 12, no. 296, pp. 346–347, 1900, doi: 10.1126/science.12.296.346-a.
[28] “Photocatalysis - an overview | ScienceDirect Topics.” [Online]. Available: https://www.sciencedirect.com/topics/earth-and-planetary-sciences/photocatalysis. [Accessed: 10-Feb-2020].
[29] K. Nakata and A. Fujishima, “TiO 2 photocatalysis: Design and applications,” *Journal of Photochemistry and Photobiology C: Photochemistry Reviews*. 2012, doi: 10.1016/j.jphotochemrev.2012.06.001.
[30] S. N. Ahmed and W. Haider, “Heterogeneous photocatalysis and its potential applications in water and wastewater treatment: A review,” *Nanotechnology*, vol. 29, no. 34, 2018, doi: 10.1088/1361-6528/aac6ea.
[31] M. N. Chong, B. Jin, C. W. K. Chow, and C. Saint, “Recent developments in photocatalytic water treatment technology: A review,” *Water Research*. 2010, doi: 10.1016/j.watres.2010.02.039.
[32] E. A. Clarke and R. Anliker, “Organic Dyes and Pigments,” *Handb. Environ. Chem.*, vol. 3, pp. 181–215, 1980, doi: 10.1007/978-3-540-38522-6-7.
[33] N. S. Iegemund *et al.*, *Ullmann’s Encyclopedia of Industrial Chemistry: Fluorine Compounds, Organic*. Wiley, 2000.
[34] M. Turabik, “Adsorption of basic dyes from single and binary component systems onto bentonite: Simultaneous analysis of Basic Red 46 and Basic Yellow 28 by first order derivative spectrophotometric analysis method,” *J. Hazard. Mater.*, vol. 158, no. 1, pp. 52–64, 2008, doi: 10.1016/j.jhazmat.2008.01.033.
[35] C. A. Martínez-Huitle and E. Brillas, “Decontamination of wastewaters containing synthetic organic dyes by electrochemical methods: A general review,” *Appl. Catal. B Environ.*, vol. 87, no. 3–4, pp. 105–145, 2009, doi: 10.1016/j.apcatb.2008.09.017.
[36] T. Robinson, B. Chandran, and P. Nigam, “Removal of dyes from an artificial textile dye effluent by two agricultural waste residues, corncob and barley husk,” *Environ. Int.*, vol. 28, no. 1–2, pp. 29–33, 2002, doi: 10.1016/S0160-4120(01)00131-3.
[37] W. Sadik and G. Shama, “UV-induced decolourization of an azo dye by homogeneous advanced oxidation processes,” *Process Saf. Environ. Prot. Trans. Inst. Chem. Eng. Part B*, vol. 80, no. 6, pp. 310–314, 2002, doi: 10.1205/095758202321154943.
[38] V. Naddeo, V. Belgiorno, D. Kassinos, D. Mantzavinos, and S. Meric, “Ultrasonic degradation, mineralization and detoxification of diclofenac in water: Optimization of operating parameters,” *Ultrason. Sonochem.*, vol. 17, no. 1, pp. 179–185, 2010, doi: 10.1016/j.ultsonch.2009.04.003.
[39] *Environmental aspects of textile dyeing The Textile Institute and Woodhead Publishing*. .
[40] D. Ue, D. E. L. Parlamento, and E. E. Del, “24.8.2013,” vol. 2013, pp. 1–17, 2013.
[41] O. J. Hao, H. Kim, and P. C. Chiang, “Decolorization of wastewater,” *Crit. Rev. Environ. Sci. Technol.*, vol. 30, no. 4, pp. 449–505, 2000, doi: 10.1080/10643380091184237.
[42] B. Noroozi, G. A. Sorial, H. Bahrami, and M. Arami, “Adsorption of binary mixtures of cationic

dyes," *Dye. Pigment.*, 2008, doi: 10.1016/j.dyepig.2007.02.003.
[43] L. Andronic and A. Duta, "Photodegradation processes in two-dyes systems - Simultaneous analysis by first-order spectra derivative method," *Chem. Eng. J.*, vol. 198–199, pp. 468–475, 2012, doi: 10.1016/j.cej.2012.06.019.
[44] F. Salinas, J. J. B. Nevado, and A. E. Mansilla, "A new spectrophotometric method for quantitative multicomponent analysis resolution of mixtures of salicylic and salicyluric acids," *Talanta*, vol. 37, no. 3, pp. 347–351, 1990, doi: 10.1016/0039-9140(90)80065-N.
[45] J. Karpińska, "Derivative spectrophotometry - Recent applications and directions of developments," *Talanta*, vol. 64, no. 4, pp. 801–822, 2004, doi: 10.1016/j.talanta.2004.03.060.
[46] B. Gözmen, M. Turabik, and A. Hesenov, "Photocatalytic degradation of Basic Red 46 and Basic Yellow 28 in single and binary mixture by UV/TiO2/periodate system," *J. Hazard. Mater.*, vol. 164, no. 2–3, pp. 1487–1495, 2009, doi: 10.1016/j.jhazmat.2008.09.075.
[47] E. Dinç, "The spectrophotometric multicomponent analysis of a ternary mixture of ascorbic acid, acetylsalicylic acid and paracetamol by the double divisor-ratio spectra derivative and ratio spectra-zero crossing methods," *Talanta*, vol. 48, no. 5, pp. 1145–1157, 1999, doi: 10.1016/S0039-9140(98)00337-3.
[48] A. J. Owen, "Uses of Derivative Spectroscopy," *Spectroscopy*, p. 8, 1995.
[49] E. Dinç, E. Baydan, M. Kanbur, and F. Onur, "Spectrophotometric multicomponent determination of sunset yellow, tartrazine and allura red in soft drink powder by double divisor-ratio spectra derivative, inverse least-squares and principal component regression methods," *Talanta*, vol. 58, no. 3, pp. 579–594, 2002, doi: 10.1016/S0039-9140(02)00320-X.
[50] A. Houas, H. Lachheb, M. Ksibi, E. Elaloui, C. Guillard, and J. M. Herrmann, "Photocatalytic degradation pathway of methylene blue in water," *Appl. Catal. B Environ.*, vol. 31, no. 2, pp. 145–157, 2001, doi: 10.1016/S0926-3373(00)00276-9.
[51] H. C. Yatmaz, A. Akyol, and M. Bayramoglu, "Kinetics of the photocatalytic decolorization of an azo reactive dye in aqueous ZnO suspensions," *Ind. Eng. Chem. Res.*, vol. 43, no. 19, pp. 6035–6039, 2004, doi: 10.1021/ie049921z.
[52] M. Bountogo *et al.*, "Efficacy of methylene blue monotherapy in semi-immune adults with uncomplicated falciparum malaria: a controlled trial in Burkina Faso.," *Trop. Med. Int. Health*, vol. 15, no. 6, pp. 713–7, Jun. 2010, doi: 10.1111/j.1365-3156.2010.02526.x.
[53] "Rhodamine B ≥95% (HPLC) | Basic Violet 10 | Sigma-Aldrich." [Online]. Available: https://www.sigmaaldrich.com/catalog/product/sigma/r6626?lang=it&region=IT&gclid=Cj0KCQjwmdzzBRC7ARIsANdqRRmWHbe7VOA9FdSvNHrX5ocPElildRJQQM0p4EOhVau5muhXGemmDRsaAqSzEALw_wcB. [Accessed: 22-Mar-2020].
[54] "Direct Red 80 Dye content 25 % | Sirius Red | Sigma-Aldrich." [Online]. Available: https://www.sigmaaldrich.com/catalog/product/sial/365548?lang=it&region=IT. [Accessed: 22-Mar-2020].
[55] R. Hajian and A. Soltaninezhad, "The Spectrophotometric Multicomponent Analysis of a Ternary Mixture of Paracetamol, Aspirin, and Caf.pdf," vol. 2013, pp. 1–7, 2013.
[56] F. A. El-Yazbi, H. H. Hammud, and S. A. Assi, "Derivative-ratio spectrophotometric method for the determination of ternary mixture of aspirin, paracetamol and salicylic acid," *Spectrochim. Acta - Part A Mol. Biomol. Spectrosc.*, vol. 68, no. 2, pp. 275–278, 2007, doi: 10.1016/j.saa.2006.11.027.
[57] R. Corbella Tena, M. A. Rodríguez Delgado, M. J. Sanchez, and F. Garcia Montelongo, "Comparative study of the zero-crossing, ratio spectra derivative and partial least-squares methods applied to the simultaneous determination of atrazine and its degradation product desethylatrazin-2-hydroxy in ground waters," *Talanta*, vol. 44, no. 4, pp. 673–683, 1997, doi: 10.1016/S0039-9140(96)02104-2.
[58] R. A. Spurr and H. Myers, "Quantitative Analysis of Anatase-Rutile Mixtures with an X-Ray Diffractometer," *Anal. Chem.*, vol. 29, no. 5, pp. 760–762, 1957, doi: 10.1021/ac60125a006.
[59] J. Yu and B. Wang, "Effect of calcination temperature on morphology and photoelectrochemical properties of anodized titanium dioxide nanotube arrays," *Appl. Catal. B Environ.*, vol. 94, no. 3–4, pp. 295–302, 2010, doi: 10.1016/j.apcatb.2009.12.003.
[60] M. Muthukumar, D. Sargunamani, and N. Selvakumar, "Statistical analysis of the effect of aromatic, azo and sulphonic acid groups on decolouration of acid dye effluents using advanced oxidation processes," *Dye. Pigment.*, vol. 65, no. 2, pp. 151–158, 2005, doi: 10.1016/j.dyepig.2004.07.012.
[61] N. M. Mahmoodi, M. Arami, N. Y. Limaee, and N. S. Tabrizi, "Decolorization and aromatic ring

degradation kinetics of Direct Red 80 by UV oxidation in the presence of hydrogen peroxide utilizing TiO2 as a photocatalyst," *Chem. Eng. J.*, vol. 112, no. 1–3, pp. 191–196, 2005, doi: 10.1016/j.cej.2005.07.008.

[62] K. Byrappa, A. K. Subramani, S. Ananda, K. M. Lokanatha Rai, R. Dinesh, and M. Yoshimura, "Photocatalytic degradation of rhodamine B dye using hydrothermally synthesized ZnO," *Bull. Mater. Sci.*, vol. 29, no. 5, pp. 433–438, 2006, doi: 10.1007/BF02914073.

[63] D. Regonini, C. R. Bowen, A. Jaroenworaluck, and R. Stevens, "A review of growth mechanism, structure and crystallinity of anodized TiO2 nanotubes," *Mater. Sci. Eng. R Reports*, vol. 74, no. 12, pp. 377–406, 2013, doi: 10.1016/j.mser.2013.10.001.

[64] A. Fujishima, T. N. Rao, and D. A. Tryk, "Titanium dioxide photocatalysis," *Journal of Photochemistry and Photobiology C: Photochemistry Reviews*. 2000, doi: 10.1016/S1389-5567(00)00002-2.

[65] A. Yokoo and H. Namatsu, "Nanoelectrode lithography: Chemical nanoimprint that transfers a pattern by electrochemical reaction," *NTT Tech. Rev.*, vol. 6, no. 8, 2008.

[66] "NexMaterials, nanotecnologie e rivoluzione Sol-Gel - Industria Italiana." [Online]. Available: https://www.industriaitaliana.it/materiali-la-rivoluzione-del-sol-gel/. [Accessed: 09-Feb-2020].

[67] M. V. Diamanti, B. Del Curto, and V. Masconale, "Colour : Design & Creativity," no. 5, pp. 1–9, 2010.

[68] J. M. Macak *et al.*, "TiO2 nanotubes: Self-organized electrochemical formation, properties and applications," *Curr. Opin. Solid State Mater. Sci.*, vol. 11, no. 1–2, pp. 3–18, 2007, doi: 10.1016/j.cossms.2007.08.004.

[69] "Methylene Blue | C16H18ClN3S | ChemSpider." [Online]. Available: http://www.chemspider.com/Chemical-Structure.5874.html. [Accessed: 11-Feb-2020].

[70] "Rhodamine B | C28H31ClN2O3 | ChemSpider." [Online]. Available: http://www.chemspider.com/Chemical-Structure.6439.html?rid=610e60e4-a4d5-4bf2-911f-af7d07d51bed. [Accessed: 11-Feb-2020].

[71] "Hexasodium (3E,3'E)-7,7'-(carbonyldiimino)bis[4-oxo-3-({2-sulfonato-4-[(E)-(4-sulfonatophenyl)diazenyl]phenyl}hydrazono)-3,4-dihydro-2-naphthalenesulfonate] | C45H26N10Na6O21S6 | ChemSpider." [Online]. Available: http://www.chemspider.com/Chemical-Structure.7845597.html?rid=4f9f0bc9-d54a-4698-b038-9b311bb6b707&page_num=0. [Accessed: 11-Feb-2020].

[72] J. Schneider *et al.*, "Understanding TiO2photocatalysis: Mechanisms and materials," *Chem. Rev.*, vol. 114, no. 19, pp. 9919–9986, 2014, doi: 10.1021/cr5001892.

[73] "Wavelength-Modulation Spectroscopy – The Goldenstein Group @ Purdue University." [Online]. Available: https://goldensteingroup.com/our-research/wavelength-modulation-spectroscopy/. [Accessed: 11-Feb-2020].